TAL TECH

DOCTORAL THESIS

Crystallographic Analysis of Organic Compounds: From Small Molecules to Supramolecular Complexes

Jevgenija Tamm

TALLINNA TEHNIKAÜLIKOOL
TALLINN UNIVERSITY OF TECHNOLOGY
TALLINN 2026

TALLINN UNIVERSITY OF TECHNOLOGY
DOCTORAL THESIS
59/2026

Crystallographic Analysis of Organic Compounds: From Small Molecules to Supramolecular Complexes

JEVGENIJA TAMM

TAL TECH PRESS

TALLINN UNIVERSITY OF TECHNOLOGY
School of Science
Department of Chemistry and Biotechnology
This dissertation was accepted for the defence of the degree 27/08/2026

Supervisor: Prof. Riina Aav
School of Science
Department of Chemistry and Biotechnology
Tallinn University of Technology
Tallinn, Estonia

Co-supervisor: Prof. Kari Rissanen
Faculty of Mathematics and Science
Department of Chemistry
University of Jyvaskyla
Jyväskylä, Finland

Opponents: Associate Prof. Magdalena Małecka
Faculty of Chemistry
Department of Physical Chemistry
University of Łódź
Łódź, Poland

Prof Marco Kirm
Faculty of Science and Technology
Institute of Physics
University of Tartu
Tartu, Estonia

Defence of the thesis: 29/09/2026, Tallinn

Declaration:
Hereby I declare that this doctoral thesis, my original investigation and achievement, submitted for the doctoral degree at Tallinn University of Technology has not been submitted for doctoral or equivalent academic degree.

Jevgenija Tamm

---
signature

European Union
European Regional
Development Fund

Investing
in your future

ISSN 2585-6898 (paperback)
ISBN 978-9916-80-563-3 (paperback)
ISSN 2585-6901 (PDF)
ISBN 978-9916-80-556-5 (PDF)
https://doi.org/10.23658/taltech.59/2026
Printed by Koopia Niini & Rauam

Tamm, J. (2026). *Crystallographic Analysis of Organic Compounds: from Small Molecules to Supramolecular Complexes* [TalTech Press]. https://doi.org/10.23658/taltech.59/2026

TALLINNA TEHNIKAÜLIKOOL
DOKTORITÖÖ
59/2026

Orgaaniliste ainete kristallstruktuuride analüüs: väikestest molekulidest supramolekulaarsete kompleksideni

JEVGENIJA TAMM

TAL TECH
KIRJASTUS

Contents

List of Publications

The list of author's publications, on the basis of which the thesis has been prepared:

I Trubitsõn, D.; **Martõnova, J**.; Kudrjašova, M.; Erkman; K.; Järving, I.; Kanger T. (2021). Enantioselective Organocatalytic Michael Addition to Unsaturated Indolyl Ketones. *Organic Letters*, 23 (5), 1820−1824. DOI: 10.1021/acs.orglett.1c00222

II Trubitsõn, D.; **Martõnova, J.**; Erkman, K.; Metsala, A.; Saame, J.; Kõster, K.; Järving, I.; Leito, I.; Kanger, T. (2020). Enantioselective N-Alkylation of Nitroindoles under Phase-Transfer Catalysis. *Synthesis*, 52 (07), 1047−1059. DOI: 10.1055/s-0039-1690751

III Kaasik, M.; **Martõnova, J**.; Erkman, K.; Metsala, A.; Järving, I.; Kanger, T. (2021). Enantioselective Michael addition to vinyl phosphonates via hydrogen bond-enhanced halogen bond catalysis. *Chemical Science*, 21, 7561−7568. DOI: 10.1039/D1SC01029H

IV Ward, J. S.; **Martõnova, J.**; Wilson, L. M. E.; Kramer, E.; Aav, R.; Rissanen, K. (2022). Carbonyl Hypoiodites from Pivalic and Trimesic Acid and their Silver(I) Intermediates. *Dalton Transactions*, 14646−14653. DOI: 10.1039/d2dt01988d

V Nikonovich, T.; Jarg, T.; **Martõnova, J.**; Kudrjašov, A.; Merzhyievskyi, D.; Kudrjašova, M.; Gallou, F.; Aav, R; Kananovich, D. (2024). Protecting-group-free mechanosynthesis of amides from hydroxycarboxylic acids: application to the synthesis of imatinib. *RSC Mechanochemistry*, 1 (2), 189−195. DOI: 10.1039/D4MR00006D

VI **Tamm, J.**; Kaabel, S.; Shubin, K.; Ward, J.S.; Adamson, J.; Aav, R. (2025). Solvent Exchange in Cobalt-Metal Organic Framework. *Supramolecular Chemistry*. DOI: 10.1080/10610278.2025.2587118

VII Suut-Tuule, E.; Jarg, T.; Tikker, P.; Lootus, K.-M.; **Martõnova, J.**; Reitalu, R.; Ustrnul, L.; Ward, J. S.; Rjabovs, V.; Shubin, K.; Nallaparaju, J. V.; Vendelin, M.; Preis, S.; Öeren, M.; Rissanen, K.; Kananovich, D.; Aav, R. (2024). Mechanochemically driven covalent self-assembly of a chiral mono-biotinylated hemicucurbit[8]uril. *Cell Reports Physical Science*, 5, 9. DOI: 10.1016/j.xcrp.2024.102161

Author's Contribution to the Publications

Contribution to the papers in this thesis are:

I The author was responsible for single-crystal measurement, data refinement and characterization of a product to assign correct absolute configuration. The author participated in the compilation of supporting material and preparation of the manuscript.

II The author was responsible for single-crystal measurement, data refinement and characterization of a product to assign correct absolute configuration. The author participated in the compilation of supporting material and preparation of the manuscript.

III The author was responsible for single-crystal measurement, data refinement and characterization of a product to assign correct absolute configuration. The author participated in the compilation of supporting material and preparation of the manuscript.

IV The author was responsible for single-crystal measurement, data refinement and characterization of a products to study halogen-bonded system. The author participated in the compilation of supporting material and preparation of the manuscript.

V The author was responsible for single-crystal measurement, data refinement and characterization of an intermediate product to prove the structure of it and potentially explain some complication steps in the system based on single-crystal data. The author participated in the compilation of supporting material and preparation of the manuscript.

VI The author was responsible for single-crystal measurement, data refinement and characterization of used materials and kinetics studies of solvent exchanged systems. The author had a significant role in the compilation of the supporting material and preparation of the manuscript.

VII The author was responsible for single-crystal measurement, data refinement and characterization of an inclusion complex to prove the structure of the main compound and showcase the host-guest binding in solid state. The author participated in the compilation of supporting material and preparation of the manuscript.

Introduction

The unambiguous determination of molecular structure in the solid state is foundational to chemistry. The ability to characterise, at atomic resolution, the three-dimensional arrangement of atoms and the non-covalent interactions that govern molecular packing is indispensable to the rational design of active pharmaceutical ingredients (APIs), the construction of supramolecular architectures, and the development of porous metal–organic frameworks (MOFs). X-ray crystallography, in particular single-crystal X-ray diffraction (SC-XRD) and powder X-ray diffraction (PXRD), remains the gold standard for this purpose, providing information inaccessible by any other analytical technique.

The relevance of this domain is underscored by a century of Nobel Prize-recognised discoveries built upon crystallographic foundations, from the wave nature of X-rays and Bragg's law to the characterisation of mechanically interlocked molecules and molecular machines and the more recent structural validation of porous MOFs. Contemporary challenges in pharmaceutical polymorphism, asymmetric organocatalysis, host–guest chemistry, and framework materials science all demand rigorous solid-state structural analysis.

X-ray crystallographic characterisation is the subject of this thesis as it remains systematically underutilised as an integrated tool across research programmes spanning synthetic organic chemistry, coordination chemistry, supramolecular chemistry, and materials science. While the technique is often applied in isolation for structural confirmation, its full analytical power – encompassing absolute configuration assignment, polymorph identification, reaction monitoring, and host–guest interaction mapping – is rarely deployed in a unified, cross-disciplinary framework.

The purpose of this thesis is to demonstrate and advance the application of X-ray diffraction methods across four interconnected areas: (1) the unambiguous assignment of absolute configuration in enantioselective organocatalytic reactions; (2) the structural characterisation of coordination compounds and hypervalent iodine reagents relevant to pharmaceutical synthesis; (3) the investigation of polymorphism, solid-state transformations, and reaction monitoring in crystalline materials; and (4) the characterisation of complex supramolecular and framework systems, including host–guest complexes and MOFs. To these ends, the thesis involved the following steps: collecting and refining high-quality SC-XRD and PXRD data for a diverse range of compounds; applying the Flack parameter for absolute structure determination; identifying and characterising new polymorphic forms; monitoring solid-state transformations in situ; and elucidating the non-covalent interaction networks – hydrogen bonding, halogen bonding, π–π stacking, and metallophilic contacts – that govern crystal packing and functional properties.

The central research question investigated is: how can X-ray crystallographic techniques be most effectively deployed – individually and in combination – to deliver structural, stereochemical, and dynamic insights across a wide range of chemical systems, from small chiral organic molecules to MOFs; and what novel structural information can such an integrated approach reveal?

The primary methodology employed was SC-XRD, with PXRD used as a complementary bulk-phase validation and reaction-monitoring tool. Supporting analytical methods included ^{1}H NMR spectroscopy for solution-state characterisation and kinetics measurements, and HPLC for compositional analysis.

The baseline information draws on the Cambridge Structural Database (CSD) for structural benchmarking, Bragg's law and classical crystallographic theory, the Flack parameter formalism, classical nucleation theory, and Ostwald's rule of stages, together with prior literature for each compound class investigated: indolyl ketone organocatalysis, silver and hypervalent iodine coordination chemistry, cucurbituril and cyclohexanohemicucurbituril host–guest systems, and cobalt-based MOFs.

The theoretical novelty of this thesis lies in the unified treatment of non-covalent interaction hierarchies across structurally diverse chemical classes, thereby demonstrating that hydrogen bonding, halogen bonding, π-stacking, van der Waals forces, and metallophilic interactions collectively determine not only crystal packing but also pharmaceutical performance, catalytic selectivity, and framework flexibility. The practical novelty encompasses the discovery of a new solvate polymorph (Cobalt-MOF*), which exhibits a contracted void volume consistent with the framework breathing phenomenon; the first crystallographic characterisation of several organocatalytic adducts and hypervalent iodine coordination compounds; unambiguous absolute configuration assignments for a series of chiral indole derivatives; and the structural elucidation of an enantiopure PF_6^-@(-)- mixHC[8] inclusion complex by SC-XRD, including modelling of 50:50 positional disorder in a co-crystal.

The outcomes of this thesis have been reported in seven publications (Publications I-VII) in peer-reviewed international journals, encompassing original research articles in the fields of asymmetric organocatalysis, coordination and supramolecular chemistry, pharmaceutical solid-state science, and MOF chemistry. The structural data reported herein have been deposited with the Cambridge Crystallographic Data Centre (CCDC). Collectively, these contributions affirm the potential role of X-ray crystallography as an integrative analytical platform capable of bridging molecular synthesis and functional materials design.

Abbreviations

SC-XRD	Single-crystal X-ray diffraction
PXRD	Powder X-ray diffraction
HPLC	High-performance liquid chromatography
NMR	Nuclear magnetic resonance spectroscopy
API	Active pharmaceutical ingredient
MOF	Metal-organic framework
SCSC	Single-crystal-to-single-crystal
ECD	Electronic circular dichroism
VCD	Vibrational circular dichroism
THP	Theophylline
DNBA	3,5-dinitrobenzoic acid
GooF	Goodness-of-fit
FWHM	Line broadening at half the maximum intensity
e.s.d	Estimated standard deviation
DMF	Dimethylformimide
DCM	Dichloromethane
DMSO	Dimethyl sulfoxide
THF	Tetrahydrofuran
MeCN	Acetonitrile
DIPE	Diisopropylether
TBME	*Tert*-butyl methyl ether
TBA	*Tert*-butyl alcohol
$TBAPF_6$	Tetrabutylammonium hexafluorophosphate
EDC	1-ethyl-3-(3-dimethylaminopropyl)carbodiimide
DMAP	4-Dimethylaminopyridine
TTPA	Tris(4-(1H-1,2,4-triazol-1-yl)phenyl)amine
BTC	Benzene-1,3,5-tricarboxylate
py	Pyridine
4-Mepy	4-methylpyridine
4-morpy	4-morpholinopyridine
OI	Hypoiodite
DBA	Dibenzylammonium
MTA	Methyl triazolium
mixHC[8]	Chiral mono-biotinylated hemicucurbit[8]uril
cycHC[n]	Cyclohexanochemicucurbit[n]uril
IUCr	The International Union of Crystallography

SAD/MAD	Single-wavelength anomalous diffraction/multi-wavelength anomalous diffraction
C-PCM	DCM continuum solvation model
APS	Ammonium Persulfate

Symbols

d_{hkl}	Distance separating multiple atomic planes
λ	X-ray wavelength
θ	angle of incidence with lattice plane
F	Structure factor
R	Value indicating the consistency of symmetry-equivalent reflections in the measured SC-XRD data set
B_M^2	Observed peak width
B_s^2	Peak width of a crystalline standard
E	Potential energy
q	Magnitude of the electric charge
r	Distance between the centres of two charges
ε_0	Permittivity of free space (vacuum permittivity)
ε	Relative permittivity (dielectric constant) of the material between the charges
4π	Geometric factor related to the spherical symmetry of the electric field, μ - the magnitude of the dipole moment
μ	Magnitude of the dipole moment
τ	Average crystallite size
K	Shape factor
β	Line broadening at half the maximum intensity (FWHM)
η	Rogers parameter
x	Flack parameter
S	Goodness-of-fit (GooF) parameter

1. Literature overview

1.1. History

Crystallography has become an essential tool for researchers, and its development and applications have been recognised in the frontline of science. Crystallography has been shaped by several Nobel Prize–winning advances, beginning with its physical foundations. Max von Laue's 1914 Nobel Prize in Physics established X-ray diffraction by crystals, confirming both the wave nature of X-rays and the ordered internal structure of crystalline solids.[1] In 1915, William Henry Bragg and William Lawrence Bragg further transformed the field by formulating Bragg's law and enabling the determination of atomic arrangements in crystals, establishing crystallography as a quantitative physical method.[2]

The technique later expanded into chemistry and biology, underpinning Nobel-recognized structure determinations of complex molecules and macromolecules. In contemporary research, crystallography remains central to supramolecular and materials chemistry. The 2016 Nobel Prize in Chemistry, awarded to Jean-Pierre Sauvage, J. Fraser Stoddart, and Bernard Feringa, relied heavily on crystallographic characterization of mechanically interlocked molecules and molecular machines, particularly in Stoddart's work.[3] Similarly, in 2025 discovery and application on porous metal-organic frameworks studied by Susumu Kitagawa, Richard Robson and Omar M. Yaghi's [4] was directly founded on crystallographic analysis and further design and validating porous crystalline materials.[5]

1.2. Non-covalent interactions to control complex structures

Non-covalent interactions play a central role in controlling the formation and stability of complex molecular and supramolecular structures. Unlike covalent bonds, these interactions—hydrogen bonding[6], π–π stacking[7], electrostatic forces[8], van der Waals interactions[9], and metal coordination[10]—are individually weak but collectively capable of directing highly ordered architectures. Their reversibility and directionality enable dynamic assembly processes, error correction, and structural adaptability, which are essential for the formation of complex crystalline and supramolecular systems.[11,12]

Hydrogen bonding[6] is among the most widely exploited interactions in crystal engineering, providing predictable geometries and strong directional preferences that guide molecular packing and polymorph formation. π–π interactions[7] and dispersion forces contribute to the stabilization of aromatic assemblies and layered structures, while electrostatic interactions influence ionic crystal organization and co-crystal formation. Together, these forces govern the self-assembly of molecular solids, host–guest complexes, and biomolecular architectures, where subtle energetic balances determine structural outcomes.

In supramolecular chemistry, non-covalent interactions enable the construction of higher-order assemblies such as rotaxanes[13,14], catenanes[15,16], and coordination frameworks[17]. These systems rely on recognition motifs and complementary binding sites, where multiple weak interactions operate cooperatively to produce robust yet dynamic structures. In materials science, the same principles underpin the formation of porous frameworks, molecular crystals with tuneable properties, and responsive solids capable of adapting to external stimuli. Consequently, understanding and controlling

non-covalent interactions is fundamental to rational design in crystal engineering, polymorphism, and functional molecular materials.

Table 1. *Different types of non-covalent interactions*
Table 1a. *Hydrogen and halogen bonding*

Hydrogen bonding				**Halogen bonding**	
Sub-type	**Strong**	**Moderate**	**Weak**		
Strength (kJ · mol^{-1})	60 – 160	16 – 60	< 12	**Strength (kJ · mol^{-1})**	10 – 150
Donor atom and molecule		Hydrogen (*H*) 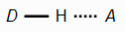		**Donor atom and molecule**	Halogen (*X = I, Br, Cl, F*)
Bond angle *(D···A)*	Linear (170˚–180˚) 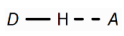	Slightly bent (130˚ – 180˚) 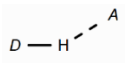	Very nonlinear (90˚ – 150˚) 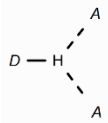	**Bond angle**	Linear (170˚ – 180˚) 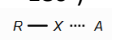
Bond length (Å, *D···A*)	2,2 – 2,5	2,5 – 3,2	> 3,2	**Bond length (Å, *D···A*)**	4,4 – 5,6
Bond length (Å, *H···A*)	1,2 – 1,5	1,5 – 2,2	2,2 – 3,2	**Bond length (Å, *X···A*)**	2,7 – 3,5
H-atom position	Often centered	Off-center	Off-center	**X-atom position**	Centered on the bond axis
***D – H ···A* interaction**	Significant covalent character	Mostly electrostatic	Electrostatic	***D – X ···A* interaction**	σ-hole
Examples	*[F···H···F]* $^-$	*O – H···O, N – H···N*	*C – H···O, C – H···π*	**Examples**	**see below*
* 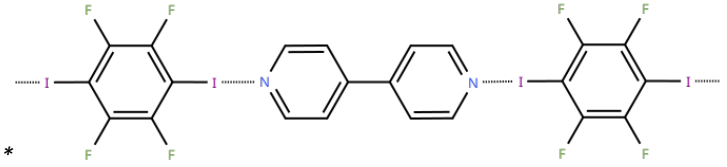					

A - hydrogen bond acceptor; *D–H* - hydrogen bond donor; *R–X* – halogen bond donor

Table 1b. *Electrostatic interactions*

Electrostatic interactions			
Sub-type	**Ion-Ion (strong)**	**Ion-dipole (moderate)**	**Dipole-dipole (weak)**
Strength (kJ mol^{-1})	200 – 300	50 – 200	5 – 50
Energy equation (dependence on distance)	$E = \frac{q_1 q_2}{4\pi\varepsilon\varepsilon_0 \boldsymbol{r}}$ 1 / r (long range forces)	$E = \frac{\mu q_2 \cos\theta}{4\pi\varepsilon\varepsilon_0 \boldsymbol{r^2}}$ 1 / r^2 (short range forces)	$E = \frac{-\mu_1\mu_2(3cos^2\theta - 1)}{4\pi\varepsilon\varepsilon_0 \boldsymbol{r^3}}$ 1 / r^3 to 1 / r^6 (short range forces)
Participants	Two ions (Cation + Anion)	An ion + A polar molecule	Two polar molecules
Examples	Sodium chloride $Na^+ Cl^-$	Hydrated sodium ions $Na^+\cdots OH_2$	Solid state of polar ICl 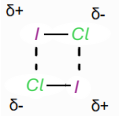

E - potential energy (J), q – magnitude of the electric charge (C), r – distance between the centres of two charges, ε_0 - the permittivity of free space (vacuum permittivity), ε - the relative permittivity (dielectric constant) of the material between the charges, 4π - a geometric factor related to the spherical symmetry of the electric field, μ - the magnitude of the dipole moment, θ - the angle between the axis of one dipole and the line connecting the centres of the two dipoles.

Table 1c. *π - interactions*

π - interactions				
Sub-type	**Cation-π (strong)**	**Anion-π (moderate)**	**π-π (weak)**	
Strength (kJ mol^{-1})	5 – 80	5 – 30	0 – 50	
Interaction character	Significant covalent character	Electrostatic and polarisation components	Face-to-face: Dispersion + Quadrupole-Quadrupole	Edge-to-face: Electrostatic
Description	A cation sits on the face of an electron-rich aromatic ring	An anion interacts with an electron-deficient aromatic ring	Two rings "stack" to minimize repulsion and maximize van der Waals forces	
Participants	Positive ion + π-cloud	Negative ion + π-cloud	Two aromatic systems	
Examples	Fullerene (C_{60}) binding Cs^+ cation	ClO_4^- anion in calix[4]arene-porphyrin conjugate receptor	π-π stacking between bases in DNA double helix	

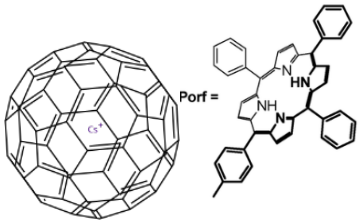

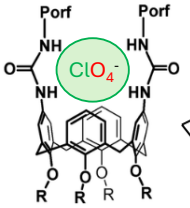

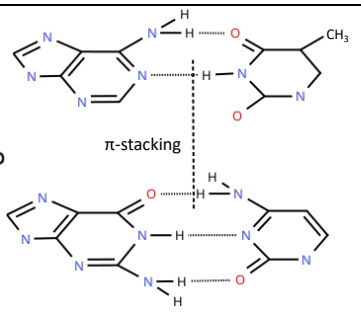

Table 1d. *Other non-covalent Interactions*

Other non-covalent Interactions			
	van der Waals	**Solvophobic**	**Metallophilic**
Strength (kJ · mol^{-1})	< 5 [a]	0 – 100 [b]	5 – 50
Interaction character	Induced Dipole (London Dispersion)	Entropy (Solvent Exclusion)	Correlation/Relativistic effects
Dependence	1 / r^6 (Very short range)	Surface area dependent	1 / r^n (Short range)
"Donor" sources	All atoms (electronrich)	Non-polar molecules	d^{10}, d^8 or s^2 metal ions
"Acceptor" sources	All atoms (electronpoor)	Non-polar molecules	Matching metal ions
Examples	Carbon nanotubes 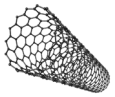	Micelle formation 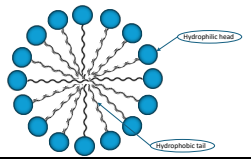	Aurophilic chains in gold-based molecular wires *see below*

*

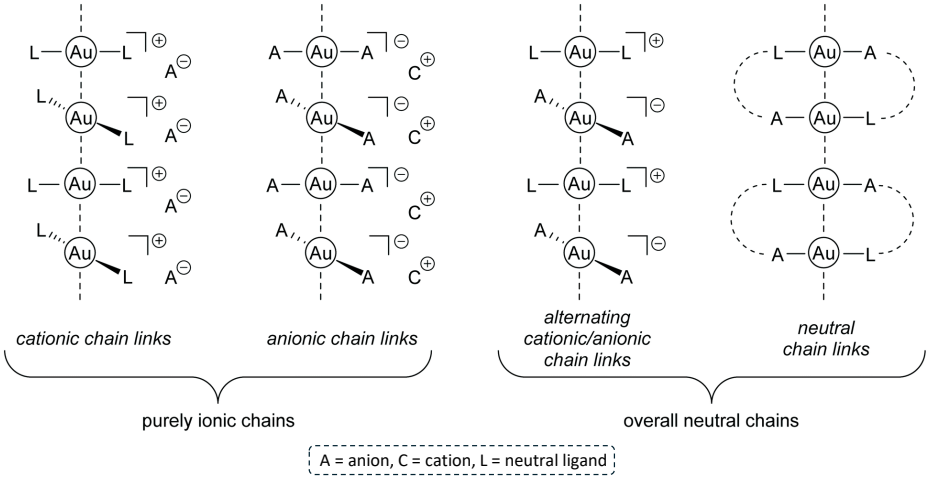

[a] Dependent on the surface area of the molecules

[b] Dependent on the solvent-solvent interactions, host geometry / size of the binding pocket, and the nature of the functional groups lining the host's binding site.

Rotaxanes are interesting class of supramolecular systems with mechanically locked macrocycles around rod-type molecule. For example, in pH-responsive rotaxanes18, the translocation of a macrocycle between disparate recognition sites on a molecular thread is driven by the relative thermodynamic stability of the resulting co-conformations and is governed by the switchable protonation state of a dialkylammonium station.

In the protonated state, the structural integrity of the rotaxane is governed by high-affinity electrostatic interactions. Upon the addition of a Brønsted base (e.g.,

phosphazene or triethylamine), the ammonium center is deprotonated to the neutral amine. This chemical modification fundamentally reorganizes the non-covalent hierarchy (Figure 1).[18]

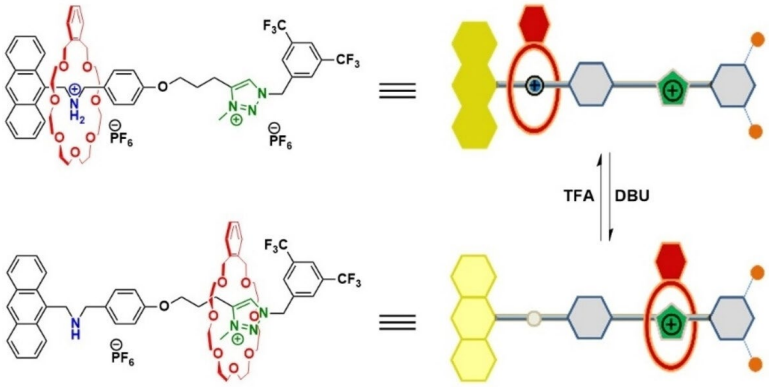

Figure 1. *[23]Crown ether shuttling between dibenzylammonium (DBA$^+$) and methyl triazolium (MTA$^+$) stations. DBA colored in blue and MTA in green*

Table 2. *Features of protonated and de-protonated state of ammonium center in rotaxane*

Feature	Protonated state	De-Protonated state
Active interaction	Ion -dipole + Hydrogen bonding	Ion -dipole + π-π stacking
Bond energy	High (strongly stabilised)	Moderate (more mobile)
Bonding Geometry	Centered, Perpendicular	Offset, Face-to-face
Conformation	Highly Localized ("Locked")	Translocated ("Shuttled")

A classic example of a crystal structure stabilized by multiple distinct non-covalent interactions is caffeine (1,3,7-trimethylpurine-2,6-dione). In its various forms, particularly in cocrystals, it demonstrates a complex interplay of forces that define its stability and packing.[19,20] Though a derivative of caffeine, theophylline (THP) serves as a similar pharmaceutical model that illustrates hierarchical stabilization.[21,22]

The THP–DNBA cocrystal adopts a 2D-layered architecture and its asymmetric unit contains one molecule of theophylline (THP) and one molecule of 3,5-dinitrobenzoic acid (DNBA). The structure is organized into flat, sheet-like layers that allow for mechanical shearing, which gives the crystal its unique plastic bending properties.[21]

The stability of this crystal is governed by three primary types of non-covalent forces that work together across different dimensions. Primary stabilisation is achieved through strong hydrogen bonding. The structure is primarily anchored by a hydrogen bond between the carboxylic acid group of DNBA and the imidazole nitrogen of THP.[23,24] Secondary bonds often connect THP molecules to each other or to the nitro groups of DNBA, forming the fundamental 2D layer.[25] Within the layers, the planar aromatic rings of both THP and DNBA stack atop one another. This stacking is "slipped-parallel," providing a large contact area that stabilizes the flat molecular geometry required for its mechanical properties.[26] Between the 2D sheets, the interactions are significantly weaker, consisting mainly of Van der Waals forces and weak contacts.[21]

Because these interlayer forces are weak, the layers can slide over one another easily, which is why the crystal can bend without shattering—a rare "plastic" behaviour for organic crystals (Figure 2).[21,27]

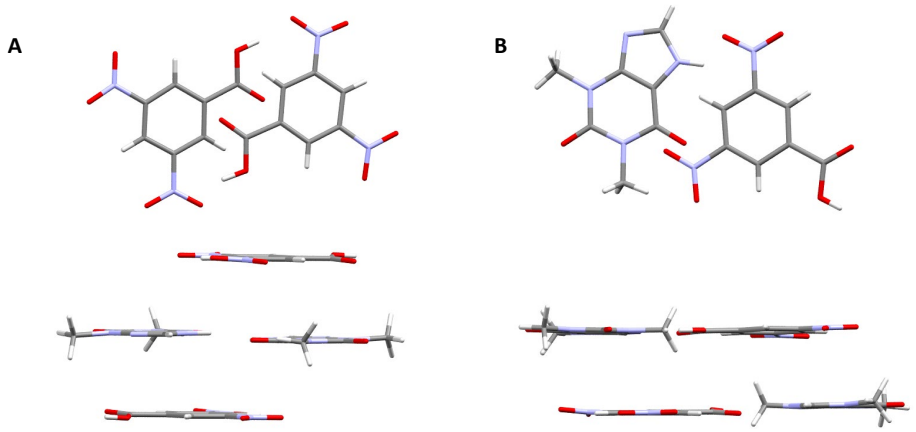

Figure 2. *A – crystal structure of caffeine and stacked caffeine molecules; B – crystal structure of theophylline and stacked theophylline molecules*[28]

1.3. Methods used for solid state structure evaluation and description

Evaluating and describing the solid-state structure of materials is essential in fields like materials science, chemistry, and crystallography.[29] Several methods and techniques are employed to characterize the atomic and molecular arrangements in solid materials. These methods can be broadly categorized into experimental techniques[30] and computational approaches[31].

By combining several of these methods, a detailed and comprehensive understanding of the solid-state structure of materials can be achieved. Each technique has its advantages, depending on the material's properties, the scale of the structure, and the required level of detail.[32]

This work concentrated on exploiting X-rays for structural analysis of small molecules, host-guest complexes and metal-organic framework prepared by various methods to aid in the characterization of target molecules[33,34], as well as monitoring of the reactions to gain perspective of processes happening during the synthesis[35–37].

1.3.1. X-ray diffraction

The analysis method relies on the dual nature of X-rays, which exhibit both wave and particle behaviour.[38,39] It involves the elastic reflection of a monochromatic X-ray beam (coherent electromagnetic radiation) from the electron clouds surrounding the atoms in a crystal lattice. This process generates a diffraction pattern, or X-ray pattern, which is an ordered arrangement of reflected beams.[38,40,41] In a crystal, atoms are arranged in parallel planes, and when X-rays strike these planes, part of the radiation is scattered at an angle equal to the angle of incidence. Because the crystal contains multiple atomic planes separated by a distance d_{hkl}, the scattered X-rays travel different optical paths.[38,42] This variation leads to either constructive or destructive interference in the scattered radiation.[38,43]

Constructive interference occurs when the phase difference between the reflected rays equals to an integral value of the wavelength (Figure 3).[38,40]

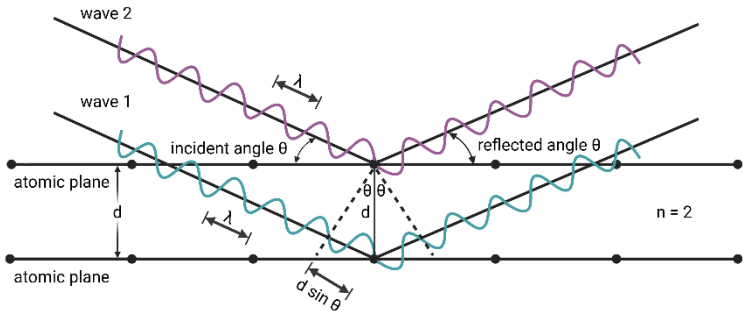

$$n\lambda = 2d \sin\theta \qquad \textbf{Equation 1.}$$

Figure 3. *Constructive interference of X-rays and Bragg's law* ***Equation 1****, where* λ *= X-ray wavelength,* d *= distance between lattice planes,* θ *= angle of incidence with lattice plane,* n *= diffraction order*

This results in the formation of diffraction lines, which can be described using Bragg's formula (Equation 1).

For Bragg's law to be satisfied, the material under study must possess a high degree of structural order to allow X-rays to scatter coherently.[44] In materials with only short-range structural order, such as liquids and amorphous solids, constructive interference cannot occur because these materials lack the regular atomic arrangements in planes required to produce well-defined diffraction peaks.[41,45] In contrast, ordered solids exhibit a structured atomic arrangement, enabling the diffraction pattern to be obtained by measuring the intensity of scattered waves as a function of the scattering angle across all atomic planes.

Two types of ordered solids can be distinguished (Figure 4). In single crystals, the lattice planes are aligned in a single direction, resulting in well-defined diffraction patterns.[46] Polycrystalline materials, however, have lattice planes oriented in multiple directions, which becomes significant when characterizing such materials.[47,48]

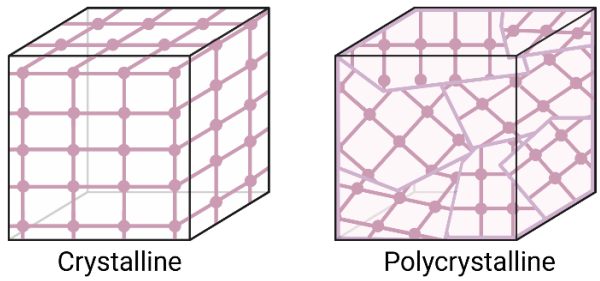

Figure 4. *Crystalline and polycrystalline solids*

1.3.2. Single-crystal X-ray diffraction

The crystal lattice is described by identifying the smallest repeating unit, known as the unit cell, which can be represented as a parallelepiped defined by the base vectors, and the angles α, β, and γ between them. When this unit cell is repeated in three-dimensional

space, it uniformly represents the entire lattice. Typically, the unit cell with the smallest possible volume is chosen. The crystal lattice can also be divided into parallel planes, each with a specific orientation relative to the unit cell. These planes are characterized by three integers, known as the Miller indices *h*, *k*, and *l* (Figure 5), and the distances d_{hkl} between them. The Miller indices *h*, *k*, and *l* are determined as the reciprocals of the points where the plane intersects the unit cell axes. The lengths of the unit cell axes a, b, and c are expressed as integers, and the intersection points are represented as reciprocal values, i.e., 1/*h*, 1/*k*, 1/*l*, and based on their distances from the origin where the axes intersect.

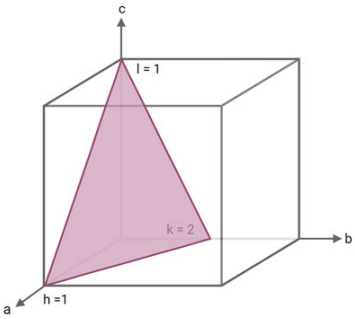

Figure 5. *The orientation of the planes with Miller indices (121) in relation to the unit cell*

The physical properties of a crystal are influenced by its symmetry, making it possible to determine the crystal lattice structure through the symmetry elements of the crystal. These elements, such as reflection planes, rotation axes, and screw axes, define the crystal's geometry. Combinations of these symmetry elements are classified into 230 space groups (including chiral variants), which significantly reduce the complexity of describing the unit cell. These space groups are categorized into seven crystal systems: triclinic, monoclinic, orthorhombic, tetragonal, hexagonal, trigonal, and cubic.

The diffraction frames collected during the measurement are analysed to determine the reflection angles and intensities of all reflections (Figure 6).

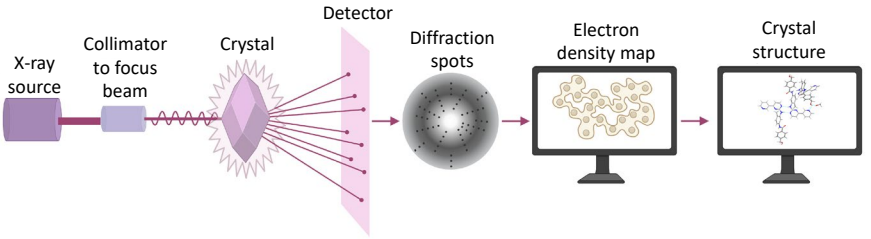

Figure 6. *Schematic representation of determination of structure of single crystal*

These data directly reveal the parameters of the crystal structure's unit cell and the space group of the crystal lattice and indirectly provide the electron density map of the unit cell. The electron density map, a three-dimensional representation of electron distribution, serves as the basis for constructing a molecular model in crystallography. To generate an interpretable electron density map, the reflection angle θ, amplitude, and phase of the reflected beam must be determined. These properties define the structure factor *F*, which comprises both real and imaginary components.

The amplitude of diffracted rays can be represented by a real component, while the phase corresponds to an imaginary component. The total amplitude and phase of the

diffracted ray account for the contributions of electrons located in the *h*, *k*, and *l* planes, as well as those from atoms outside these planes. Experimentally, it is not possible to directly determine the phase; only the intensity of the diffracted beam can be measured, which is proportional to the square of the structure factors, F^2_{obs} . To determine the phase of the reflected beam, a model structure must be developed where the atomic coordinates (x, y, z) relative to the unit cell origin (0, 0, 0) align with the diffraction pattern. Discrepancies between the electron density map derived from the model and the one obtained from experimental data suggest that the model does not fully match the actual structure and requires refinement. For accurate calculation of the electron density map from the structure factors F_{obs} , at least 30–50% of the molecular structure must be correctly modelled. Without this, the phase components of the calculated structure factors F_{cal}, combined with the measured intensities, cannot reliably produce the desired electron density map.

Various methods are used to determine the model structure, with the most common approaches for organic molecules being direct methods, suitable for structures composed of light atoms, and Patterson's function, applicable when the molecule contains at least one heavy atom. The model structure is optimized using the least-squares method, where the process continues until the difference between the squares of the calculated structure factors (F^2_{cal}) and the observed intensities (F^2_{obs}) is minimized. From this, the *R-int* value is determined, indicating the consistency of symmetry-equivalent reflections in the measured SC-XRD data set. For a successful result, the R_1-value of the optimal model structure should be below 0.05, and the weighted ωR_2-value should be less than 0.15. Additionally, the goodness-of-fit (GooF) parameter *S*, which should be close to 1, must also be considered.[49,50]

For crystal structures containing small molecules, the lower limit for the measurement results is given as which corresponds to a maximum allowable d_{min} value of 0.83 Å (Equation 2).

$$d_{min} = \frac{\lambda}{2 \sin \theta_{max}}$$

Equation 2.

Equation 2. Relationship between the maximum permissible interplane distance d_{min} and the IUCr resolution limit

Like any analytical method, SC-XRD has its advantages and limitations. SC-XRD is a highly powerful technique. The scattering of X-rays by atoms within crystal structures enables it to provide invaluable information about atomic and molecular distances and structures. Single-crystal XRD provides exceptional insights into the atomic structure of a crystal, including precise bond lengths and angles. As it is mostly non-destructive technique, the sample is not damaged or altered in this, enabling repeated measurements or additional analyses on the same specimen. As XRD achieves highly accurate atomic position determination, often to within a picometer range, this method is exceptionally precise. Though being very advanced and advantageous method, SC-XRD also has some disadvantages. Due to single-crystal XRD requiring relatively large (a common size is approximately 0.2×0.2×0.2, but anything from 0.1 mm to 0.4 mm is often suitable), high-quality crystals and is more effective with single-crystal samples than with polycrystalline ones, method is limited to growing the appropriate crystal for measurement. Besides that, a complete data collection may require anywhere between

6-24 hours, depending on the specimen and the diffractometer, making this method more time-consuming compared to other analytical techniques.

1.3.3. Powder X-ray diffraction

When X-rays are directed at a crystal, they diffract in a pattern unique to its structure. In powder X-ray diffraction, the diffraction pattern is obtained from a powdered sample of the material instead of a single crystal (Figure 7). This method is often more convenient than single-crystal diffraction, as it does not require the preparation of individual crystals. Powder XRD also provides a diffraction pattern representing the bulk material of a crystalline solid, offering a more comprehensive view than a single crystal, which may not fully represent the entire material. The resulting diffraction pattern is a plot of intensity versus the detector angle, 2θ.

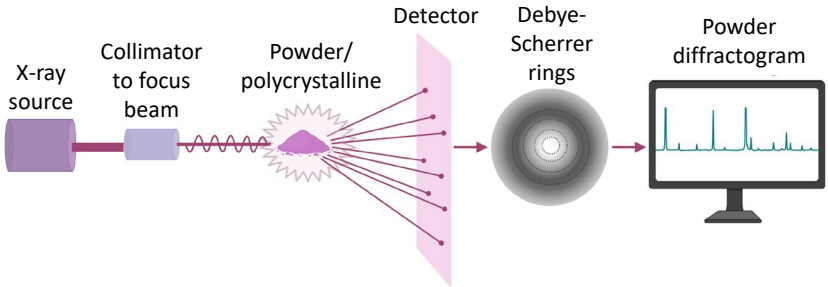

Figure 7. *Schematic representation of determination of diffraction pattern of powder*

Because most materials have unique diffraction patterns, compounds can be identified by comparing their patterns to a database. The diffraction pattern can also reveal the sample's purity and the composition of any impurities present. Additionally, it can be used to determine and refine the lattice parameters of a crystal structure. A theoretical structure can be further refined using the Rietveld refinement method. Moreover, the particle size of the powder can be calculated using the Scherrer formula (Equation 3), which relates particle size to the width of the diffraction peaks.

$$\tau = \frac{K\lambda}{\beta \cos\theta}$$

Equation 3.

Equation 3. Scherrer formula, τ - the average crystallite size, K- the shape factor, λ - the X-ray wavelength used in the experiment, β - the line broadening at half the maximum intensity (FWHM), measured in radians, θ -the Bragg angle (the position of the peak maximum)

Powder XRD patterns may appear less complex than single-crystal patterns, and their simplicity is their strength. They are practical and relatively easy to use, making them indispensable for identifying unknown crystalline substances or evaluating the purity of known materials. Compared to SC-XRD, results from PXRD can often be obtained in under 20 minutes. The entire process, from directing X-rays to obtaining results, typically takes only a few hours, making it ideal when time is critical. This method is also more user-friendly and resource efficient as sample needs minimal preparation often just needing

to be powdered to specific dimensions. Furthermore, powder XRD excels at analysing samples with multiple components. It can distinguish and separate the diffraction peaks of different components, providing detailed structural information. Finally, powder XRD can be applied to various sample forms, including powders, sintered pellets, and coatings on substrates, making it highly versatile for diverse applications.

1.3.4. Applications of crystallography

The crystal structure of a compound provides critical insights into its properties, offering a detailed understanding of the relationship between structure, function, and reactivity—an essential aspect of modern scientific advancements.[51] Single-Crystal X-ray Diffraction[52] and Powder X-ray Diffraction[53,54] are among the most powerful techniques for obtaining this information, making them indispensable tools for discovery.[55] Crystal structure analysis can reveal supramolecular interactions that must be considered to explore the applications of more complex systems effectively.[56–58]

The primary function of the single-crystal X-ray diffraction (SC-XRD) method is to provide definitive confirmation that the synthesized compound of interest corresponds precisely to the intended structure.[59] While the synthetic pathway used to obtain the molecule may, in some cases, allow for reasonable speculation about the final product, obtaining the crystal structure offers an unequivocal and reliable means to validate both the efficacy and accuracy of the proposed reaction scheme.[60]

The development of X-ray crystallography over the past century has been marked by extraordinary advances in both instrumentation and methodology, transforming what was once a laborious technique capable of resolving only the simplest ionic structures into a powerful analytical tool of remarkable precision and versatility.[61] From the pioneering work of W.L. Bragg in 1913[62] — in which the sodium chloride structure was deduced from a handful of ionisation-chamber measurements — to the ultra-high-resolution data obtainable at modern synchrotron beamlines[63,64], each successive generation of instrumentation has expanded the boundaries of structural information accessible to the crystallographer.[65] Table 3 summarises the key technical and quality parameters across three representative generations of X-ray diffraction instrumentation.

Table 3. *Key technical and quality parameters across three representative generations of X-ray diffraction instrumentation*

	Early laboratory NaCl, W.L. Bragg (1913)	**Modern home-lab Typical organic, 2010s–present**	**Synchrotron Beamline, 2000s–present**
INSTRUMENTATION			
X-ray source	Sealed gas-discharge tube (unfiltered, polychromatic)	Sealed microfocus tube or rotating anode (Mo Kα or Cu Kα)	3rd/4th-generation storage ring; tunable undulator
Detector	Ionisation chamber; photographic film	CCD or CMOS hybrid pixel area detector	Photon-counting pixel detector (PILATUS, EIGER)

Crystal size required	> 1 mm^3 (macroscopic)	~0.1–0.5 mm on each face	< 0.01 mm; microcrystals feasible
DATA COLLECTION			
Data collection time	Days to weeks (manual rotation, film exposure)	Minutes to ~24 h	Seconds to minutes
Wavelength tunability	None (fixed, polychromatic)	Fixed (Mo Kα 0.71 Å or Cu Kα 1.54 Å)	Continuously tunable; anomalous experiments (SAD/MAD) possible
Number of measured reflections	~10–100 (ionic structure, 2 atoms)	5,000–50,000 (typical organic, ~30–80 non-H atoms)	50,000–500,000+
STRUCTURE QUALITY			
Resolution limit (Å)	~2.0–5.0 Å (estimated from Bragg spacings)	0.77–1.0 Å (routine); < 0.7 Å possible	0.40–0.70 Å (charge-density quality)
R_1 factor (wR_2)	Not reported; estimated > 20–30 %	2–6 % (wR_2 < 12 %)	1–3 % (wR_2 < 6 %)
Completeness (%)	Partial (selected planes only)	98–99.5 %	99.5–100 %
STRUCTURAL INFORMATION ACCESSIBLE			
Bond lengths/angles	Na–Cl distance only (~2.81 Å)	All non-H bonds; e.s.d. ~0.002–0.005 Å	All bonds incl. H; e.s.d. < 0.001 Å
Hydrogen atoms	Not detectable	Geometrically placed (riding model)	Freely refined; charge density visible
Absolute configuration (Flack)	Not determinable	Cu Kα: routine (Flack x ± 0.05–0.10); Mo Kα: light atoms difficult	Reliable for all elements; Flack x ± < 0.02

e.s.d. = estimated standard deviation of bond length

The structures of sodium chloride and diamond, determined by W.L. Bragg in 1913, were the first crystal structures solved by X-ray diffraction, determined by using and ionisation-chamber spectrometer designed by his father. The method yielded only a single interatomic distance (the Na–Cl contact of ca. 2.81 Å) and a space group assignment, whereas modern home-laboratory instruments provide routine sub-ångström resolution for well-ordered small organic crystals, with R_1 factors typically in the 2–6% range.[62] Furthermore, synchrotron sources represent the current ceiling of capability. Compared with laboratory based sources, synchrotron properties of high spectral brightness and tunability have enabled higher resolution structure determinations, greater use of anomalous dispersion phasing, studies of much larger

molecular weight structures, and the use of smaller crystals.[66,67] At atomic resolution (≤ 0.7 Å), multipole or Hirshfeld-atom refinement becomes possible, granting access to experimental electron density and freely refined hydrogen atoms – a qualitative leap over anything achievable in a home laboratory.[68–70] A progression from ~10 measured reflections for a two-atom unit cell in 1913, to hundreds of thousands of precisely measured reflection at sub-0.5 Å resolution today, encapsulates over a century of instrumentation development[61] and illustrates why modern crystallography is now the gold standard for absolute configuration assignment, supramolecular interaction analysis and charge-density studies. [71,72]

A landmark development in the determination of absolute configuration came with Howard D. Flack's 1983 paper.[73] Prior to this work, absolute structure assignment relied on the Rogers η parameter, which compared R-values from refinements of both enantiomeric models[74] — an approach Flack identified as prone to false and over-precise indications of chirality, particularly for nearly centrosymmetric structures[75]. As an alternative, Flack introduced a new parameter, x, grounded in a physically meaningful inversion-twinning model: the crystal is treated as a twin in which one domain corresponds to the refined model and the other to its inverse.[76] The parameter is defined in the range 0.0–1.0, where the limiting values indicate the two pure enantiomers and an intermediate value indicates a racemic mixture.[77,78] The value of x is refined simultaneously with all other structural parameters in a standard least-squares procedure, making it a seamless addition to routine structure refinement.[76] To validate the approach, Flack examined the behaviour of both η and x theoretically and experimentally on simulated intensity data for seven well-assorted compounds[79], spanning light-atom organics to heavier-element structures, demonstrating consistently superior reliability over the η method[73,80].

The impact was transformative. The Flack parameter is now almost universally reported for all chiral materials characterised by X-ray crystallography[81], and with advances in detector technology and X-ray sources, it is now possible to confidently determine the absolute configuration even with oxygen as the heaviest atom present[82] — a task that once required deliberate introduction of a heavier anomalous scatterer.[72]

1.3.5. Determination of absolute configuration

In the rational design of Active Pharmaceutical Ingredients (APIs), molecular architecture is the primary determinant of biological performance.[83,84] Beyond simple chemical connectivity, the chirality and solid-state morphology of a molecule dictate its therapeutic efficacy[85–87], pharmacokinetic profile[88,89], and toxicological safety[90–92].[84,93–96] Chiral molecules represent one of the most fundamentally important subgroups of organic compounds, and single-crystal X-ray diffraction remains the most unambiguous method for determining their absolute configuration (Figure 8).[80] This knowledge is of particular importance in pharmaceutical development, where distinct enantiomers of the same molecule can exhibit profoundly different biological activities, pharmacokinetic profiles, and therapeutic outcomes, making the unambiguous assignment of absolute configuration a critical step in drug development and quality assurance.[83,84,97–99]

Beyond stereochemical identity, a thorough understanding of the complete three-dimensional structure of a molecule provides invaluable insight into its reactivity and preferred reaction pathways. Subtle structural features — including functional group orientation, minor variations in bond angles and distances, and the coordination of solvent molecules or ionic species — can collectively exert significant influence on

chemical behavior.[100] This is especially relevant for molecules bearing sterically demanding substituents, which can impose steric hindrance, restrict access to reactive sites, and govern reaction selectivity by favoring specific mechanistic pathways or preventing the approach of certain reagents.[101–109]

The inherent chirality of biological targets—such as enzymes and receptors—renders them highly sensitive to the "handedness" of a ligand. Enantiomers, while sharing identical physical properties in achiral environments, often exhibit divergent behaviour *in vivo*. A quintessential case is the antidepressant citalopram (Figure 8); its (*S*)-enantiomer (escitalopram) effectively inhibits the serotonin transporter, whereas the (*R*)-enantiomer displays minimal activity and may even antagonize the therapeutic effect of its counterpart.[110,111] Such insights led to the development of escitalopram (Lexapro), which offers superior clinical outcomes with a reduced side-effect profile.[112,113] Consequently, the unambiguous determination of absolute configuration via SC-XRD is a non-negotiable requirement in modern pharmaceutical characterization.

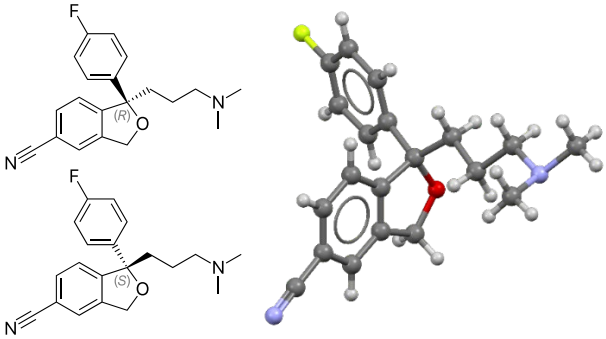

Figure 8. *Left - absolute configuration of the R and S enantiomers of citalopram. Right - crystal structure of (S)-enantiomer (escitalopram), CCDC entry 638334[114] and 748144[115]*

Beyond chirality, the crystal structure of an API fundamentally governs its physicochemical stability and bioavailability. The spatial arrangement of molecules within the lattice determines the lattice energy, which in turn dictates solubility and dissolution rates.[85,88,89] Structural analysis allows researchers to select the most robust crystalline form, ensuring that the drug remains stable against environmental stressors like humidity and temperature throughout its shelf-life.[90–92] Understanding these crystalline properties is essential for the optimization of industrial manufacturing, mitigating risks such as inconsistent crystallization or unwanted phase transformations during scale-up.[94,96,101,116–119]

To determine the absolute configuration of chiral APIs, researchers employ a suite of spectroscopic, synthetic, and crystallographic methodologies, each governed by specific instrumental and structural constraints.[120,121] While standard Nuclear Magnetic Resonance (NMR) spectroscopy cannot inherently distinguish between enantiomers due to signal overlap[122], the Mosher method provides an indirect solution through chiral derivatization.[123] By reacting the analyte with a Mosher reagent to form diastereomeric esters, the resulting chemical shift differences allow for the assignment of the chiral centre.[124–130] Similarly, chiroptical methods such as Electronic[131] and Vibrational Circular Dichroism[132] (ECD/VCD) exploit the rotation of plane-polarized light.[120] By comparing the experimental optical rotation spectrum of a drug with a structurally analogous reference under identical conditions, the configuration can be accurately inferred.[120,131–137]

Historically, chemical correlation via organic synthesis was the primary route for stereochemical assignment.[84,93,138,139] This labour-intensive approach relies on converting a precursor of known chirality into the target molecule through stereo controlled reactions, followed by verification using polarimetry or chromatography.[140,141] However, Single-Crystal X-ray Diffraction (SC-XRD) remains the most definitive technique. The Bijvoet method leverages anomalous scattering to distinguish between enantiomorphs, though its efficacy depends on the presence of atoms with sufficient anomalous dispersion—typically requiring at least an oxygen atom for copper radiation or a silicon-weight atom for Molybdenum sources.[72,142] In modern crystallography, the Flack parameter (x) has become the definitive diagnostic tool, a value of $x \approx 0$ confirms the correct absolute structure, $x \approx 1$ indicates the inverted model, and intermediate values suggest the presence of inversion twinning within the crystal lattice.[78]

1.3.6. Examples of polymorphism and reaction monitoring

A central challenge in solid-state chemistry is polymorphism—the ability of a single chemical entity to crystallize in multiple lattice arrangements.[143] Although chemically identical, polymorphs possess distinct hydrogen-bonding networks and van der Waals packing, leading to significant variations in mechanical strength, solubility, and chemical reactivity.[144,145]

The emergence of specific polymorphs is governed by a delicate competition between thermodynamics and kinetics.[146,147] Thermodynamically, the system seeks the global free energy minimum. Depending on whether one form is stable across all temperatures or if a transition point exists, the system is classified as monotropic or enantiotropic, respectively.[146,147] Kinetically, the formation of a phase is dictated by the rate of nucleation and growth, often influenced by supersaturation, solvent choice, and mechanical agitation.[146,147] Two primary models describe these pathways: Ostwald's Rule of Stages (ORS), which posits that a system evolves through increasingly stable metastable states[148], and Classical Nucleation Theory (CNT), which suggests that all potential phases compete simultaneously, with the fastest-growing phase predominating[149].[143] Given that an unexpected polymorphic transition can render a drug ineffective or unsafe, an integrated analytical strategy is required. PXRD serves as the primary "fingerprinting" tool for bulk phase identification, while SC-XRD provides the high-resolution atomic map necessary to understand the intermolecular forces driving these transitions.[150]

The ability to monitor chemical reactions in real-time is indispensable for elucidating mechanisms and identifying short-lived intermediates.[35] While spectroscopic methods like NMR and IR (infrared spectroscopy) provide molecular-level data, XRD offers a unique advantage for solid-state systems by tracking changes in the long-range order of the material.[151,152] PXRD is particularly potent for *in situ* studies, allowing for the observation of phase evolution under biomimetic or industrial conditions (e.g., varying pressure or temperature).[153–155] It enables the quantification of phase compositions and the detection of amorphous-to-crystalline transitions.[156–164] Conversely, while SC-XRD is often limited by the requirement for high-quality crystals, its application in monitoring SCSC transformations provides a "frame-by-frame" visualization of atomic movement during a reaction.[165,166]

Ritonavir, an HIV-1 protease inhibitor introduced in 1996, represents one of the most consequential case studies in pharmaceutical polymorphism. In 1998, a thermodynamically more stable polymorph (Form 2) appeared unexpectedly, causing

slowed dissolution of the marketed dosage form and compromising oral bioavailability, ultimately forcing the removal of the capsule formulation from the market.[167] Ritonavir was found to exhibit conformational polymorphism, with the two forms possessing unique crystal lattices and significantly different solubility properties.[168] Thermodynamically, the transition from polymorph 1 to polymorph 2 is exothermic and accompanied by an increase in specific volume, with the two forms exhibiting a monotropic relationship at ordinary pressure that becomes enantiotropic at elevated pressure.[169] Form 1 displays more efficient intermolecular packing, lower void space, and higher density, whereas Form 2 adopts a less stable molecular conformation in which the hydroxyl group acts as both a hydrogen bond donor and acceptor, resulting in a stronger intermolecular hydrogen bond network and a more stable crystal structure despite being less dense. Kinetically, the transformation proceeded via a solvent-mediated mechanism, with heterogeneous nucleation of Form 2 seeds driving the progressive displacement of Form 1 throughout the supply chain. The two polymorphs were characterized using an array of solid-state techniques, including single-crystal X-ray diffraction (SC-XRD) and powder X-ray diffraction (PXRD), which were employed to determine the crystal structures and hydrogen bonding networks of each form.[167] SC-XRD established the distinct space groups and conformational differences between the forms, while PXRD was used to monitor polymorph interconversion, with quantitative phase analysis performed via Rietveld refinement enabling tracking of the Form 1 to Form 2 transformation under controlled processing conditions.[170,171]

More recently, the polymorphic landscape of ritonavir was extended by the identification of Form 3, a third true polymorph.[172,173] Although a crystalline form first observed in 2014 via melt crystallization was initially attributed to a new polymorph designated Form 4 (Figure 9), subsequent PXRD comparison revealed it to be a mixture of Form III and amorphous material; Form 3 was therefore not formally recognized as a distinct polymorph until 2022.[174] Form 3 and possesses the lowest melting point and heat of fusion among the three forms, confirming it as the least thermodynamically stable polymorph in a monotropic relationship with Forms 1 and 2.[175] Solubility measurements further established the rank order Form 3 > Form 1 > Form 2, consistent with the thermodynamic stability hierarchy, and Form 3 exhibits a two-dimensional hydrogen bonding network — more complex than the one-dimensional motifs of Forms 1 and 2.[174] Crystal structure of, Form 3 was ultimately determined by SC-XRD using single crystals grown via a microdroplet partial-melt strategy.[174]

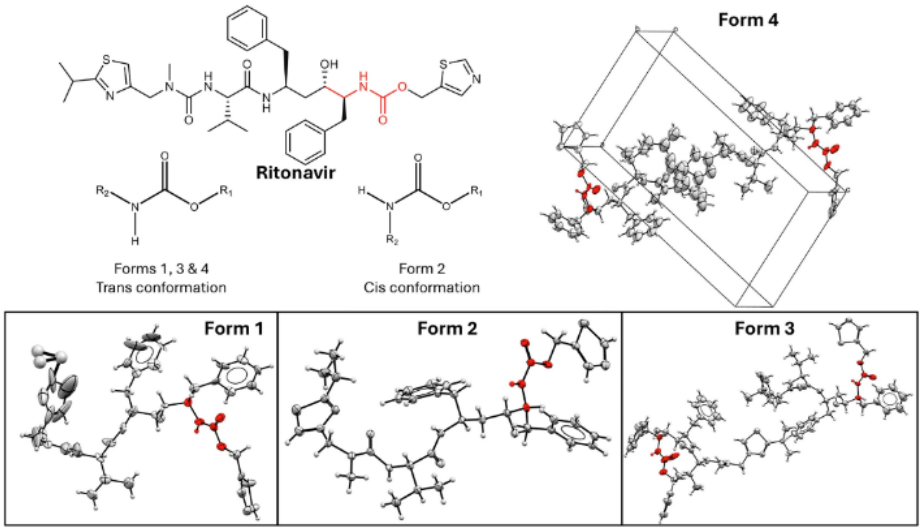

Figure 9. *Two-dimensional molecular structure of ritonavir, visualization of the unit cell of the crystal structure of ritonavir form 4, and of the conformations contained in the unit cells of forms 1, 2, and 3. The carbamate configurations contained in all four forms are highlighted in red. Disorder is shown by larger thermal ellipsoids*[176]

1.3.7. Characterization of Complex Supramolecular and Framework Systems

Powder X-ray Diffraction (PXRD) and Single-Crystal X-ray Diffraction (SC-XRD) are both predicated upon the long-range periodic order inherent to crystalline solids.[177–180] This periodicity manifests as discrete Bragg reflections—sharp peaks in the case of powder samples and a three-dimensional lattice of reflections in single crystals. The presence and morphology of these features serve as the primary diagnostic evidence for crystallinity and phase purity.[44,181]

In supramolecular chemistry, the characterization of host–guest complexes is paramount to understanding the non-covalent forces that stabilize these assemblies. SC-XRD remains the gold standard for this purpose, as it provides an unambiguous spatial map of the host–guest interface.[182–184]

A representative example is the encapsulation of hydrophobic guests within the pumpkin-shaped macrocycle cucurbit[7]uril (CB[7]). Structural analysis of a 1:1 complex between CB[7] and a substituted ferrocene derivative revealed that the guest is oriented along the principal symmetry axis of the host cavity. The resulting diffraction data elucidated the stabilizing role of C–H···O hydrogen bonds and the entropic cost associated with the conformational rigidity of the encapsulated guest. In such studies, PXRD serves as a critical bulk-validation tool; by comparing the experimental powder pattern of the bulk material with the pattern simulated from the SC-XRD model, one can confirm that the single crystal is truly representative of the macroscopic phase.[185]

Recent advancements in cyclohexanohemicucurbituril (cycHC[n]) chemistry further underscore this dual-method approach. While SC-XRD[177] has been instrumental in identifying size-selective anion encapsulation—such as the radially symmetric stabilization of chloride ions within cycHC[8] via multiple CH···Cl interactions[177] (Figure 10) —PXRD[179] has proven indispensable for monitoring solid-state reactivity.[178,180] For instance, in mechanochemical syntheses, PXRD patterns have been used to track the

evolution from amorphous precursors to crystalline macrocycles during aging steps, thereby providing a kinetic window into solvent-free macrocyclization.[179]

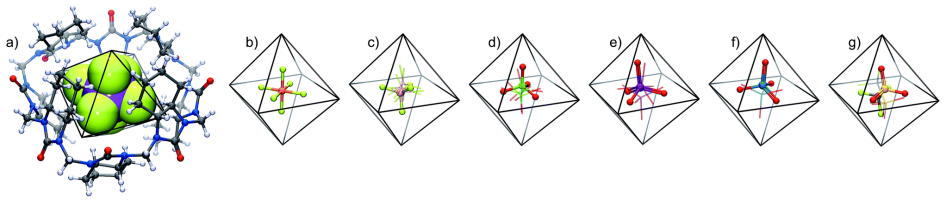

Figure 10. *The crystal structures of 1 : 1 host–guest complexes of (a) SbF_6^-, (b) PF_6^-, (c) BF_4^-, (d) ClO_4^-, (e) IO_4^-, (f) ReO_4^- and (g) $CF_3SO_3^-$ anions in the cycHC[8] cavity. Minor disorder components are shown as a wireframe model. The host in (b–f) is represented by an octahedron depicting the cavity of cycHC[8]*[178]

The characterization of Metal–Organic Frameworks (MOFs) often presents a significant challenge: many high-performance frameworks, particularly those synthesized via mechanochemistry or rapid solvothermal methods, yield only microcrystalline powders unsuitable for conventional SC-XRD. In these instances, PXRD is the primary vehicle for structural elucidation and the study of phase transitions.[186] Utilization of PXRD extends beyond static characterization to the study of nucleation and growth kinetics as time-resolved *in situ* PXRD has been successfully employed to follow the crystallization pathways of Zr-based frameworks (e.g., MOF-808 and MOF-801 (Figure 11)). Monitoring the evolution of crystalline phases in real-time, enables researchers to correlate linker solubility and coordination geometry with the resulting framework topology, allowing the rational design of synthesis protocols for phase-pure Zr-MOFs.[187]

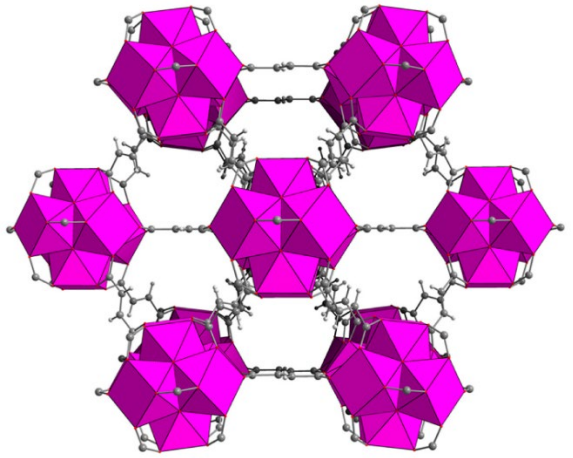

Figure 11. *Crystal structure of MOF-801. Colour code: Zr, pink; C, grey; O, red; H, white*[188]

When crystallite size permits, the simultaneous application of SC-XRD and PXRD provides a comprehensive understanding of framework flexibility. This is particularly evident in aromatic, multidentate copper-based MOFs, where SC-XRD defines the initial coordination environment and topology, while PXRD is utilized to monitor SCSC transformations. Such integrated studies allow for the precise tracking of how steric hindrance and solvent exchange influence the stability and responsiveness of the framework lattice.[189]

2. Aims of the study

The overall aim of this thesis is to demonstrate the breadth and depth of X-ray crystallographic methods as an integrated analytical platform in chemistry, applied across five structurally and functionally distinct research domains. The work spans from small chiral organic molecules to coordination compounds, supramolecular host-guest assemblies, and porous metal-organic frameworks, with the unifying thread being the extraction of meaningful structural, stereochemical, and dynamic information from diffraction data.

The specific aims are as follows:

1. Absolute configuration assignment in enantioselective synthesis (Publications I–III). To unambiguously determine the absolute configuration of chiral products arising from asymmetric organocatalytic reactions — specifically Michael additions to unsaturated indolyl ketones and enantioselective N-alkylation of nitroindoles under phase-transfer catalysis — using SC-XRD and the Flack parameter, and to characterise the supramolecular packing and non-covalent interactions in the resulting crystal structures.
2. Structural characterisation of coordination and hypervalent iodine compounds (Publication IV). To elucidate the solid-state structures of silver carboxylate coordination compounds and hypervalent iodine(III) reagents, establishing the coordination geometries, intermolecular interactions, and the influence of ancillary ligands on crystal packing.
3. Pharmaceutical solid-state chemistry and structural validation (Publication V). To characterise key intermediates and precursors in the synthesis of pharmacologically active compounds — including an imatinib amide precursor — and to confirm the identity and purity of synthetic targets through crystallographic analysis.
4. Polymorphism and solid-state transformations (Publication VI). To investigate polymorphism in crystalline materials, including the discovery and structural characterisation of a new solvate polymorph of a cobalt-based MOF (Cobalt-MOF*), and to monitor phase transitions, solvent exchange kinetics, and guest-accommodation behaviour in flexible framework architectures.
5. Supramolecular host–guest chemistry (Publication VIII). To characterise the solid-state structures of inclusion complexes involving cucurbituril-type macrocycles — in particular cyclohexanohemicucurbituril (cycHC[n]) and its mixed analogue mixHC[8] — resolving the geometry of anion encapsulation, determining the absolute configuration of enantiopure macrocycles, and correlating crystallographic findings with solution-state behaviour and HPLC analysis.

Across all five aims, a secondary objective is to evaluate the complementarity of SC-XRD and PXRD — demonstrating when single-crystal analysis alone is sufficient and when powder diffraction is essential for bulk-phase validation, kinetic monitoring, or characterisation of microcrystalline materials.

3. Materials and methods

A brief description of the methods is provided below. Further details can be found in Publications I-VII.

Single crystal X-ray diffraction data was collected at 120 K using a Rigaku XtaLAB Synergy-R diffractometer with a HyPix-Arc 100 detector using mirror-monochromated Cu-Kα (λ = 1.54184 Å) radiation. The data was solved by intrinsic phasing (SHELXT) and refined by full-matrix least squares on F^2 using Olex2, utilising the SHELXL module. Anisotropic displacement parameters were assigned to non-H atoms and isotropic displacement parameters for all H atoms were constrained to multiples of the equivalent displacement parameters of their parent atoms with U_{iso}(H) = 1.2 U_{eq}(methylene, methine) or U_{iso}(H) = 1.5 U_{eq}(methyl, hydroxy) of their respective parent atoms.

Single crystal X-ray diffraction data was collected at 123K on Rigaku Compact HomeLab diffractometer, equipped with a Saturn 944 HG CCD detector and Oxford Cryostream cooling system using monochromatic Cu-Kα radiation (1.54178Å) from a MicroMaxTM-003 sealed tube microfocus X-ray source. The strategy of data collections was calculated and implemented through the program package HKL-3000. 11 Data was collected using ω-scans. CrysAlisPro was used for data reduction and empirical absorption correction using spherical harmonics implemented in SCALE3 ABSPACK scaling algorithm. The structures were solved using SHELXT and refined by full-matrix least-squares method against F^2 with SHELXL-2016 through OLEX2 program package. All non-hydrogen atoms were refined with anisotropic atomic displacement parameters. Hydrogen atoms attached to carbon atoms were treated as riding atoms, using isotropic displacement parameters U_{iso}(H) = 1.2; U_{iso}(C) for CH and CH_2; U_{iso}(H) = 1.5; U_{iso}(C or O) for CH_3 and OH.

1 *((R)-3-(7-methoxy-1H-indol-1-yl)-4-nitro-1-phenylbutan-1-one) (Publication I)*

Crystals suitable for single-crystal X-ray diffraction were obtained for the representative ***1*** *((R)-3-(7-methoxy-1H-indol-1-yl)-4-nitro-1-phenylbutan-1-one)* by slow evaporation from chloroform/hexane (1:40) at room temperature over 72 hours. Yellowish block shaped crystals of approximate dimensions 0.31 × 0.16 × 0.11 mm were mounted on a MiTeGen loop and subjected to data collection on a Rigaku Compact HomeLab diffractometer, equipped with a Saturn 944 HG CCD detector and Oxford Cryostream cooling system using monochromatic Cu-*Kα* radiation (1.54178Å) from a MicroMaxTM-003 sealed tube microfocus X-ray source. The strategy of data collections was calculated and implemented through the program package HKL-3000. Data was collected using ω-scans. CrysAlisPro was used for data reduction and empirical absorption correction using spherical harmonics implemented in SCALE3 ABSPACK scaling algorithm. The structures were solved using SHELXT and refined by full-matrix least-squares method against F^2 with SHELXL-2016 through OLEX2 program package. All non-hydrogen atoms were refined with anisotropic atomic displacement parameters. Hydrogen atoms attached to carbon atoms were treated as riding atoms, using isotropic displacement parameters U_{iso}(H) = 1.2U_{iso}(C) for CH and CH_2; U_{iso}(H) = 1.5U_{iso}(C) for CH_3. The absolute configuration of compound 3g was not known from the synthesis; therefore, it was confirmed based on the anomalous dispersion effects. The figures were drawn using the program Mercury 4.0.

2 *(3-(4-nitro-1H-1-yl)-1-phenylbutan-1-one) (Publication II)*

Crystals suitable for single-crystal X-ray diffraction were obtained for the ***2*** *(3-(4-nitro-1H-1-yl)-1-phenylbutan-1-one)* by slow evaporation from hexane/chloroform solution at room temperature over 72 hours. Yellowish needle shaped crystals of approximate dimensions 0.314 × 0.100 × 0.064 mm were mounted on a MiTeGen loop and subjected to data collection on a Rigaku Compact HomeLab diffractometer, equipped with a Saturn 944 HG CCD detector and Oxford Cryostream cooling system using monochromatic Cu-*Kα* radiation (1.54178Å) from a MicroMaxTM-003 sealed tube microfocus X-ray source. The strategy of data collections was calculated and implemented through the program package HKL-3000. Data was collected using ω-scans. CrysAlisPro was used for data reduction and empirical absorption correction using spherical harmonics implemented in SCALE3 ABSPACK scaling algorithm. The structures were solved using SHELXT and refined by full-matrix least-squares method against F^2 with SHELXL-2016 through OLEX2 program package. All non-hydrogen atoms were refined with anisotropic atomic displacement parameters. Hydrogen atoms attached to carbon atoms were treated as riding atoms, using isotropic displacement parameters $U_{iso}(H) = 1.2U_{iso}(C)$ for CH and CH_2; $U_{iso}(H) = 1.5U_{iso}(C)$ for CH_3. The absolute configuration of compound 6c was anticipated from the synthesis. The figures were drawn using the program Mercury 3.9.

3 *(ethyl (2R*,3S*)-4,4-dicyano-2-(diethoxyphosphoryl)-3-(4-nitrophenyl)butanoate) (Publication III)*

Single crystals of the of the representative Michael adduct ***3*** *(ethyl (2R*,3S*)-4,4-dicyano-2-(diethoxyphosphoryl)-3-(4-nitrophenyl)butanoate)* were obtained from *tert*-butyl ether and hexane. Colourless needle shaped crystals of approximate dimensions 0.07 × 0.07 × 0.06 mm were mounted on a MiTeGen loop and subjected to data collection on a Rigaku Compact HomeLab diffractometer, equipped with a Saturn 944 HG CCD detector and Oxford Cryostream cooling system using monochromatic Cu-Kα radiation (1.54178Å) from a MicroMaxTM-003 sealed tube microfocus X-ray source. The strategy of data collections was calculated and implemented through the program package HKL-3000. Data was collected using ω-scans. CrysAlisPro was used for data reduction and empirical absorption correction using spherical harmonics implemented in SCALE3 ABSPACK scaling algorithm. The structures were solved using SHELXT and refined by full-matrix least-squares method against F2 with SHELXL-2016 through OLEX2 program package. All non-hydrogen atoms were refined with anisotropic atomic displacement parameters. Hydrogen atoms attached to carbon atoms were treated as riding atoms, using isotropic displacement parameters Uiso(H) = 1.2Uiso(C) for CH and CH2; Uiso(H) = 1.5Uiso(C) for CH3. The absolute configuration of compound 6c was anticipated from the synthesis. The figures were drawn using the program Mercury 2.0. Appropriate restraints were applied to the geometry and thermal displacement parameters of the atoms involved in the disordered parts of the structures. Restrain SADI was used to fix the distance between two carbon atoms (C13-C13a bond distance was fixed to be the same as C13-C13b) to be equal within the standard uncertainty s value 0.02. Restrain SIMU restrains the anisotropic displacement parameters of adjacent atoms (C13, C13a and C13b) to be similar. The default values for the standard deviations are 0.04 SIMU (0.08 for terminal atoms, which tend to move more strongly). The absolute configuration was assigned based on the anomalous dispersion effects – absolute configuration is (*S*) at C7 and (*S*) at C11.

4-12 *data for* ***4, 5, 6, 7, 8, 9, 10***, ***11*** and ***12*** *(Publication IV)*

Single crystal X-ray data for ***4, 5, 6, 7, 8***, and ***9b*** were collected at 120 K using an Agilent SuperNova dual wavelength diffractometer with an Atlas detector using mirror-monochromated Cu-Kα (λ = 1.54184 Å) radiation. The single crystal X-ray data for ***10, 11*** and ***12*** were collected at 120 K using an Agilent SuperNova diffractometer with an Eos detector using mirror-monochromated Mo-Kα (λ = 0.71073 Å) radiation. The program CrysAlisPro was used for the data collection and reduction on the SuperNova diffractometers. All structures were solved by intrinsic phasing (SHELXT) and refined by full-matrix least squares on F^2 using Olex2, utilising the ShelXL-2015 module. Anisotropic displacement parameters were assigned to non-H atoms and isotropic displacement parameters for all H atoms were constrained to multiples of the equivalent displacement parameters of their parent atoms with U_{iso}(H) = 1.2U_{eq} (aromatic; cyclic alkyl) or U_{iso}(H) = 1.5U_{eq} (acyclic alkyl) of their respective parent atoms.

Crystals suitable for single crystal X-ray diffraction were obtained from a DCM/DMSO solution of Ag(pivalate) **1** vapour diffused with DIPE. Crystals suitable for single crystal X-ray diffraction were obtained from a DCM solution (doped with several drops of DMSO to complete dissolution) of Ag(pivalate)(4-Mepy) **1b** vapour diffused with pentane. Crystals suitable for single crystal X-ray diffraction were obtained from a DCM solution of (pivalyl-OI)(DMAP) **2c** vapour diffused with pentane. Crystals suitable for single crystal X-ray diffraction were obtained from a DCM solution of (pivalyl-OI)(4-morpy) **2d** vapour diffused with DIPE. Crystals suitable for single crystal X-ray diffraction were obtained from a DCM solution of (trimesyl-OI)$(py)_3$ **4a** vapour diffused with pentane. Crystals suitable for single crystal X-ray diffraction were obtained from a DCM solution of (trimesyl-OI)$(4\text{-Mepy})_3$ **4b** vapour diffused with TBME.

Crystals suitable for single crystal X-ray diffraction were obtained by evaporation of an acetone solution (doped with several drops of DMSO to complete dissolution) of Ag(pivalate)(DMAP) **1c.** Crystals suitable for single crystal X-ray diffraction were obtained from a toluene solution of (pivalyl-OI)(4-Mepy) **2b** vapour diffused with pentane. Crystals suitable for single crystal X-ray diffraction were obtained from a pyridine solution (doped with several drops of DMSO to complete dissolution) of Ag_3(trimesate) **3** vapour diffused with TBME.

13 *Precursor of imatinib amide (Publication V)*

Single crystals of the compound were obtained from a methanol solution of amide ***13*** by slow evaporation of the solvent. Single crystal X-ray diffraction data was collected at 123K on Rigaku Compact HomeLab diffractometer, equipped with a Saturn 944 HG CCD detector and Oxford Cryostream cooling system using monochromatic Cu-Kα radiation (1.54178Å) from a MicroMaxTM-003 sealed tube microfocus X-ray source. The data was solved by intrinsic phasing (SHELXT) and refined by full-matrix least squares on F^2 using Olex2 utilising the SHELXL module. Anisotropic displacement parameters were assigned to non-H atoms and isotropic displacement parameters for all H atoms were constrained to multiples of the equivalent displacement parameters of their parent atoms with U_{iso}(H) = 1.2 U_{eq} (methylene, methine) or U_{iso}(H) = 1.5 U_{eq}(methyl, hydroxy) of their respective parent atoms. Appropriate restraints were applied to the geometry and thermal displacement parameters of the atoms involved in the disordered parts of the structures. Restrain DFIX was used to fix the distance between carbon and oxygen atoms (C1A O1A bond distance was fixed to be 1.43) to be equal within the standard uncertainty s value 0.02. Terminal OH-group was modelled as a 60:40% disorder model.

***14** Cobalt_MOF (Publication VI)*

The cobalt-based metal-organic framework $\{[Co_{1.5}(TTPA)(BTC)(H_2O)]_2 \cdot 13H_2O\}_n$ (Cobalt-MOF) was synthesised following the established procedure described in the literature (CCDC 1414118), employing the tripodal ligand tris(4-(1H-1,2,4-triazol-1-yl)phenyl)amine (TTPA) and trimesic acid (BTC) as bridging components coordinated to high-spin cobalt(II) ions. Single-crystal X-ray diffraction (SCXRD) confirmed that the bulk crystalline product corresponded to the previously reported framework structure. Notably, repetition of the synthesis yielded, alongside the known Cobalt-MOF phase, a previously undescribed solvate polymorph, designated Cobalt-MOF*, which accommodates primarily water with trace quantities of DMF within its pores. Structural comparison revealed that Cobalt-MOF* exhibits a slightly contracted void volume of approximately 2000 Å³ relative to the ~2800 Å³ observed in the parent Cobalt-MOF, consistent with the well-documented breathing phenomenon in flexible MOF architectures, wherein reversible structural contraction and expansion occur in response to changes in the chemical environment. The co-occurrence of both phases necessitated careful consideration during subsequent solvent exchange experiments, as the two variants display subtly different guest-accommodation behaviour.

Single crystal X-ray diffraction data were collected at 123K on Rigaku Compact HomeLab diffractometer, equipped with a Saturn 944 HG CCD detector and Oxford Cryostream cooling system using monochromatic Cu-Kα radiation (1.54178Å) from a MicroMaxTM-003 sealed tube microfocus X-ray source, or at 120 K on a Rigaku XtaLAB Synergy-R diffractometer with a HyPix-Arc 100 detector. All structures were solved by intrinsic phasing (SHELXT) and refined by full-matrix least squares on F2 using Olex2 utilising the SHELXL module. Anisotropic displacement parameters were assigned to non-H atoms and isotropic displacement parameters for all H atoms were constrained to multiples of the equivalent displacement parameters of their parent atoms with $U_{iso}(H)$ = 1.2 U_{eq} (methylene, methine) or $U_{iso}(H)$ = 1.5 U_{eq}(methyl, hydroxy) of their respective parent atoms.

^{1}H NMR spectra were measured on a Bruker Avance III 800 MHz spectrometer at 298 K using DUL (D/H/C) and Cryoprobe (D/H/C/N/P) probes. The spectrometer is connected to an 18.8T magnet and the diameter of the measuring hole is 54 mm. The measurement parameters of 1H spectra corresponded to quantitative conditions and a pulse angle of 30° was used (pulse length 5 μs), a relaxation time of 24 s, so that all signals could relax before the next pulse, the signal recording time was 2.4 s. The program MestreNova was used for viewing, processing and data analysis of 1H NMR spectra. The data of the integrals obtained from the spectra were further processed in Microsoft Excel, where the necessary recalculations were also carried out to prepare the kinetics curves. The curves of solvent exchange and guest insertion kinetics were made with the SigmaPlot program, which can be used for mathematical transformations and statistical analyses.

A mixture of tris(4-bromophenyl)amine (10.0 mmol, 4.82 g), 1,2,4-triazole (100.0 mmol, 6.91 g), CuI (0.5 mmol, 0.1 g), 18-crown-6 (1.0 mmol, 0.26 g), and K_2CO_3 (100.0 mmol, 13.82 g) was suspended in 50 mL of DMF. The mixture in a 100-mL round-bottom flask under argon was mixed at 160 °C for 2 days and then cooled to room temperature. Solvent was removed by distillation under a vacuum, and the reaction mixture was added into 100 mL H_2O. The deposit was filtered and washed with water and dried in vacuum to obtain light blue powder. Then the crude product was separated by column chromatography (isocratic $CH_3COOCH_3CH_2$/DCM 1:1, $CH_3COOCH_3CH_2$, gradient 0-10% CH_3OH/$CH_3COOCH_3CH_2$) to afford off-white crystalline powder. Product was

recrystallised from methanol to obtain white crystalline powder (yield: ~26%, 1,179g, based on tris(4- bromophenyl)amine). ^{1}H NMR (400 MHz, DMSO-d6), δ (ppm): 9.24 (s, 3H), 8.22 (s, 3H), 7.83 (d, J = 8.8 Hz, 6H), 7.25 (d, J = 9.1 Hz, 6H).

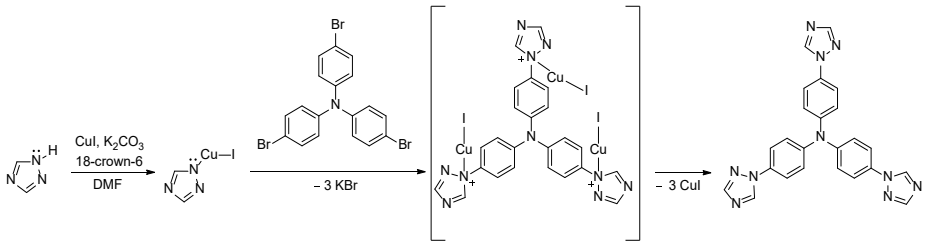

A mixture of TTPA (22.3 mg, 0.05 mmol), H_3BTC (21.0 mg, 0.1 mmol), and $Co(NO_3)_2{\cdot}6H_2O$ (29.1 mg, 0.1 mmol) was dissolved in 8 mL of DMF/CH_3CN/H_2O (2:4:2, v/v/v). The final mixture was placed in a Teflon vessel (15 mL) under autogenous pressure and heated at 85 °C for 3 days and then cooled to room temperature over 24 h. Purple block-shaped crystals of 14 were obtained, dried in air and collected in 47% yield (based on Co(II) salt).

15 *PF_6^-@(−)-mixHC[8] inclusion complex (Publication VII)*

Data collection was performed at 120 K on a Rigaku XtaLAB Synergy-R diffractometer equipped with a HyPix-Arc 100 detector, using mirror-monochromated Cu-Kα radiation (λ = 1.54184 Å). Structure solution by intrinsic phasing (SHELXT) and full-matrix least-squares refinement on F^2 (SHELXL/Olex2) converged to $R_1 = 0.083$ and $wR_2 = 0.238$, with a Flack parameter of 0.015(10) unambiguously confirming the absolute configuration of the enantiopure macrocycle. The crystal belongs to the orthorhombic chiral space group $P2_12_12_1$ with unit cell parameters a = 20.2233(2) Å, b = 20.5002(2) Å, c = 20.7796(2) Å, and a unit cell volume of 8614.84(15) Å^3 (Z = 2). The moderate R-factor is attributable to a crystallographically significant complication: the asymmetric unit was found to contain a 1:1 co-crystal of the target PF_6^-@(−)-mixHC[8] inclusion complex alongside PF_6^-@cycHC[8], with the biotin five-membered thiolane ring and one of the cyclohexyl groups exhibiting 50:50 positional disorder across the shared macrocyclic framework. This disorder was modelled with a single free occupancy variable, and the co-crystalline composition was independently validated by HPLC analysis of dissolved crystals, which confirmed 96.7% mixHC[8] and 2.0% cycHC[8], consistent with trace co-crystallization of the homomeric product present in the purified sample.

Single crystals of the complex were obtained from a methanol solution of (−)-((*S,S,R*)(*R,R*)$_7$)-mixHC[8] with twofold excess of $TBAPF_6$ by slow evaporation of the solvent. The resulting crystals were found to be of an inclusion complex of the PF_6^- in a 1:1 co-crystal of (−)-((*S,S,R*)(*R,R*)$_7$)-mixHC[8] and cycHC[8].

Table 4. *Compound numbes relating thesis and publications*

Compound number in thesis	Compound number in publication	Reference
1	***3q***	Publication I
2	***6c***	Publication II
3	***3d***	Publication III
4,5,6,7,8,9	***1, 1b, 2c, 2e, 4a and 4b***	Publication IV

Compound number in thesis	Compound number in publication	Reference
10,11,12	***$(1c)_2$, 2b and 3a·$(py)_4$***	Publication IV
13	***18***	Publication V
14	**-**	Publication VI
15	**-**	Publication VII

4. Results and discussion

4.1. Absolute configuration assignment for small molecules (Publications I, II and III)

Enantioselective synthesis is one of the most challenging areas of organic chemistry and in papers I -III highlight complementary studies on enantioselective organocatalytic transformations of indole-based substrates and use of halogen bonding (XB) in asymmetric organocatalysis. Publication I describes the Michael addition of 1,3-dicarbonyl compounds to unsaturated indolyl ketones under cinchona alkaloid-derived organocatalysis, while Publication II reports the enantioselective N-alkylation of nitroindoles via phase-transfer catalysis (PTC). In both cases, single-crystal X-ray diffraction (SCXRD) was employed as the primary technique for unambiguous determination of absolute configuration, and the resulting crystal structures were analysed in detail with respect to intermolecular interactions and crystal packing. The structural data obtained by crystallography are discussed alongside spectroscopic characterisation, stereochemical analysis, and mechanistic considerations.

The central challenge in both studies is the stereocontrol exercised by chiral catalysts over prochiral substrates, generating stereocentres whose absolute configuration must be rigorously assigned. While optical rotation, circular dichroism, and NMR methods provide supporting evidence, X-ray crystallography—particularly when combined with anomalous scattering—remains the gold standard for absolute structure determination. The results presented herein demonstrate how crystallographic analysis not only confirms the sense of asymmetric induction but also reveals the supramolecular architecture that governs crystal packing and, by extension, provides insight into the non-covalent interactions underpinning catalytic selectivity.

Compound ***1*** crystallises in the monoclinic space group $P2_1$ with two molecules in the unit cell (Z = 2). And compound ***2*** crystallises in the orthorhombic space group $P2_12_12_1$ with four molecules in the unit cell (Z = 4). The absence of a crystallographic inversion centre or mirror plane in both structures is consistent with the enantiopure nature of the samples, and the systematic absences unambiguously determine the space group.

The absolute configuration of compounds ***1*** and **2** were determined by the Flack method, exploiting the anomalous scattering of the nitrogen atoms present in the structure. The Flack parameter refined to x = 0.01(8) for compound 1 and x = -0.02(7) for compound 2, where values close to zero indicate that the absolute configurations of the crystals are correctly assigned. This conclusively establishes the absolute configuration for compound **1** as (*R*) and the compound **2 as** (*S*) at the stereocentres.

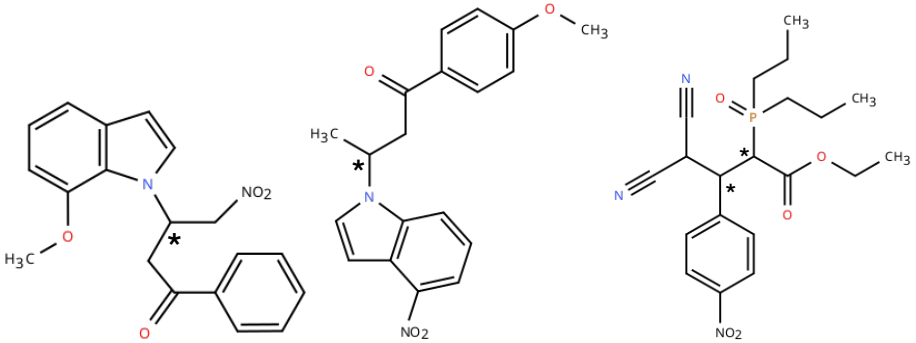

Figure 12 *Structure of compounds **1,2** and **3***

Table 5 *and Figure 13. Selected crystallographic data and refinement parameters and crystal structure for compound* ***1***

Parameter	Compound *1*
Formula	$C_{19}H_{18}N_2O_4$
Crystal system	Monoclinic
Space group	$P2_1$
a (Å)	9.19250(10)
b (Å)	6.30440(10)
c (Å)	14.4946(2)
α (°)	90
β (°)	90.8890(10)
γ (°)	90
V (Å³)	839.91(2)
Z	2
R_1 [I>2σ(I)]	0.0354
wR_2	0.0863
Flack parameter	0.01(8)
S	1.162
Abs. config.	(*R*)

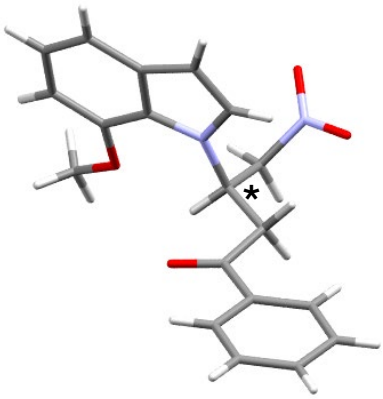

Table 6 and Figure 14. *Selected crystallographic data and refinement parameters and crystal structure for compound* ***2***

Parameter	Compound *2*
Formula	$C_{19}H_{18}N_2O_4$
Crystal system	Orthorhombic
Space group	$P2_12_12_1$
a (Å)	5.67946(4)
b (Å)	14.74353(12)
c (Å)	20.23168(17)
α (°)	90
β (°)	90
γ (°)	90
V (Å³)	1694.11(2)
Z	4
R_1 [I>2σ(I)]	0.0351
wR_2	0.0986
Flack parameter	-0.02(7)
S	1.032
Abs. config.	(*S*)

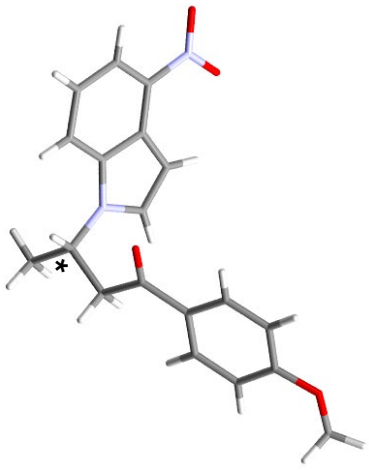

In Paper III, the first enantioselective XB-catalysed activation of an organophosphorus substrate is reported, with single-crystal analysis serving to confirm the absolute configuration of the chiral product and to elucidate intermolecular interactions in the crystalline state.

Publication III focuses on development of a bifunctional halogen-bond (XB) catalyst, enhanced by hydrogen-bonding, to activate vinyl phosphonates for enantioselective Michael addition of malononitrile. From the structural analysis, salient observations were made, including, the phosphonate moiety was coordinated via O atoms in a geometry

consistent with the activation by the XB donor: the iodo-perfluorophenyl unit of the catalyst aligns such that the substrate phosphonate oxygen is proximate, indicating a halogen-bond interaction (I···O). The crystal packing revealed a defined arrangement of substrate–catalyst complex (or product) showing supporting hydrogen bonds that feed into the halogen bond motif, supporting the mechanistic hypothesis of hydrogen-bond-enhanced halogen bonding. Moreover, the absolute stereochemistry of the adduct was confirmed and correlated with the major enantiomer produced under catalysis and conformational features derived from crystal structure of the vinyl phosphonate adduct showed limited torsional flexibility around the P=O bond and the vinyl–phosphonate substituent, which implies that the catalyst preorganises the substrate in a favourable geometry for nucleophilic attack.

These structural data supported the mechanistic proposal of the paper: that the catalyst utilises both halogen bonding and hydrogen bonding synergistically to orient and activate the vinyl phosphonate.

Compound ***3*** which is a major enantiomer of minor diastereoisomer crystallises in the monoclinic space group $P2_1$ with two molecules in the unit cell (Z = 2). The absolute configuration of compound ***3*** was determined by the Flack method, exploiting the anomalous scattering of the nitrogen and phosphorous atoms present in the structure. The Flack parameter refined to x = 0.011(5). This conclusively establishes the absolute configuration as (*S*) at the stereocentres C7 and C11.

Table 7 and Figure 15. *Selected crystallographic data and refinement parameters and crystal structure for compound* ***3***

Parameter	Compound *3*
Formula	$C_{18}H_{22}N_3O_7P$
Crystal system	Monoclinic
Space group	$P2_1$
a (Å)	10.09140(10)
b (Å)	9.98510(10)
c (Å)	10.52040(10)
α (°)	90
β (°)	92.7200(10)
γ (°)	90
V (Å³)	1058.879(18)
Z	2
R_1 [I>2σ(I)]	0.0351
wR_2	0.0940
Flack parameter	0.011(5)
S	1.046
Abs. config.	(*S*) at C7 and (*S*) at C11

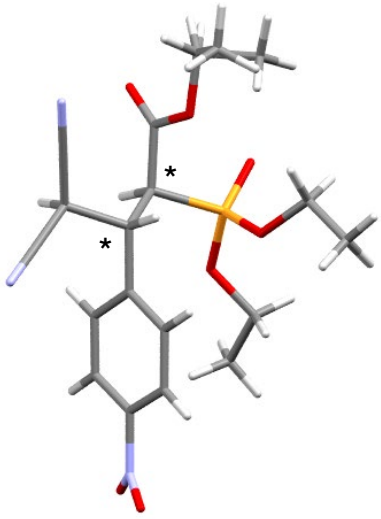

Single-crystal X-ray diffraction remains the gold standard for the unambiguous determination of absolute configuration, providing direct, atom-resolved structural evidence that no other analytical technique can match in certainty. Its ability to exploit anomalous scattering — most powerfully through the Flack parameter — renders it indispensable in the stereochemical characterization of chiral molecules, from pharmaceuticals to natural products, where configurational assignment carries profound chemical and biological consequences.

In these publications, Flack parameter was exploited to confirm the absolute configuration of the compounds anticipated from the synthesis route.

4.2. Halogen bonding in Carbonyl Hypoiodites (Publication IV)

As shown in previous chapter halogen bonding is an important interaction in synthetic transformations therefore thesis includes also detailed study of new halogen-bonded species. In Paper IV, the synthesis and definitive structural characterisation of novel carbonyl hypoiodite XB donors are described, with an emphasis on X-ray diffraction as the primary tool for establishing connectivity, geometry, and the nature of the O–I–N halogen bond in the solid state.

In publication IV carbonyl hypoiodites—compounds bearing an O–I bond in which the iodine formally carries a +1 oxidation state—occupy a unique position in the landscape of halogen bond donors. The oxygen atom withdraws electron density from iodine through its high electronegativity, generating an exceptionally deep and focused σ-hole at the iodine terminus. Consequently, carbonyl hypoiodites form extremely strong O–I···N halogen bonds with Lewis basic nitrogen donors, and these complexes—denoted O–I–N—are among the strongest non-covalent halogen bond interactions known to chemistry, rivalling in strength the three-centre four-electron $[N–I–N]^+$ halonium complexes that have attracted significant recent interest.

Despite their fundamental importance, the structural chemistry of carbonyl hypoiodites remained poorly characterised prior to Paper IV, particularly for systems beyond the simplest benzoic acid derivatives. Two goals motivated the present work: first, to synthesise and structurally characterise carbonyl hypoiodites based on pivalic acid (trimethylacetic acid), which are more soluble than aromatic analogues and thus amenable to study both in solution and in the solid state; and second, to extend the chemistry to trimesic acid (benzene-1,3,5-tricarboxylic acid), which would in principle allow the construction of the first tris(O–I–N) three-arm XB donor, a topologically novel species potentially useful in crystal engineering and supramolecular assembly.

The synthetic approach exploits the silver(I) carboxylate exchange reaction, in which a silver(I) carboxylate is reacted with molecular iodine in the presence of a Lewis basic nitrogen donor (a substituted pyridine) to give the desired O–I–N carbonyl hypoiodite complex. The silver(I) carboxylate intermediate is itself of structural interest, and Paper VI reports, for the first time, the characterisation of the direct silver(I) precursor of a pivalic acid-derived carbonyl hypoiodite by SCXRD.

Compound *4*

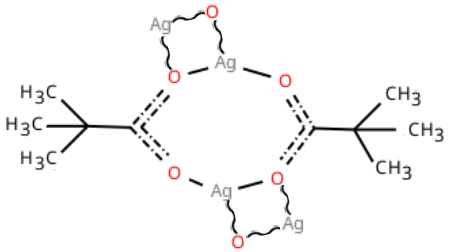

Compound *6*

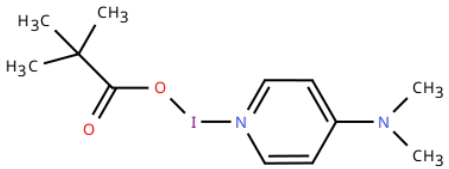

Compound *7*

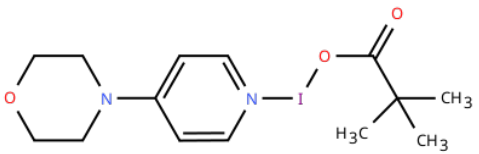

Compound *8*

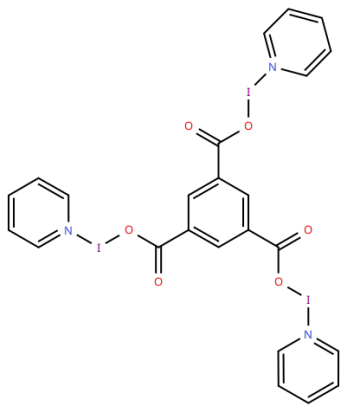

Compound *9*

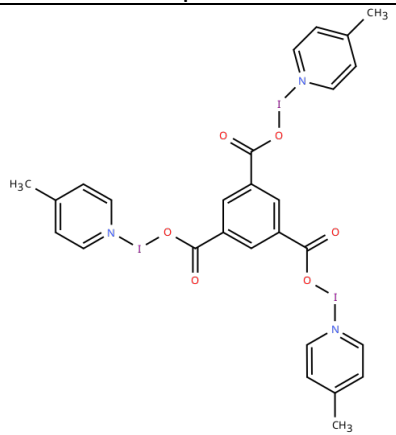

Figure 16. *Structures of compounds* ***4-9***

Table 8 and Figure 17. *Selected crystallographic data and refinement parameters and crystal structures for compounds* ***4-9***

Parameter	**Compound 4**	**Compound *5*** (connectivity only)	**Compound *6***	**Compound *7***	**Compound *8***	**Compound *9***
Formula	$C_{10}H_9Ag_2O_4)_n$	$C_{11}H_{16}AgNO_2$	$C_{12}H_{19}IN_2O_2$	$C_{14}H_{21}IN_2O_3$	$C_{24}H_{18}I_3N_3O_6{\cdot}H_2O$	$C_{27}H_{24}I_3N_3O_6$
Crystal system	Triclinic	Triclinic	Triclinic	Triclinic	Monoclinic	Monoclinic
Space group	*P*-1	*P*-1	*P*-1	*P*-1	$P2_1/n$	$P2_1/n$
a (Å)	5.7752(4)	5.688(2)	10.4936(5)	10.6593(3)	9.7621(2)	15.6502(4)
b (Å)	13.483(1)	8.659(3)	14.6196(7)	12.9198(4)	24.2101(5)	9.9201(2)
c (Å)	16.9347(12)	13.226(6)	14.9627(7)	13.3925(5)	11.4785(2)	19.5464(5)
α (°)	108.220(7)	76.65(4)	95.341(4)	83.712(3)	90	90
β (°)	90.240(5)	78.93(4)	91.077(4)	71.291(3)	91.437(2)	109.522(3)
γ (°)	94.770(6)	85.96(3)	107.447(4)	65.959(3)	90	90
V (Å³)	1247.57(16)	621.8(5)	2177.71(19)	1594.89(10)	2711.99(9)	2860.16(13)
Z	4	2	6	4	4	4
R_1 [I>2σ(I)]	0.037	0.261	0.036	0.030	0.026	0.035
wR_2	0.086	0.666	0.097	0.082	0.066	0.100
GooF	0.98	1.02	1.03	1.03	1.01	1.05

Compound *4*

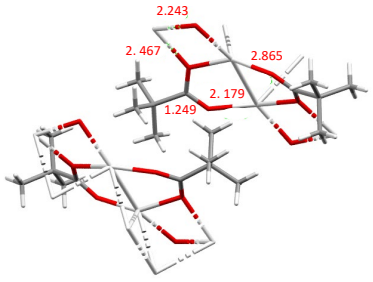

Compound *6*

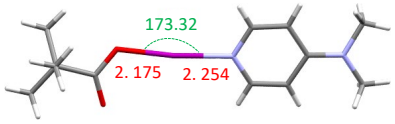

Compound *7*

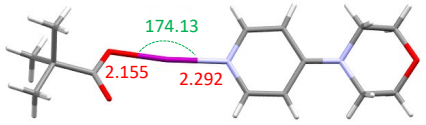

Compound *8*

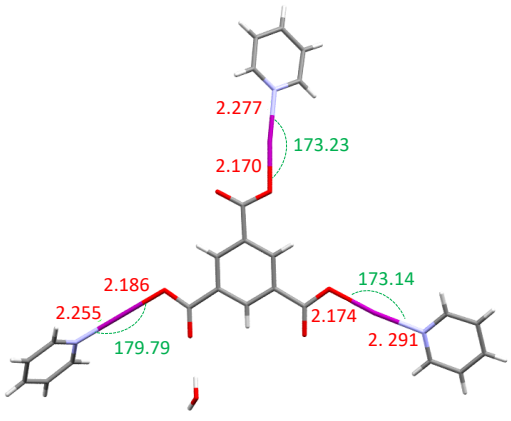

Compound *9*

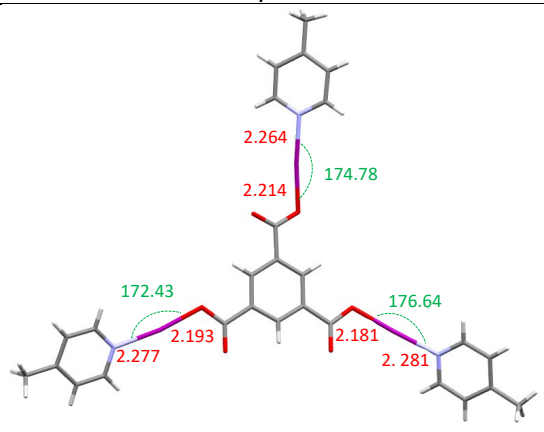

Compound *10*	Compound *11*	Compound *12*

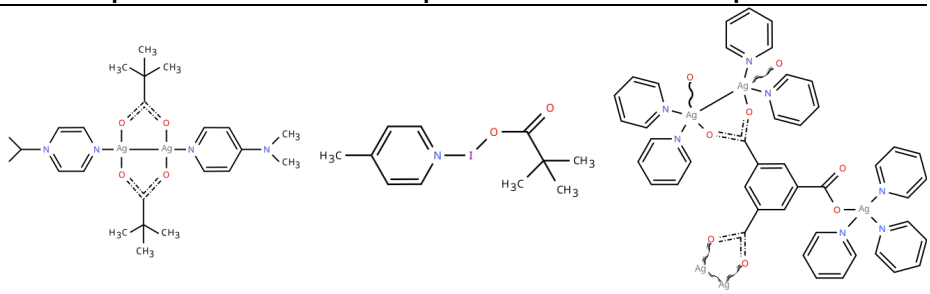

Figure 18. *Structures of compounds* ***10-12***

Table 9 and Figure 19. *Selected crystallographic data and refinement parameters and crystal structures for compounds* ***10, 11*** *and* ***12***

Parameter	Compound *10*	Compound *11*	Compound *12*
Formula	$C_{24}H_{38}Ag_2N_4O_4$	$C_{11}H_{16}INO_2$	$C_{44}H_{38}Ag_3N_7O_6$
Crystal system	Triclinic	Triclinic	Monoclinic
Space group	*P*-1	*P*-1	$P2_1/c$
a (Å)	6.8349(11)	5.6777(3)	20.8504(9)
b (Å)	9.4356(18)	8.6359(5)	10.5290(3)
c (Å)	11.4549(19)	13.1369(8)	19.2520(4)
α (°)	82.991(14)	76.766(5)	90
β (°)	72.900(14)	78.689(5)	91.048(3)
γ (°)	73.381(15)	86.009(4)	90
V (Å³)	676.0(2)	614.64(6)	4225.8(2)
Z	1	2	4
R_1 [I>2σ(I)]	0.054	0.036	0.079
wR_2	0.112	0.066	0.132
GooF	0.90	1.02	1.21

Compound *10*	Compound *11*	Compound *12*

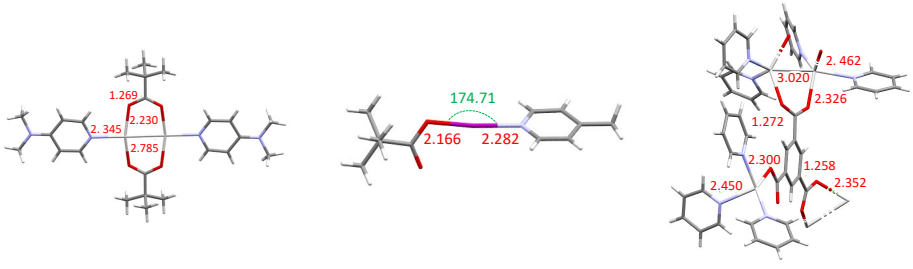

The solid-state structure of silver(I) pivalate (***4***), determined by single crystal X-ray diffraction, revealed a one-dimensional (1D) coordination polymer assembled from dimeric subunits. Each dimeric unit is held together by short argentophilic Ag···Ag contacts (2.8613(8) and 2.8649(8) Å) and bridging carboxylate oxygen atoms (Ag–O = 2.170(6)–2.255(6) Å), characteristic of the familiar paddlewheel-type silver(I) carboxylate motif. These dimeric units are further organised into bilayered chains through additional intermolecular argentophilic interactions (2.9479(7)–3.0662(8) Å) and secondary Ag···O

contacts (2.457(5)–2.530(5) Å). The extensive network of intra- and intermolecular bonding inherent to this polymeric architecture provides a satisfactory structural rationale for the near-complete insolubility of ***4*** in common organic solvents such as DCM and MeCN, since dissolution of a single monomeric unit would require the simultaneous disruption of multiple argentophilic and coordinative interactions.

Upon coordination of Lewis base ligands to ***4***, the silver(I) intermediates were isolated. The X-ray crystal structure of ***6*** (Ag–O–py derivative) confirmed a linear, two-coordinate O–Ag–N geometry, directly analogous to the O–I–N bonding motif observed in stabilised carbonyl hypoiodites. The structural characterisation of ***10*** revealed a discrete dimeric complex, ***10,*** in which a shorter argentophilic interaction (2.7854(8) Å) and two bridging pivalate ligands (Ag–O = 2.225(3) and 2.230(4) Å) persist, but without the extended intermolecular interactions present in ***4***. This contraction of coordination sphere relative to ***4***, and the consequent suppression of the polymeric network, accounts for the improved, albeit still limited, solubility of **1a**–**1d** in DCM and MeCN. The linear O–Ag–N geometry exhibited by ***6*** is particularly noteworthy: it establishes that the silver(I) intermediates faithfully preorganise the coordination environment later adopted by the iodine(I) centre in the hypoiodite products, lending structural credibility to the mechanistic proposal that the silver(I) precursor geometry influences the outcome of subsequent reactions with I_2.

Single crystal X-ray diffraction studies confirmed the formation of the stabilised carbonyl hypoiodite complexes. All three compounds exhibit the characteristic linear O–I–N halogen bonding motif, with O–I–N bond angles of 174.7(1)° (***11***), 172.7(1)–175.8(1)° (***7***, three crystallographically independent molecules), and 174.13(9)–174.2(1)° (***8***, two crystallographically independent molecules). These values deviate modestly from the ideal linear geometry of 180°, and in several cases surpass the maximum deviation reported for $[N–I–N]^+$ iodine(I) complexes (175.2(2)° for $[I(4\text{-}CF_3py)_2]BF_4$). The observed deviations are attributed to crystal packing forces rather than intrinsic electronic effects, as similarly wide angular dispersions are documented for structurally related O–I–N compounds bearing identical or comparable pyridine substituents.

The I–O bond lengths across these (2.155(3)–2.175(3) Å) are effectively invariant within the 3σ tolerance, reflecting their common pivalate scaffold. The I–N bond lengths (2.254(3)–2.292(3) Å) show slightly greater variability but remain well within the established range for crystallographically characterised $[N–I–N]^+$ complexes (2.23(1)–2.316(6) Å), confirming the iodine(I) character of the bonding. Comparison of 2c with the literature compounds (acetyl-OI)(DMAP) (I–O = 2.20(1) Å; I–N = 2.24(1) Å) and (benzoyl-OI)(DMAP) (I–O = 2.210(3) Å; I–N = 2.241(3) Å) reveals that ***7*** possesses the shortest I–O and longest I–N bond lengths of the three, consistent with the electron-donating inductive effect of the tert-butyl group of the pivalyl substituent. A more electron-rich carbonyl oxygen attenuates charge transfer toward iodine, reducing iodopyridinium (O···I–N) character and elongating the I–N bond. This electronic sensitivity of the halogen bond to the identity of the acyl group constitutes a valuable handle for tuning the reactivity profile of stabilised hypoiodites.

Computational geometry optimisations at the M06-2X/def2-TZVP level, employing a DCM continuum solvation model (C-PCM), yielded structures in good agreement with their experimental counterparts, validating the theoretical approach. The computed model of **2a**, for which no crystal structure was obtained, returned an I–N bond length of 2.318 Å — at the far end of the known range for solid-state $[N–I–N]^+$ complexes — consistent with the experimentally observed lability of this complex in solution and its

tendency toward rapid decomposition. This convergence of crystallographic, spectroscopic, and computational evidence supports the conclusion that the Lewis basicity of the stabilising pyridine ligand exerts a decisive influence over the strength and persistence of the O–I–N halogen bond.

The trimesate-derived compounds ***8*** and ***9*** represent the first crystallographically authenticated examples of tris(O–I–N) stabilised carbonyl hypoiodites, a landmark in the development of multi-iodination reagents. Both compounds crystallise in the monoclinic space group $P2_1/n$. The three crystallographically distinct O–I–N moieties within each structure display I–O bond lengths of 2.170(3)–2.186(3) Å (***8***) and 2.181(4)–2.214(4) Å (***9***), and I–N bond lengths of 2.255(3)–2.291(3) Å (***8***) and 2.264(4)–2.281(4) Å (***9***). The average I–O bond length is marginally longer in ***9*** (2.196 Å) than in ***8*** (2.177 Å), concordant with the stronger Lewis basicity of 4-methylpyridine relative to pyridine augmenting the iodopyridinium character of the O–I–N interaction. The O–I–N angles span 173.1(1)–179.8(1)° in ***8*** and 172.4(2)–176.6(2)° in ***9***, exhibiting the wide angular dispersion previously attributed to packing effects.

Structural comparison of ***8*** with its mono(O–I–N) analogue (benzoyl-OI)(pyridine) (I–O = 2.14(1) Å; I–N = 2.29(1) Å) reveals a systematic elongation of the I–O and shortening of the I–N bonds in ***8*** relative to the mononuclear reference. This trend indicates that the presence of two additional O–I–N units on the same aromatic scaffold renders the trimesyl carbonyl group more electron-withdrawing than the benzoyl group, thereby enhancing iodopyridinium character at each iodine centre. The elevated electrophilicity at iodine implied by these metrics is fully consistent with the pronounced reactivity and rapid decomposition observed experimentally for ***8*** and ***9***. Compound ***8*** was additionally found to include one molecule of water of crystallisation per formula unit, which bridges the carbonyl oxygen atoms of two adjacent ***8*** molecules via O–H···O hydrogen bonds, contributing to the crystal packing but not directly perturbing the halogen bond geometry.

Taken together, these crystallographic observations demonstrate that while individual O–I–N metrics in ***8*** and ***9*** superficially resemble those of mono(O–I–N) analogues, the multiplicative electronic and steric consequences of incorporating three such units onto a single scaffold produce a reagent of substantially greater intrinsic reactivity.

Presented study has direct implications for the future design of efficient, multi-electrophilic iodination platforms. The importance of this study is that it expands the toolkit of halogen bond donors (larger σ-holes, new topologies), reveals the mechanism of their formation through Ag(I) intermediates, and provides systematic structure–property relationships — all confirmed crystallographically by SCXRD.

4.3. Characterization of solvate of imatinib intermediate (Publications V)

X-ray diffraction (XRD) occupies a central position in the characterisation of both molecular and solid-state architectures produced by mechanochemical synthesis. In this chapter of this thesis single-crystal X-ray diffraction (SC-XRD) helped to uncover intermediate structure as a solvate (Publication V).

Compound ***13*** crystallises in the monoclinic space group $P2_1/c$ with four molecules in the unit cell (Z = 4).

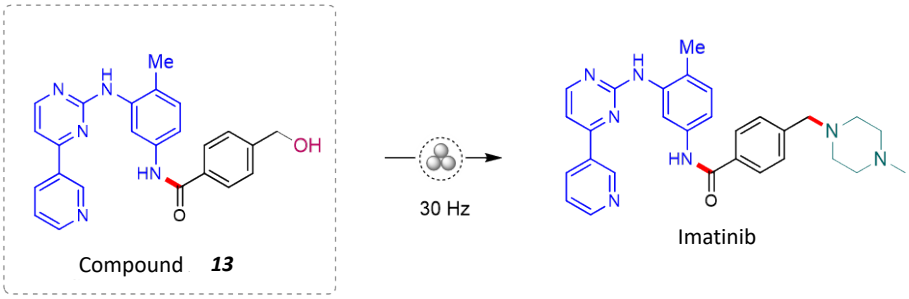

Table 10 and Figure 20. *Selected crystallographic data and refinement parameters and crystal structures for compound* ***13***

Parameter	Compound *13*
Formula	$C_{25}H_{25}N_5O_3$
Crystal system	Monoclinic
Space group	$P2_1/c$
a (Å)	14.3819(4)
b (Å)	15.9349(5)
c (Å)	9.4755(3)
α (°)	90
β (°)	99.199(3)
γ (°)	90
V (Å³)	2143.61(11)
Z	4
R_1 [I>2σ(I)]	0.061
wR_2	0.188
S	1.095

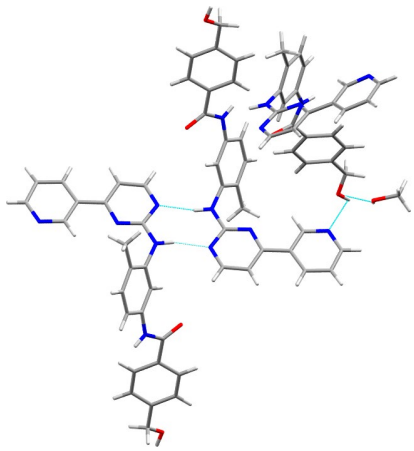

The synthesis of imatinib proceeded via a two-step mechanochemical sequence, with intermediate ***13*** serving as a pivotal structural species whose solid-state characterization provided important insight into molecular geometry and non-covalent interactions governing the crystalline architecture. Single crystals of ***13***, suitable for X-ray diffraction analysis, were obtained by slow evaporation from methanol solution, yielding a methanol solvate. The crystallographic analysis revealed the connectivity and three-dimensional arrangement of this amide intermediate, confirming the regiochemical outcome of the EDC-mediated mechanochemical coupling and establishing the structural basis for the subsequent nucleophilic substitution step.

The molecular structure of ***13*** confirmed the anticipated amide bond geometry, with the C–N bond exhibiting partial double bond character consistent with resonance delocalization across the amide linkage, as evidenced by shortened C–N bond distances relative to typical amine C–N single bonds. The planar arrangement of the amide nitrogen and its substituents indicated restricted rotation, a hallmark of the conjugated amide system. The benzylic hydroxyl group, retained intact through the coupling step, was found to participate in directional hydrogen bonding within the crystal lattice. The hydroxyl oxygen acted as both a hydrogen bond donor and acceptor, forming O–H···O and N–H···O interactions with neighbouring molecules and co-crystallized methanol solvent molecules, thereby stabilizing the solvate packing arrangement.

The secondary amide N–H group engaged in characteristic N–H···O=C hydrogen bonding with adjacent amide carbonyls, generating a hydrogen-bonded network that

propagated through the crystal. These intermolecular interactions, alongside weak C–H···π contacts between aromatic rings, contributed to the overall crystal cohesion. The pyrimidine and aniline-derived aromatic rings adopted a nearly coplanar conformation, suggesting conjugation across the amide bridge, which has direct implications for the electronic properties relevant to the drug's biological activity. The methanol solvate geometry further underscored the strong hydrogen bonding capacity of the hydroxyl and amide functionalities, rationalizing the observed selectivity in the coupling reaction: the directionality and strength of N–H···O interactions thermodynamically favour amide formation over ester formation under the EDC·HCl mechanochemical conditions, consistent with the near-complete chemoselectivity observed. These structural findings thus provide a crystallographic rationale for the chemoselective behaviour of EDC·HCl, corroborating the solution-phase analogy and reinforcing the mechanistic understanding of selectivity in mechanochemical amide coupling of hydroxycarboxylic acids.

4.4. Characterisation of Metal Organic Framework and host-guest supramolecular complexes (Publications VI and VII)

To evaluate the suitability of compound ***14*** Cobalt-MOF as a crystalline sponge in the Publication VI, the as-synthesised crystals, which contained approximately nine DMF molecules per unit cell, were subjected to sequential immersion in seven structurally and chemically diverse solvents: cyclohexane, diethyl ether, chloroform, 1,4-dioxane, tetrahydrofuran (THF), pyridine, and dichloromethane (CH_2Cl_2). These solvents were selected to span a broad range of polarities, molecular sizes, and surface tensions, enabling a systematic assessment of their capacity to displace DMF without compromising framework integrity.

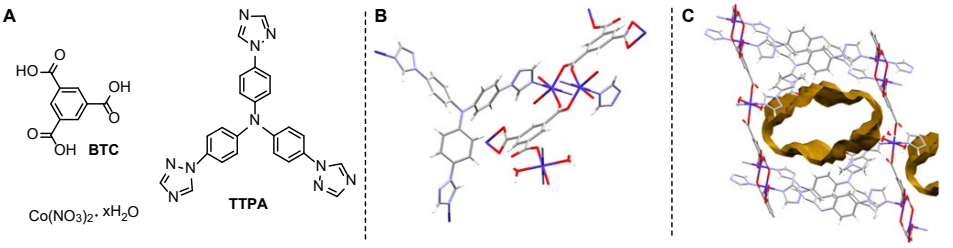

Figure 21. *Structures of starting compounds (**A**), crystal structure of {[$Co_{1.5}$(TTPA)(BTC)(H_2O)]$_2$·13H_2O}$_n$ CCDC 1414118 highlighting coordination centres (**B**) and voids (**C**), water molecules omitted for clarity*

SCXRD analysis following solvent treatment revealed a markedly solvent-dependent outcome. The framework retained its porous integrity upon exchange with chloroform, 1,4-dioxane, diethyl ether, CH_2Cl_2, and cyclohexane. Among these, chloroform, dioxane, and diethyl ether preserved unit cell parameters consistent with the parent Cobalt-MOF structure, whilst CH_2Cl_2 and cyclohexane produced unit cells in agreement with the contracted Cobalt-MOF* polymorph. Structural analysis further indicated that, for the majority of post-exchange structures, residual water molecules occupied portions of the pore voids within poorly ordered hydrogen-bonding networks. This observation suggests that the introduced organic solvents selectively displaced DMF from regions of the pore not already occupied and stabilised by water, implying a partial, spatially heterogeneous exchange process.

***Table 11**. Crystallographic data of metal-organic framework before and after solvent exchange*

	Before solvent exchange		**After solvent exchange**				
	Cobalt-MOF	Cobalt-MOF*	Cobalt-MOF in cyclohexane	Cobalt-MOF in $CHCl_3$	Cobalt-MOF* in DCM	Cobalt-MOF in Et_2O	Cobalt-MOF in dioxane
Used diffractometer	Rigaku Compact HomeLab	Rigaku XtaLAB Synergy-R	Rigaku Compact HomeLab	Rigaku XtaLAB Synergy-R	Rigaku XtaLAB Synergy-R	Rigaku XtaLAB Synergy-R	Rigaku XtaLAB Synergy-R
Space group	triclinic, $\bar{P}1$	triclinic, $\bar{P}1$	triclinic, $\bar{P}1$	triclinic, $\bar{P}1$	triclinic, $\bar{P}1$	triclinic, $\bar{P}1$	triclinic, $\bar{P}1$
a(Å)	10.0510(8)	9.9791(2)	10.0511(3)	10.0438(3)	9.9444(2)	10.03296(17)	10.0333(4)
b(Å)	17.7700(13)	14.0230(3)	17.7249(6)	17.3598(7)	14.2769(3)	17.5783(4)	17.5723(7)
c(Å)	17.9534(13)	15.6091(3)	17.9019(6)	17.9641(5)	15.8819(3)	17.9182(3)	18.2496(5)
α(°)	67.2500(10)	103.290(2)	63.454(4)	64.739(3)	104.1356(17)	63.781(2)	110.735(3)
β(°)	74.9280(10)	105.302(2)	76.276(3)	75.646(2)	106.5159(19)	76.3896(16)	100.847(3)
γ(°)	81.5690(10)	97.938(2)	80.256(2)	81.276(3)	98.5902(18)	80.6866(16)	102.523(4)
V($Å^3$)	2851.6(4)	2003.93(8)	2764.28(18)	2740.48(17)	2037.46(8)	2749.27(10)	2811.14(19)
R	0.0994	0.0613	0.1967	0.0575	0.0620	0.0617	0.0515

In stark contrast, exposure to pyridine resulted in complete loss of crystallinity, attributed to the strong Lewis base character of pyridine competing with the triazole groups of the TTPA ligand for coordination to Co(II) centres. Given that pyridine was introduced in substantial excess, displacement of the coordinated triazole units from the metal nodes appears highly plausible, leading to irreversible framework disintegration. THF likewise proved incompatible with the framework, causing complete dissolution of the crystals. These results underscore the critical importance of solvent-framework chemical compatibility, particularly with respect to competitive coordination, when designing activation protocols for cobalt-based MOFs.

The kinetics of DMF release during solvent exchange were monitored by ^{1}H NMR spectroscopy, tracking the concentration of free DMF in solution as a function of time over three consecutive exchange cycles. For cyclohexane, CH_2Cl_2, and pyridine, the observed DMF release profiles were well-described by a mono-exponential decay function across all three cycles, indicative of a single predominant exchange mechanism. Cyclohexane yielded reproducible and well-fitted exponential kinetics across all exchange steps, consistent with maintained crystalline order and uniform pore accessibility throughout the exchange process. This consistency reinforces the suitability of cyclohexane as an activation solvent for Cobalt-MOF.

The behaviour of CH_2Cl_2 was more ambiguous: the gradual rise of the NMR kinetics curve across cycles was interpreted as indicative of a sample containing a mixture of Cobalt-MOF and Cobalt-MOF*, with the denser-packed Cobalt-MOF* polymorph releasing DMF more slowly due to its contracted pore geometry. Chloroform and 1,4-dioxane displayed comparatively rapid DMF release in the initial hours, though the observation that chloroform-treated crystals floated to the surface of the solvent; implying a bulk density lower than that of chloroform suggests that this rapid exchange may reflect superficial rather than thorough pore penetration. Diethyl ether exhibited anomalous first-cycle kinetics described by a linear, rather than exponential, function, with subsequent cycles reverting to the common exponential pattern; this irregularity likely reflects a transitional disruption of the pore structure during the initial exchange event.

Following successful DMF evacuation, the capacity of the activated Cobalt-MOF to act as a crystalline sponge was evaluated by introducing the bicyclic diol isosorbide as a representative small organic guest. The uptake of isosorbide from solution was monitored by ^{1}H NMR spectroscopy, tracking the decay of solution-phase isosorbide concentration over time in the presence of cyclohexane-, CH_2Cl_2-, and diethyl ether-exchanged Cobalt-MOF crystals.

In all three systems, the isosorbide uptake profiles were best described by a bi-exponential decay model, revealing the coexistence of two kinetically distinct sorption processes occurring in parallel. This biphasic behaviour is interpreted as reflecting, first, the relatively rapid displacement of residual bulk solvent molecules within the open MOF channels by incoming isosorbide, and second, a slower conformational rearrangement of the isosorbide guest within the pore environment to achieve a more thermodynamically stable, tightly packed configuration. The latter process is postulated to involve the formation of specific hydrogen bonds between the hydroxyl groups of isosorbide and the polar functional groups of the framework, conferring enhanced guest stability. This mechanistic interpretation is consistent with the rigid, stereochemically defined structure of isosorbide, which would impose a significant conformational energy barrier to achieving optimal packing within a confined pore geometry.

Comparison across solvents highlighted notable differences in guest uptake efficiency. Cyclohexane-activated crystals achieved the greatest total isosorbide incorporation, supporting the conclusion that this non-polar, chemically inert solvent optimally preserves pore accessibility whilst minimising competitive host-solvent interactions. The CH_2Cl_2 system exhibited a pronounced initial concentration drop within the first ten minutes, followed by a marked deceleration, with the final incorporation level falling below that observed for cyclohexane. This profile is consistent with partial pore collapse in the Cobalt-MOF* phase, which would restrict guest diffusion after the initial surface uptake event. Diethyl ether-treated samples showed a trajectory initially comparable to cyclohexane but plateaued at lower incorporation levels, suggesting incomplete exchange and only partial pore availability for guest binding. Despite confirmed guest uptake by NMR, SCXRD analysis of post-binding crystals did not yield a resolved guest structure, attributed to either insufficient guest loading density or pronounced orientational disorder of isosorbide within the pores, both common challenges in crystalline sponge applications involving flexible or symmetric guest molecules.

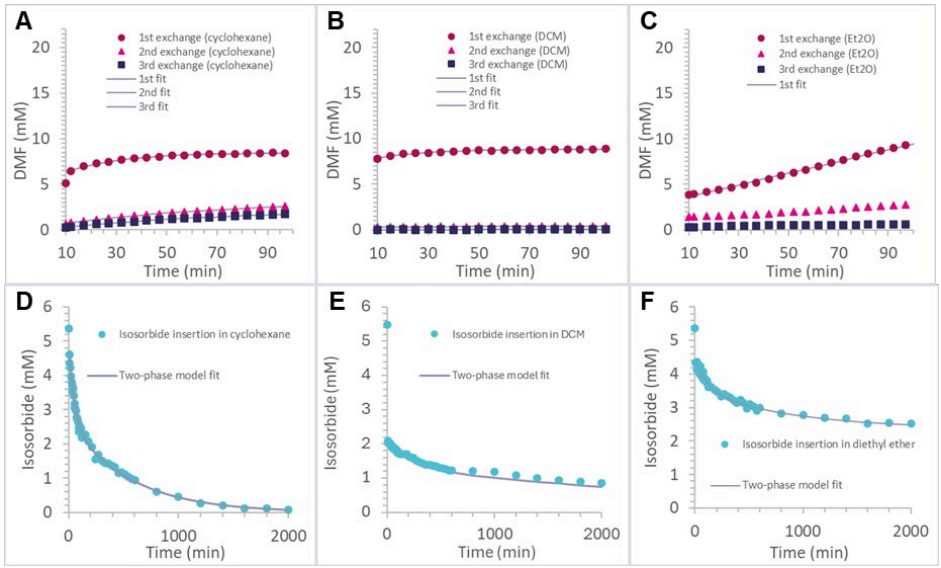

Figure 22. *Kinetic data of solvent exchanges with cyclochexane (**A**), with CH_2Cl_2 (**B**), with Et_2O (**C**) and subsequent isosorbide binding to cobalt-MOF in cyclohexane (**D**), in CH_2Cl_2 (**E**) and in Et_2O (**F**).*

Table 12*. Rate constants of solvent exchange and guest insertion*

Rate constants of solvent exchange				
Solvent	Rate constant (1^{st} exchange, min^{-1})	Rate constant (2^{nd} exchange, min^{-1})	Rate constant (3^{rd} exchange, min^{-1})	Fit function
DMF	-	-	-	-
cyclohexane-d_{12}	0.046	0.015	0.012	$y = y_0 + a(1 - e^{-bx})$
DCM-d_2	0.048	0.036	0.012	$y = y_0 + a(1 - e^{-bx})$
Et_2O -d_{10}	0.064	-	-	$y = y_0 + a * x$

pyridine-d_5	0.019	0.009	0.023	$y = y_0 + a(1 - e^{-bx})$
Rate constants of guest insertion				
Solvent	Rate constant (fast exchange, min^{-1})		Rate constant (slow exchange, min^{-1})	Fit function
cyclohexane-d_{12}	0.046		0.015	$y = ae^{-bx} + ce^{-dx}$
DCM-d_2	0.0049		0.0003	$y = ae^{-bx} + ce^{-dx}$
Et_2O -d_{10}	0.0081		0.0011	$y = y_0 + ae^{-bx} + ce^{-dx}$
pyridine-d_5	0.0218		-	$y = y_0 + ae^{-bx}$

Collectively, these results establish a clear hierarchy of solvent suitability for the activation and guest-loading of Cobalt-MOF. Cyclohexane emerges as the optimal activation solvent, combining effective DMF removal, preservation of crystalline order, and maximal capacity for subsequent guest incorporation. The mechanistic insights afforded by biphasic guest sorption kinetics advance the understanding of guest-MOF interactions beyond simple diffusion models, highlighting the importance of post-insertion conformational dynamics in determining guest-binding efficiency and stability. The observed sensitivity of the framework to Lewis-basic and highly coordinating solvents, particularly pyridine, sets important boundary conditions for the practical use of Cobalt-MOF as a crystalline sponge and underlines the necessity of carefully matching solvent properties to the chemical identity of the framework's coordination centres.

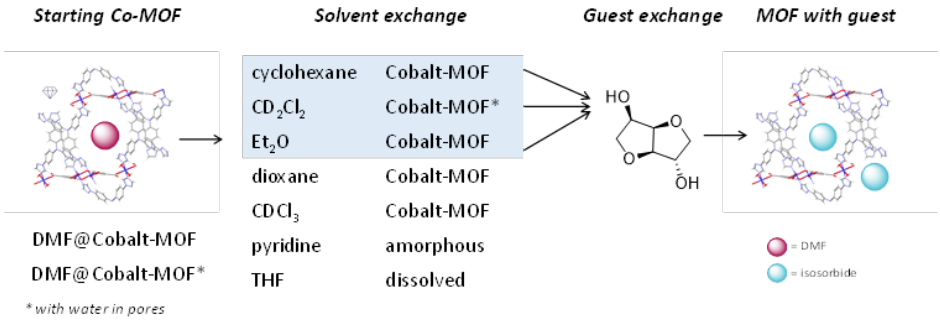

Figure 23. *Outline of performed solvent and subsequent isosorbide exchange.*

In Publication VII, single crystal X-ray diffraction (SC-XRD) provided definitive structural confirmation of the chimeric mono-biotinylated hemicucurbit[8]uril (mixHC[8]) and its anion-binding mode in the solid state. Despite extensive crystallization screening employing a range of counter-cations (Ag^+, K^+, Na^+) and anions (ClO_4^-, PF_6^-), single crystals suitable for diffraction were obtained exclusively from the slow evaporation of a methanol solution of compound ***15*** (−)-((*S,S,R*)(*R,R*)$_7$)-mixHC[8] in the presence of a twofold excess of tetrabutylammonium hexafluorophosphate ($TBAPF_6$). The (+)-pseudo-enantiomer did not yield crystals under any condition attempted, likely reflecting differences in packing efficiency imposed by the altered stereochemistry of the biotin-derived subunit.

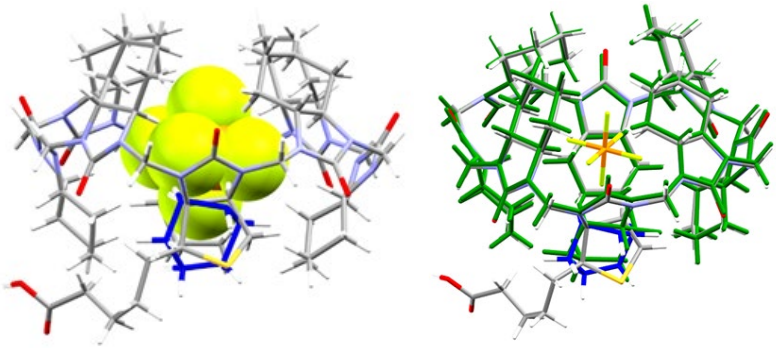

***Figure 24**. Left - Crystal structure of a co-crystal with the cycHC[8] and (−)-((S,S,R)(R,R)$_7$)-mixHC[8] with the 50:50 disorder of the cyclohexyl and biotin 5-membered ring (cyclohexyl unit is coloured blue for clarity). Right - Overlay of SC-XRD of regular cycHC[8] with PF_6^- and (−)-((S,S,R)(R,R)$_7$)-mixHC[8] with PF_6^- inclusion complexes (regular cycHC[8] is presented in green).*

Table 13.** Selected crystallographic data and refinement parameters for compound **15

Parameter	Compound *15*
Formula	$C_{163}H_{268}F_{12}N_{34}O_{18}P_2S$
Crystal system	Orthorhombic
Space group	$P2_12_12_1$
a (Å)	20.2233(2)
b (Å)	20.5002(2)
c (Å)	20.7796(2)
α (°)	90
β (°)	90
γ (°)	90
V (Å³)	8614.84(15)
Z	2
R_1 [I>2σ(I)]	0.083
wR_2	0.238
S	1.00
Flack parameter	0.015(10)

The resulting crystal structure unambiguously establishes a 1:1 host–guest stoichiometry for the PF_6^-@(−)-mixHC[8] inclusion complex in the solid state. The encapsulated hexafluorophosphate anion occupies the center of the macrocyclic cavity without disorder, adopting an orientation in which two fluorine atoms point axially toward the macrocyclic portals and the remaining four fluorine atoms lie in the equatorial plane, directed toward the four corners of the square-shaped methylene belt. This binding geometry mirrors that previously established for the parent PF_6^-@cycHC[8] complex; structural overlay of the two inclusion complexes using PF_6^- as the alignment center demonstrates near-identical spatial arrangements of the macrocyclic framework, confirming that the incorporation of a single biotin unit does not substantially perturb the overall topology of the HC[8] scaffold.

Hirshfeld surface analysis of the encapsulated PF_6^- anion, mapped with d_norm over the range −0.1 to 1.0, revealed that the dominant stabilizing interactions are C–H···F contacts between the methine/methylene protons of the macrocycle and the fluorine atoms of the guest. Critically, the shortest observed contact distance of 2.45 Å (C2D–

H2D···F2, Δ = −0.11 Å relative to the sum of van der Waals radii) involves monomeric unit D, identified as the biotin five-membered ring, indicating that the biotin subunit makes a particularly strong and geometrically favorable contribution to guest encapsulation. This finding provides a structural rationale for the ITC-derived observation that the (+)-diastereomer, which presents its biotin unit in a sterically distinct orientation, exhibits 1.5–2.5-fold higher association constants for PF_6^- compared to (−)-mixHC[8].

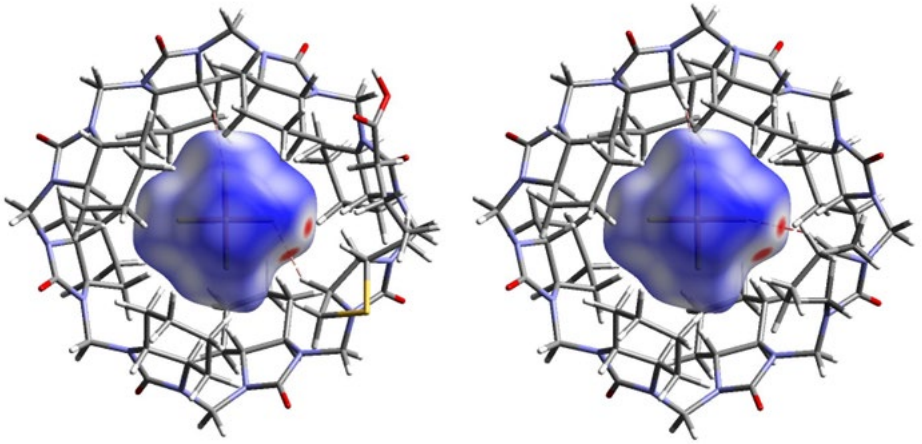

***Figure 25**. Hirshfeld surface for the encapsulated PF_6^- anion, mapped with d_{norm} over the range −0.1 to 1.0. Close contacts where d(DH···F) is shorter than ∑r(vdW)[H, A] are displayed with a dashed line. Hirshfeld surface for PF_6^- anion with biotin 5-membered ring as monomeric unit (left) and Hirshfeld surface for PF_6^- anion with cyclohexyl ring as monomeric unit (right)*

Hexafluorophosphate (PF_6^-)

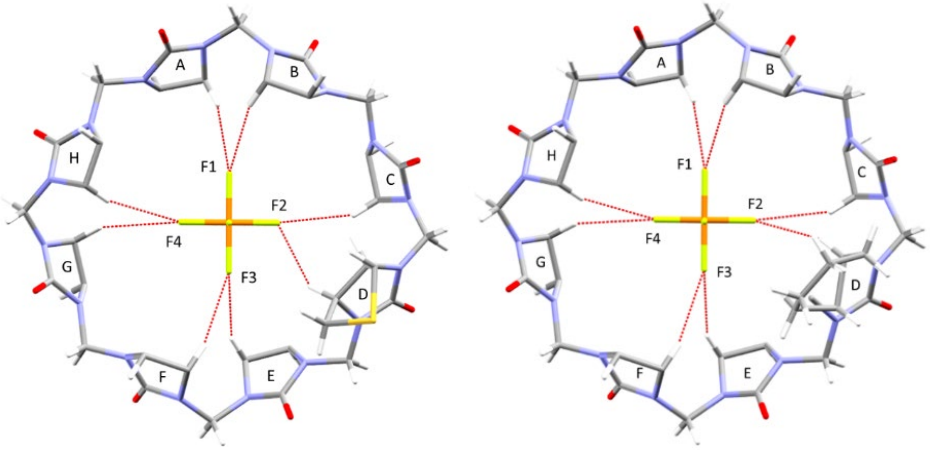

***Figure 26**. Left - Close contacts within PF_6@(−)-((S,S,R)(R,R)7)-mixHC[8]. $(CH_2)_4$ groups are omitted for clarity, atoms involved in equivalent monomeric units are denoted with suffixes A-H. Monomeric unit D is biotin 5-membered ring. Right - Close contacts within PF_6@(−)-((S,S,R)(R,R)7)-mixHC[8]. $(CH_2)_4$ groups are omitted for clarity, atoms involved in equivalent monomeric units are denoted with suffixes A-H. Monomeric unit D is cyclohexyl ring.*

Table 14. *Shortest d(D-H···A) distances from the crystal structure of TBA(PF6–@(–)-((S,S,R)(R,R)7)-mixHC[8]), between the encapsulated PF_6^- and the host*

D–H···A	***d*(H···A), Å**	**D(H···A) – ∑r(v*dW*)[H, A], Å**
C2A–H2A…F1	**2.53**	**-0.03**
C2B–H2B…F1	2.61	0.05
C2C–H2C…F2	2.81	0.25
C2D–H2D…F2	**2.45**	**-0.11**
C2E–H2E…F3	2.63	0.07
C2F–H2F…F3	2.64	0.08
C2G–H2G…F3	2.92	0.36
C2H–H2H…F3	2.67	0.11

Table 15. *Shortest d(D-H···A) distances from the crystal structure of TBA(PF6–@(–)-((S,S,R)(R,R)7)-mixHC[8]), between the encapsulated PF_6^- and the host*

D–H···A	***d*(H···A), Å**	**D(H···A) – ∑r(v*dW*)[H, A], Å**
C2A–H2A…F1	**2.53**	**-0.03**
C2B–H2B…F1	2.61	0.05
C2C–H2C…F2	2.81	0.25
C2D–H2D…F2	**2.50**	**-0.06**
C2E–H2E…F3	2.63	0.07
C2F–H2F…F3	2.64	0.08
C2G–H2G…F3	2.92	0.36
C2H–H2H…F3	2.67	0.11

A key structural feature resolved by SC-XRD concerns the conformation of the biotin thiolane envelope. DFT calculations had predicted two energetically nearly equivalent conformers — one with the sulfur atom directed into the macrocyclic cavity (endo) and one directed outward (exo) — with an energy difference of less than 1 kJ mol^{-1}. Examination of the electron density in the crystal structure identified sulphur exclusively in the exo conformation, pointing away from the cavity. Molecular overlay of the SC-XRD structure with the DFT-optimized geometry shows excellent agreement in the overall spatial arrangement of atoms, with only minor deviations, while confirming the outward-pointing thiolane geometry in the solid state. This preference in the crystal is interpreted as a consequence of electrostatic repulsion between the electron-rich sulphur atom and the electron-dense PF_6^- guest, which energetically selects the exo conformer in the

complex despite its near-isoenergetic relationship with the endo form in the free macrocycle. Furthermore, the crystal structure confirms that the pendant carboxylic acid group of the biotin unit is directed away from the binding cavity and plays no direct role in anion complexation, an observation of considerable practical importance: it establishes that this functional handle is fully available for covalent surface immobilization — as subsequently exploited in the preparation of the perchlorate-extracting mixHC[8]-APS material — without compromising the anion-binding function of the macrocycle. Taken together, the crystallographic data provide an atomic-resolution foundation for understanding the structure–property relationships of this novel chimeric macrocyclic receptor.

Conclusion

This thesis has demonstrated the power and versatility of X-ray diffraction methods as an integrated analytical platform across four interconnected domains of chemistry: enantioselective synthesis, coordination and pharmaceutical chemistry, solid-state transformations and polymorphism, and supramolecular host-guest and framework systems. Spanning seven publications, the work establishes that SC-XRD and PXRD, when applied in a deliberate and complementary manner, yield structural insight that no other single analytical technique can provide.

In the area of enantioselective organocatalysis (Papers I–III), SC-XRD combined with the Flack parameter provided unambiguous absolute configuration assignments for chiral indole derivatives and Michael adducts, confirming the sense of asymmetric induction achieved under cinchona alkaloid-derived catalysis and phase-transfer conditions. Flack parameter values consistently close to zero validated the correct absolute structure, while the crystal packing analyses revealed the non-covalent interaction networks—hydrogen bonding, π–π stacking, and van der Waals contacts—that govern the solid-state architecture of these enantiopure compounds. These results affirm SC-XRD as the definitive tool for stereochemical assignment in asymmetric synthesis, particularly where spectroscopic methods alone are insufficient.

Structural characterisation of silver carboxylate coordination compounds and hypervalent iodine(III) reagents (Paper IV) established precise coordination geometries and elucidated the role of ancillary ligands—including pyridine derivatives and morpholine-functionalised analogues—in modulating intermolecular interactions and crystal packing. The crystallographic data provided a structural foundation for understanding the reactivity and selectivity of these reagents in synthetic applications. Similarly, the characterisation of the imatinib amide precursor (Publication V), including modelling of terminal hydroxyl disorder, demonstrated the importance of SC-XRD in validating pharmaceutical intermediates at atomic resolution.

In the domain of polymorphism and solid-state dynamics (Paper VI), the re-synthesis of the cobalt-based MOF $\{[Co_{1.5}(TTPA)(BTC)(H_2O)]_2 \cdot 13H_2O\}_n$ yielded a previously undescribed solvate polymorph, Cobalt-MOF*, exhibiting a contracted void volume of approximately 2000 Å³ relative to the ~2800 Å³ of the parent phase—consistent with the breathing behaviour characteristic of flexible framework architectures. Combined SC-XRD and ^{1}H NMR kinetics measurements enabled quantitative monitoring of solvent exchange and guest insertion processes, linking solid-state structural changes to solution-phase dynamics. These findings illustrate the complementarity of diffraction and spectroscopic methods for studying responsive materials.

The structural studies of cyclohexanohemicucurbituril host-guest complexes and the enantiopure mixed macrocycle (Paper VII) advanced the understanding of anion recognition and size-selective encapsulation in cucurbituril-type systems. SC-XRD resolved the geometry of anion binding within the cycHC[8] cavity and confirmed the absolute configuration of the chiral (-)-(mixHC[8]) macrocycle via a Flack parameter of 0.015(10). The successful modelling of 50:50 positional disorder in the PF_6^-@(-)-mixHC[8] co-crystal, independently validated by HPLC analysis, exemplifies the rigour required for structural characterisation of complex supramolecular assemblies.

Taken together, the results presented in this thesis confirm that non-covalent interactions—hydrogen bonding, halogen bonding, π–π stacking, electrostatic forces, and metallophilic contacts—are not merely structural motifs but active determinants of

chemical reactivity, pharmaceutical performance, catalytic selectivity, and framework responsiveness. The ability to map these interactions at atomic resolution, across systems ranging from sub-millimetre organic crystals to porous coordination networks, constitutes the principal scientific contribution of this work.

From a methodological standpoint, this thesis demonstrates that SC-XRD and PXRD are most powerful when deployed in tandem: single-crystal analysis provides the high-resolution atomic map, while powder diffraction delivers bulk-phase validation, polymorph fingerprinting, and real-time monitoring of solid-state processes. The integration of these techniques with solution-state NMR spectroscopy and chromatographic analysis further extends the analytical reach, enabling a comprehensive picture of structure, dynamics, and composition across multiple length scales. This integrated approach is recommended as a general strategy for structural studies in synthetic, pharmaceutical, and materials chemistry.

References

1. Nobel Prize in Physics 1914. *NobelPrize.org* https://www.nobelprize.org/prizes/physics/1914/perspectives/.
2. Nobel Prize in Physics 1915. *NobelPrize.org* https://www.nobelprize.org/prizes/physics/1915/perspectives/.
3. Nobel Prize in Chemistry 2016. *NobelPrize.org* https://www.nobelprize.org/prizes/chemistry/2016/popular-information/.
4. Nobel Prize in Chemistry 2025. *NobelPrize.org* https://www.nobelprize.org/prizes/chemistry/2025/popular-information/.
5. Nobel Prize winners. https://www.iucr.org/people/nobel-prize.
6. Arunan, E. *et al.* Definition of the hydrogen bond (IUPAC Recommendations 2011). *Pure Appl. Chem.* **83**, 1637–1641 (2011).
7. On the Importance and Origin of Aromatic Interactions in Chemistry and Biodisciplines | Accounts of Chemical Research. https://pubs.acs.org/doi/10.1021/ar300083h.
8. Garratt, P. J. *et al.* Molecular design using electrostatic interactions. 1. Synthesis and properties of flexible tripodand tri- and hexa-cations with restricted conformations. Molecular selection of ferricyanide from ferrocyanide. *Tetrahedron* **54**, 949–968 (1998).
9. Kitaĭgorodskiĭ, A. I. (Aleksandr I. *Organic Chemical Crystallography*. (New York, Consultants Bureau, 1961).
10. Strong Closed-Shell Interactions in Inorganic Chemistry | Chemical Reviews. https://pubs.acs.org/doi/10.1021/cr940396v.
11. Experimental Binding Energies in Supramolecular Complexes | Chemical Reviews. https://pubs.acs.org/doi/10.1021/acs.chemrev.5b00583.
12. Supramolecular Chemistry, 3rd Edition | Wiley. *Wiley.com* https://www.wiley.com/en-kr/Supramolecular+Chemistry%2C+3rd+Edition-p-9781119582519.
13. Faiz, J. A., Heitz, V. & Sauvage, J.-P. Design and synthesis of porphyrin-containing catenanes and rotaxanes. *Chem. Soc. Rev.* **38**, 422–442 (2009).
14. Leigh, D. A., Marcos, V. & Wilson, M. R. Rotaxane Catalysts. *ACS Catal.* **4**, 4490–4497 (2014).
15. Mena-Hernando, S. & Pérez, E. M. Mechanically interlocked materials. Rotaxanes and catenanes beyond the small molecule. *Chem. Soc. Rev.* **48**, 5016–5032 (2019).
16. Taghavi Shahraki, B. *et al.* The flowering of Mechanically Interlocked Molecules: Novel approaches to the synthesis of rotaxanes and catenanes. *Coord. Chem. Rev.* **423**, 213484 (2020).
17. Li, X. *et al.* 2D and 3D metal–organic frameworks constructed with a mechanically rigidified [3]rotaxane ligand. *Chem. Commun.* **58**, 5829–5832 (2022).
18. Synthesis of [2]Rotaxane-Based pH-Responsive Molecular Switch Involving a [23]Crown Ether Wheel, Dibenzylammonium and Methyl Triazolium Recognition Stations - Prakashni - 2023 - ChemistrySelect - Wiley Online Library. https://chemistry-europe.onlinelibrary.wiley.com/doi/abs/10.1002/slct.202300553.

19. Guo, M., Sun, X., Chen, J. & Cai, T. Pharmaceutical cocrystals: A review of preparations, physicochemical properties and applications. *Acta Pharm. Sin. B* **11**, 2537–2564 (2021).
20. Sun, C. C. & Hou, H. Improving Mechanical Properties of Caffeine and Methyl Gallate Crystals by Cocrystallization. *Cryst. Growth Des.* **8**, 1575–1579 (2008).
21. Bhowmik, A., Bamane, S., Saxena, A. K. & Mishra, M. K. Caffeine vs. Theophylline Cocrystals: Insights into Structure–Mechanical Behavior and Piezoelectricity. *Cryst. Growth Des.* **25**, 5007–5021 (2025).
22. Jia, Y. *et al.* Recent advances in pharmaceutical cocrystals of theophylline. *Nat. Prod. Bioprospecting* **14**, 53 (2024).
23. Karagianni, A., Malamatari, M. & Kachrimanis, K. Pharmaceutical Cocrystals: New Solid Phase Modification Approaches for the Formulation of APIs. *Pharmaceutics* **10**, 18 (2018).
24. Sarma, B. & Saikia, B. Hydrogen bond synthon competition in the stabilization of theophylline cocrystals. *CrystEngComm* **16**, 4753–4765 (2014).
25. Konovalova, I. S., Shishkina, S. V., Wyshusek, M., Patzer, M. & Reiss, G. J. Supramolecular architecture of theophylline polymorphs, monohydrate and co-crystals with iodine: study from the energetic viewpoint. *RSC Adv.* **14**, 29774–29788.
26. Bora, P., Saikia, B. & Sarma, B. Regulation of π···π Stacking Interactions in Small Molecule Cocrystals and/or Salts for Physiochemical Property Modulation. *Cryst. Growth Des.* **18**, 1448–1458 (2018).
27. Lan, L. *et al.* Stiffening Organic Crystals through Polymerization Using Visible Light. *J. Am. Chem. Soc.* **147**, 41034–41045 (2025).
28. Bhowmik, A., Bamane, S., Saxena, A. K. & Mishra, M. K. Caffeine vs. Theophylline Cocrystals: Insights into Structure–Mechanical Behavior and Piezoelectricity. *Cryst. Growth Des.* **25**, 5007–5021 (2025).
29. Weidenthaler, C. 1 In situ tools for the exploration of structure–property relationships. in *Crystallography in Materials Science: From Structure-Property Relationships to Engineering* (eds Schorr, S. & Weidenthaler, C.) 1–54 (De Gruyter, 2021).
30. Bryce, D. L. NMR crystallography: structure and properties of materials from solid-state nuclear magnetic resonance observables. *IUCrJ* **4**, 350–359 (2017).
31. Ziletti, A., Kumar, D., Scheffler, M. & Ghiringhelli, L. M. Insightful classification of crystal structures using deep learning. *Nat. Commun.* **9**, 2775 (2018).
32. Gándara, F. & Bennett, T. D. Crystallography of metal–organic frameworks. *IUCrJ* **1**, 563–570 (2014).
33. Danylyuk, O. Host–guest complexes in the crystal land: a plethora of crystal forms and crystallization peculiarities. *Crystallogr. Rev.* **30**, 5–30 (2024).
34. Yakovenko, A. A. *et al.* Study of Guest Molecules in Metal–Organic Frameworks by Powder X-ray Diffraction: Analysis of Difference Envelope Density. *Cryst. Growth Des.* **14**, 5397–5407 (2014).
35. Katsenis, A. D. *et al.* In situ X-ray diffraction monitoring of a mechanochemical reaction reveals a unique topology metal-organic framework. *Nat. Commun.* **6**, 6662 (2015).
36. Bercha, S., Rathod, S., Zavorotynska, O. & Chavan, S. M. Probing Ce- and Zr-Fumarate Metal–Organic Framework Formation in Aqueous Solutions with In

Situ Raman Spectroscopy and Synchrotron X-ray Diffraction. *ACS Omega* **9**, 44321–44335 (2024).
37. Wu, Y. *et al.* Time-Resolved In Situ X-ray Diffraction Reveals Metal-Dependent Metal–Organic Framework Formation. *Angew. Chem. Int. Ed.* **55**, 14081–14084 (2016).
38. Massa, W. *Crystal Structure Determination*. (Springer Science & Business Media, 2010).
39. Particle and Wave Duality of X-Rays | Springer Nature Link. https://link.springer.com/chapter/10.1007/978-981-19-7361-1_1.
40. Hammond, C. Two-dimensional patterns, lattices and symmetry. https://academic.oup.com/book/43705/chapter/367199318.
41. 3 The diffraction of X-rays by crystals. in *Fundamentals of Crystallography* (eds Giacovazzo, C. et al.) 0 (Oxford University Press, 2011). doi:10.1093/acprof:oso/9780199573653.003.0003.
42. Describing lattice planes and directions in crystals: Miller indices and zone axis symbols | The Basics of Crystallography and Diffraction | Oxford Academic. https://academic.oup.com/book/43705/chapter-abstract/367199738?redirectedFrom=fulltext.
43. Fundamentals of Powder Diffraction and Structural Characterization of Materials, Second Edition | Springer Nature Link. https://link.springer.com/book/10.1007/978-0-387-09579-0.
44. Bragg, W. H. & Bragg, W. L. The reflection of X-rays by crystals. *Proc. R. Soc. Lond. Ser. Contain. Pap. Math. Phys. Character* **88**, 428–438 (1913).
45. Vranic, E. AMORPHOUS PHARMACEUTICAL SOLIDS. *Bosn. J. Basic Med. Sci.* **4**, 35–39 (2004).
46. Cullity, B. D. & Stock, S. R. *Elements of X-Ray Diffraction*. (Pearson Education, 2014).
47. X-ray diffraction of polycrystalline materials | The Basics of Crystallography and Diffraction | Oxford Academic. https://academic.oup.com/book/43705/chapter-abstract/367200609?redirectedFrom=fulltext.
48. Dinnebier, R. E. & Billinge, S. J. L. *Powder Diffraction: Theory and Practice*. (Royal Society of Chemistry, 2008).
49. Single-crystal Structure Refinement (SREF). *Methods* https://serc.carleton.edu/msu_nanotech/methods/SREF.html.
50. (IUCr) IUCr checkCIF procedure. https://journals.iucr.org/services/cif/checking/PLAT084.html.
51. Xiao, Y. *et al.* Current trends and advancements in crystallization and single-crystal structural analysis of small molecules. *Coord. Chem. Rev.* **517**, 216035 (2024).
52. Goeta, A. E. & Howard, J. a. K. Low temperature single crystal X-ray diffraction: advantages, instrumentation and applications. *Chem. Soc. Rev.* **33**, 490–500 (2004).
53. Alex Mayo, R., M. Marczenko, K. & R. Johnson, E. Quantitative matching of crystal structures to experimental powder diffractograms. *Chem. Sci.* **14**, 4777–4785 (2023).

54. Crystal Structure Determination from Powder Diffraction Patterns with Generative Machine Learning | Journal of the American Chemical Society. https://pubs.acs.org/doi/10.1021/jacs.4c10244.
55. Taylor, G. The phase problem. *Acta Crystallogr. D Biol. Crystallogr.* **59**, 1881–1890 (2003).
56. Intermolecular Interactions in Functional Crystalline Materials: From Data to Knowledge. https://www.mdpi.com/2073-4352/9/9/478.
57. Bourne, S. A. Chemistry and crystal engineering. *IUCrJ* **11**, 434–435 (2024).
58. Tsering, D., Islam, S., Slathia, N., Kapoor, K. K. & Seth, S. K. Structural elucidation and quantitative analysis of noncovalent interaction in spiropyrrolidine compounds: Experimental and theoretical quantum mechanical studies. *J. Mol. Struct.* **1329**, 141448 (2025).
59. Newman, J. A. *et al.* From Powders to Single Crystals: A Crystallographer's Toolbox for Small-Molecule Structure Determination. *Mol. Pharm.* **19**, 2133–2141 (2022).
60. Altowyan, M. S. *et al.* Synthesis, Characterization and Single Crystal X-ray Diffraction Analysis of Fused Triazolo/Thiadiazole Clubbed with Indole Scaffold. *Crystals* **13**, 423 (2023).
61. Kemp, T. J. & Alcock, N. W. 100 Years of X-ray Crystallography. *Sci. Prog.* **100**, 25–44 (2017).
62. Bragg, W. L. The structure of some crystals as indicated by their diffraction of X-rays. *Proc. R. Soc. Lond. Ser. Contain. Pap. Math. Phys. Character* **89**, 248–277 (1913).
63. Kim, C. D., Pillet, S., Wu, G., Fullagar, W. K. & Coppens, P. Excited-state structure by time-resolved X-ray diffraction. *Acta Crystallogr. Sect. A* **58**, 133–137 (2002).
64. Coppens, P. *et al.* A very large Rh–Rh bond shortening on excitation of the [Rh2(1,8-diisocyano-p-menthane)4]2+ ion by time-resolved synchrotron X-ray diffraction. *Chem. Commun.* 2144–2145 (2004) doi:10.1039/B409463H.
65. The reflection of X-rays by crystals.
66. Helliwell, J. R. & Mitchell, E. P. Synchrotron radiation macromolecular crystallography: science and spin-offs. *IUCrJ* **2**, 283–291 (2015).
67. Grabowski, M. *et al.* Synchrotron Radiation as a Tool for Macromolecular X-Ray Crystallography: a XXI Century Perspective. *Nucl. Instrum. Methods Phys. Res. Sect. B Beam Interact. Mater. At.* **489**, 30–40 (2021).
68. Capelli, S. C., Bürgi, H.-B., Dittrich, B., Grabowsky, S. & Jayatilaka, D. Hirshfeld atom refinement. *IUCrJ* **1**, 361–379 (2014).
69. Chodkiewicz, M., Patrikeev, L., Pawlędzio, S. & Woźniak, K. Transferable Hirshfeld atom model for rapid evaluation of aspherical atomic form factors. *IUCrJ* **11**, 249–259 (2024).
70. Ferreira Guimarães, H. & Lages Rodrigues, B. Multipolar model and Hirshfeld atom refinement of tetra-aqua-bis-(hydrogenmaleato)iron(II). *Acta Crystallogr. Sect. B Struct. Sci. Cryst. Eng. Mater.* **81**, 350–362 (2025).
71. Deschamps, J. R. X-Ray Crystallography of Chemical Compounds. *Life Sci.* **86**, 585–589 (2010).
72. Parsons, S. Determination of absolute configuration using X-ray diffraction. *Tetrahedron Asymmetry* **28**, 1304–1313 (2017).
73. Flack, H. D. On enantiomorph-polarity estimation. *Acta Crystallogr. Sect. A* **39**, 876–881 (1983).

74. (IUCr) On the application of Hamilton's ratio test to the assignment of absolute configuration and an alternative test. https://journals.iucr.org/paper?S0567739481001629.
75. Flack, H. D. & Bernardinelli, G. Reporting and evaluating absolute-structure and absolute-configuration determinations. *J. Appl. Crystallogr.* **33**, 1143–1148 (2000).
76. Flack, H. D. & Bernardinelli, G. Absolute structure and absolute configuration. *Acta Crystallogr. A* **55**, 908–915 (1999).
77. Full article: The Nobel Science: One Hundred Years of Crystallography. https://www.tandfonline.com/doi/full/10.1179/0308018815Z.000000000116.
78. Watkin, D. J. & Cooper, R. I. Howard Flack and the Flack Parameter. *Chemistry* **2**, 796–804 (2020).
79. Small-rotative fixed-target serial synchrotron crystallography (SR-FT-SSX) for molecular crystals | Communications Chemistry. https://www.nature.com/articles/s42004-024-01360-7.
80. Flack, H. D. Absolute-Structure Determination: Past, Present and Future. *CHIMIA* **68**, 26 (2014).
81. When Stereochemistry Raised Its Ugly Head in Coordination Chemistry—An Appreciation of Howard Flack. https://www.mdpi.com/2624-8549/2/3/49.
82. Dubach, V. R. A. & Guskov, A. The Resolution in X-ray Crystallography and Single-Particle Cryogenic Electron Microscopy. *Crystals* **10**, 580 (2020).
83. Songsermsawad, S., Nalaoh, P., Promarak, V. & Flood, A. E. Chiral Resolution of RS-Baclofen via a Novel Chiral Cocrystal of R-Baclofen and L-Mandelic Acid. *Cryst. Growth Des.* **22**, 2441–2451 (2022).
84. Peng, S. *et al.* Chiral drugs: Sources, absolute configuration identification, pharmacological applications, and future research trends. *LabMed Discov.* **1**, 100008 (2024).
85. Chettri, A., Subba, A., Singh, G. P. & Bag, P. P. Pharmaceutical co-crystals: A green way to enhance drug stability and solubility for improved therapeutic efficacy. *J. Pharm. Pharmacol.* **76**, 1–12 (2024).
86. Zhou, Y. *et al.* An Overview on Polymorph Preparation Methods of Active Pharmaceutical Ingredients. *Cryst. Growth Des.* **24**, 584–600 (2024).
87. Liu, L., Wang, J.-R. & Mei, X. Enhancing the stability of active pharmaceutical ingredients by the cocrystal strategy. *CrystEngComm* **24**, 2002–2022 (2022).
88. Braga, D., Casali, L. & Grepioni, F. The Relevance of Crystal Forms in the Pharmaceutical Field: Sword of Damocles or Innovation Tools? *Int. J. Mol. Sci.* **23**, 9013 (2022).
89. Nasrallah, S., Alhadid, A. & Minceva, M. Revealing the Solubility Enhancement of Active Pharmaceutical Ingredients through Eutectic Mixtures Formation: A Parameter Study. *Cryst. Growth Des.* **24**, 6364–6372 (2024).
90. Feng, Y. *et al.* Polymorph transformation of solid drugs and inhibiting strategies. *CrystEngComm* **26**, 6510–6544 (2024).
91. Shi, Q. *et al.* Recent advances in drug polymorphs: Aspects of pharmaceutical properties and selective crystallization. *Int. J. Pharm.* **611**, 121320 (2022).
92. Kar, A., Giri, L., Kenguva, G., Rout, S. R. & Dandela, R. Polymorphism, phase transition, and physicochemical property investigation of Ensifentrine. *CrystEngComm* **26**, 3783–3790 (2024).

93. Tamatam, R. & Shin, D. Asymmetric Synthesis of US-FDA Approved Drugs over Five Years (2016–2020): A Recapitulation of Chirality. *Pharmaceuticals* **16**, 339 (2023).
94. Trampuž, M., Teslić, D. & Likozar, B. Crystal-size distribution-based dynamic process modelling, optimization, and scaling for seeded batch cooling crystallization of Active Pharmaceutical Ingredients (API). *Chem. Eng. Res. Des.* **165**, 254–269 (2021).
95. Ramos Ojeda, N. A. & Kind, M. Evaluation of Crystallization Kinetics to Achieve Equant-Shaped Crystals from an Acicular Active Pharmaceutical Ingredient. *Cryst. Growth Des.* **24**, 7961–7980 (2024).
96. Lin, W. H., Yu, Z.-Q., Chow, P. S. & Tan, R. B. H. The Crystallization of Active Pharmaceutical Ingredients with Low Melting Points in the Presence of Liquid–Liquid Phase Separation. *Crystals* **11**, 1326 (2021).
97. Karan, G., Sahu, S., Metya, A. & Maji, M. S. Asymmetric 1,2-Migration at Vicinal Tetrasubstituted Stereocenters Constructed from α-Keto Imines. *Angew. Chem. Int. Ed.* **63**, e202405212 (2024).
98. McVicker, R. U. & O'Boyle, N. M. Chirality of New Drug Approvals (2013–2022): Trends and Perspectives. *J. Med. Chem.* **67**, 2305–2320 (2024).
99. Gholami, H., Chakraborty, D., Zhang, J. & Borhan, B. Absolute Stereochemical Determination of Organic Molecules through Induction of Helicity in Host–Guest Complexes. *Acc. Chem. Res.* **54**, 654–667 (2021).
100. Eckhoff, M., Diedrich, J. V., Mücke, M. & Proppe, J. Quantitative Structure–Reactivity Relationships for Synthesis Planning: The Benzhydrylium Case. *J. Phys. Chem. A* **128**, 343–354 (2024).
101. Dalessandro, E. V. & Pliego, J. R. Reactivity and stability of ion pairs, dimers and tetramers versus solvent polarity: SNAr fluorination of 2-bromobenzonitrile with tetramethylammonium fluoride. *Theor. Chem. Acc.* **139**, 27 (2020).
102. Hernández-Lima, J. *et al.* How solvent determines the molecular reactive conformation and the selectivity: Solvation spheres and energy. *Front. Chem.* **10**, (2022).
103. Trotta, C. *et al.* Boosting Effect of Sterically Protected Glucosyl Substituents in Formic Acid Dehydrogenation by Iridium(III) 2-Pyridineamidate Catalysts. *ChemSusChem* **17**, e202400612 (2024).
104. Pramanik, S., Saha, P., Ghosh, P. & Mukhopadhyay, C. Steric-Hindrance-Induced Diastereoselective Radical Nitration of 3-Alkylidene-2-oxindoles Followed by Tosylhydrazine-Mediated Sulfonation. *J. Org. Chem.* **88**, 3386–3402 (2023).
105. Formica, M. *et al.* Second Generation Catalytic Enantioselective Nucleophilic Desymmetrization at Phosphorus (V): Improved Generality, Efficiency and Modularity. *Angew. Chem. Int. Ed.* **63**, e202400673 (2024).
106. Vala, R. M., Patel, D. M., Sharma, M. G. & Patel, H. M. Impact of an aryl bulky group on a one-pot reaction of aldehyde with malononitrile and N-substituted 2-cyanoacetamide. *RSC Adv.* **9**, 28886–28893 (2019).
107. Tang, J. *et al.* Unlocking regioselectivity: steric effects and conformational constraints of Lewis bases in alkyllithium-initiated butadiene polymerization. *Chem. Sci.* **15**, 20493–20502 (2024).
108. Putatunda, S. *et al.* Proline bulky substituents consecutively act as steric hindrances and directing groups in a Michael/Conia-ene cascade reaction under synergistic catalysis. *Chem. Sci.* **10**, 4107–4115 (2019).

109. Yuan, M. *et al.* Influence of steric hindrance on the molecular packing and the anchoring of quinonoid zwitterions on gold surfaces. *New J. Chem.* **40**, 5782–5796 (2016).
110. Bezchlibnyk-Butler, K., Aleksic, I. & Kennedy, S. H. Citalopram--a review of pharmacological and clinical effects. *J. Psychiatry Neurosci.* **25**, 241–254 (2000).
111. Sharbaf Shoar, N., Fariba, K. A. & Padhy, R. K. Citalopram. in *StatPearls* (StatPearls Publishing, Treasure Island (FL), 2025).
112. Laux, G. Serotonin Reuptake Inhibitors: Citalopram, Escitalopram, Fluoxetine, Fluvoxamine, Paroxetine, and Sertraline. in *NeuroPsychopharmacotherapy* 1–13 (Springer, Cham, 2021). doi:10.1007/978-3-319-56015-1_413-1.
113. Yin, J., Song, X., Wang, C., Lin, X. & Miao, M. Escitalopram versus other antidepressive agents for major depressive disorder: a systematic review and meta-analysis. *BMC Psychiatry* **23**, 876 (2023).
114. Harrison, W. T. A., Yathirajan, H. S., Bindya, S., Anilkumar, H. G. & Devaraju. Escitalopram oxalate: co-existence of oxalate dianions and oxalic acid mol-ecules in the same crystal. *Acta Crystallogr. C* **63**, o129–o131 (2007).
115. de Diego, H. L., Bond, A. D. & Dancer, R. J. Formation of solid solutions between racemic and enantiomeric citalopram oxalate. *Chirality* **23**, 408–416 (2011).
116. Velásco-Mejía, A. *et al.* Modeling and optimization of a pharmaceutical crystallization process by using neural networks and genetic algorithms. *Powder Technol.* **292**, 122–128 (2016).
117. Eren, A., Civati, F., Ma, W., Gamekkanda, J. C. & Myerson, A. S. Continuous crystallization and its potential use in drug substance Manufacture: A review. *J. Cryst. Growth* **601**, 126958 (2023).
118. Burcham, C. L. *et al.* Pharmaceutical Digital Design: From Chemical Structure through Crystal Polymorph to Conceptual Crystallization Process. *Cryst. Growth Des.* **24**, 5417–5438 (2024).
119. Stauffer, F. *et al.* Raw material variability of an active pharmaceutical ingredient and its relevance for processability in secondary continuous pharmaceutical manufacturing. *Eur. J. Pharm. Biopharm.* **127**, 92–103 (2018).
120. Saito, F. & Schreiner, P. R. Determination of the Absolute Configurations of Chiral Alkanes – An Analysis of the Available Tools. *Eur. J. Org. Chem.* **2020**, 6328–6339 (2020).
121. Ceramella, J. *et al.* A Look at the Importance of Chirality in Drug Activity: Some Significative Examples. *Appl. Sci.* **12**, 10909 (2022).
122. Cabral, T. L. G., Poggetto, G. D., Brussolo da Silva, J. P., Nilsson, M. & Tormena, C. F. Determining the Absolute Configuration of Small Molecules by Diffusion NMR Experiments. *Angew. Chem. Int. Ed.* **64**, e202418508 (2025).
123. Li, G.-W. *et al.* Azaheterocyclic diphenylmethanol chiral solvating agents for the NMR chiral discrimination of alpha-substituted carboxylic acids. *RSC Adv.* **10**, 34605–34611 (2020).
124. Balzano, F., Iuliano, A., Uccello-Barretta, G. & Zullo, V. Renewable Resources for Enantiodiscrimination: Chiral Solvating Agents for NMR Spectroscopy from Isomannide and Isosorbide. *J. Org. Chem.* **87**, 12698–12709 (2022).
125. Brzezicki, A. & Garbacz, P. Differentiation and identification of enantiomers by nuclear magnetic resonance spectroscopy with support of quantum mechanical computations. *Chirality* **36**, e23623 (2024).

126. Jang, S., Park, H., Duong, Q. H., Kwahk, E.-J. & Kim, H. Determining the Enantiomeric Excess and Absolute Configuration of In Situ Fluorine-Labeled Amines and Alcohols by 19F NMR Spectroscopy. *Anal. Chem.* **94**, 1441–1446 (2022).
127. Cimmino, A., Masi, M., Evidente, M., Superchi, S. & Evidente, A. Application of Mosher's method for absolute configuration assignment to bioactive plants and fungi metabolites. *J. Pharm. Biomed. Anal.* **144**, 59–89 (2017).
128. Lee, H.-S., Kang, J. S., Cho, D.-Y., Choi, D.-K. & Shin, H. J. Isolation, Structure Determination, and Semisynthesis of Diphenazine Compounds from a Deep-Sea-Derived Strain of the Fungus Cystobasidium laryngis and Their Biological Activities. *J. Nat. Prod.* **85**, 857–865 (2022).
129. Kessler, J., Dračínský, M. & Bouř, P. Determination of Absolute Configuration in Chiral Solvents with Nuclear Magnetic Resonance. A Combined Molecular Dynamics/Quantum Chemical Study. *J. Phys. Chem. A* **119**, 5260–5268 (2015).
130. Wehrle, R. J., Powell, D. R. & Masterson, D. S. Direct determination of absolute stereochemistry of α-methylselenocysteine using the Mosher method. *Results Chem.* **3**, 100114 (2021).
131. Pescitelli, G. ECD exciton chirality method today: a modern tool for determining absolute configurations. *Chirality* **34**, 333–363 (2022).
132. Bogaerts, J. *et al.* Tackling Stereochemistry in Drug Molecules with Vibrational Optical Activity. *Pharmaceuticals* **14**, 877 (2021).
133. Ozcelik, A., Pereira-Cameselle, R., Poklar Ulrih, N., Petrovic, A. G. & Alonso-Gómez, J. L. Chiroptical Sensing: A Conceptual Introduction. *Sensors* **20**, 974 (2020).
134. Katoono, R., Obara, Y., Sakamoto, K. & Miyashita, R. Study of optical rotation based on the molecular structure in fused oligomers of macrocycles. *RSC Adv.* **14**, 20735–20742 (2024).
135. Liu, X., Yang, J., Geng, Z. & Jia, H. Simultaneous measurement of optical rotation dispersion and absorption spectra for chiral substances. *Chirality* **32**, 1072–1079 (2020).
136. Tranter, G. E. 8.21 Spectroscopic Analysis: Polarimetry and Optical Rotatory Dispersion. in *Comprehensive Chirality* 411–421 (Elsevier, 2012). doi:10.1016/B978-0-08-095167-6.00843-0.
137. Lu, J.-M., Yang, B.-B. & Li, L. Specific Optical Rotation and Absolute Configuration of Flexible Molecules Containing a 2-Methylbutyl Residue. *Eur. J. Org. Chem.* **2020**, 4768–4774 (2020).
138. Kaya, C., Birgül, K. & Bülbül, B. Fundamentals of chirality, resolution, and enantiopure molecule synthesis methods. *Chirality* **35**, 4–28 (2023).
139. Selka, A. *et al.* Recent Advances in Sustainable Total Synthesis and Chiral Pool Strategies with Emphasis on (−)-Sclareol in Natural Products Synthesis. *Eur. J. Org. Chem.* **28**, e202400983 (2025).
140. Dandawate, M., Choudhury, R., Rama Krishna, G. & Srinivasa Reddy, D. Total synthesis and absolute configuration determination of Ktedonoketone, a benzenoid metabolite from *Thermophilic bacterium*. *Tetrahedron Lett.* **61**, 152526 (2020).
141. Choudhury, U. M., Mendhekar, K. L., Kunwar, A. C. & Mohapatra, D. K. Total Synthesis and Determination of Absolute Configuration of Cryptorigidifoliol G. *J. Org. Chem.* **89**, 5219–5228 (2024).

142. Li, Y. *et al.* Hydrogen-bonded frameworks for molecular structure determination. *Nat. Commun.* **10**, 4477 (2019).
143. Tang, W. *et al.* Form selection of concomitant polymorphs: A case study informed by crystallization kinetics modeling. *AIChE J.* **67**, e17129 (2021).
144. Hilfiker, R., Blatter, F. & Raumer, M. von. Relevance of Solid-state Properties for Pharmaceutical Products. in *Polymorphism* 1–19 (John Wiley & Sons, Ltd, 2006). doi:10.1002/3527607889.ch1.
145. *Polymorphism in Pharmaceutical Solids*. (CRC Press, 2018). doi:10.3109/9781420073225.
146. Lohani, S. & Grant, D. J. W. Thermodynamics of Polymorphs. in *Polymorphism* 21–42 (John Wiley & Sons, Ltd, 2006). doi:10.1002/3527607889.ch2.
147. Morris, K. R. *et al.* An integrated approach to the selection of optimal salt form for a new drug candidate. *Int. J. Pharm.* **105**, 209–217 (1994).
148. Cardew, P. T. Ostwald Rule of Stages–Myth or Reality? *Cryst. Growth Des.* **23**, 3958–3969 (2023).
149. Kashchiev, D. Classical nucleation theory approach to two-step nucleation of crystals. *J. Cryst. Growth* **530**, 125300 (2020).
150. Ochsenbein, P. & Schenk, K. J. Crystallography for Polymorphs. in *Polymorphism* 139–166 (John Wiley & Sons, Ltd, 2006). doi:10.1002/3527607889.ch6.
151. Park, E., Lee, J., Kim, J.-H. & Moon, J.-K. X-ray crystal structure, UV–Vis and NMR spectroscopic, and molecular docking studies of pyribencarb isomers. *Appl. Biol. Chem.* **66**, 21 (2023).
152. Uzun, S., Demircioğlu, Z., Taşdoğan, M. & Ağar, E. Synthesis, X-ray diffraction, spectroscopic (FT-IR, UV-Vis, 1H-NMR, 13C-NMR and TGA), DFT and molecular docking studies of (E)-3-(((3-chloro-4-(4-chlorphenoxy) phenyl) imino) methyl) benzene-1,2-diol. *Mol. Cryst. Liq. Cryst.* **742**, 25–39 (2022).
153. Comodi, P. *et al.* The High-Pressure Phase Transition in Jamesonite: A Single-Crystal Synchrotron X-ray Diffraction Study. *Crystals* **13**, 1258 (2023).
154. Plech, A. *et al.* Visualizing Chemical Reactions in Solution by Picosecond X-Ray Diffraction. *Phys. Rev. Lett.* **92**, 125505 (2004).
155. Mączka, M., Collings, I. E., Leite, F. F. & Paraguassu, W. Raman and single-crystal X-ray diffraction evidence of pressure-induced phase transitions in a perovskite-like framework of [(C3H7)4N] [Mn(N(CN)2)3]. *Dalton Trans.* **48**, 9072–9078 (2019).
156. Lee, J.-W. *et al.* A data-driven XRD analysis protocol for phase identification and phase-fraction prediction of multiphase inorganic compounds. *Inorg. Chem. Front.* **8**, 2492–2504 (2021).
157. Lee, J.-W., Park, W. B., Lee, J. H., Singh, S. P. & Sohn, K.-S. A deep-learning technique for phase identification in multiphase inorganic compounds using synthetic XRD powder patterns. *Nat. Commun.* **11**, 86 (2020).
158. Popović, S. Quantitative Phase Analysis by X-ray Diffraction—Doping Methods and Applications. *Crystals* **10**, 27 (2020).
159. Prasianakis, N. I. AI-enhanced X-ray diffraction analysis: towards real-time mineral phase identification and quantification. *IUCrJ* **11**, 647–648 (2024).
160. Klimakow, M. *et al.* Combined Synchrotron XRD/Raman Measurements: In Situ Identification of Polymorphic Transitions during Crystallization Processes. *Langmuir* **26**, 11233–11237 (2010).

161. Levenstein, M. A. *et al.* Dynamic Crystallization Pathways of Polymorphic Pharmaceuticals Revealed in Segmented Flow with Inline Powder X-ray Diffraction. *Anal. Chem.* **92**, 7754–7761 (2020).
162. Egusa, K., Okazaki, F., Schiewe, J., Werthmann, U. & Wolkenhauer, M. Identification of Polymorphic Forms of Active Pharmaceutical Ingredient in Low-Concentration Dry Powder Formulations by Synchrotron X-Ray Powder Diffraction. *Drugs RD* **17**, 413–418 (2017).
163. Michalchuk, A. A. L. & Emmerling, F. Time-Resolved In Situ Monitoring of Mechanochemical Reactions. *Angew. Chem. Int. Ed.* **61**, e202117270 (2022).
164. Zieliński, M., Kaszkur, Z., Juszczyk, W. & Sobczak, J. In situ diffraction monitoring of nanocrystals structure evolving during catalytic reaction at their surface. *Sci. Rep.* **13**, 1469 (2023).
165. Hu, F.-L., Wang, S.-L., Lang, J.-P. & Abrahams, B. F. In-situ X-ray diffraction snapshotting: Determination of the kinetics of a photodimerization within a single crystal. *Sci. Rep.* **4**, 6815 (2014).
166. Konieczny, K., Bąkowicz, J. & Turowska-Tyrk, I. Monitoring Photochemical Reactions in Single Crystals by X-ray Diffraction: Practical Aspects. *J. Chem. Crystallogr.* **46**, 77–83 (2016).
167. Morissette, S. L., Soukasene, S., Levinson, D., Cima, M. J. & Almarsson, Ö. Elucidation of crystal form diversity of the HIV protease inhibitor ritonavir by high-throughput crystallization. *Proc. Natl. Acad. Sci.* **100**, 2180–2184 (2003).
168. Bauer, J. *et al.* Ritonavir: An Extraordinary Example of Conformational Polymorphism. *Pharm. Res.* **18**, 859–866 (2001).
169. Céolin, R. & Rietveld, I. B. The topological pressure-temperature phase diagram of ritonavir, an extraordinary case of crystalline dimorphism. *Ann. Pharm. Fr.* **73**, 22–30 (2015).
170. Iuzzolino, L. *et al.* Predicting the ritonavir crisis by revisiting the polymorph landscape with crystal structure prediction and form 4 structure solution. *Commun. Chem.* **8**, 404 (2025).
171. Sacchi, P. *et al.* Crystal size, shape, and conformational changes drive both the disappearance and reappearance of ritonavir polymorphs in the mill. *Proc. Natl. Acad. Sci.* **121**, e2319127121 (2024).
172. Yao, X., Henry, R. F. & Zhang, G. G. Z. Ritonavir Form III: A New Polymorph After 24 Years. *J. Pharm. Sci.* **112**, 237–242 (2023).
173. Parent, S. D. *et al.* Ritonavir Form III: A Coincidental Concurrent Discovery. *Cryst. Growth Des.* **23**, 320–325 (2023).
174. Molecular, Solid-State and Surface Structures of the Conformational Polymorphic Forms of Ritonavir in Relation to their Physicochemical Properties | Pharmaceutical Research | Springer Nature Link. https://link.springer.com/article/10.1007/s11095-021-03048-2.
175. Bauer, J. *et al.* Ritonavir: An Extraordinary Example of Conformational Polymorphism. *Pharm. Res.* **18**, 859–866 (2001).
176. Predicting the ritonavir crisis by revisiting the polymorph landscape with crystal structure prediction and form 4 structure solution | Communications Chemistry. https://www.nature.com/articles/s42004-025-01814-6.
177. Kaabel, S. *et al.* Size-Control by Anion Templating in Mechanochemical Synthesis of Hemicucurbiturils in the Solid State. *Angew. Chem. Int. Ed.* **58**, 6230–6234 (2019).

178. Kaabel, S. *et al.* Chiral hemicucurbit[8]uril as an anion receptor: selectivity to size, shape and charge distribution. *Chem. Sci.* **8**, 2184–2190 (2017).
179. Jarg, T. *et al.* How reliable is internal standard method in monitoring mechanochemical synthesis? A case study of triphenylmethane in HPLC-UV-MS analysis of hemicucurbit[n]urils. *RSC Mechanochemistry* **2**, 507–515 (2025).
180. Shalima, T. *et al.* Cyclohexanohemicucurbit[8]uril Inclusion Complexes With Heterocycles and Selective Extraction of Sulfur Compounds From Water. *Front. Chem.* **9**, (2021).
181. Cranswick, L. M. D. An Overview of Powder Diffraction. in *Principles and Applications of Powder Diffraction* 1–72 (John Wiley & Sons, Ltd, 2009). doi:10.1002/9781444305487.ch1.
182. Introduction: Noncovalent Interactions. *Chem. Rev.* **116**, 4911–4912 (2016).
183. Ma, X. & Zhao, Y. Biomedical Applications of Supramolecular Systems Based on Host–Guest Interactions. *Chem. Rev.* **115**, 7794–7839 (2015).
184. Huang, F. & Anslyn, E. V. Introduction: Supramolecular Chemistry. *Chem. Rev.* **115**, 6999–7000 (2015).
185. Jeon, W. S. *et al.* Complexation of Ferrocene Derivatives by the Cucurbit[7]uril Host: A Comparative Study of the Cucurbituril and Cyclodextrin Host Families. *J. Am. Chem. Soc.* **127**, 12984–12989 (2005).
186. Martí-Rujas, J. Structural elucidation of microcrystalline MOFs from powder X-ray diffraction. *Dalton Trans.* **49**, 13897–13916 (2020).
187. Petersen, E. E. *et al.* Insights to the formation of Zr-based metal–organic frameworks from in situ powder x-ray diffraction. *J. Phys. Mater.* **8**, 015006 (2024).
188. An Optimised Compaction Process for Zr-Fumarate (MOF-801). https://www.mdpi.com/2304-6740/7/9/110.
189. Edwards, A. *et al.* Structural diversity and solvent-induced transformations of a copper-based metal–organic framework with highly aromatic ligands. *Dalton Trans.* **53**, 14496–14504 (2024).

Acknowledgements

This work was conducted in the Department of Chemistry and Biotechnology of the School of Science at Tallinn University of Technology. The research was supported by the Estonian Ministry of Education and Research (Grant No PRG399), the European Union H2020-FETOPEN grant 828779 (INITIO), COST Action CA18112 "Mechanochemistry for Sustainable Industry", ASTRA "TUT Institutional Development Program for 2016-2022" Graduate School of Functional Materials and Technologies (2014–2020.4.01.16–0032), Erasmus+ and ESF Dora Programs.

I am deeply grateful to my supervisor Prof. Riina Aav for noticing my interest in chemistry already in my Bachelor level studies and providing me with opportunity to join her research group. Thank you for being big inspiration to me academically, personally and professionally. Your abiding support, trust and freedom given to me in my work are the things that I am so grateful for. Your perpetual encouragement and sometimes harsher words to push me forward have been inspiring.

I would also like to express my deepest gratitude to my co-supervisor Prof. Kari Rissanen for welcoming me at the University of Jyvaskyla to polish my skills in SC-XRD making me much more confident in my knowledge of the field. My heartfelt thanks go to Prof. Rissanen's at that time postdoctoral fellow Jas. S. Ward, who was by my side during my visit to Finland eagerly teaching me and giving me countless tips and tricks to use in my research. I am forever thankful to my first supervisor Assoc. Prof. Sandra Kaabel who introduced me to the fascinating world of crystallography and with whom shared passion for art and chemistry made the work fun and almost effortless.

I am fortunate to say that my doctoral studies were not only about the research, thus, my appreciation goes to all the present and former colleagues, collaborators and co-authors with whom all this research was conducted during these years. I want to praise and acknowledge all my colleagues at TalTech, as well as everyone who has contributed to this research with valuable advice, guidance, or assistance. Input from the members of TalTech supramolecular chemistry group has played big part in my progress and I am grateful for everyone's readiness to listen, discuss and help me. I want to thank Dr. Dzmitry Kananovich and Dr. Lukas Ustrnul for passing their knowledge on and helping see things outside of the box. Nele, Marko, Ngan, Kristjan, Kamini, Karin, Aivar, Marina, Mario, Elena, Riin, Ece and Rauno – it has been a pleasure to have you all along on this journey. All the group seminars, outings and trips have been exceptional due to you. Especially I want to thank my lovely ladies from 331 – Tanya, Mari-Liis, Elina, Ketren and Eve. I cannot even begin to describe how important these friendships are to me.

I am extremely grateful to my family, friends for their constant love and support. Most of all, I want to thank my parents - your presence in my mind and heart has been one of the biggest driving forces in my life and I wish to believe that wherever you are, you can be proud. My best friends Helena and Dalia, thank you for standing by my side for ages and supporting me no matter what.

Last but not least, want to express my heartfelt gratitude to my husband Jaagup. Your endless love, encouragement, and support really have been the biggest driving force in my life. Thank you for pushing me, discussing all the topics and for sharing all the ups and downs with me along the way. No matter what, you always find a way to make my mood better and put a smile on my face. I would not have made it without you.

Abstract

Crystallographic analysis of organic compounds: from small molecules to supramolecular complexes

This thesis presents a systematic investigation of X-ray diffraction as an integrated analytical platform in chemistry, applied across eight publications spanning enantioselective synthesis, coordination and pharmaceutical chemistry, polymorphism and solid-state dynamics, and supramolecular host–guest and framework systems. The central premise is that single-crystal X-ray diffraction (SC-XRD) and powder X-ray diffraction (PXRD), when applied in a deliberate and complementary manner, yield structural, stereochemical, and dynamic insight that no other analytical technique can provide.

In the domain of enantioselective organocatalysis (Publications I–III), SC-XRD was employed as the primary tool for unambiguous absolute configuration assignment of chiral indole derivatives and phosphonate adducts obtained under cinchona alkaloid-derived catalysis, phase-transfer catalysis, and bifunctional halogen bond catalysis. Application of the Flack parameter—exploiting anomalous scattering from nitrogen and phosphorus atoms under Cu-Kα radiation—yielded Flack values consistently close to zero, definitively establishing the sense of asymmetric induction in each case. Crystal packing analyses revealed the non-covalent interaction networks governing solid-state architecture and provided structural support for proposed catalytic mechanisms.

The structural characterisation of silver(I) carboxylate coordination polymers and carbonyl hypoiodite halogen bond donors (Publication IV) established precise coordination geometries and argentophilic interaction networks in the silver(I) precursors, and demonstrated for the first time the solid-state structure of tris(O–I–N) carbonyl hypoiodite complexes derived from trimesic acid—the first crystallographically authenticated three-arm halogen bond donor of this class. Bond length trends across the O–I–N series were rationalised in terms of the Lewis basicity of the pyridine ligand and the electron-donating character of the acyl substituent, with computational data at the M06-2X/def2-TZVP level supporting the experimental structure–property relationships. Crystallographic analysis of an imatinib amide precursor (Publication V) confirmed the chemoselective outcome of a mechanochemical EDC–mediated coupling and revealed the hydrogen-bonding network stabilising the methanol solvate.

Investigation of a cobalt-based metal–organic framework (Publication VI) led to the discovery and structural characterisation of a previously undescribed solvate polymorph, Cobalt-MOF*, exhibiting a contracted void volume of approximately 2000 Å³ relative to the ~2800 Å³ of the parent phase, consistent with the breathing phenomenon in flexible porous frameworks. Combined SC-XRD and quantitative ^{1}H NMR spectroscopy (800 MHz) enabled kinetic monitoring of solvent exchange and guest insertion processes, linking crystallographically observed structural changes to solution-phase dynamics.

Structural studies of cyclohexanohemicucurbituril (cycHC[n]) host–guest complexes and an enantiopure mixed macrocycle (Publication VII) resolved the geometry of size-selective anion encapsulation within the cycHC[8] cavity and confirmed the absolute configuration of the chiral (−)-mixHC[8] macrocycle via a Flack parameter of 0.015(10) in the orthorhombic chiral space group $P2_12_12_1$. The successful modelling of 50:50 positional disorder in the PF_6^-@(−)-mixHC[8] co-crystal—independently validated by HPLC analysis confirming 96.7% mixHC[8] composition—demonstrates the rigour required for structural characterisation of complex supramolecular assemblies.

Across all studies, the results confirm that non-covalent interactions—hydrogen bonding, halogen bonding, π–π stacking, electrostatic forces, van der Waals contacts, argentophilic interactions, and metal coordination—collectively determine not only crystal packing but also pharmaceutical performance, catalytic selectivity, and framework responsiveness. The thesis advances both the theoretical understanding of these interactions and their practical exploitation in crystal engineering, asymmetric synthesis, and functional materials design, and demonstrates that SC-XRD and PXRD are most powerful when deployed in tandem, integrated with solution-state spectroscopy and chromatographic analysis.

Lühikokkuvõte

Orgaaniliste ainete kristallstruktuuride analüüs: väikestest molekulidest supramolekulaarsete kompleksideni

Käesolev väitekiri esitab röntgendifraktsiooni süstemaatilise uurimuse keemia integreeritud analüütilise platvormina. Töö põhineb seitsmel publikatsioonil, mis hõlmavad enantioselektiivset sünteesi, koordinatsiooni- ja farmaatsiakeemiat, polümorfismi ja tahkisedünaamikat ning supramolekulaarseid peremees-külaline- ja raamstruktuure. Töö keskseks lähtekohaks on seisukoht, et monokristalli röntgendifraktsioon (SC-XRD) ja pulberröntgendifraktsioon (PXRD) annavad – teadlikult ja teineteist täiendavalt rakendatuna – struktuurilise, stereokeemilise ja dünaamilise ülevaate, mida ükski teine analüütiline meetod pakkuda ei suuda.

Enantioselektiivse organokatalüüsi valdkonnas (artiklid I–III) kasutati SC-XRD-d peamise vahendina kiraalsete indoolderivaatide ja fosfonaatadduktide absoluutse konfiguratsiooni üheseks määramiseks. Ühendid saadi kiinapuu alükloidide katalüüsi, faasiülekandekatalüüsi ja bifunktsionaalse halogeensideme katalüüsi teel. Flacki parameetri rakendamine – kasutades lämmastiku- ja fosforiatomite anomaalset hajumist Cu-Kα kiirguse korral – andis nullilähedased Flacki väärtused, mis kinnitasid lõplikult asümmeetrilise induktsiooni suuna igal üksikjuhul. Kristallpakkimise analüüs paljastas tahkise arhitektuuri kujundavad mittekovalentsed interaktsioonivõrgustikud ning toetas pakutud katalüütilisi mehhanisme.

Hõbe(I) karboksülaatkoordinatsioonipolümeeride ja karbonüülhüpojodiidhalogeensideme doonorite struktuurne iseloomustus (artikkel IV) võimaldas täpselt kirjeldada koordinatsioonigeomeetriaid ja argentofiilseid interaktsioonivõrgustikke hõbe(I) lähteühendites. Lisaks demonstreeriti esmakordselt trimesiinhappel põhinevate tris(O–I–N) karbonüülhüpojodiitkomplekside tahkisstruktuuri – tegemist on selle klassi esimese kristallograafiliselt tõestatud kolmeharulise halogeensideme doonoriga. O–I–N seeria sidemepikkuste trende selgitati püridiinligandi Lewise aluselisuse ja atsüülrühma elektrondoonori iseloomu kaudu; M06-2X/def2-TZVP tasemel arvutustulemused toetasid eksperimentaalselt leitud struktuuri-omaduste seoseid. Imatiniibamiidi eelkäija kristallograafiline analüüs (artikkel V) kinnitas mehhanokeemilise EDC-vahendatud kondensatsiooni kemoselektiivse tulemuse ning paljastas vesiniksidemete võrgustiku, mis stabiliseerib metanoolsolvaati.

Koobaltipõhise metall-orgaanilise raamistiku uurimine (artikkel VI) viis varem kirjeldamata solvaatpolümorfi Cobalt-MOF* avastamise ja iseloomustamiseni. Sellel on kokkutõmbunud tühimiku maht ligikaudu 2000 Å³, võrreldes lähtefaasi ~2800 Å³-ga, mis on kooskõlas hingamisnähtusega painduvates poorses raamistikes. SC-XRD ja kvantitatiivse ^{1}H TMR spektroskoopia (800 MHz) ühendamine võimaldas lahustivahetuse ja külalismolekulide sisestamise kineetilist jälgimist, sidudes kristallograafiliselt täheldatud struktuurimuutused lahusefaasi dünaamikaga. Tsükloheksanohemikukurbituriili (cycHC[n]) peremees-külaliskomplekside ning enantiopuhta segamakrotsükli struktuuriuuringud (artikkel VII) lahhendasid suurusselektiivse anioonkapseldamise geomeetria cycHC[8] õõnsuses ja kinnitasid kiraalse (−)-mixHC[8] makrotsükli absoluutset konfiguratsiooni Flacki parameetri väärtusega 0,015(10) ortorombilises kiraalses ruumirühmas $P2_12_12_1$. PF_6^-@(−)-mixHC[8] kookristalli edukas 50:50 positsioonilise häire modelleerimine – mida kinnitas sõltumatu HPLC analüüs, tõendades 96,7% mixHC[8] koostist – näitlikustab keerukate

supramolekulaarsete struktuuride iseloomustamiseks vajalikku täpsust ja ranget lähenemist.

Kõigi uuringute tulemused kinnitavad, et mittekovalentsed interaktsioonid – vesiniksidemed, halogeensidemed, π–π sidemed, elektrostaatilised jõud, van der Waalsi kontaktid, argentofiilsed interaktsioonid ja metallide koordinatsioon – määravad ühiselt nii kristallpakkimise kui ka farmatseutilise toimivuse, katalüütilise selektiivsuse ja raamistiku reageerimisvõime. Väitekiri süvendab nende interaktsioonide teoreetilist mõistmist ning avab uusi võimalusi nende praktiliseks rakendamiseks kristallinseneeria, asümmeetrilise sünteesi ja funktsionaalsete materjalide disaini valdkondades. Töö näitab veenvalt, et SC-XRD ja PXRD on kõige jõulisemad siis, kui neid kasutatakse koos – lahusefaasi spektroskoopia ja kromatograafilise analüüsiga lõimitud tervikuna.

Appendix 1

Publication I

Trubitsõn, D.; Martõnova, J.; Kudrjašova, M.; Erkman; K.; Järving, I.; Kanger T. (2021). Enantioselective Organocatalytic Michael Addition to Unsaturated Indolyl Ketones. *Organic Letters*, 23 (5), 1820−1824. DOI: 10.1021/acs.orglett.1c00222

OL Organic Letters

pubs.acs.org/OrgLett Letter

Enantioselective Organocatalytic Michael Addition to Unsaturated Indolyl Ketones

Dmitri Trubitsõn, Jevgenija Martõnova, Marina Kudrjašova, Kristin Erkman, Ivar Järving, and Tõnis Kanger*

Cite This: *Org. Lett.* 2021, 23, 1820–1824 Read Online

ACCESS | Metrics & More | Article Recommendations | Supporting Information

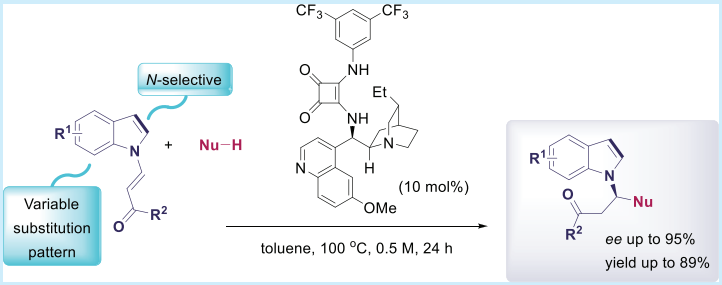

ABSTRACT: An efficient enantioselective organocatalytic method for the synthesis of *N*-alkylated indoles with α-branched alkyl substituents from the corresponding unsaturated indolyl ketones via a Michael addition has been developed. The resulting products were obtained in high enantioselectivities and in good yields. Various nucleophiles (nitroalkanes, malononitrile, malonic esters) can be used. The substitution pattern of the indole ring had no significant impact on the reaction outcome. Both electron-withdrawing and electron-donating substituents in any position of the heteroaromatic ring were well-tolerated.

Molecules bearing indole scaffolds can be found in a wide range of natural products, pharmaceutical compounds, and agrochemicals.[1] Some biologically active indoles contain a stereogenic center at the α-position of the *N*-atom (Figure 1). Therefore, such compounds have recently gained wide interest in synthetic chemistry[2−4] and in medicinal chemistry.[5]

The stereoselective derivatization of indole at the nitrogen atom with electrophilic reagents is still challenging because the most reactive nucleophilic center of the indole core is at C3.[6] To avoid C3-alkylation and to achieve high *N*-selectivity, the third position of the ring can be protected by substitution or, alternatively, the *N*−*H* acidity and nucleophilicity of the nitrogen atom can be increased by substituents in different positions of the indole core. The application of these two additional conditions provides high regioselectivity of the nucleophilic attack but also changes electronic and steric properties of indole core and limits the scope of the synthetic methodologies.[7]

During the past two decades, the interest in new enantioselective methodologies for the synthesis of chiral *N*-substituted indoles with a branched alkyl substituent has increased considerably.[8] Both direct methods of the derivatization of the indole core and indirect methods starting from other nitrogen-containing heterocycles (isatin, indoline, dihydroindole, etc.) via metal-catalyzed or organocatalytic reactions have been used. Since Trost et al. demonstrated the first enantioselective synthesis of chiral indolocarbazole derivatives (Scheme 1, **I**),[9] several other strategies have been exploited. These methods generally consider indole to be a nucleophilic coupling fragment reacting with different electrophilic partners. However, difficulty in controlling regioselectivity is often a problem.

Recently, Buchwald et al. reported the first polarity reversal strategy where an indole derivative was used as an electrophile in the enantioselective ligand-controlled metal-catalyzed reaction to achieve *N*-alkylated products (Scheme 1, **II**).[10] The method is based on the CuH-catalyzed *N*-alkylation of *N*-(2,4,6-trimethylbenzoyloxy)indole with alkenes.

Based on the approach where an indole derivative was applied as a non-nucleophile,[11] we decided to employ the electrophilic activation mode of the α-carbon of the nitrogen atom by converting an indole to a Michael acceptor (Scheme

Received: January 20, 2021
Published: February 24, 2021

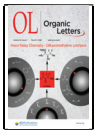

https://dx.doi.org/10.1021/acs.orglett.1c00222
Org. Lett. 2021, 23, 1820−1824

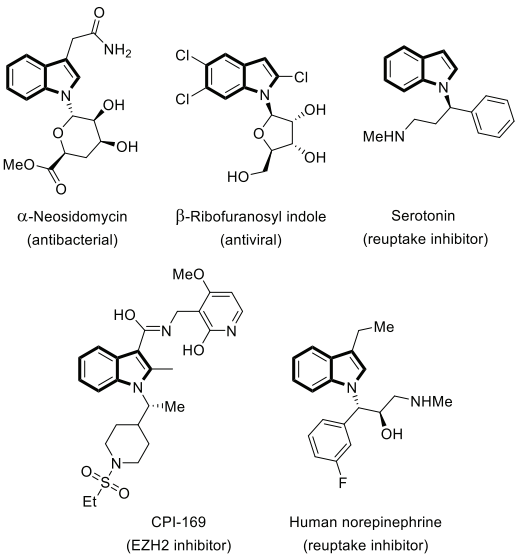

Figure 1. Selected biologically active enantiomeric *N*-substituted indoles.

Scheme 1. Different Approaches to the Enantioselective Synthesis of *N*-Substituted Indoles with Branched Substituents

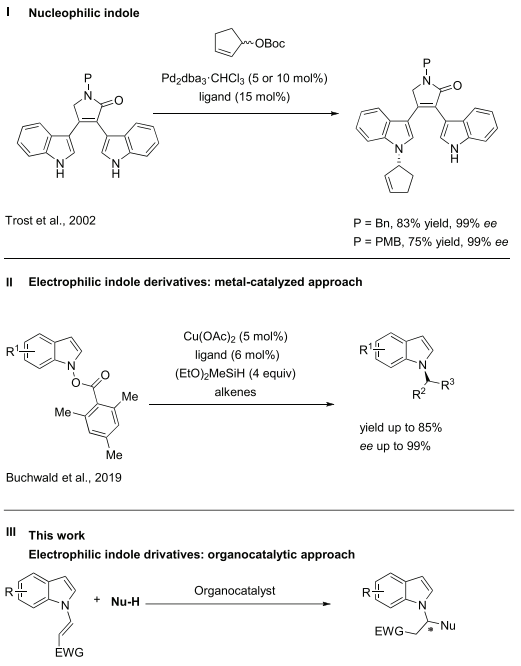

1, **III**). An appropriate starting material can be prepared by the hydroamination of the corresponding silyl alkynes with an indole (Scheme 2).[12] It is a specific reaction where the only

Scheme 2. Hydroamination of Indoles

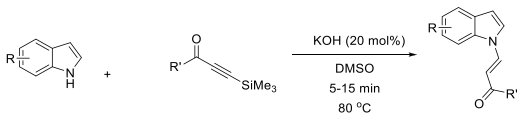

reaction center in the indole ring is the *N*-atom. The simple synthetic route provides easy access to enaminones possessing indole core and Michael acceptor moiety. An asymmetric 1,4-conjugate addition to the acceptor provides a direct entry to the enantioselective synthesis *N*-substituted indoles with a branched alkyl substituents. This two-step sequence totally excludes the formation of C3-side product due to the application of indole *N*-adducts as electrophiles.

Here, we describe the first enantioselective organocatalytic formal *N*-alkylation of indoles using an indole derivative as a Michael acceptor. To test our hypothesis, compound **1** was synthesized and used as a model compound in a reaction with nitromethane **2** in the presence of organocatalysts (Table 1). For the stereoselective conjugate addition of nitroalkanes to electron-deficient alkenes, various catalysts have been used.[13] The screening of the catalyst was started with hydrogen

Table 1. Optimization of the Reaction Conditions[a]

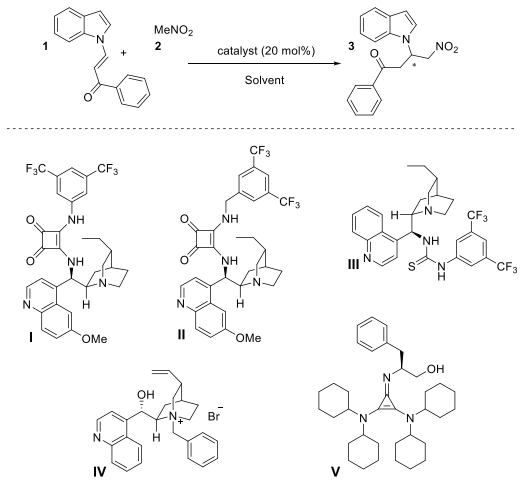

entry	catalyst	time (h)	temp (°C)	solvent	conv[b] (%)	ee[c] (%)
1	**I**	48	rt	DCM	nr	nd
2	**I**	48	80	DCE	71	92
3	**II**	48	80	DCE	traces	nd
4	**III**	48	80	DCE	12	−88
5[d]	**IV**	1	rt	DCE	99	*rac*
6	**V**	24	rt	DCE	31	*rac*
7	**I**	48	80	1.4-dioxane	69	94
8	**I**	48	80	toluene	82	94
9	**I**	48	100	toluene	85	94
10[e]	**I**	48	100	toluene	93	92

[a]Reaction conditions: 0.1 mmol scale, 1 equiv of **1**, 10 equiv of **2**, 20 mol % of catalyst, solvent (0.5 mL). [b]Conversion was determined by ^{1}H NMR from the crude mixture. [c]Determined by chiral HPLC analysis. [d]1 equiv of Rb_2CO_3 was added. [e]Toluene (0.2 mL).

https://dx.doi.org/10.1021/acs.orglett.1c00222
Org. Lett. 2021, 23, 1820−1824

bonding catalysts. Bifunctional cinchona alkaloid-based squaramides **I**, **II**, and thiourea **III** are widely used with nitro-group containing Michael donors.[14,15] The reaction did not take place in the presence of catalyst **I** at room temperature in DCM, although increasing the temperature to 80 °C led to moderate conversion (71%) and afforded product in high ee (92%) in DCE in 2 days (Table 1, entries 1 and 2). Only traces of the product were detected in the presence of the catalyst **II** under the same conditions (Table 1, entry 3). The reaction in the presence of quinine-based thiourea **III** afforded product in high enantioselectivity but the conversion was unreasonably low (Table 1, entry 4). According to our previous experience with indole chemistry with phase-transfer catalysis,[7a] PTC **IV** was used (Table 1, entry 5). Full conversion was achieved at room temperature but the formed product was racemic. Next, cyclopropenimines as enantioselective Brønsted base catalysts were applied.[16] With the catalyst **V**, low conversion of the starting material and obtained racemic product were characteristic (Table 1, entry 6). Next, a brief screening of the solvents with the most selective catalyst **I** revealed that toluene was the best solvent in terms of both yield and enantioselectivity (Table 1, entry 8). A slightly higher reactivity was achieved when the temperature was raised to 100 °C (Table 1, entry 9). Moreover, almost full conversion was reached by increasing the concentration from 0.2 to 0.5 M without a significant impact on the stereoselectivity (Table 1, entry 10).

Additionally, the influence of the catalyst amount on the reaction rate was examined (see, Figure S1). There was no significant difference when 10 or 20 mol % of the catalyst was used. However, the experiment with 5 mol % of the catalyst was inefficient demonstrating a considerable decline in reaction rate and the conversion was only 78% in 26 h. Notably, the catalyst amount did not affect the enantioselectivity of the reaction, and the ee value remained constant and high during the entire experiment.

Under optimized reaction conditions (toluene, 100 °C, 10 mol % of catalyst **I**, and reaction time 24 h), the substrate scope of the reaction was investigated. Initially, variations on the indolyl scaffold were evaluated (Scheme 3, **I**). The reaction was run with monosubstituted indole derivatives that differentiated from each other in the position and nature of the substituent. The incorporation of the methyl group into the C2- or C3-position did not have a significant impact on the reaction yield or on the enantioselectivity. Substrates with electron-withdrawing substituents at the C3- or C4-positions tolerated the reaction well, providing the products **3c** and **3d** in good yields (88 and 81%) and high *ee*-s (92% and 94%). A drastic decline in the reaction yield was detected (most probably a retro-Michael reaction occurred) when the 7-nitro-substituted Michael acceptor **1e** was used (yield 12%). However, the *ee* value of the product **3e** remained high (93%). The tolerance toward electron-donating groups (and also the substituent at the seventh position) on the indolyl ring was well represented by 4- and 7-metoxy-substituted *N*-functionalized indoles. The electron-donating groups did not affect the reactivity, and the desired products **3f** and **3g** were isolated in good yields (83% and 68%) and excellent enantioselectivities (94% and 95%). Halogen-substituted C5- and C6-unsaturated *N*-indolyl ketones reacted smoothly, affording *N*-alkylated indoles **3h** and **3i** in good yields (71% and 78%) and high ee's (93% and 91%). Thus, the substitution pattern of the indole ring is not essential and the method is applicable to the monosubstituted indole derivatives possessing

Scheme 3. Scope and Limitations of the Reaction with Nitromethane[a]

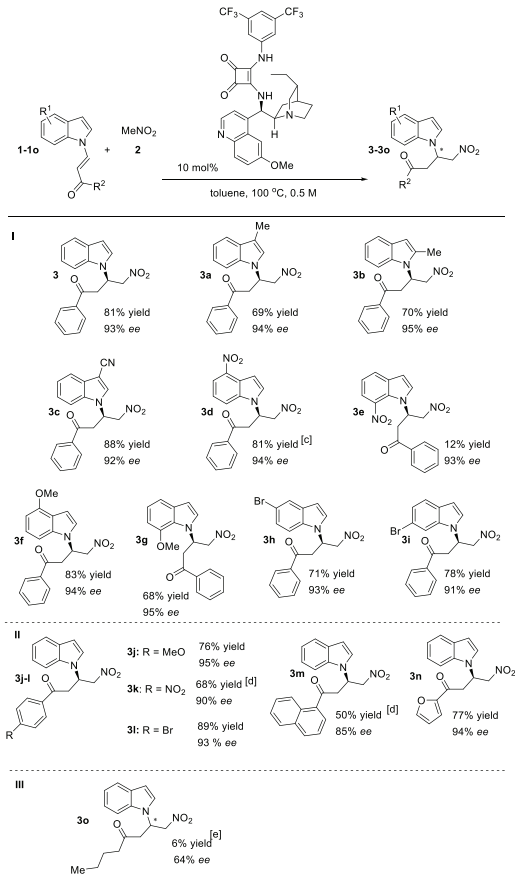

[a]Reaction conditions: 0.2 mmol scale, 1 equiv of **1**−**1o**, 10 equiv of nitromethane, 10 mol % of catalyst **I**, in 0.4 mL of toluene (0.5 M), 24 h. [b]ee was determined by chiral HPLC analysis. [c]0.2 M. [d]0.1 mmol scale. [e]Reaction time 7 days.

substituents in any position. The absolute stereochemistry of product **3g** was unambiguously assigned by single-crystal X-ray diffraction (see the SI), and other compounds in the series were assigned based on the analogy.

Next, we turned our attention to the scope of Michael acceptors with parent indolyl scaffolds (Scheme 3, **II**). Both electron-withdrawing and electron-donating substituents at the *para*-position of a phenyl ring did not have a significant impact on the reaction yield (68% and 76%), but slightly better enantioselectivity (95%) was achieved in the case of methoxy-substituted substrate **1j**. The *p*-bromo-substituted product **3l** was isolated in high yield (89%), and the achieved ee was comparable with the model compound **3**. The bulky 1-naphthyl substituent of **1m** led to a moderate yield (50%) and slightly decreased the *ee* value (85%). Heteroaromatic furyl derivative **3n** was obtained in high yield and ee (77% and 94%, respectively). Notably, the reaction rate and stereoselectivity dropped drastically when the substrate **1o** with the aliphatic

https://dx.doi.org/10.1021/acs.orglett.1c00222
Org. Lett. 2021, 23, 1820−1824

butyl chain was used instead of a phenyl ring (Scheme 3, **III**). The reaction was unacceptably slow, indicating the importance of $\pi-\pi$ interactions. The product **3o** was isolated after 7 days in only 6% yield.

Next, the scope of Michael donors and acceptors was studied briefly (Scheme 4). The reaction with malononitrile

Scheme 4. Scope of Michael Donors and Acceptors[a]

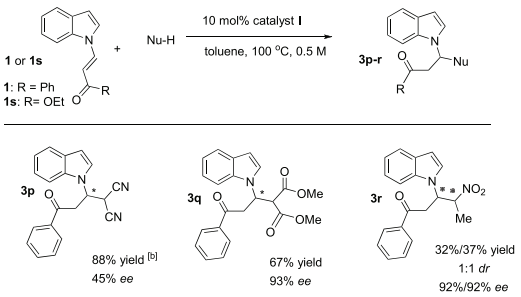

[a]Reaction conditions: 0.2 mmol scale, 1 equiv of **1** or **1o**, 10 equiv of nucleophile, 10 mol % of catalyst **I**, in 0.4 mL of toluene (0.5 M), 24 h. [b]Reaction time 1 h.

was complete with 1h but the enantiomeric purity of the product **3p** was considerably lower. There was no reaction with acetonitrile. Malonic ester reacted smoothly affording product **3q** in 67% yield and 93% ee. A 1:1 mixture diastereomers **3r** was obtained with nitroethane in high ee's (92%/92%). To our delight, the diastereomers of **3r** were chromatographically separable. The reaction with 2,4-pentanedione led to the mixture of products. The substitution of the phenyl ring with an alkoxycarbonyl group in the indole-based Michael acceptor (compound **1s**) led to the substantial decrease of the reactivity and no reaction was detected with nitromethane.

To evaluate the synthetic potential of the current methodology, a gram-scale experiment was performed with substrate **1** (Scheme 5, **I**). The scale-up of the reaction did not affect either the reaction yield or enantioselectivity (78% yield, 92% ee). Furthermore, the synthetic transformation of compound **3** was

Scheme 5. Demonstration of Synthetic Utility

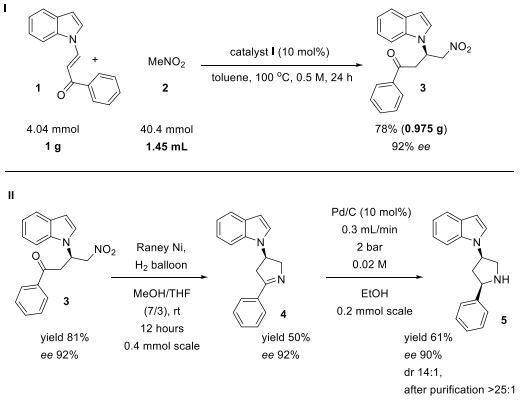

explored. It was converted to a 5-HT_6 receptor modulator analogue precursor **5**.[17] The treatment of compound **3** with Raney nickel induced the reduction of the nitro group to an amino group followed by intramolecular cyclization, affording the corresponding chiral imine **4** without the loss of enantioselectivity (Scheme 5, **II**). The imine **4** was later easily hydrogenated in a flow reactor with Pd/C cartridge providing chiral pyrrolidine derivative **5** in high dr ratio (14:1) and good yield (62%). The *cis*-configuration of the substituents in the pyrrolidine ring was determined by selective NOESY (details in the SI). The diastereomeric ratio of the product **5** was improved after the purification of the reaction (>25:1).

In summary, we have developed the first enantioselective organocatalytic method for the synthesis of *N*-alkylated indoles starting from unsaturated indolyl ketones. The main feature of our method is exploiting an indole derivative as an electrophile totally avoiding the regioselectivity problems common with other *N*-alkylation methods. A wide range of electrophilic indole *N*-adducts bearing various substituents provide exclusively *N*-alkylated indoles with a branched substitutents in good yields (up to 89%) and high to excellent ee values (up to 95%). The enantioselectivity of the reaction does not depend on the substitution pattern of the indole ring.

■ ASSOCIATED CONTENT

Supporting Information

The Supporting Information is available free of charge at https://pubs.acs.org/doi/10.1021/acs.orglett.1c00222.

Synthesis of starting compounds, copies of ^{1}H and ^{13}C spectra, and HPLC chromatograms (PDF)

Accession Codes

CCDC 2054770 contains the supplementary crystallographic data for this paper. These data can be obtained free of charge via www.ccdc.cam.ac.uk/data_request/cif, or by emailing data_request@ccdc.cam.ac.uk, or by contacting The Cambridge Crystallographic Data Centre, 12 Union Road, Cambridge CB2 1EZ, UK; fax: +44 1223 336033.

■ AUTHOR INFORMATION

Corresponding Author

Tõnis Kanger − *Department of Chemistry and Biotechnology, Tallinn University of Technology, 12618 Tallinn, Estonia;* orcid.org/0000-0001-5339-9682; Email: tonis.kanger@taltech.ee

Authors

Dmitri Trubitsõn − *Department of Chemistry and Biotechnology, Tallinn University of Technology, 12618 Tallinn, Estonia*

Jevgenija Martõnova − *Department of Chemistry and Biotechnology, Tallinn University of Technology, 12618 Tallinn, Estonia*

Marina Kudrjašova − *Department of Chemistry and Biotechnology, Tallinn University of Technology, 12618 Tallinn, Estonia*

Kristin Erkman − *Department of Chemistry and Biotechnology, Tallinn University of Technology, 12618 Tallinn, Estonia*

Ivar Järving − *Department of Chemistry and Biotechnology, Tallinn University of Technology, 12618 Tallinn, Estonia*

Complete contact information is available at:

https://pubs.acs.org/10.1021/acs.orglett.1c00222

Notes

The authors declare no competing financial interest.

■ ACKNOWLEDGMENTS

The authors thank the Estonian Ministry of Education and Research (Grant Nos. PRG1031 and PRG399) and the Centre of Excellence in Molecular Cell Engineering (2014-2020.4.01.15-0013) for financial support. The authors thank Dr. Aleksander-Mati Müürisepp (Tallinn University of Technology) for IR spectra.

■ REFERENCES

(1) Singh, T. P.; Singh, O. M. Recent Progress in Biological Activities of Indole and Indole Alkaloids. *Mini-Rev. Med. Chem.* **2017**, *18*, 9−25.

(2) Wang, Le.; Zhou, J.; Ding, T.-M.; Yan, Z.-Q.; Hou, S.-H.; Zhu, G.-D.; Zhang, S.-Y. Asymmetric *N*-Hydroxyalkylation of Indoles with Ethyl Glyoxalates Catalyzed by a Chiral Phosphoric Acid: Highly Enantioselective Synthesis of Chiral *N,O*-Aminal Indole Derivatives. *Org. Lett.* **2019**, *21*, 2795−2799.

(3) Jang, S. H.; Kim, H. W.; Jeong, W.; Moon, D.; Rhee, Y. H. Palladium-Catalyzed Asymmetric Nitrogen-Selective Addition of Indoles to Alkoxyallenes. *Org. Lett.* **2018**, *20*, 1248−1251.

(4) Kim, S. W.; Schempp, T. T.; Zniег, J. R.; Stivala, C. E.; Krische, M. J. Regio-and Enantioselective Iridium-Catalyzed N-Allylation of Indoles and Related Azoles with Racemic Branched Alkyl-Substituted Allylic Acetates. *Angew. Chem., Int. Ed.* **2019**, *58*, 7762−7766.

(5) Jain, P.; Utreja, D.; Sharma, P. An efficacious synthesis of N-1−, C-3−substituted indole derivatives and their antimicrobial studies. *J. Heterocycl. Chem.* **2020**, *57*, 428−435.

(6) Lakhdar, S.; Westermaier, M.; Terrier, F.; Goumont, R.; Boubaker, T.; Ofial, A. R.; Mayr, H. Nucleophilic Reactivities of Indoles. *J. Org. Chem.* **2006**, *71*, 9088−9095.

(7) (a) Trubitsõn, D.; Martõnova, J.; Erkman, K.; Metsala, A.; Saame, J.; Kõster, K.; Järving, I.; Leito, I.; Kanger, T. Enantioselective *N*-Alkylation of Nitroindoles under Phase-Transfer Catalysis. *Synthesis* **2020**, *52*, 1047−1059. (b) Hong, L.; Sun, W.; Liu, C.; Wang, L.; Wang, R. Asymmetric Organocatalytic N-Alkylation of Indole-2-carbaldehydes with α,β-Unsaturated Aldehydes: One-Pot Synthesis of Chiral Pyrrolo[1,2-α]indole-2-carbaldehydes. *Chem. - Eur. J.* **2010**, *16*, 440−444. (c) Xu, C.-J.; Du, W.; Albrecht, Ł.; Chen, Y.-C. Lewis Basic Amine Catalyzed Aza-Michael Reaction of Indole- and Pyrrole-3-carbaldehydes. *Synthesis* **2020**, *52*, 2650−2661. (d) Mukherjee, S.; Shee, S.; Poisson, T.; Besset, T.; Biju, A. T. Enantioselective N-Heterocyclic Carbene-Catalyzed Cascade Reaction for the Synthesis of Pyrroloquinolines via N-H functionalization of indoles. *Org. Lett.* **2018**, *20*, 6998−7002. (e) Wang, C.; Li, Z.; Zhang, J.; Hui, X.-P. Asymmetric N-alkylation of indoles with isatins catalyzed by N-heterocyclic carbene: efficient synthesis of functionalized cyclic N,O-aminal indole derivatives. *Org. Chem. Front.* **2020**, *7*, 1647−1652. (f) Wang, Le.; Zhou, J.; Ding, T.-M.; Yan, Z.-Q.; Hou, S.-H.; Zhu, G.-D.; Zhang, S.-Y. Asymmetric N-Hydroxyalkylation of Indoles with Ethyl Glyoxalates Catalyzed by a Chiral Phosphoric Acid: Highly Enantioselective Synthesis of Chiral *N,O*-Aminal Indole Derivatives. *Org. Lett.* **2019**, *21*, 2795−2799.

(8) For reviews, see: (a) Trubitsõn, D.; Kanger, T. Enantioselective Catalytic Synthesis of *N*-alkylated Indoles. *Symmetry* **2020**, *12*, 1184. (b) Karchava, A. V.; Melkonyan, F. S.; Yurovskaja, M. A. New Strategies for the synthesis of *N*-alkylated indoles. *Chem. Heterocycl. Compd.* **2012**, *48*, 391−407. (c) Bandini, M.; Eichholzer, A. Catalytic Functionalization of Indoles in a New Dimension. *Angew. Chem., Int. Ed.* **2009**, *48*, 9608−9644. (d) Bartoli, G.; Bencivenni, G.; Dalpozzo, R. Organocatalytic strategies for the asymmetric functionalization of indoles. *Chem. Soc. Rev.* **2010**, *39*, 4449−4465. (e) Dalpozzo, R. Strategies for the asymmetric functionalization of indoles: an update. *Chem. Soc. Rev.* **2015**, *44*, 742−778.

(9) Krische, M.; Berl, V.; Grenzer, E. M.; Trost, B. M. Chemo-, Regio-, and Enantioselective Pd-Catalyzed Allylic Alkylation of Indolocarbazole Pro-aglycons. *Org. Lett.* **2002**, *4*, 2005−2008.

(10) Ye, Y.; Kim, S.-T.; Jeong, J.; Baik, M.-H.; Buchwald, S. L. CuH-Catalyzed Enantioselective Alkylation of Indole Derivatives with Ligand-Controlled Regiodivergence. *J. Am. Chem. Soc.* **2019**, *141*, 3901−3909.

(11) (a) Lavernhe, R.; Alexy, E. J.; Zhang, H.; Stoltz, B. M. Palladium-Catalyzed Enantioselective Decarboxylative Allylic Alkylation of Acyclic α-N-Pyrrolyl/Indolyl Ketones. *Org. Lett.* **2020**, *22*, 4272−4275. (b) Shen, J.-J.; Gao, Q.; Wang, G.; Tong, M.; Chen, L.; Xu, S. Cu-NHC-Catalyzed Enantioselective Conjugate Silyl addition to Indol-1-ylacrylate Derivatives. *ChemistrySelect* **2019**, *4*, 11358−11361.

(12) Joshi, M.; Patel, M.; Tiwari, R.; Verma, A. K. Base-Mediated Selective Synthesis of Diversely Substituted *N*-Heterocyclic Enamines and Enaminones by the Hydroamination of Alkynes. *J. Org. Chem.* **2012**, *77*, 5633−5645.

(13) Firsts organocatalytic examples: (a) Hanessian, S.; Pham, V. *Org. Lett.* **2000**, *2*, 2975−2978. (b) Halland, N.; Hazell, R. G.; Jørgensen, K. A. Organocatalytic Asymmetric Conjugate Addition of Nitroalkanes to α,β-Unsaturated Enones Using Novel Imidazoline Catalysts. *J. Org. Chem.* **2002**, *67*, 8331−8338. For reviews, see: (c) Scheffler, U.; Mahrwald, R. Recent Advances in Organocatalytic Methods for Asymmetric C-C Bond Formation. *Chem. - Eur. J.* **2013**, *19*, 14346−14396. (d) Roca-Lopez, D.; Sadaba, D.; Delso, I.; Herrera, R. P.; Tejero, T.; Merino, P. Asymmetric organocatalytic synthesis of γ-nitrocarbonyl compounds through Michael and Domino reactions. *Tetrahedron: Asymmetry* **2010**, *21*, 2561−2601.

(14) (a) Grayson, M. N. Mechanism and Origins of Stereoselectivity in the Cinchona Thiourea- and Squaramide-Catalyzed Asymmetric Michael Addition of Nitroalkanes to Enones. *J. Org. Chem.* **2017**, *82*, 4396−4401. (b) Yang, W.; Du, D.-M. Highly Enantioselective Michael Addition of Nitroalkanes to Chalcones Using Chiral Squaramides as Hydrogen Bonding Organocatalysts. *Org. Lett.* **2010**, *12*, 5450−5453.

(15) For general reviews of squaramides, see: (a) Alemán, J.; Parra, A.; Jiang, H.; Jørgensen, K. A. Squaramides: Bridging from Molecular Recognition to Bifunctional Organocatalysis. *Chem. - Eur. J.* **2011**, *17*, 6890−6899. (b) Chauhan, P.; Mahajan, S.; Kaya, U.; Hack, D.; Enders, D. Bifunctional Amine-Squaramides: Powerful Hydrogen-Bonding Organocatalysts for Asymmetric Domino/Cascade Reactions. *Adv. Synth. Catal.* **2015**, *357*, 253−281.

(16) (a) Bandar, J. S.; Lambert, T. H. Enantioselective Brønsted Base Catalysis with Chiral Cyclopropenimines. *J. Am. Chem. Soc.* **2012**, *134*, 5552−5555. (b) Ošeka, M.; Kimm, M.; Järving, I.; Lippur, K.; Kanger, T. Two Catalytic Methods of an Asymmetric Wittig [2,3]-Rearrangement. *J. Org. Chem.* **2017**, *82*, 2889−2897.

(17) Bernotas, R. C.; Antane, S.; Shenoy, R.; Le, V.-D.; Chen, P.; Harrison, B. L.; Robichaud, A. J.; Zhang, G. M.; Smith, D.; Schechter, L. E. 3-(Arylsulfonyl)-1-(azacyclyl)-1H-indoles are 5-HT_6 receptor modulators. *Bioorg. Med. Chem. Lett.* **2010**, *20*, 1657−1660.

Appendix 2

Publication II

Trubitsõn, D.; Martõnova, J.; Erkman, K.; Metsala, A.; Saame, J.; Kõster, K.; Järving, I.; Leito, I.; Kanger, T. (2020). Enantioselective N-Alkylation of Nitroindoles under Phase-Transfer Catalysis. *Synthesis*, 52 (07), 1047−1059. DOI: 10.1055/s-0039-1690751

Synthesis D. Trubitsõn et al. Paper

Enantioselective *N*-Alkylation of Nitroindoles under Phase-Transfer Catalysis

Dmitri Trubitsõn[a]
Jevgenija Martõnova[a]
Kristin Erkman[a]
Andrus Metsala[a]
Jaan Saame[b]
Kristjan Kõster[b]
Ivar Järving[a]
Ivo Leito[b]
Tõnis Kanger*[a]

[a] Department of Chemistry and Biotechnology, Tallinn University of Technology, 12618 Tallinn, Estonia
tonis.kanger@taltech.ee
[b] Institute of Chemistry, University of Tartu, 50411 Tartu, Estonia

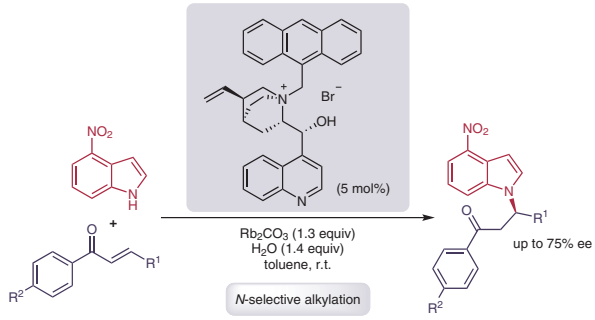

Received: 26.09.2019
Accepted after revision: 04.11.2019
Published online: 26.11.2019
DOI: 10.1055/s-0039-1690751; Art ID: ss-2019-t0554-op

Abstract An asymmetric phase-transfer-catalyzed *N*-alkylation of substituted indoles with various Michael acceptors was studied. Acidities of nitroindoles were determined in acetonitrile by UV-Vis spectrophotometric titration. There was essentially no correlation between acidity and reactivity in the aza-Michael reaction. The position of the nitro group on the indole ring was essential to control the stereoselectivity of the reaction. Michael adducts were obtained in high yields and moderate enantioselectivities in the reaction between 4-nitroindole and various Michael acceptors in the presence of cinchona alkaloid based phase-transfer catalysts. In addition to outlining the scope and limitations of the method, the geometries of the transition states of the reaction were calculated.

Key words asymmetric catalysis, heterocycles, Michael addition, organocatalysis, phase-transfer catalysis

Indole and its derivatives are very important scaffolds in medicinal chemistry,[1] being among the most prevalent ring system in small molecule drugs.[2] *N*-Substituted indole derivatives are used more seldom but there are still examples of biologically active pharmaceutical compounds containing this structural moiety (Figure 1).[3] The direct functionalization of the indole ring system has been an active area of research for decades.[4] The most widely exploited reaction is an electrophilic aromatic substitution at the C3 position.[5] Recently, methods have been developed for the direct electrophilic reactions at the C2 position via a transition-metal-catalyzed C–H activation.[6] At the same time, the enantioselective *N*-alkylation of indole remains underdeveloped. The aromaticity of the indole ring and, correspondingly, low nucleophilicity of the nitrogen atom make it challenging.

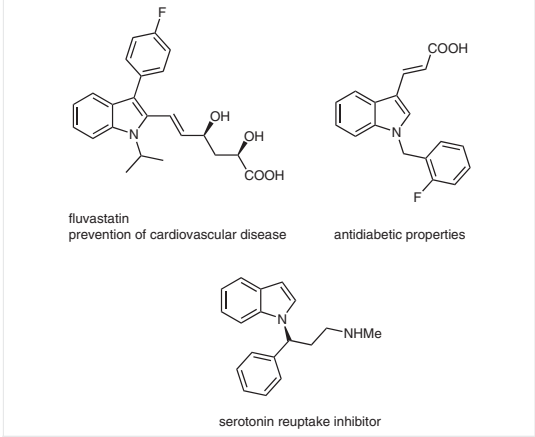

Figure 1 Examples of biologically active *N*-alkylated indoles

Mainly transition-metal-catalyzed reactions have been applied for the enantioselective *N*-addition to indole derivatives.[7] Only limited methodologies have been developed by employing asymmetric organocatalytic strategies for *N*-alkylation. Chiral phosphoric acids were applied as catalysts for the synthesis of *N*-substituted indoles (Scheme 1a).[8] In these examples strong electrophiles are generated under acidic conditions or the simultaneous activation of the electrophile and nucleophile takes place. Alternatively, under basic conditions an intramolecular *N*-alkylation led to the formation of tricyclic products via phase-transfer catalysis (Scheme 1b).[9] The introduction of an electron-withdrawing group reduces the p*Ka* value of the indole and increases the

Georg Thieme Verlag KG, Rüdigerstraße 14, 70469 Stuttgart, Germany

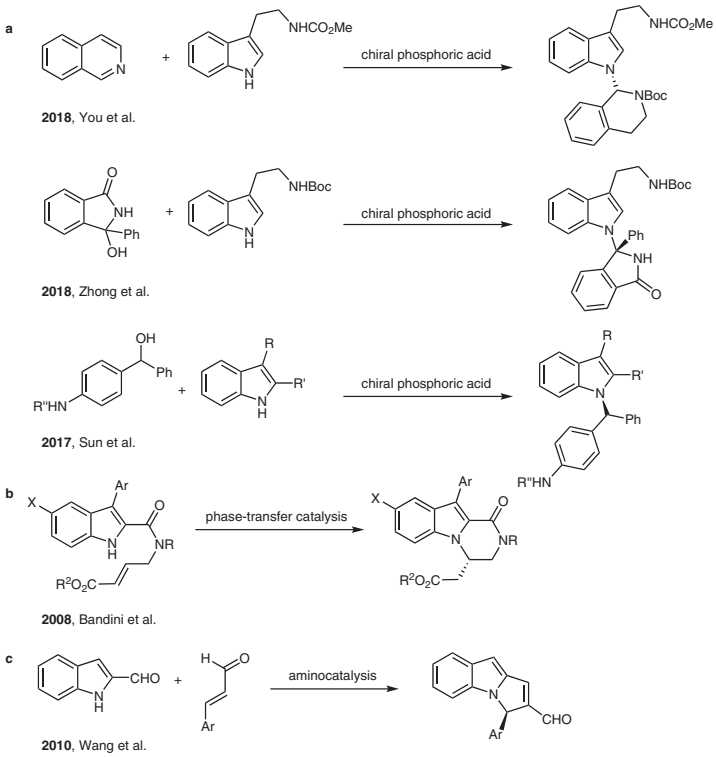

Scheme 1 Organocatalytic enantioselective *N*-alkylation of indole derivatives

nucleophilicity of the N1 position, enabling an aminocatalytic intramolecular aza-Michael/aldol cascade reaction of 2-formyl-substituted indole, also affording tricyclic products in high enantio- and regioselectivities (Scheme 1c).[10]

In this article, we studied the dependence of the N–H acidity versus the position of the electron-withdrawing group on the indole ring; the synthetic potential of it was further harnessed to access enantiomerically pure indole derivatives via an aza-Michael reaction.[11]

Our initial studies focused on the reaction of 3-cyanoindole (**1**) with *trans*-crotonophenone **2**. An EWG on the third position of the indole ring increases the acidity of the N–H proton and protects the most reactive C3 position. Recently, Yang et al. published a non-asymmetric method consisting of a potassium hydroxide catalyzed intermolecular aza-Michael addition of indole derivatives to aromatic enones.[12] We studied an asymmetric phase-transfer-catalyzed (PTC) version of it. A library of different phase-transfer catalysts based on cinchona alkaloids was screened (Table 1).

The model reaction was performed at room temperature in toluene in the presence of an enantiomerically pure catalyst (20 mol%) and potassium carbonate as a base. First, the steric effect of the substituents of the ammonium salts **I–III** derived from cinchonidine on the reaction was studied. Almost full conversion of the starting compounds **1** and **2** was achieved in the case of benzyl-, naphthyl-, and anthracenyl-substituted catalysts (Table 1, entries 1–3). There was a clear dependence of the steric effect of the catalyst on the enantioselectivity of the reaction. Sterically more demanding catalysts afforded higher enantioselectivities but they remained modest (in the best case 42% ee; entry 3). Catalyst **IV** demonstrated the same conversion and quite similar stereoselectivity as the anthracenyl-substituted catalyst **III** (entry 4). Due to the low solubility of the ammonium salt **V** in toluene, the conversion and ee of product **3** were low (entry 5). The replacement of the bromide anion in catalyst **I** by the tetrakis[3,5-bis(trifluoromethyl)phenyl]borate (BARF) anion dramatically affected the reaction rate and enantioselectivity (entry 6). The influence of the hydrogen-bond donor of the catalyst was essential.[13] Protecting the OH group as an allyl ether (catalyst **VII**) provided full conversion of the starting materials but the product was racemic (entry 7). The thiourea derived catalyst **VIII** afforded the opposite enantiomer **3** with low selectivity (entry 8). The obtained results were unsatisfying, and

Table 1 Catalyst Screening for the Reaction between 3-Cyanoindole and *trans*-Crotonophenone[a]

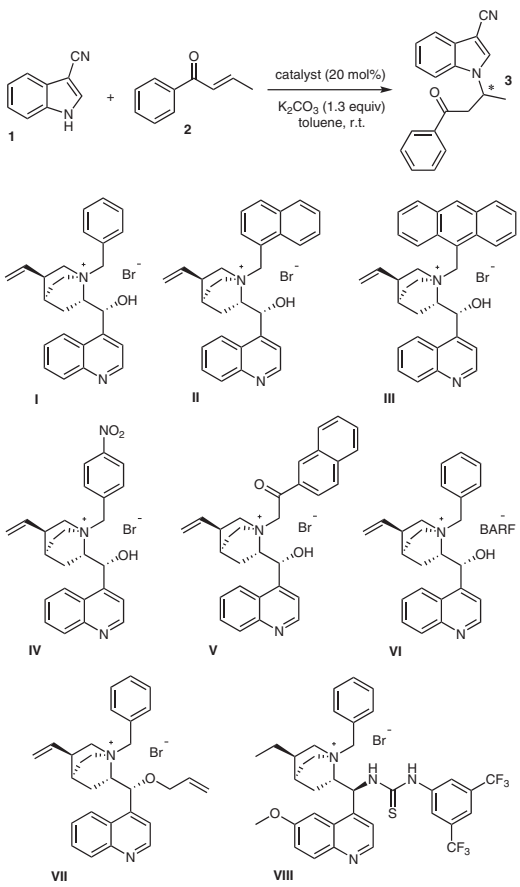

Entry	Catalyst	Time (h)	Conv. (%)[b]	ee (%)[c]
1	**I**	18	98	18
2	**II**	18	99	26
3	**III**	16	83	42
4	**IV**	16	80	36
5	**V**	16	26	4
6	**VI**	18	5	6
7	**VII**	16	99	*rac*
8	**VIII**	20	29	–28

[a] Reaction conditions: **1** (1.2 equiv), **2** (1 equiv), catalyst (20 mol%), base (1.3 equiv), r.t.
[b] Conversion determined by ^{1}H NMR of crude mixture.
[c] Determined by chiral HPLC analysis of the sample obtained by preparative TLC.

therefore a more systematic study of substituted indoles was performed. Nitroindoles were the compounds of choice because of their possible interaction with the phase-transfer catalyst.[14]

First, the acidities of the nitrosubstituted indoles were determined (Table 2). As expected, nitroindoles and 3-cyanoindole behave in acetonitrile as weak acids, with pK_a values in the range of 22–30, thus being by their acid strength approximately between benzoic acid[15] and phenol.[16] By acid strength, the nitroindoles fall into two distinct groups – the ones with nitro group on the five-membered ring (pK_a between 22 and 24) and the ones with the nitro group on the six-membered ring (pK_a between 27 and 30). The reason is evidently the good match between the electron-withdrawing abilities of the nitro group on the one hand and the vicinity of the nitro group to the acidity center in the five-membered ring, as well as the overall higher electron density in the five-membered ring. The strongest of the nitroindoles – 3-nitroindole – benefits from highly efficient resonance stabilization of the negative charge in the anion via conjugation of the nitro group with the acidity center.

In the following reactions, commercially available 4-nitroindole was used as a model compound. It was found that under similar conditions applied to 3-cyanoindole the reaction with 4-nitroindole in the presence of catalyst **III** was more selective (Table 3, entry 1). The reaction rate was increased when rubidium carbonate was used as a base, affording the *N*-alkylated product in 95% yield within 5 hours without any decrease in enantioselectivity (entry 2, 65% ee). An aqueous solution of rubidium carbonate decreased the rate of the reaction substantially and for the full conversion a reaction time of 24 hours was needed (entry 3). The enantiomeric purity of the product was increased to 74% by lowering the temperature of the reaction to –20 °C (entry 5). Cesium carbonate induced a less selective reaction (entry 6).

During the optimization of the reaction conditions the effect of water on the reaction rate was revealed. Small amounts of water could significantly affect the rate of the reactions catalyzed by the quaternary ammonium salts.[17] The balance between the amount of water and amount of phase-transfer catalyst was screened (for the full optimization process, see the Supporting Information). It was found that both low concentrations and high concentrations of water decreased the reaction rate. With the optimum water concentration the amount of the catalyst **III** was decreased to 5 mol%. Increasing the amount of *trans*-crotonophenone from 1.2 equivalents to 2.1 equivalents afforded the *N*-alkylated 4-nitroindole **5a** in a reasonable time (5 h), high yield (95%), and moderate ee (69%).

Next, the influence of the position of the nitro group on the aza-Michael reaction was studied under the optimal conditions (Table 4). It was found that the most reactive

Table 2 Results of pK_a Measurements in Acetonitrile

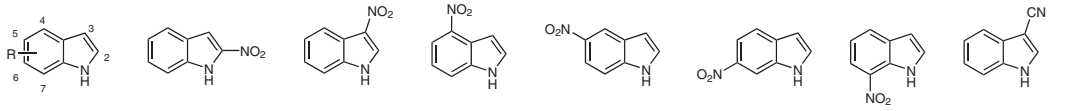

Acid (A)	Reference acid (Ra)	pK_a(Ra)	pK_a[a]	pK_a(A)	Assigned pK_a(A)
2-nitroindole	2-nitrophenol	22.85	–0.80	23.65	23.64
	9-MeO_2C-fluorene	23.53	–0.10	23.63	
3-nitroindole	2-nitrophenol	22.85	0.10	22.75	22.77
	9-MeO_2C-fluorene	23.53	0.74	22.79	
4-nitroindole	(4-MeC_6F_4)(C_6H_5)CHCN	26.96	–0.88	27.84	27.8
	5-nitroindole	28.1	0.28	27.8	
5-nitroindole	(4-MeC_6F_4)(C_6H_5)CHCN	26.96	–1.12	28.08	28.1
6-nitroindole	(4-MeC_6F_4)(C_6H_5)CHCN	26.96	–0.85	27.81	27.7
	4-nitroindole	27.83	0.14	27.69	
7-nitroindole	5-nitroindole	28.1	–1.74	29.8	29.9
	6-nitroindole	27.74	–2.21	29.95	
	9-C_6F_5-fluorene	28.11	1.88	29.99	
3-cyanoindole	(4-MeC_6F_4)(C_6H_5)CHCN	26.96	0.93	26.03	26.0
	(C_6F_5)(C_6H_5)CHCN	26.14	0.18	25.96	

[a] pK_a(Ra) – pK_a(A)

derivatives were 4- and 5-nitroindoles (entries 1 and 3), but the former was more selective (69% and 38% ee, respectively). Also, 3- and 6-nitroindoles were less attractive substrates, affording products in low enantioselectivities (entries 2 and 4). In the case of 2- and 7-nitroindole, no reaction was detected during 24 hours, most probably because of steric reasons (entries 5 and 6). The obtained results show that the position of the nitro group is essential in determining the enantioselectivity and it participates in the transition state. Comparison of Tables 2 and 4 reveals that there is essentially no correlation between acidity and reactivity in the aza-Michael reaction. There is, however, a connection between reactivity and steric hindrance: the least reactive are 2- and 7-nitroindole, where the nitro groups are spatially closest to the acidity center.

The scope of the reaction was studied with the most selective 4-nitroindole **4a** (Scheme 2). Various α,β-unsaturated carbonyl compounds **2a–l**, unsaturated ester **2m**, and nitrostyrene **2n** were used as Michael acceptors. It was found that aromatic and heteroaromatic enones were the most reactive and selective starting compounds, affording products within 5 hours in moderate to high yields and moderate to good enantioselectivities. Neither electron-withdrawing (**4b**), nor electron-donating groups (**4c**) in the phenyl ring influenced the reaction substantially. The heteroaromatic furyl substituent did not affect the reaction enantioselectivity, and product **6d** was obtained in high yield. Steric hindrance in the β-position of the enone decreased the reaction rate, as demonstrated in experiments with the vinyl-substituted enones **2e** and **2f**.

Table 3 Optimization of the Reaction between 4-Nitroindole (**4a**) and *trans*-Crotonophenone (**2**)[a]

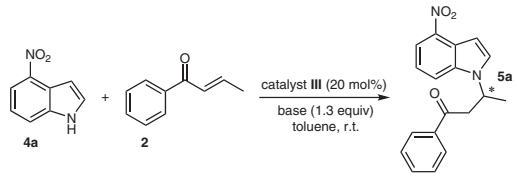

Entry	Base	Time	Yield (%)[b]	ee (%)[c]
1	K_2CO_3	21 h	95	65
2	Rb_2CO_3	5 h	92	65
3	5 M aq Rb_2CO_3	24 h	95	64
4[d]	Rb_2CO_3	24 h	97	70
5[e]	Rb_2CO_3	6 d	97	74
6	Cs_2CO_3	18 h	95	54

[a] Reaction conditions: **4a** (0.1 mmol, 1 equiv), **2** (2.1 equiv), catalyst **III** (20 mol%), Rb_2CO_3 (1.3 equiv), r.t.
[b] Isolated yield.
[c] Determined by chiral HPLC analysis.
[d] Reaction at 5 °C.
[e] Reaction at –20 °C

The absolute stereochemistry of compound **6c** was unambiguously assigned by single-crystal X-ray diffraction (Figure 2). The configurations of other compounds in the series were assigned by analogy.

To our disappointment, the reaction had limitations that could be divided into two categories: either the reaction proceeded, but racemic products were formed (**6h**, **6i**, **6j**), or there was no reaction (starting compounds **2k–n**). Sterically more hindered aliphatic cyclic ketone **2h** and *trans*-chalcone **2i** provided racemic products with lower reaction rates compared to the model compound **2a**. It was assumed that the long reaction time gave rise to a nonselective background reaction, leading to racemic products. In the case of the 1,4-diketone **6j**, racemization of the α-position of the carbonyl group through enolization under basic conditions is most probable. The reaction did not proceed

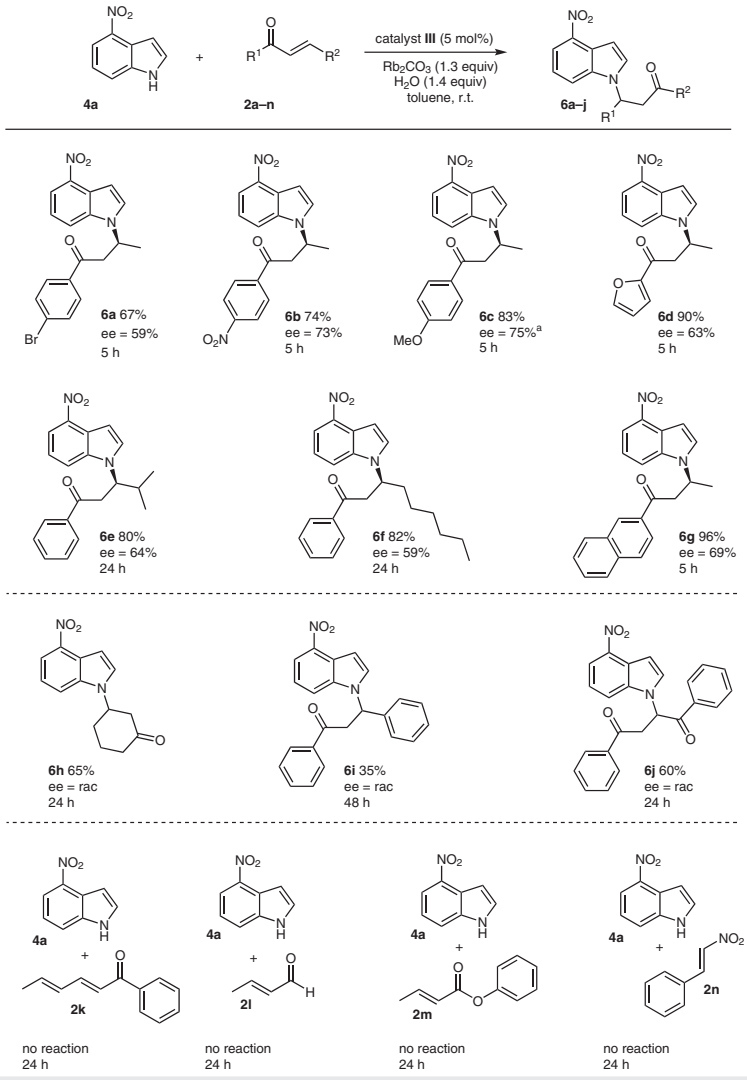

Scheme 2 The reaction scope and limitations. *Reagents and conditions*: **4a** (0.1 mmol, 1 equiv), **2a–n** (2.1 equiv), catalyst **III** (5 mol%), Rb_2CO_3 (1.3 equiv), H_2O (1.4 equiv), under argon atmosphere; all yields are isolated yields; ee values were determined by chiral HPLC analysis; [a] 90% ee was obtained after a single recrystallization.

Table 4 Effect of the Position of the Nitro Group on Nitroindole **4** on the Aza-Michael Reaction[a]

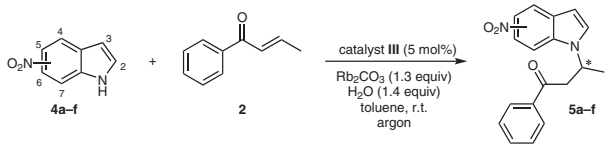

Entry	Product	NO_2 position	Time (h)	Yield (%)[b]	ee (%)[c]
1	**5a**	4	5	92	69
2	**5b**	3	5	65	42
3	**5c**	5	5	95	38
4	**5d**	6	5	82	35
5	**5e**	2	24	nr[d]	–
6	**5f**	7	24	nr[d]	–

[a] Reaction conditions: 0.1 mmol scale, 1 equiv of **4a–f**, 2.1 equiv of **2**, 5 mol% of catalyst **III**, 1.3 equiv of Rb_2CO_3 and 1.4 equiv of H_2O under argon atmosphere.
[b] Isolated yield.
[c] Determined by chiral HPLC analysis.
[d] nr = no reaction.

with (2*E*,4*E*)-1-phenylhexa-2,4-dien-1-one (**2k**), crotonaldehyde (**2l**), phenyl (*E*)-but-2-enoate (**2m**), and β-nitrostyrene (**2n**).

Generally, aromatic ketones were the best substrates for the *N*-alkylation of nitroindoles. The obtained results suggested the importance of π–π interactions in the transition state. To gain insight into the reaction mechanism, computational studies were conducted based on the density functional M062X/def2SVP method. In order to assess noncovalent interactions, a Natural Bond Orbital (NBO) analysis was performed using the M062X/def2TZVP method (for calculation details and NBO energies, see the Supporting Information). In the ternary complex INT1-S a strong hydrogen bond between the deprotonated N atom of indole **4a** and the hydroxyl group of catalyst **III**, together with the π–π interactions between the quinolone ring of the catalyst **III** and indole **4a**, form (Figure 3A). Distortion of the complex leads to the intermediate (INT2-S) with reorganized geometry: a hydrogen bond forms between the nitro group of indole and the hydroxyl of the catalyst (Figure 3B). The intermediate forms a product via a bond-forming step (TS1) (distance between Michael acceptor and donor site is 2.28

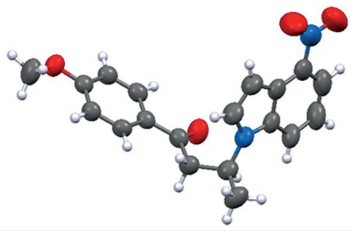

Figure 2 X-ray crystal structure of compound **6c** (CCDC 1923379)

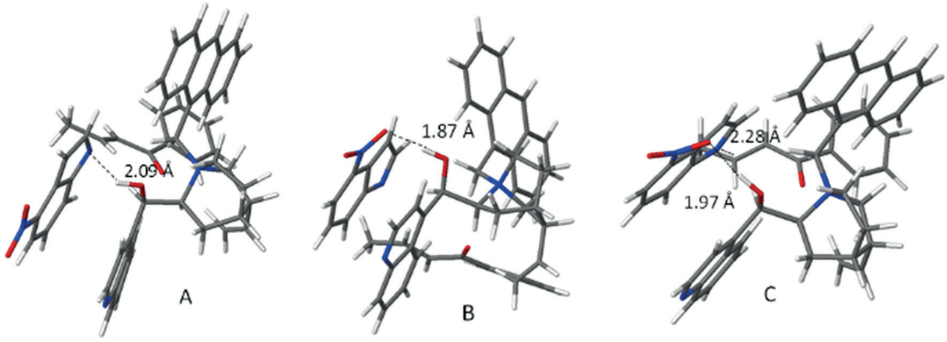

Figure 3 Optimized geometries of intermediates and transition state: A: INT1-S; B: INT2-S; C: TS1-S

Å) (Figure 3C). Throughout the reaction, π–π interactions remain important.

We have revealed here a systematic study of the *N*-alkylation of nitroindoles. It was found that a *Cinchona* alkaloid-derived PTC reaction with various Michael acceptors led exclusively to aza-Michael adducts in high yields and moderate to good enantioselectivities. The acidity of the N–H proton was not the decisive factor in determining the reactivity and selectivity of the reaction. Instead, the position of the nitro group on the indole ring plays a crucial role in the reaction.

All commercially available reagents were used without further purification. All air- or moisture-sensitive reactions were carried out under an argon atmosphere using oven-dried glassware. The reactions were monitored by TLC with silica-gel-coated aluminum plates (Merck 60 F254) and visualized with $KMnO_4$, anisaldehyde, vaniline, or ninhydrine stain. Yields refer to chromatographically purified products. ^{1}H NMR spectra were recorded on a Bruker Avance III instrument at 400 MHz and are reported in ppm (δ) referenced to the residual solvent signal ($CDCl_3$: δ = 7.26; CD_3OD, δ = 3.31). ^{13}C NMR spectra were recorded at 101 MHz and are reported in parts per million (δ) referenced to the residual solvent signal ($CDCl_3$: δ = 77.16; CD_3OD: δ = 49.00). HRMS spectra were recorded with an Agilent Technologies 6540 UHD Accurate-Mass Q-TOF LC/MS spectrometer by using AJ-ESI ionization. IR spectra were recorded on a Bruker Tensor 27 FT-IR spectrophotometer. Optical rotations were obtained with an Anton Paar GWB Polarimeter MCP500 at 20 °C in $CHCl_3$ and are calibrated with pure solvent as a blank. Chiral HPLC was performed by using Chiralpak AD-H (250 × 4.6 mm), Chiralcel OJ-H (250 × 4.6 mm), or Chiralcel OD-H (250 × 4.6 mm) columns. Column chromatography was performed on a preparative purification system with silica gel Kieselgel 40–63 µm. The measured melting points are uncorrected. All crystalline products are obtained from chloroform. Purchased chemicals and solvents were used as received. DCM was distilled over phosphorus pentoxide. PE has a boiling point of 40–60 °C. The reactions were performed under air without additional moisture elimination unless stated otherwise.

Acidity Measurements

UV-Vis spectrophotometric titration was used to determine the acidity (pK_a values) of the nitroindoles and 3-cyanoindole in acetonitrile. Measurements were carried out in a glovebox, applying a method described earlier.[15] The argon atmosphere (5.0) as the environment for all experiments was kept dry and oxygen-free (both contents below 1 ppm) and only freshly prepared solutions in MeCN (H_2O < 5 ppm) were used. UV-Vis spectra were collected on Agilent Cary 60 and PerkinElmer Lambda 12 spectrophotometers using an external cell compartment inside the glovebox. CF_3SO_2OH and $EtN{=}P_2(dma)_5$ (or *tert*-butyliminotri(pyrrolidino)phosphorane) solutions in MeCN were used as acidic and basic titrants, respectively. In titration experiments the concentration of the indoles and reference acids were in the range of 10^{-5} to 10^{-4} M.

Phase-transfer catalysts **I–III**,[18] **VII**,[18] **IV**,[19,20] **V**,[21] **VI**,[22] and **VIII**[23] were prepared by corresponding literature procedures and the

Analytical data matched those in the literature.

Indole derivatives **1**, **4a**, **4c**, **4d**, and **4f** were purchased from Fluorochem Ltd and used as received. 2-Nitroindole (**4e**)[24] and 3-nitroindole (**4b**)[25] were prepared according to literature procedures and the analytical data matched those in the literature.

Synthesis of Unsaturated α,β-Enones 2 and 2a–n

(*E*)-1-Phenylbut-2-en-1-one (2)[26]

To a 1 M solution of phenylmagnesium bromide in THF (25 mL, 25 mmol) in THF (75 mL) crotonaldehyde (2.07 mL, 25 mmol) was added dropwise at 0 °C under argon. The mixture was stirred for 45 min at the same temperature and then quenched with sat. aq NH_4Cl (25 mL). The organic solvent was removed under reduced pressure and aq NH_4Cl (20 mL) was added. The reaction mixture was extracted with EtOAc (5 × 50 mL). The organic phase was dried with $MgSO_4$, filtered, and concentrated to dryness under reduced pressure to provide a yellow oil. The Grignard product was dissolved in DCM (40 mL) and MnO_2 (21.7 g, 250 mmol, 10 equiv) was added under vigorous stirring. The reaction mixture was stirred overnight. The mixture was filtered through a pad of Celite, washed with DCM, and purified by column chromatography (silica gel, 2–10% EtOAc–PE).

Yield: 1.988 g (54%); colorless oil.

^{1}H NMR (400 MHz, $CDCl_3$): δ = 7.96–7.89 (m, 2 H), 7.58–7.51 (m, 1 H), 7.49–7.43 (m, 2 H), 7.07 (dq, *J* = 15.3, 6.8 Hz, 1 H), 6.91 (dq, *J* = 15.3, 1.6 Hz, 1 H), 2.00 (dd, *J* = 6.8, 1.6 Hz, 3 H).

Analytic data were in agreement with the literature data.

2-En-1-ones 2a,c–f,k by Wittig Reaction; General Procedure

The aldehyde (1.2 equiv) was added to the mixture of phosphonium ylide (1 equiv) in DCM (0.2 M). The reaction was monitored by TLC. Upon completion of the reaction, the DCM was evaporated to give a solid residue that was triturated with hexane. The solid triphenylphosphine oxide was filtered off and the hexane layer was dried over Na_2SO_4, filtered, and concentrated to dryness under reduced pressure. The crude mixture was purified by column chromatography (silica gel).

(*E*)-1-(4-Bromophenyl)but-2-en-1-one (2a)

Following the general procedure, starting from 1-(4-bromophenyl)-2-(triphenyl-λ^5-phosphaneylidene)ethan-1-one (1.75 g, 3.8 mmol) and acetaldehyde (256 µL, 4.56 mmol), the mixture was stirred for 7 d. The title compound was obtained after purification by column chromatography (silica gel, 1–6% EtOAc–PE).

Yield: 611 mg (71%); white crystals.

^{1}H NMR (400 MHz, $CDCl_3$): δ = 7.83–7.75 (m, 2 H), 7.64–7.56 (m, 2 H), 7.08 (dq, *J* = 15.3, 6.9 Hz, 1 H), 6.86 (dq, *J* = 15.3, 1.6 Hz, 1 H), 2.00 (dd, *J* = 6.9, 1.6 Hz, 3 H).

Analytic data were in agreement with the literature data.[27]

(*E*)-1-(4-Methoxyphenyl)but-2-en-1-one (2c)

Following the general procedure starting from 1-(4-metoxyphenyl)-2-(triphenyl-λ^5-phosphaneylidene)ethan-1-one (1.97 g, 4.8 mmol) and acetaldehyde (326 µL, 5.8 mmol), the mixture was stirred for 7 d. The title compound was obtained after purification by column chromatography (silica gel, 1–10% EtOAc–PE).

Yield: 700 mg (83%); colorless oil.

^{1}H NMR (400 MHz, $CDCl_3$): δ = 7.99–7.90 (m, 2 H), 7.06 (dq, *J* = 15.2, 6.7 Hz, 1 H), 6.97–6.89 (m, 3 H), 3.87 (s, 3 H), 1.99 (dd, *J* = 6.8, 1.5 Hz, 3 H).

Analytic data were in agreement with the literature data.[28]

(*E*)-1-(Furan-2-yl)but-2-en-1-one (2d)

Following the general procedure starting from 1-(4-furan-2-yl)-2-(triphenyl-λ^5-phosphaneylidene)ethan-1-one (1.4 g, 3.78 mmol) and acetaldehyde (255 μL, 4.54 mmol), the mixture was stirred for 6 d. The title compound was obtained after purification by column chromatography (silica gel, 2–8% EtOAc–PE).

Yield: 210 mg (41%); white crystals.

^{1}H NMR (400 MHz, $CDCl_3$): δ = 7.64–7.57 (m, 1 H), 7.24–7.22 (m, 1 H), 7.22–7.11 (m, 1 H), 6.82 (dq, *J* = 15.4, 1.7 Hz, 1 H), 6.55 (dd, *J* = 3.5, 1.7 Hz, 1 H), 1.99 (dd, *J* = 6.9, 1.7 Hz, 3 H).

Analytic data were in agreement with the literature data.[28]

(*E*)-4-Methyl-1-phenylpent-2-en-1-one (2e)

Following the general procedure starting from 1-phenyl-2-(triphenyl-λ^5-phosphaneylidene)ethan-1-one (1.75 g, 4.6 mmol) and isobutyraldehyde (440 μL, 4.8 mmol, 1.05 equiv), the mixture was stirred for 6 d. The title compound was obtained after purification by column chromatography (silica gel, 2% EtOAc–PE).

Yield: 220 mg (28%); colorless oil.

^{1}H NMR (400 MHz, $CDCl_3$): δ = 7.97–7.89 (m, 2 H), 7.59–7.52 (m, 1 H), 7.50–7.42 (m, 2 H), 7.03 (dd, *J* = 15.5, 6.7 Hz, 1 H), 6.82 (dd, *J* = 15.5, 1.4 Hz, 1 H), 2.66–2.51 (m, 1 H), 1.14 (d, *J* = 6.8 Hz, 6 H).

Analytic data were in agreement with the literature data.[29]

(*E*)-1-Phenylnon-2-en-1-one (2f)

Following the general procedure starting from 1-phenyl-2-(triphenyl-λ^5-phosphaneylidene)ethan-1-one (1.1 g, 2.9 mmol) and heptanal (494 μL, 3.5 mmol), the mixture was stirred for 5 d. The title compound was obtained after purification by column chromatography (silica gel, 1–6% EtOAc–PE).

Yield: 250 mg (40%); colorless oil.

^{1}H NMR (400 MHz, $CDCl_3$): δ = 7.96–7.90 (m, 2 H), 7.59–7.52 (m, 1 H), 7.51–7.42 (m, 2 H), 7.07 (dt, *J* = 15.4, 6.9 Hz, 1 H), 6.87 (dt, *J* = 15.4, 1.4 Hz, 1 H), 2.37–2.27 (m, 2 H), 1.58–1.46 (m, 2 H), 1.42–1.21 (m, 6 H), 0.93–0.84 (m, 3 H).

Analytic data were in agreement with the literature data.[29]

(2*E*,4*E*)-1-Phenylhexa-2,4-dien-1-one (2k)

Following the general procedure starting from 1-phenyl-2-(triphenyl-λ^5-phosphaneylidene)ethan-1-one (1.1 g, 2.9 mmol) and (*E*)-but-2-enal (290 μL, 3.5 mmol), the mixture was stirred for 5 d. The title compound was obtained after purification by column chromatography (silica gel, 2–4% EtOAc–PE).

Yield: 250 mg (40%); yellow amorphous solid.

^{1}H NMR (400 MHz, $CDCl_3$): δ = 7.96–7.90 (m, 2 H), 7.57–7.51 (m, 1 H), 7.50–7.36 (m, 3 H), 6.87 (dd, *J* = 15.1, 0.8 Hz, 1 H), 6.40–6.19 (m, 2 H), 1.90 (dd, *J* = 6.1, 1.0 Hz, 3 H).

Analytic data were in agreement with the literature data.[30]

(*E*)-1-(4-Nitrophenyl)but-2-en-1-one (2b)

3-Hydroxy-1-(4-nitrophenyl)butan-1-one

To a dry flask under argon was added diisopropylamine (1.4 mL, 10 mmol) in THF (15 mL). The mixture was cooled to –20 °C and 2.5 M *n*-BuLi in hexane (4 mL, 10 mmol, 1.05 equiv) was added. The mixture was stirred for 30 min, cooled to –78 °C, and *p*-nitroacetophenone (1 equiv) was added. The reaction mixture was stirred for 20 min at –78 °C and acetaldehyde (590 μL, 10.5 mmol, 1.1 equiv) was added. After 1 h the mixture was quenched with sat. aq $NaHCO_3$ and warmed to r.t. The crude mixture was poured into Et_2O and washed with H_2O, 1% aq HCl (2 × 50 mL), sat. aq $NaHCO_3$ (2 × 50 mL), and brine (2 × 50 mL). The organic layer was dried over Na_2SO_4 and concentrated to dryness under reduced pressure. The crude mixture was purified by column chromatography (silica gel, 5–30% EtOAc–PE) providing 3-hydroxy-1-(4-nitrophenyl)butan-1-one; yield: 470 mg (24%).

^{1}H NMR (400 MHz, $CDCl_3$): δ = 8.34–8.29 (m, 2 H), 8.14–8.09 (m, 2 H), 4.54–4.37 (m, 1 H), 3.18–3.12 (m, 2 H), 2.98 (s, 1 H, OH), 1.33 (d, *J* = 6.4 Hz, 3 H).

Analytic data were in agreement with the literature data.[31]

2b

3-Hydroxy-1-(4-nitrophenyl)butan-1-one (470 mg, 2.25 mmol) was dissolved in a mixture of DCM (7 mL) and pyridine (1.8 mL) and treated with mesyl chloride (174 μL, 2.25 mmol) under an argon atmosphere for 4 h. H_2O (10 mL) was added and reaction mixture was extracted with DCM (3 × 20 mL). The organic phase was washed with sat. aq $CuSO_4$ (4 × 30 mL) and brine (2 × 30mL), dried over Na_2SO_4, and concentrated to dryness under reduced pressure. The title compound was obtained after purification by column chromatography (silica gel, 2–10% EtOAc–PE).

Yield: 175 mg (41%); white solid.

^{1}H NMR (400 MHz, $CDCl_3$): δ = 8.34–8.26 (m, 2 H), 8.07–7.99 (m, 2 H), 7.12 (dq, *J* = 15.4, 6.9 Hz, 1 H), 6.87 (dq, *J* = 15.3, 1.7 Hz, 1 H), 2.03 (dd, *J* = 6.9, 1.7 Hz, 3 H).

Analytic data were in agreement with the literature data.[32]

(*E*)-1-(Naphthalen-2-yl)but-2-en-1-one (2g)

3-Hydroxy-1-(2-naphthalenyl)-1-butanone

Diisopropylamine (1.37 mL, 9.8 mmol) was dissolved in THF (18 mL) under argon. The mixture was cooled to –20 °C and 2.5 M *n*-BuLi in hexane (3.92 mL, 9.8 mmol) was added; then the mixture was stirred for 30 min and cooled to –78 °C before 1-(naphthalen-2-yl)ethan-1-one (1.59 g, 9.3 mmol) was added. The mixture was stirred for 20 min at –78 °C and acetaldehyde (570 μL, 10.26 mmol) was added. The mixture was stirred for an additional 1 h and was quenched with sat. aq $NaHCO_3$ and warmed to r.t. The crude mixture was poured into Et_2O, washed with H_2O, 1% aq HCl (2 × 50 mL), sat. aq $NaHCO_3$ (2 × 50 mL), and brine (2 × 50 mL). The organic layer was dried over Na_2SO_4 and concentrated to dryness under reduced pressure. The crude mixture was purified by column chromatography (silica gel, 5–30% EtOAc–PE); this provided 3-hydroxy-1-(2-naphthalenyl)-1-butanone; yield: 1.788 g (90%).

^{1}H NMR (400 MHz, $CDCl_3$): δ = 8.46 (d, *J* = 1.7 Hz, 1 H), 8.11–7.80 (m, 4 H), 7.67–7.52 (m, 2 H), 4.53–4.41 (m, 1 H), 3.41 (d, *J* = 3.0 Hz, 1 H, OH), 3.31 (dd, *J* = 17.6, 2.8 Hz, 1 H), 3.18 (dd, *J* = 17.6, 8.9 Hz, 1 H), 1.35 (d, *J* = 6.4 Hz, 3 H).

Analytic data were in agreement with the literature data.[31]

2g

3-Hydroxy-1-(2-naphthalenyl)-1-butanone (900 mg, 4.2 mmol) was dissolved in pyridine (3.2 mL) and treated with mesyl chloride (325 µL, 4.2 mmol) under argon for 24 h. After H_2O was added to the flask, the mixture was extracted with Et_2O (3 × 50 mL). The organic phase was washed with sat. aq $CuSO_4$ (4 × 30 mL) and brine (2 × 40 mL), dried over Na_2SO_4, and concentrated to dryness under reduced pressure. The crude 4-(naphthalen-2-yl)-4-oxobutan-2-yl methanesulfonate and TEA (608 µL, 4.2 mmol) were mixed in Et_2O (20 mL) overnight. The crude mixture was concentrated and purified by column chromatography (silica gel, 1–8% EtOAc–PE), providing product **2g**.

Yield: 480 mg (70%).

^{1}H NMR (400 MHz, $CDCl_3$): δ = 8.47–8.42 (m, 1 H), 8.03 (dd, *J* = 8.6, 1.8 Hz, 1 H), 8.00–7.94 (m, 1 H), 7.94–7.85 (m, 2 H), 7.63–7.51 (m, 2 H), 7.21–7.02 (m, 2 H), 2.05 (dd, *J* = 6.4, 1.1 Hz, 3 H).

Analytic data were in agreement with the literature data.[33]

Phenyl (*E*)-But-2-enoate (2m)

Compound **2m** was prepared according to a literature procedure.[34]

Yield: 573 mg (35%); colorless liquid.

^{1}H NMR (400 MHz, $CDCl_3$): δ = 7.42–7.34 (m, 2 H), 7.27–7.07 (m, 4 H), 6.05 (dq, *J* = 15.6, 1.7 Hz, 1 H), 1.96 (dd, *J* = 6.9, 1.7 Hz, 3 H).

***N*-Alkylation of Nitroindoles; General Procedure**

Indole **1** or **4** (0.1 mmol), phase-transfer catalyst **III** (0.005 mmol), and Rb_2CO_3 (0.13 mmol) were loaded in a 1 mL vial. The mixture of compounds was held for 1 h under vacuum. The vial was filled with an argon atmosphere. Toluene (1 mL), ketone **2** (0.21 mmol), and H_2O (0.14 mmol) were added and the reaction mixture was stirred at r.t. for 5 h under argon unless stated otherwise. The progress of the reaction was monitored by TLC and NMR spectroscopy. After completion of the reaction, the reaction mixture was directly purified by column chromatography to afford pure products **3**, **5**, or **6**.

(*S*)-3-(4-Nitro-1*H*-indol-1-yl)-1-phenylbutan-1-one (5a)

The reaction time was 24 h. Title compound **5a** was obtained according to the general procedure from 4-nitroindole (**4a**; 162.2 mg, 1 mmol) and **2** (307 mg, 2.1 mmol). The product was isolated by direct column chromatography (silica gel; 5–25% EtOAc–PE).

Yield: 281 mg (91%); orange amorphous solid; 65% ee [HPLC (Daicel Chiralpak AD-H, hexane–^{i}PrOH, 90:10, flow rate 1.0 mL/min, *T* = 25 °C, λ = 254 nm): t_R = 21.3 (major), t_R = 29.9 (minor)]; $[\alpha]_D^{20}$ –21.4 (*c* 0.033, $CHCl_3$); R_f = 0.4 (PE–EtOAc, 3:1).

IR (KBr): 2979, 1685, 1597, 1511, 1498, 1448, 1361, 1332, 1312, 1268, 755, 735 cm^{-1}.

^{1}H NMR (400 MHz, $CDCl_3$): δ = 8.12 (dd, *J* = 8.0, 0.8 Hz, 1 H), 7.91–7.86 (m, 2 H), 7.83 (d, *J* = 8.2 Hz, 1 H), 7.60–7.54 (m, 1 H), 7.51 (d, *J* = 3.3 Hz, 1 H), 7.47–7.41 (m, 2 H), 7.31–7.26 (m, 2 H), 5.42–5.31 (m, 1 H), 3.58 (dd, *J* = 17.3, 5.8 Hz, 1 H), 3.47 (dd, *J* = 17.3, 7.3 Hz, 1 H), 1.70 (d, *J* = 6.8 Hz, 3 H).

^{13}C NMR (101 MHz, $CDCl_3$): δ = 196.8, 140.6, 137.9, 136.4, 133.9, 128.9 (2 C), 128.6, 128.1 (2 C), 123.1, 120.6, 117.8, 116.6, 101.1, 48.2, 42.7, 20.1.

HRMS (ESI): *m*/*z* [M + H]$^+$ calcd for $C_{18}H_{17}N_2O_3$: 309.1234; found: 309.1227.

(*S*)-3-(3-Nitro-1*H*-indol-1-yl)-1-phenylbutan-1-one (5b)

Title compound **5b** was obtained according to the general procedure from 3-nitroindole (**4b**; 16.2 mg, 0.1 mmol) and **2** (30.9 mg, 0.21 mmol). The product was isolated by direct column chromatography (silica gel; 5–25% EtOAc–PE).

Yield: 20 mg (65%); rose amorphous solid; 42% ee [HPLC (Daicel Chiralpak OD-H, hexane–^{i}PrOH, 90:10, flow rate 1.0 mL/min, *T* = 25 °C, λ = 254 nm): t_R = 41.0 (major), t_R = 45.1 (minor)]; $[\alpha]_D^{20}$ –4.7 (*c* 0.034, $CHCl_3$); R_f = 0.4 (PE–EtOAc, 3:1).

IR (KBr): 3128, 1685, 1597, 1525, 1481, 1449, 1379, 1303, 1225, 750, 689 cm^{-1}

^{1}H NMR (400 MHz, $CDCl_3$): δ = 8.34–8.26 (m, 2 H), 7.94–7.89 (m, 2 H), 7.63–7.54 (m, 2 H), 7.49–7.44 (m, 2 H), 7.44–7.36 (m, 2 H), 5.42–5.29 (m, 1 H), 3.62 (dd, *J* = 17.6, 5.4 Hz, 1 H), 3.53 (dd, *J* = 17.6, 7.5 Hz, 1 H), 1.73 (d, *J* = 6.8 Hz, 3 H).

^{13}C NMR (101 MHz, $CDCl_3$): δ = 196.0, 136.1, 135.0, 134.1, 129.5, 129.0 (2 C), 128.1 (2 C), 127.8, 124.7, 124.5, 121.14, 121.12, 111.0, 48.9, 45.2, 21.0.

HRMS (ESI): *m*/*z* [M + H]$^+$ calcd for $C_{18}H_{17}N_2O_3$: 309.1234; found: 309.1228.

(*S*)-3-(5-Nitro-1*H*-indol-1-yl)-1-phenylbutan-1-one (5c)

Title compound **5c** was obtained according to the general procedure from 5-nitroindole (**4c**; 16.2 mg, 0.1 mmol) and **2** (30.9 mg, 0.21 mmol). The product was isolated by direct column chromatography (silica gel; 5–25% EtOAc–PE).

Yield: 29.3 mg (95%); orange amorphous solid; 38% ee [HPLC (Daicel Chiralpak AD-H, hexane–^{i}PrOH, 90:10, flow rate 1.0 mL/min, *T* = 25 °C, λ = 254 nm): t_R = 31.8 (minor), t_R = 35.9 (major)]; $[\alpha]_D^{20}$ –76.4 (*c* 0.032, $CHCl_3$); R_f = 0.5 (PE–EtOAc, 3:1).

IR (KBr): 2980, 1685, 1610, 1580, 1470, 1450, 1319, 1219, 1070, 743, 690 cm^{-1}.

^{1}H NMR (400 MHz, $CDCl_3$): δ = 8.55 (d, *J* = 2.3 Hz, 1 H), 8.12 (dd, *J* = 9.1, 2.3 Hz, 1 H), 7.93–7.84 (m, 2 H), 7.60–7.54 (m, 1 H), 7.51 (d, *J* = 9.2 Hz, 1 H), 7.48–7.38 (m, 3 H), 6.71 (d, *J* = 3.4 Hz, 1 H), 5.39–5.26 (m, 1 H), 3.58 (dd, *J* = 17.3, 6.0 Hz, 1 H), 3.46 (dd, *J* = 17.3, 7.1 Hz, 1 H), 1.69 (d, *J* = 6.9 Hz, 3 H).

^{13}C NMR (101 MHz, $CDCl_3$): δ = 196.7, 141.7, 138.5, 136.4, 133.8, 128.9 (2 C), 128.1 (2 C), 127.7, 127.4, 118.4, 117.4, 109.8, 105.0, 48.3, 45.5, 21.3.

HRMS (ESI): *m*/*z* [M + H]$^+$ calcd for $C_{18}H_{17}N_2O_3$: 309.1234; found: 309.1232.

(*S*)-3-(6-Nitro-1*H*-indol-1-yl)-1-phenylbutan-1-one (5d)

Title compound **5d** was obtained according to the general procedure from 6-nitroindole (**4d**; 16.2 mg, 0.1 mmol) and **2** (30.9 mg, 0.21 mmol). The product was isolated by direct column chromatography (silica gel; 5–15% EtOAc–PE).

Yield: 25.3 mg (82%); yellow solid; mp 168–170 °C; 35% ee [HPLC (Daicel Chiralpak OD-H, hexane–^{i}PrOH, 90:10, flow rate 1.0 mL/min, *T* = 25 °C, λ = 254 nm): t_R =16.6 (major), t_R = 22.6 (minor)]; $[\alpha]_D^{20}$ –76.4 (*c* 0.035, $CHCl_3$); R_f = 0.5 (PE–EtOAc, 3:1).

IR (KBr): 2978, 1684, 1580, 1511, 1495, 1462, 1330, 1219, 1070, 777, 730, 689 cm^{-1}.

^{1}H NMR (400 MHz, $CDCl_3$): δ = 8.50–8.43 (m, 1 H), 8.00 (dd, *J* = 8.7, 2.0 Hz, 1 H), 7.93–7.86 (m, 2 H), 7.63 (d, *J* = 8.7 Hz, 1 H), 7.60–7.49 (m, 2 H), 7.45 (t, *J* = 7.7 Hz, 2 H), 6.62 (d, *J* = 3.2 Hz, 1 H), 5.41–5.29 (m, 1 H), 3.62 (dd, *J* = 17.2, 6.1 Hz, 1 H), 3.50 (dd, *J* = 17.2, 7.1 Hz, 1 H), 1.71 (d, *J* = 6.8 Hz, 3 H).

^{13}C NMR (101 MHz, $CDCl_3$): δ = 196.5, 143.1, 136.4, 134.2, 133.8, 133.5, 130.5, 128.9 (2 C), 128.1 (2 C), 121.0, 115.2, 107.0, 103.1, 48.6, 45.4, 21.4.

HRMS (ESI): *m*/*z* [M + H]$^+$ calcd for $C_{18}H_{17}N_2O_3$: 309.1234; found: 309.1226.

(*S*)-1-(4-Bromophenyl)-3-(4-nitro-1*H*-indol-1-yl)butan-1-one (6a)

Title compound **6a** was obtained according to the general procedure from 4-nitroindole (**4a**; 16.2 mg, 0.1 mmol) and (*E*)-1-(4-bromophenyl)but-2-en-1-one (**2a**; 47.3 mg, 0.21 mmol). Following a modification of the general procedure, ketone **2a** was added before evacuation of the system. The product was isolated by direct column chromatography (silica gel; 2–15% EtOAc–PE).

Yield: 25.9 mg (67%); orange amorphous solid; 59% ee [HPLC (Daicel Chiralpak AD-H, hexane–^{i}PrOH, 90:10, flow rate 1.0 mL/min, *T* = 25 °C, λ =254 nm): t_R =27.2 (major), t_R = 35.2 (minor)]; $[\alpha]_D^{20}$ –25.4 (*c* 0.050, $CHCl_3$); R_f = 0.4 (PE–EtOAc, 10:1).

IR (KBr): 2979, 1686, 1585, 1568, 1511, 1498, 1361, 1331, 1304, 1269, 1105, 790, 737 cm^{-1}.

^{1}H NMR (400 MHz, $CDCl_3$): δ = 8.15–8.09 (m, 1 H), 7.82 (d, *J* = 8.3 Hz, 1 H), 7.76–7.70 (m, 2 H), 7.60–7.54 (m, 2 H), 7.49 (d, *J* = 3.3 Hz, 1 H), 7.32–7.26 (m, 2 H), 5.40–5.29 (m, 1 H), 3.54 (dd, *J* = 17.3, 5.9 Hz, 1 H), 3.42 (dd, *J* = 17.4, 7.2 Hz, 1 H), 1.69 (d, *J* = 6.8 Hz, 3 H).

^{13}C NMR (101 MHz, $CDCl_3$): δ = 195.7, 140.5, 137.8, 135.0, 132.1 (2 C), 129.5 (2 C), 129.0, 128.4, 122.5, 120.6, 117.7, 116.5, 102.9, 47.9, 45.5, 21.3

HRMS (ESI): *m*/*z* [M + H]$^+$ calcd for $C_{18}H_{16}N_2O_3Br$: 387.0339; found: 387.0342.

(*S*)-3-(4-Nitro-1*H*-indol-1-yl)-1-(4-nitrophenyl)butan-1-one (6b)

Title compound **6b** was obtained according to the general procedure from 4-nitroindole (**4a**; 16.2 mg, 0.1 mmol) and (*E*)-1-(4-nitrophenyl)but-2-en-1-one (**2b**; 40.1 mg, 0.21 mmol). Following a modification of the general procedure, ketone **2b** was added before evacuation of the system. The product was isolated by direct column chromatography (silica gel; 3–20% EtOAc–PE).

Yield: 26.1 mg (74%); yellow solid; mp 64–68 °C; 73% ee [HPLC (Daicel Chiralpak OD-H, hexane–^{i}PrOH, 70:30, flow rate 0.9 mL/min, *T* = 35 °C, λ = 254 nm): t_R =23.2 (minor), t_R = 49.8 (major)]; $[\alpha]_D^{20}$ –40.2 (*c* 0.041, $CHCl_3$); R_f = 0.5 (PE–EtOAc, 3:1).

IR (KBr): 3109, 2929, 1693, 1603, 1524, 1347, 1318, 1269, 790, 786 cm^{-1}.

^{1}H NMR (400 MHz, $CDCl_3$): δ = 8.30–8.24 (m, 2 H), 8.16–8.09 (m, 1 H), 8.05–8.00 (m, 2 H), 7.85–7.80 (m, 1 H), 7.50 (d, *J* = 3.3 Hz, 1 H), 7.33–7.27 (m, 2 H), 5.45–5.29 (m, 1 H), 3.64 (dd, *J* = 17.6, 6.0 Hz, 1 H), 3.51 (dd, *J* = 17.7, 6.9 Hz, 1 H), 1.73 (d, *J* = 6.8 Hz, 3 H).

^{13}C NMR (101 MHz, $CDCl_3$): δ = 195.3, 150.7, 140.63, 140.61, 137.8, 129.2 (2 C), 128.4, 124.1 (2 C), 122.6, 120.8, 117.9, 116.5, 103.2, 47.9, 46.2, 21.4.

HRMS (ESI): *m*/*z* [M + H]$^+$ calcd for $C_{18}H_{16}N_3O_5$: 354.1084; found: 354.109.

(*S*)-1-(4-Methoxyphenyl)-3-(4-nitro-1*H*-indol-1-yl)butan-1-one (6c)

Title compound **6c** was obtained according to the general procedure from 4-nitroindole (**4a**; 16.2 mg, 0.1 mmol) and (*E*)-1-(4-methoxyphenyl)but-2-en-1-one (**2c**; 37 mg, 0.21 mmol). The product was isolated by direct column chromatography (silica gel; 3–20% EtOAc–PE).

Yield: 28 mg (83%); yellow crystals; mp 100–104 °C; 75% ee [HPLC (Daicel Chiralpak AD-H, hexane–^{i}PrOH, 80:20, flow rate 1.0 mL/min, *T* = 35 °C, λ= 254 nm): t_R =15.8 (major), t_R = 23.6 (minor)]; $[\alpha]_D^{20}$ –34.3 (*c* 0.065, $CHCl_3$); R_f = 0.3 (PE–EtOAc, 3:1).

IR (KBr): 2976, 1675, 1600, 1575, 1511, 1456, 1361, 1308, 1266, 1171, 759, 737 cm^{-1}.

^{1}H NMR (400 MHz, $CDCl_3$): δ = 8.10 (d, *J* = 7.9 Hz, 1 H), 7.88–7.79 (m, 3 H), 7.49 (d, *J* = 3.3 Hz, 1 H), 7.29–7.23 (m, 2 H), 6.91–6.85 (m, 2 H), 5.39–5.28 (m, 1 H), 3.83 (s, 3 H), 3.49 (dd, *J* = 17.0, 5.8 Hz, 1 H), 3.39 (dd, *J* = 17.0, 7.3 Hz, 1 H), 1.67 (d, *J* = 6.8 Hz, 3 H).

^{13}C NMR (101 MHz, $CDCl_3$): δ = 195.2, 164.1, 140.5, 137.9, 130.4 (2 C), 129.5, 128.7, 122.6, 120.6, 117.7, 116.7, 114.0 (2 C), 102.8, 55.7, 48.3, 45.3, 21.4.

HRMS (ESI): *m*/*z* [M + H]$^+$ calcd for $C_{19}H_{19}N_2O_4$: 339.1339; found: 339.1341.

CCDC 1923379 contains the supplementary crystallographic data for **6c**. These data can be obtained free of charge from The Cambridge Crystallographic Data Centre via www.ccdc.cam.ac.uk/getstructures.

(*S*)-1-(Furan-2-yl)-3-(4-nitro-1*H*-indol-1-yl)butan-1-one (6d)

Title compound **6d** was obtained according to the general procedure from 4-nitroindole (**4a**; 16.2 mg, 0.1 mmol) and (*E*)-1-(furan-2-yl)but-2-en-1-one (**2d**; 28.6 mg, 0.21 mmol). Following a modification of the general procedure, ketone **2d** was added before evacuation of the system. The product was isolated by direct column chromatography (silica gel; 5–25% EtOAc–PE).

Yield: 26.8 mg (90%); orange crystals; mp 85–90 °C; 63% ee [HPLC (Daicel Chiralpak AD-H, hexane–^{i}PrOH, 90:10, flow rate 1.0 mL/min, *T* = 25 °C, λ = 254 nm): t_R =19.4 (major), t_R = 26.5 (minor)]; $[\alpha]_D^{20}$ –37.8 (*c* 0.030, $CHCl_3$); R_f = 0.3 (PE–EtOAc, 3:1).

IR (KBr): 3132, 2980, 1672, 1567, 1511, 1499, 1467, 1361, 1332, 1308, 760, 737 cm^{-1}.

^{1}H NMR (400 MHz, $CDCl_3$): δ = 8.08 (dd, *J* = 8.0, 0.8 Hz, 1 H), 7.78 (d, *J* = 8.1 Hz, 1 H), 7.54–7.43 (m, 2 H), 7.25–7.20 (m, 2 H), 7.09 (d, *J* = 3.6 Hz, 1 H), 6.46 (dd, *J* = 3.6, 1.7 Hz, 1 H), 5.33–5.20 (m, 1 H), 3.41 (dd, *J* = 16.5, 6.4 Hz, 1 H), 3.26 (dd, *J* = 16.5, 7.1 Hz, 1 H), 1.64 (d, *J* = 6.9 Hz, 3 H).

^{13}C NMR (101 MHz, $CDCl_3$): δ = 185.8, 152.5, 147.0, 140.6, 137.9, 128.5, 122.6, 120.7, 117.82, 117.78, 116.6, 112.8, 103.0, 48.1, 45.5, 21.4.

HRMS (ESI): *m*/*z* [M + H]$^+$ calcd for $C_{16}H_{15}N_2O_4$: 299.1026; found: 299.1032.

(*R*)-4-Methyl-3-(4-nitro-1*H*-indol-1-yl)-1-phenylpentan-1-one (6e)

The reaction time was 24 h. Title compound **6e** was obtained according to the general procedure from 4-nitroindole (**4a**; 16.2 mg, 0.1 mmol) and (*E*)-4-methyl-1-phenylpent-2-en-1-one (**2e**; 36.6 mg, 0.21 mmol). The product was isolated by direct column chromatography (silica gel; 5–25% EtOAc–PE).

Yield: 26.9 mg (80%); orange amorphous solid; 64% ee [HPLC (Daicel Chiralpak AD-H, hexane–^{i}PrOH, 90:10, flow rate 1.0 mL/min, T = 25 °C, λ = 254 nm): t_R =17.3 (major), t_R = 20.8 (minor)]; $[\alpha]_D^{20}$ –31.9 (*c* 0.037, $CHCl_3$); R_f = 0.7 (PE–EtOAc, 3:1).

IR (KBr): 2966, 1686, 1597, 1565, 1512, 1499, 1448, 1361, 1327, 1302, 1273, 758, 737 cm^{-1}.

^{1}H NMR (400 MHz, $CDCl_3$): δ = 8.16–8.07 (m, 1 H), 7.88 (d, J = 8.2 Hz, 1 H), 7.86–7.79 (m, 2 H), 7.58–7.50 (m, 1 H), 7.45–7.36 (m, 3 H), 7.32–7.23 (m, 2 H), 5.00–4.90 (m, 1 H), 3.67 (dd, J = 17.3, 8.4 Hz, 1 H), 3.55 (dd, J = 17.3, 4.3 Hz, 1 H), 2.38–2.23 (m, 1 H), 1.09 (d, J = 6.6 Hz, 3 H), 0.74 (d, J = 6.6 Hz, 3 H).

^{13}C NMR (101 MHz, $CDCl_3$): δ = 196.9, 140.5, 139.1, 136.5, 133.7, 129.2, 128.9 (2 C), 128.1 (2 C), 122.2, 120.6, 117.7, 117.2, 103.0, 58.4, 42.0, 34.2, 20.4, 19.4.

HRMS (ESI): m/z [M + H]$^+$ calcd for $C_{20}H_{21}N_2O_3$: 337.1547; found: 337.1543.

(*S*)-3-(4-Nitro-1*H*-indol-1-yl)-1-phenylnonan-1-one (6f)

The reaction time was 24 h. Title compound **6f** was obtained according to the general procedure from 4-nitroindole (**4a**; 16.2 mg, 0.1 mmol) and (*E*)-1-phenylnon-2-en-1-one (**2f**; 45.4 mg, 0.21 mmol). The product was isolated by direct column chromatography (silica gel; 2–15% EtOAc–PE).

Yield: 31.0 mg (82%); orange amorphous solid; 59% ee [HPLC (Daicel Chiralpak AD-H, hexane–^{i}PrOH, 95:5, flow rate 1.0 mL/min, T = 25 °C, λ = 254 nm): t_R =19.4 (major), t_R = 22.4 (minor)]; $[\alpha]_D^{20}$ –12.2 (*c* 0.064, $CHCl_3$); R_f = 0.6 (PE–EtOAc, 4:1).

IR (KBr): 3106, 2928, 2856, 1685, 1597, 1580, 1361, 1323, 1274, 755, 737 cm^{-1}.

^{1}H NMR (400 MHz, $CDCl_3$): δ = 8.12 (dd, J = 8.0, 0.8 Hz, 1 H), 7.89–7.82 (m, 3 H), 7.59–7.51 (m, 1 H), 7.48–7.38 (m, 3 H), 7.32–7.24 (m, 2 H), 5.26–5.15 (m, 1 H), 3.58 (dd, J = 17.3, 6.7 Hz, 1 H), 3.46 (dd, J = 17.3, 6.1 Hz, 1 H), 2.08–1.92 (m, 2 H), 1.35–0.97 (m, 8 H), 0.81 (t, J = 6.9 Hz, 3 H).

^{13}C NMR (101 MHz, $CDCl_3$): δ = 197.1, 140.8, 138.9, 136.6, 134.0, 129.1 (2 C), 129.0, 128.3 (2 C), 122.6, 120.9, 117.9, 117.0, 103.3, 52.8, 45.0, 36.1, 31.8, 29.1, 26.4, 22.8, 14.3.

HRMS (ESI): m/z [M + H]$^+$ calcd for $C_{23}H_{27}N_2O_3$: 379.2016; found: 379.2021.

(*S*)-1-(Naphthalen-2-yl)-3-(4-nitro-1*H*-indol-1-yl)butan-1-one (6g)

Title compound **6g** was obtained according to the general procedure from 4-nitroindole (**4a**; 16.2 mg, 0.1 mmol) and (*E*)-1-(naphthalen-2-yl)but-2-en-1-one (**2g**; 41.2 mg, 0.21 mmol). Following a modification of the general procedure, ketone **2g** was added before evacuation of the system. The product was isolated by direct column chromatography (silica gel; 3–20% EtOAc–PE).

Yield: 34.2 mg (96%); orange amorphous solid; 69% ee [HPLC (Daicel Chiralpak AD-H, hexane–^{i}PrOH, 90:10, flow rate 1.0 mL/min, T = 25 °C, λ = 254 nm): t_R =27.8 (major), t_R = 42.4 (minor)]; $[\alpha]_D^{20}$ –87.9 (*c* 0.032, $CHCl_3$); R_f = 0.5 (PE–EtOAc, 3:1).

IR (KBr): 2979, 1680, 1626, 1565, 1510, 1498, 1469, 1361, 1331, 1302, 1269, 756, 737 cm^{-1}.

^{1}H NMR (400 MHz, $CDCl_3$): δ = 8.37 (d, J = 1.7 Hz, 1 H), 8.12 (dd, J = 8.0, 0.8 Hz, 1 H), 7.97–7.81 (m, 5 H), 7.64–7.52 (m, 3 H), 7.39–7.19 (m, 2 H), 5.47–5.36 (m, 1 H), 3.70 (dd, J = 17.2, 5.8 Hz, 1 H), 3.61 (dd, J = 17.1, 7.2 Hz, 1 H), 1.74 (d, J = 6.8 Hz, 3 H).

^{13}C NMR (101 MHz, $CDCl_3$): δ = 196.7, 140.5, 137.9, 135.9, 133.7, 132.5, 130.0, 129.7, 129.0, 128.8, 128.7, 127.9, 127.2, 123.5, 122.7, 120.6, 117.8, 116.7, 102.9, 48.3, 45.8, 21.5.

HRMS (ESI): m/z [M + H]$^+$ calcd for $C_{22}H_{19}N_2O_3$: 359.1390; found: 359.1389.

3-(4-Nitro-1*H*-indol-1-yl)cyclohexan-1-one (6h)

The reaction time was 24 h. Title compound **6h** was obtained according to the general procedure from 4-nitroindole (**4a**; 16.2 mg, 0.1 mmol) and cyclohex-2-en-1-one (**2h**; 20.2 mg, 0.21 mmol). The product was isolated by direct column chromatography (silica gel; 5–30% EtOAc–PE).

Yield: 16.8 mg (65%); yellow amorphous solid; racemic [HPLC (Daicel Chiralpak AD-H, hexane–^{i}PrOH, 90:10, flow rate 1.0 mL/min, T = 25 °C, λ = 254 nm): t_{R1} = 23.2, t_{R2} = 26.8]; R_f = 0.1 (PE–EtOAc, 3:1).

IR (KBr): 2952, 1713, 1512, 1498, 1449, 1362, 1333, 1307, 1284, 792, 757 cm^{-1}.

^{1}H NMR (400 MHz, $CDCl_3$): δ = 8.15 (d, J = 8.0 Hz, 1 H), 7.68 (d, J = 8.2 Hz, 1 H), 7.47 (d, J = 3.3 Hz, 1 H), 7.36–7.27 (m, 2 H), 4.80–4.70 (m, 1 H), 2.99–2.87 (m, 1 H), 2.87–2.74 (m, 1 H), 2.62–2.32 (m, 3 H), 2.30–2.12 (m, 2 H), 1.91–1.76 (m, 1 H).

^{13}C NMR (101 MHz, $CDCl_3$): δ = 207.2, 140.8, 137.6, 128.2, 122.8, 120.9, 118.0, 116.0, 103.2, 54.7, 48.4, 40.9, 31.7, 22.3.

HRMS (ESI): m/z [M + H]$^+$ calcd for $C_{14}H_{15}N_2O_3$: 259.1077; found: 259.1081.

3-(4-Nitro-1*H*-indol-1-yl)-1,3-diphenylpropan-1-one (6i)

The reaction time was 48 h. Title compound **6i** was obtained according to the general procedure from 4-nitroindole (**4a**; 16.2 mg, 0.1 mmol) and (2*E*)-1,3-diphenylprop-2-en-1-one (**2i**; 43.7 mg, 0.21 mmol). Following a modification of the general procedure, ketone **2i** was added before evacuation of the system. The product was isolated by direct column chromatography (silica gel; 5–25% EtOAc–PE).

Yield: 13.0 mg (35%); yellow solid; mp = 79–83 °C; racemic [HPLC (Daicel Chiralpak OD-H, hexane–^{i}PrOH, 70:30, flow rate 1.0 mL/min, T = 35 °C, λ = 254 nm): t_{R1} = 15.7, t_{R2} = 33.4]; R_f = 0.3 (PE–EtOAc, 3:1).

IR (KBr): 3063, 1685, 1596, 1580 1521, 1497, 1448, 1361, 1329, 1296, 753, 737, 697 cm^{-1}.

^{1}H NMR (400 MHz, $CDCl_3$): δ = 8.12 (dd, J = 8.0, 0.8 Hz, 1 H), 7.98–7.90 (m, 2 H), 7.76 (d, J = 8.2 Hz, 1 H), 7.63–7.56 (m, 1 H), 7.51–7.44 (m, 3 H), 7.36–7.18 (m, 7 H), 6.50–6.43 (m, 1 H), 4.07 (dd, J = 17.4, 7.8 Hz, 1 H), 3.95 (dd, J = 17.4, 6.1 Hz, 1 H).

^{13}C NMR (101 MHz, $CDCl_3$): δ = 195.8, 140.6, 139.7, 138.4, 136.3, 134.0, 129.6 (2 C), 129.3 (2 C), 129.0, 128.5, 128.2 (2 C), 126.4 (2 C), 123.0, 121.0, 117.9, 117.1, 103.0, 55.7, 43.9.

HRMS (ESI): m/z [M + H]$^+$ calcd for $C_{23}H_{19}N_2O_3$: 371.1390; found: 371.1387.

2-(4-Nitro-1*H*-indol-1-yl)-1,4-diphenylbutane-1,4-dione (6j)

The reaction time was 24 h. Title compound **6j** was obtained according to the general procedure from 4-nitroindole (**4a**; 16.2 mg, 0.1 mmol) and (*E*)-1,4-diphenylbut-2-ene-1,4-dione (**2j**; 49.6 mg, 0.21 mmol). Following a modification of the general procedure, ketone **2i** was added before evacuation of the system. The product was isolated by two sequential column chromatography procedures (silica gel; first: 3–20% EtOAc–PE; second: 50% DCM–PE).

Yield: 22.6 mg (60%); yellow amorphous solid; racemic [HPLC (Daicel Chiralpak OD-H, hexane–^{i}PrOH, 70:30, flow rate 1.0 mL/min, T = 35 °C, λ = 254 nm): t_{R1} = 11.1, t_{R2} = 20.8]; R_f = 0.7 (PE–EtOAc, 3:1).

IR (KBr): 3063, 1680, 1596, 1580, 1516, 1502, 1359, 1332, 1293, 1230, 760, 737, 688 cm^{-1}.

^{1}H NMR (400 MHz, $CDCl_3$): δ = 8.15 (dd, J = 8.0, 0.8 Hz, 1 H), 8.00–7.88 (m, 5 H), 7.63–7.57 (m, 1 H), 7.57–7.50 (m, 1 H), 7.50–7.44 (m, 2 H), 7.43 (d, J = 3.3 Hz, 1 H), 7.42–7.34 (m, 3 H), 7.28 (dd, J = 3.4, 0.8 Hz, 1 H), 6.74 (dd, J = 8.1, 5.0 Hz, 1 H), 4.33 (dd, J = 17.8, 8.1 Hz, 1 H), 3.53 (dd, J = 17.8, 5.0 Hz, 1 H).

^{13}C NMR (101 MHz, $CDCl_3$): δ = 196.6, 194.2, 140.9, 137.6, 135.9, 134.7, 134.4, 134.1, 130.7, 129.1 (2 C), 129.0 (2 C), 128.6 (2 C), 128.3 (2 C), 123.3, 121.6, 118.2, 116.2, 104.3, 55.9, 40.7.

HRMS (ESI): m/z [M + H]$^+$ calcd for $C_{43}H_{19}N_2O_4$: 399.1339; found: 399.1347.

(*S*)-1-(4-Oxo-4-phenylbutan-2-yl)-1*H*-indole-3-carbonitrile (3)

Title compound **3** was obtained according to the general procedure from 3-cyanoindole (**1**; 14.2 mg, 0.1 mmol) and (*E*)-1-phenylbut-2-en-1-one (**2**; 30.9 mg, 0.21 mmol). The product was isolated by direct column chromatography (silica gel; 5–25% EtOAc–PE).

Yield: 27.4 mg (95%); white solid; mp 59–61 °C; 42% ee [HPLC (Daicel Chiralpak OJ-H, hexane–^{i}PrOH, 80:20, flow rate 1.0 mL/min, T = 25 °C, λ = 254 nm): t_R = 41.7 (major), t_R = 46.2 (minor)]; $[\alpha]_D^{20}$ –19.6 (*c* 0.033, $CHCl_3$); R_f = 0.4 (PE–EtOAc, 3:1).

IR (KBr): 3121, 2217, 1685, 1597, 1580, 1530, 1461, 1449, 1361, 1288, 1214, 1184, 744, 689 cm^{-1}.

^{1}H NMR (400 MHz, $CDCl_3$): δ = 7.92–7.86 (m, 2 H), 7.79–7.71 (m, 2 H), 7.63–7.51 (m, 2 H), 7.49–7.40 (m, 2 H), 7.39–7.26 (m, 2 H), 5.39–5.26 (m, 1 H), 3.58 (dd, J = 17.4, 5.4 Hz, 1 H), 3.47 (dd, J = 17.4, 7.6 Hz, 1 H), 1.71 (d, J = 6.8 Hz, 3 H).

^{13}C NMR (101 MHz, $CDCl_3$): δ = 196.4, 136.3, 135.0, 134.0, 132.0, 129.0 (2 C), 128.11 (2 C), 128.06, 124.0, 122.4, 120.2, 116.0, 111.0, 86.6, 48.8, 45.2, 21.0.

HRMS (ESI): m/z [M + H]$^+$ calcd for $C_{19}H_{17}N_2O$: 289.1335; found: 289.1325.

Funding Information

The authors thank the Estonian Ministry of Education and Research (grant nos. IUT 19-32, IUT 19-9, IUT 20-14, PRG399, and PUT 1468) and the Centre of Excellence in Molecular Cell Engineering (2014-2020.4.01.15-0013) for financial support. This work has been partially supported by ASTRA 'TUT Institutional Development Programme for 2016-2022' Graduate School of Functional Materials and Technologies (2014-2020.4.01.16-0032).

Acknowledgment

The authors thank Dr Marina Kudrjashova for her assistance in NMR studies and Dr Aleksander-Mati Müürisepp for IR spectra.

Supporting Information

Supporting information for this article is available online at https://doi.org/10.1055/s-0039-1690751.

References

(1) For a recent review, see: Ciulla, M. G.; Kumar, K. *Tetrahedron Lett.* **2018**, *59*, 3223.
(2) Taylor, R. D.; MacCoss, M.; Lawson, A. D. G. *J. Med. Chem.* **2014**, *57*, 5845.
(3) For reviews of pharmaceutically active indole derivatives, see: (a) Kochanowska-Karamyan, A. J.; Hamann, M. T. *Chem. Rev.* **2010**, *110*, 4489. (b) Sravanthi, T. V.; Manju, S. L. *Eur. J. Pharm. Sci.* **2016**, *91*, 1. (c) Singh, T. P.; Singh, O. M. *Mini-Rev. Med. Chem.* **2018**, *18*, 9.
(4) For reviews, see: (a) Bandini, M.; Eichholzer, A. *Angew. Chem. Int. Ed.* **2009**, *48*, 9608. (b) Dalpozzo, R. *Chem. Soc. Rev.* **2015**, *44*, 742. (c) Chen, J.-B.; Jia, Y.-X. *Org. Biomol. Chem.* **2017**, *15*, 3550.
(5) (a) Fan, Y.; Kass, S. R. *J. Org. Chem.* **2017**, *82*, 13288. (b) Liu, L.; Ma, H.; Xiao, Y.; Du, F.; Qin, Z.; Li, N.; Fu, B. *Chem. Commun.* **2012**, *48*, 9281. (c) Wu, K.; Jiang, Y.-J.; Fan, Y.-S.; Sha, D.; Zhang, S. *Chem. Eur. J.* **2013**, *19*, 474.
(6) (a) Zhou, Y.; Li, C.; Yuan, X.; Zhang, F.; Liu, X.; Liu, P. *Org. Biomol. Chem.* **2019**, *17*, 3343. (b) Chaudhary, B.; Diwaker, M.; Sharma, S. *Org. Chem. Front.* **2018**, *5*, 3133. (c) Sandtorv, A. H. *Adv. Synth. Catal.* **2015**, *357*, 2403.
(7) (a) Trost, B. M.; Osipov, M.; Dong, G. *J. Am. Chem. Soc.* **2010**, *132*, 15800. (b) Sevov, C. S.; Zhou, J. S.; Hartwig, J. F. *J. Am. Chem. Soc.* **2014**, *136*, 3200. (c) Trost, B. M.; Gnanamani, E.; Hung, C.-I. *Angew. Chem. Int. Ed.* **2017**, *56*, 10451. (d) Ye, Y.; Kim, S.-T.; Jeong, J.; Baik, M.-H.; Buchwald, S. L. *J. Am. Chem. Soc.* **2019**, *141*, 3901.
(8) (a) Zhang, L.; Wu, B.; Chen, Z.; Hu, J.; Zeng, X.; Zhong, G. *Chem. Commun.* **2018**, *54*, 9230. (b) Cai, Y.; Gu, Q.; You, S.-L. *Org. Biomol. Chem.* **2018**, *16*, 6146. (c) Chen, M.; Sun, J. *Angew. Chem. Int. Ed.* **2017**, *56*, 4583. (d) Cai, Q.; Zheng, C.; You, S.-L. *Angew. Chem. Int. Ed.* **2010**, *49*, 8666.
(9) (a) Bandini, M.; Eichholzer, A.; Tragni, M.; Umani-Ronchi, A. *Angew. Chem. Int. Ed.* **2008**, *47*, 3238. (b) Bandini, M.; Bottoni, A.; Eichholzer, A.; Miscione, G. P.; Stenta, M. *Chem. Eur. J.* **2010**, *16*, 12462.
(10) Hong, L.; Sun, W.; Liu, C.; Wang, L.; Wang, R. *Chem. Eur. J.* **2010**, *16*, 440.
(11) For our previous articles on aza-Michael reactions, see: (a) Žari, S.; Kudrjashova, M.; Pehk, T.; Lopp, M.; Kanger, T. *Org. Lett.* **2014**, *16*, 1740. (b) Metsala, A.; Žari, S.; Kanger, T. *ChemCatChem* **2016**, *8*, 2961. (c) Žari, S.; Metsala, A.; Kudrjashova, M.; Kaabel, S.; Järving, I.; Kanger, T. *Synthesis* **2015**, *47*, 875. (d) Kriis, K.; Melnik, T.; Lips, K.; Juhanson, I.; Kaabel, S.; Järving, I.; Kanger, T. *Synthesis* **2017**, *49*, 604.
(12) Yang, J.; Li, T.; Zhou, H.; Li, N.; Xie, D.; Li, Z. *Synlett* **2017**, *28*, 1227.
(13) For PTC with hydrogen bond donors, see: Wang, H. *Catalysts* **2019**, *9*, doi: 10.3390/catal9030244.
(14) Gomez-Bengoa, E.; Linden, A.; López, R.; Múgica-Mendiola, I.; Oiarbide, M.; Palomo, C. *J. Am. Chem. Soc.* **2008**, *130*, 7955.
(15) Kütt, A.; Leito, I.; Kaljurand, I.; Sooväli, L.; Vlasov, V. M.; Yagupolskii, L. M.; Koppel, I. A. *J. Org. Chem.* **2006**, *71*, 2829.
(16) Raamat, E.; Kaupmees, K.; Ovsjannikov, G.; Trummal, A.; Kütt, A.; Saame, J.; Koppel, I.; Kaljurand, I.; Lipping, L.; Rodima, T.; Pihl, V.; Koppel, I. A.; Leito, I. *J. Phys. Org. Chem.* **2013**, *26*, 162.
(17) Sasson, Y.; Bilman, N. *J. Chem. Soc., Perkin Trans. 2* **1989**, 2029.
(18) Denmark, S. E.; Weintraub, R. C. *Heterocycles* **2011**, *82*, 1527.
(19) Nicolaou, K. C.; Liu, G.; Beabout, K.; McCurry, M. D.; Shamoo, Y. *J. Am. Chem. Soc.* **2017**, *139*, 3736.
(20) Bernal, P.; Fernández, R.; Lassaletta, J. M. *Chem. Eur. J.* **2010**, *16*, 7714.

(21) Wang, X.; Lv, J.; Liu, L.; Wang, Y.; Wu, Y. *J. Mol. Catal. A: Chem.* **2007**, *276*, 102.
(22) He, Z.; Yang, X.; Jiang, W. *Org. Lett.* **2015**, *17*, 3880.
(23) Reitel, K.; Kriis, K.; Järving, I.; Kanger, T. *Chem. Heterocycl. Compd.* **2018**, *54*, 929.
(24) Pelkey, E. T.; Gribble, G. W. *Tetrahedron Lett.* **1997**, *38*, 5603.
(25) Cheng, Q.; Zhang, F.; Guo, Y.-L.; You, S.-L. *Angew. Chem. Int. Ed.* **2018**, *57*, 2134.
(26) (a) Therkelsen, F. D.; Hansen, A.-L.; Pedersen, E. B.; Nielsen, C. *Org. Biomol. Chem.* **2003**, *1*, 2908. (b) Chen, S.-j.; Lu, P.-G.; Cai, C. *RSC Adv.* **2015**, *5*, 13208.
(27) Oare, D. A.; Henderson, M. A.; Sanner, M. A.; Heathcock, C. H. *J. Org. Chem.* **1990**, *55*, 132.
(28) Manjolinho, F.; Grünberg, M. F.; Rodríguez, N.; Gooßen, L. J. *Eur. J. Org. Chem.* **2012**, 4680.
(29) Khopade, T. M.; Warghude, P. K.; Mete, T. B.; Bhat, R. G. *Tetrahedron Lett.* **2019**, *60*, 197.
(30) Liu, D.-N.; Tian, S.-K. *Chem. Eur. J.* **2009**, *15*, 4538.
(31) Berti, F.; Bincoletto, S.; Donati, I.; Fontanive, G.; Fregonesea, M.; Benedetti, F. *Org. Biomol. Chem.* **2011**, *9*, 1987.
(32) Al-Masum, M.; Liu, K.-Y. *Tetrahedron Lett.* **2011**, *52*, 5090.
(33) Pan, G.-F.; Zhu, X.-Q.; Guo, R.-L.; Gao, Y.-R.; Wang, Y.-Q. *Adv. Synth. Catal.* **2018**, *360*, 4774.
(34) Bentley, S. C.; Davies, S. G.; Lee, J. A.; Roberts, P. M.; Thomson, J. E. *Org. Lett.* **2011**, *13*, 2544.

Appendix 3

Publication III

Kaasik, M.; Martõnova, J.; Erkman, K.; Metsala, A.; Järving, I.; Kanger, T. (2021). Enantioselective Michael addition to vinyl phosphonates via hydrogen bond-enhanced halogen bond catalysis. *Chemical Science*, 21, 7561−7568. DOI: 10.1039/D1SC01029H

Chemical Science

ROYAL SOCIETY OF CHEMISTRY

EDGE ARTICLE

View Article Online
View Journal | View Issue

Cite this: *Chem. Sci.*, 2021, **12**, 7561

All publication charges for this article have been paid for by the Royal Society of Chemistry

Received 22nd February 2021
Accepted 24th April 2021

DOI: 10.1039/d1sc01029h

rsc.li/chemical-science

Enantioselective Michael addition to vinyl phosphonates *via* hydrogen bond-enhanced halogen bond catalysis†

Mikk Kaasik, Jevgenija Martõnova, Kristin Erkman, Andrus Metsala, Ivar Järving and Tõnis Kanger *

An asymmetric Michael addition of malononitrile to vinyl phosphonates was accomplished by hydrogen bond-enhanced bifunctional halogen bond (XB) catalysis. NMR titration experiments were used to demonstrate that halogen bonding, with the support of hydrogen-bonding, played a key role in the activation of the Michael acceptors through the phosphonate group. This is the first example of the use of XBs for the activation of organophosphorus compounds in synthesis. In addition, the iodo-perfluorophenyl group proved to be a better directing unit than different iodo- and nitro-substituted phenyl groups. The developed approach afforded products with up to excellent yields and diastereoselectivities and up to good enantioselectivities.

Introduction

Halogen bonds (XBs), noncovalent interactions between electrophilic halogen atoms and Lewis bases,[1] are exploited in areas ranging from crystal engineering to catalysis.[2] The use of XBs in catalysis was first implemented by C. Bolm in 2008 for the reduction of quinolines.[3] Since then several studies have demonstrated the viability of XBs to achieve catalysis.[4] Notably, XBs have been used for the activation of imines in Mannich[5] and aza-Diels–Alder reactions,[6] for the activation of haloalkanes in halogen abstraction reactions,[7] and for the activation of carbonyl compounds in Diels–Alder,[8] Michael[9] and Nazarov reactions.[10] In addition, XBs have been used to activate other substrate classes, such as silyl halides,[11] thioamides[12] and the π-system of indoles.[13] Yet there are no examples of the activation of phosphorus compounds by XBs. This is surprising as XBs to phosphine oxides, phosphonates and phosphates have received attention in several solution studies.[14] Thus, organophosphorus compounds should be suitable substrates for XB catalysis.

Phosphorus compounds are an important class of molecules in organic synthesis both as valuable reagents and end targets.[15] More specifically, (chiral) organophosphonates and their phosphonic acid derivatives can be used in the much-acclaimed Horner–Wadsworth–Emmons reaction[16] and are also valuable biomolecules.[17] Therefore, the asymmetric synthesis of organophosphonates has received significant attention over the years.[18] In several instances this has been successfully achieved through the use of well-developed asymmetric hydrogen-bond catalysis, which can be compared to the less explored XB catalysis. The two major advantages of XBs compared to HBs are their high directionality,[19] due to the formation of the XB at the elongation of the covalent bond to the halogen atom, and their high degree of variability. Namely, there is a choice among XB donor atoms, which can be ranked by the increase in their donor ability in the order of Cl < Br < I, corresponding to the increase in the polarisability of the halogen atom.[20] Although several examples can be found for the use of XBs in asymmetric synthesis, the deliberate use of XBs for catalytic purposes is still in its infancy.[4e] Notably, in 2018 the Arai group used a bifunctional alkaloid-based XB catalyst to carry out an asymmetric Mannich reaction,[5a] in 2020 the Huber group carried out the first solely XB-catalysed asymmetric reaction using the Mukaiyama-aldol reaction as a model[21] and in 2021 the Mancheño group demonstrated that a neutral tetrakis-iodo-triazole can be used as an asymmetric XB catalyst in the Reissert-type dearomatization of quinolone.[22]

We envisioned that the bifunctional alkaloid-based XB catalyst could be used to activate vinyl phosphonates in a Michael reaction with a nucleophile. Achieving this would both expand the chemical space of asymmetric XB catalysis and that of optically active phosphorus chemistry. We were also curious to see what influence the modification of the electronic properties and substitution pattern of the XB donor motif of the catalyst would have on the outcome of the reaction. So far, perfluorinated[3,5,7b] and azolium-type[6a,7d,8a,13,21] XB donor fragments have commonly been used in XB catalysts.

Department of Chemistry and Biotechnology, Tallinn University of Technology, Akadeemia tee 15, 12618 Tallinn, Estonia. E-mail: tonis.kanger@taltech.ee

† Electronic supplementary information (ESI) available: Solvent screening, experimental procedures, titration experiments, computational information, crystallographic information, and copies of NMR spectra and HPLC chromatograms. CCDC 2063122. For ESI and crystallographic data in CIF or other electronic format see DOI: 10.1039/d1sc01029h

Results and discussion

Initial experiments involving vinyl phosphonate **1a** and malononitrile **2** (Scheme 1) revealed that no reaction occurred in two days at RT in DCM (Table 1, entry 1). Gratifyingly, alkaloid-based XB catalysts facilitated the reaction, resulting in the formation of enantioenriched product **3a**. Quinidine- and dihydroquinine-derived catalysts **A** and **B** provided product **3a** in similar quantities and enantioenrichment levels (Table 1, entries 2 and 3). As expected, the enantioselectivity was opposite, because the catalysts were derived from pseudo-enantiomeric alkaloids (although in addition to this difference, the vinyl group connected to the quinuclidine fragment had been reduced in catalyst **B**). It was also observed that a side reaction resulting in compounds **4a** and **5** took place that reduced the yield of the product. To hinder this, catalyst loading was dropped to 10 mol% for the following experiments. In addition, 1,3,5-trimethoxybenzene ($(MeO)_3C_6H_3$) was used as a quantitative internal standard to determine the distribution of starting materials and products in the reaction mixture by ^{1}H NMR spectroscopy. Cinchonidine-derived catalyst **C** performed much more sluggishly compared to catalysts **B**, providing product **3a** in lower conversion and enantioselectivity (Table 1, compare entries 4 and 5). In all cases, similar levels of moderate diastereoselectivity were observed. It was decided to continue with dihydroquinine-derived catalyst **B** due to its superiority in enhancing the rate of the reaction compared to **A**.

Next, an extensive solvent screening was conducted (for full details, see the ESI†), which revealed that the reaction performed well in apolar aprotic solvents, as would be expected of noncovalent catalysis. While the solvent influenced the reactivity and enantioselectivity significantly, the diastereoselectivity was not greatly affected. For further optimisation experiments, toluene was chosen as the solvent (Table 2, entry 1). During the last stage of optimisation, other reaction conditions were varied. The reaction slowed down when run under more diluted conditions (Table 2, entry 2). Gratifyingly this also resulted in an increase in enantioselectivity. The reduction of catalyst loading under the diluted conditions had little effect on the enantioselectivity, yet resulted in a slower reaction (Table 2, entries 3 and 4). An increase of the temperature to 40 °C with a catalyst loading of 5 mol% resulted in full conversion within 2 days; however it also resulted in the increase of the retro-Michael process and did not have a positive influence on enantioselectivity (Table 2, entry 5). A decrease in temperature helped to somewhat improve the enantioselectivity at the expense of conversion (Table 2, entries 6 and 8). However, the retro-Michael process was significantly hindered at lower temperatures. As a compromise, the reaction was run at 0 °C, with 10 mol% catalyst loading and at a concentration of 0.2 M to hinder product decomposition (Table 2, entry 7). The product was formed in excellent NMR yield, with moderate

Table 1 Initial results of the Michael reaction[a]

Entry	Catalyst	Time (h)	NMR yield of **3a**[b] (%)	d.r.[c]	ee[d] (%)
1	—	48	NR	ND	ND
2	**A**	48	89	85 : 15	−39/−40
3	**B**	22	84	87 : 13	40/43
4	**C**[e]	24	48	77 : 23	26/28
5	**B**[e]	24	86	85 : 15	45/46

[a] Unless otherwise noted, all reactions were carried out with 0.1 mmol of **1a**, 0.2 mmol of **2**, and 0.02 mmol of catalyst in 0.2 mL of DCM at RT; NR – no reaction, ND – not determined. [b] Relative amount of **3a** compared to the total amount of **1a**, **3a** and **5**; determined from the reaction mixture by ^{1}H NMR spectroscopy. [c] Determined from the reaction mixture by ^{1}H NMR spectroscopy. [d] Determined by HPLC analysis on a chiral stationary phase. [e] 10 mol% of catalyst instead of 20 mol% and $(MeO)_3C_6H_3$ was used as an internal standard.

Table 2 Optimisation of the reaction conditions[a]

Entry	T (°C)	C (M)	**B** (mol%)	Time (h)	Conv.[b] (%)	**5**[c] (%)	ee[d] (%)
1	RT	0.5	10	16	100	20	64/66
2	RT	0.1	10	39	87	7	76/77
3	RT	0.1	7.5	48	94	10	76/76
4	RT	0.1	5	48	76	5	79/76
5	40	0.1	5	48	100	25	76/73
6	0	0.1	10	48	81	0	79/81
7	0	0.2	10	48	97	2	76/76
8	−20	0.2	10	72	86	0	79/78

[a] Unless otherwise noted, all reactions were carried out with 0.1 mmol of **1a**, 0.2 mmol of **2**, and 0.05 mmol of $(MeO)_3C_6H_3$ in toluene; d.r. was determined from the reaction mixture by ^{1}H NMR spectroscopy and varied between 81 : 19 to 87 : 13; for full details see the ESI. [b] Conversion depicts the amount of reacted **1a** based on ^{1}H qNMR measurements using $(MeO)_3C_6H_3$ as an internal standard. Generally, the total amount of the formed **3a** and retro-Michael product **5** corresponded to the amount of **1a** depleted. [c] Describes the extent of product decomposition through the retro-Michael reaction determined by ^{1}H qNMR, using the methylene proton signal of triethyl phosphonoacetate **5**. [d] Determined by HPLC analysis on a chiral stationary phase.

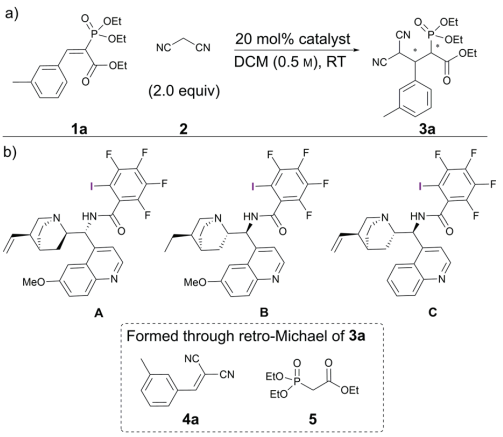

Scheme 1 (a) Catalytic Michael reaction under study; (b) screened catalysts and decomposition products of **3a**.

diastereoselectivity and acceptable enantioselectivities for both enantiomers. These conditions were then designated as optimal.

Throughout the studies, we were interested in changing the XB donor fragment of the catalyst. Usually, perfluorinated haloalkyl or -aryl groups are used for this purpose in neutral XB donors, which somewhat limits catalyst design. Yet, there are several other electron-withdrawing groups that can significantly increase the magnitude of the σ-hole on the halogen atom. To explore this, we synthesised catalysts **D–F** using benzoic acids with different iodo- and nitro-substitution patterns (Fig. 1). This would have also permitted us to explore the importance of the position of the iodine atom relative to the linker substituent. As references, the non-halogenated analogues **G–J** were also synthesised (Fig. 1). During the initial studies in DCM and under the optimised conditions in toluene, catalyst **B** always performed significantly better than its non-halogenated analogue **G**, in terms of both reactivity and selectivity (Fig. 1). These results demonstrate the positive effect of the iodine atom on catalyst activity and support XB involvement in the catalytic process. In contrast, catalysts **D–F**, containing nitro-substituted XB donor motifs, did not altogether demonstrate better performance compared to their non-halogenated analogues (Fig. 1, catalysts **H**, **I** and **J**). Moreover, all of the nitro-substituted catalysts were inferior to catalyst **B** in terms of enantioinduction, although some demonstrated better performance in terms of catalytic activity. Generally, the iodinated and non-halogenated catalysts resulted in products with similar diastereoselectivities, which overall varied between 79 : 21 and 89 : 11. Unfortunately, it was also not apparent whether the 1,2- or the 1,3- substitution pattern between the iodine atom and the linker site was more beneficial for enantioinduction and catalytic activity. It can be reasoned that the steric influence of iodine in catalyst **B** results in higher levels of enantioselectivity. Catalysts **D**, **E** and **I** also contain a bulky substituent in the same position, yet these catalysts led to significantly lower levels of product enantioselectivity. Therefore, the steric influence of the large iodine atom alone cannot be used to explain the levels of enantioselectivity obtained with **B**. On the other hand, if as initially proposed the iodine acted as a directing group, then the XB donor ability of the iodine atom could provide an answer. Therefore, molecular electrostatic potentials were calculated (CAM-B3LYP functional,[23] DEF2TZVP basis set,[24] with the Gaussian 09 program,[25] solvent effects with PCM[26]) for the catalysts to determine the magnitude of the σ-hole on the iodine atom (Fig. 1a). The substitution pattern influenced the magnitude of the σ-hole considerably. In addition, the XB donor ability (represented by the σ-hole value) of these compounds seems to be dependent on the environment as catalyst **B** had the largest σ-hole in DCM, while catalyst **F** had the largest σ-hole in a vacuum. Unfortunately, no clear correlation between product selectivity and the XB donor ability of the catalyst can be drawn, although the calculations support the fact that catalyst **B** was the best XB donor in DCM.

Next, the scope and limitations of the method were explored under the optimised conditions. Aromatic substituents containing electron-withdrawing and electron-donating substituents were tolerated (Scheme 2, compare **3c** and **3d**), as well as variations in the position of different substituents either in the *ortho*, *meta* or *para* position (Scheme 2, compare **3e**, **3f** and **3g** to **3b**). The reaction could be carried out with halogenated (**3e–h**), sterically demanding naphthyl (**3k**), heteroaromatic (**3j**) and polyconjugated substrates (**3l**). It should be noted that the substitution pattern greatly affected the speed of the reaction.

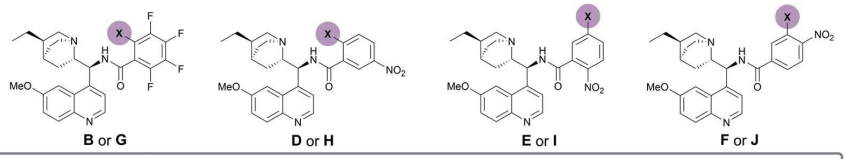

a) DCM (0.5 M), 20 mol% catalyst, RT[a]

	B, X = I[b]	G, X = H[b]	D, X = I[b]	H, X = H[b]	E, X = I[b]	I, X = H[b]	F, X = I[c]	J, X = H[c]
Time	22 h	32 h	23 h	8 h	7 h	8 h	24 h	24 h[d]
NMR yield of **3a**[d]	88%	72%	78%	72%	84%	80%	81%	84%
ee[e]	40%/43%	10%/11%	12%/14%	20%/25%	22%/26%	14%/20%	21%/25%	18%/23%
σ-hole[f]								
DCM	0.0501		0.0438		0.0500		0.0391	
vacuum	0.0450		0.0411		0.0448		0.0464	

b) toluene (0.2 M), 10 mol% catalyst, 0 °C[a]

	B, X = I	G, X = H	D, X = I	H, X = H	E, X = I	I, X = H	F, X = I	J, X = H
Time	48 h	48 h	48 h	45 h	42 h	18 h	42 h	41 h
NMR yield of **3a**[d]	95%	62%	87%	82%	92%	89%	86%	88%
ee[e]	76%/76%	40%/39%	40%/40%	31%/32%	43%/43%	40%/43%	41%/41%	40%/39%

[a] Unless otherwise noted, the reactions were carried out with 0.1 mmol of **1a**, 0.2 mmol of **2** and 0.05 mmol of $(MeO)_3C_6H_3$ with a catalyst in the stated solvent at the stated temperature. [b] $(MeO)_3C_6H_3$ not added initially, but prior to the end of the reaction. [c] 10 mol% of catalyst instead of 20 mol%. [d] NMR yield of **3a** based on ^{1}H qNMR measurements using $(MeO)_3C_6H_3$ as an internal standard. [e] Determined by HPLC analysis on a chiral stationary phase. [f] Energy values given in atomic units.

Fig. 1 Comparison of different XB/HB catalysts in (a) DCM and (b) toluene.

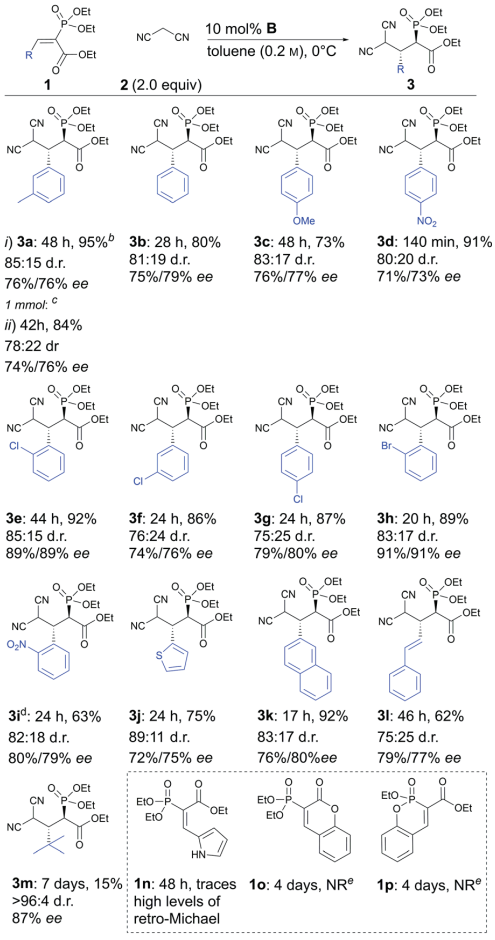

[a] Unless otherwise noted, all reactions were carried out with 0.2 mmol of **1**, 0.4 mmol of **2** and 0.02 mmol of **B** in 1.0 mL of toluene at 0 °C, yields refer to isolated **3**, d.r. was determined from the reaction mixture by ^{1}H NMR and *ee* determined by HPLC analysis on a chiral stationary phase; the depicted configuration describes the relative configuration of substituents for the major diastereoisomer and was deduced from the absolute configuration of the major enantiomer of the the minor diastereoisomer of **3d**, assigned by single-crystal X-ray diffraction analysis, for further details see ESI; [b] 0.1 mmol scale, see Table 2, entry 7; [c] carried out on a 1 mmol scale, *T* varied between 0–4 °C; [d] carried out on a 0.1 mmol scale; [e] At 50 °C, no reaction.

Scheme 2 Scope of the enantioselective Michael reaction.

For example, the reaction was complete within hours in the case of compound **3d**, while two days were needed to obtain products **3a**, **3c** and **3e**, with sterically more demanding or electron-donating substituents. In addition, *tert*-butyl-substituted substrate **1m** reacted very sluggishly, although the product was obtained in excellent diastereoselectivity and good enantioselectivity. The method was also successfully used on a 1 mmol scale (**3a**). Unfortunately, in all cases product decomposition through a retro-Michael reaction was observed despite the lower temperature. This resulted in somewhat lower yields for the products. All in all, the products were obtained in low to excellent yields (15% to 92%) and diastereoselectivities (75 : 25 to >96 : 4 d.r.) and moderate to good enantioselectivities (71% to 91% ee). It seems that *ortho*-substituents in the aromatic ring of **1** have a beneficial effect on enantioselectivity (products **3e**, **3h** and **3i**). We also observed that substrates with a *Z*-configuration of the double bond were not compatible with this catalytic system. These substrates reacted very sluggishly, leading to racemic or near racemic products, although the diastereomeric preference (with similar d.r. levels) was the same as for the corresponding *E*-isomers (for details, see the ESI†).‡ In the case of the pyrrole-containing compound **1n**, trace amounts of product were observed, along with significant levels of the retro-Michael product. This indicates that compound **1n** was less reactive than the other substrates and, at the same time, the corresponding Michael product **3n** was even more labile than the other products. Unfortunately, cyclic phosphonates **1o** and **1p** did not react even under elevated temperatures. The increased stability of **1o** and **1p** might have been caused by the existence of aromatic resonance structures.

Next, some control experiments were conducted. To ascertain the possible cause of product **3** decomposition, product **3a** and catalyst **B** were stirred at RT in toluene for seven days. It was observed that compound **3a** decomposed, resulting in the formation of retro-Michael products **4a** and **5**. Interestingly, at first the minor diastereoisomer was consumed to a greater extent than the major diastereoisomer, leading to an increase in the diastereomeric ratio. Fortunately, no racemisation took place; in contrast, a slight increase in the enantioenrichment of both enantiomers (see Fig. S3 in the ESI† for details) was observed. This confirmed that the catalyst brought about the decomposition of **3a**, which is otherwise relatively stable.§ Then experiments were conducted to explore the influence of the carbonyl and phosphonate groups on the reaction. A sluggish reaction took place with substrate **6**, in which the phosphonate group was exchanged for an ethoxycarbonyl group (Scheme 3a). In two days, 50% conversion was obtained, although by NMR only 25% of product **7** had formed, along with 25% of the corresponding retro-Michael products. The stereoselectivity of the reaction was also poor: only 19% ee. This example highlights the importance of the phosphonate group both for reactivity and selectivity (Scheme 3, compare (a) and (c)). The result was also expected, as an ethoxycarbonyl group should be a weaker XB acceptor than a phosphonate group. Unfortunately, compound **8** in which the ethoxycarbonyl group had been omitted did not react with malononitrile under the optimal conditions (Scheme 3b). The presence of the electron-withdrawing ethoxycarbonyl group must therefore have been critical for reactivity.[27]

In addition, control experiments were conducted with catalyst analogues (**G**, **K**, **L** and **M**, Scheme 3c). As with substrate **1a**, the hydrogen analogue of catalyst **B** (catalyst **G**) also performed sluggishly with substrate **1b**. Pentafluorophenyl substituted catalyst **K** was as active as catalyst **B**, but caused the formation of the product with diminished diastereoselectivity and enantioselectivity. These results again demonstrate the importance of

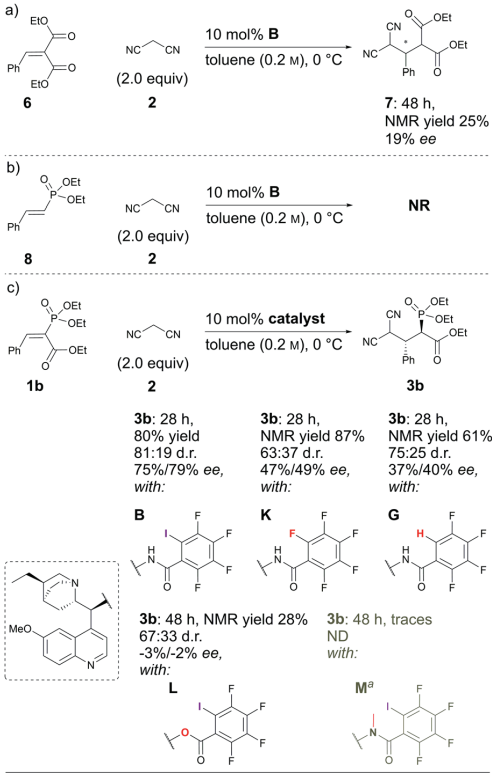

[a] **M** was not used as a single compound, but as a mixture of conformational isomers.

Scheme 3 Comparative experiments using (a) **6**, (b) **8** and (c) **1b** as Michael acceptors with different catalysts.

Table 3 Association constants for XB donor and Michael reaction substrate pairs

Entry	XB acceptor	XB donor	K_{obs}[a] (M^{-1})
1	**1b**	**9**	9.4
2	**1b**	**10**	2.5
3	**1b**	**11**	0.5
4	**1b**	**12**	0.4
5	**1b**	**13**	12.6
6[b]	**1b**	**B**	3.4
7	**6**	**9**	1.3
8	**8**	**9**	14.0

[a] The K_{obs} was measured in toluene-d8 and determined by fitting the ^{1}H NMR titration data of the *N*- or *O*-methyl protons to the 1 : 1 binding isotherm of BindFit.[28] The given K_{obs} is the calculated approximate mean value of two parallel experiments; in all cases the estimated standard errors fall below 10%. Full details are given in the ESI. [b] Determined by fitting the ^{19}F NMR titration data of the fluorine atom *ortho* to the iodine atom to the 1 : 1 binding isotherm of BindFit.

the iodine atom. Next, catalyst analogues were used in which the amidic hydrogen atom was omitted. Unfortunately, the *N*-methylated analogue **M** could not be isolated as a single compound and as a result the corresponding ester **L** was also synthesised. In both instances, the catalysts demonstrated poor catalytic activity and no enantioinduction. Therefore, the amidic hydrogen atom was also a critical design element of the catalyst.

To probe the participation of XBs in the reaction, ^{1}H NMR titration experiments in toluene-d8 were carried out between the substrates of the reaction and catalyst analogues **9** to **13** of the XB donor motif (Table 3). In these achiral analogues the alkaloid moiety was omitted, although a possible hydrogen bond donor site in amides **9**, **10** and **13** was still present. Compounds **1b** and **9** formed complex [**1b–9**], with an association constant value of $K_{obs} = 9.4\ M^{-1}$ (Table 3, entry 1), which was in the expected range based on the literature.[14a] Surprisingly, the non-halogenated analogue **10** also formed a relatively strong complex with compound **1b** (Table 3, entry 2), yet the corresponding association constant of $K_{obs} = 2.5\ M^{-1}$ is about four times smaller. When the amidic hydrogen atom was omitted from the analogue, the interaction was more than an order of magnitude weaker for analogues **11** and **12** (Table 3, compare entries 1, 3 and 4). Based on the control experiments, association constant values of $K_{obs} = 0.5\ M^{-1}$ and $K_{obs} = 0.4\ M^{-1}$ do not correspond to a sufficiently strong XB with the substrate to achieve a significant interaction with the substrate. Analogue **13** interacted strongly with substrate **1b**, which most likely was due to hydrogen-bonding between the two and reflects the increase of acidity of the amidic hydrogen atom in **13** by the perfluorophenyl group (Table 3, entry 5). Titration experiments were also carried out between catalyst **B** and compound **1b**. The association constant values of $K_{obs} = 3.4\ M^{-1}$ signifies a favourable interaction between the two (Table 3, entry 6). In this instance, the change in the chemical shift of the fluorine atom *ortho* to the iodine atom was used as input for the calculation of the association constant value. The observed upfield shift upon the formation of complex [**1b–B**] is indicative of halogen bonding.[29]

Malonic ester-derived compound **6** and phosphonate **8** also formed complexes with XB donor **9**. The association constant corresponding to complex [**8–9**] (Table 3, entry 8) was larger than that for the [**1b–9**] complex. On the other hand, the association constant corresponding to complex [**6–9**] (Table 3, entry 7) was almost an order of magnitude smaller than that for the [**1b–9**] complex. Thus, the phosphonate group should be the

primary interaction site in the substrates and not the carbonyl group. This is also supported by the fact that when ethyl acetate was used as a solvent the reaction was not significantly hindered, as 87% conversion was reached in 24 hours and the ee of the product was 55% (this should be compared to entry 1 in Table 2; for further details, see the ESI†). The increase in the strength of the observable association constant in the series [**6–9**] < [**1b–10**] < [**1b–9**] < [**1b–13**] also aligns with the increase in reactivity in the corresponding catalytic reactions (comparison of results with catalysts **B**, **G** and **K** and reactions with substrates **1b** and **6** in Scheme 3). The higher binding potential of the amide fragment also seems to correspond to increased levels of product enantioselectivity, although an iodine atom needs to be present for the best results. Therefore, the amide fragment acted as both a coordinating and an activating unit.

Based on these observations, we supposed that an XB is formed to substrate **1b** and the interaction is strengthened by the participation of a hydrogen bond, either directly with the substrate or through hydrogen-bond-assisted halogen bonding.[14b,30] In the latter case, the 1,3-substitution pattern between the iodine atom and the linker substituent would not be favourable for catalytic purposes, which could be one reason for the poor performance of catalysts **E** and **F** (Fig. 1). To evaluate the interaction between catalyst **B** and substrate **1a**, computations were performed (see the ESI† for details). These revealed that while an XB is formed to the oxygen atom of the phosphonate group, hydrogen-bonding to other acceptor sites in the substrate is not preferred. The calculated lowest energy conformers had an energy difference of 1.2 kcal mol^{-1} (Fig. 2). It was observed that a stronger HB from the amide group to the iodine atom also resulted in the shortening of the XB to the oxygen atom of the phosphonate group. NCI analysis also confirmed the presence of hydrogen-bonding to the iodine atom (see Fig. S2 in the ESI† for details).

With the obtained knowledge, we now propose a catalytic cycle similar to the one proposed by the Arai group to describe the XB catalytic Mannich reaction.[5] First, malononitrile **2** is deprotonated and activated by the base in catalyst **B** (Fig. 3). Electrophile **1** is activated through an XB formed between the iodine atom in catalyst **B** and the oxygen atom of the phosphonate group in **1** (Fig. 3, [**Y**]). A hydrogen bond from the amide group of the catalyst to the iodine atom would enhance the XB to the phosphonate group (Fig. 3, middle). Direct activation of the phosphonate by hydrogen-bonding is also plausible and cannot be ruled out with the current experimental

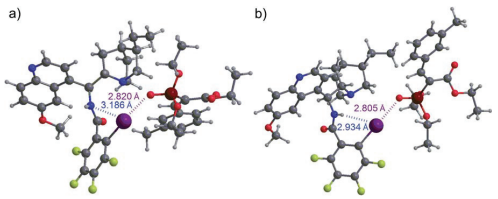

Fig. 2 XB formation from **B** to the oxygen atom of the phosphonate group of **1a**: (a) without HB enhancement and (b) with HB enhancement.

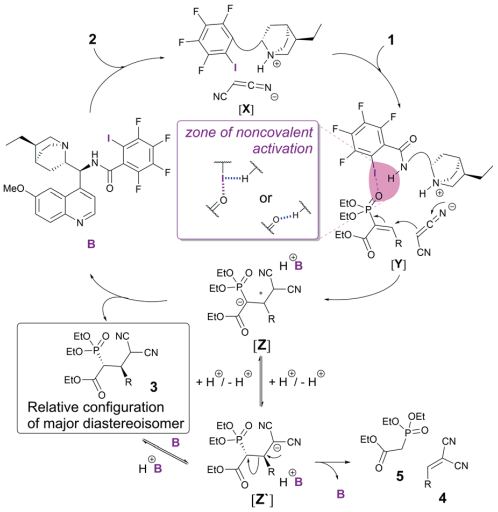

Fig. 3 Possible catalytic cycle for the enantioselective Michael reaction.

data. Next, a Michael reaction between **1** and **2** would result in the formation of intermediate [**Z**]. Protonation of this species leads to product **3**. This in turn could be deprotonated by the catalyst, which could lead to a retro-Michael reaction through [**Z′**]. Alternatively, it is possible that proton transfer in intermediate [**Z**] could also lead to intermediate [**Z′**], which in turn could be protonated to give product **3** or lead again to a retro-Michael reaction giving **4** and **5**.

Conclusions

A new asymmetric organocatalytic methodology was developed that utilises a hydrogen bond-enhanced bifunctional XB catalyst for the activation of vinyl phosphonates in a Michael reaction. This approach describes the first use of organophosphorus compounds as substrates in XB catalysis and furthermore expands the field of asymmetric XB catalysis. Comparative experiments with catalysts containing different XB donor units and their hydrogen-analogues confirmed the superiority of the iodoperfluoro group as an activating and enantioinducing unit. Furthermore, NMR titration experiments and computations demonstrated that this was primarily the result of halogen bonding, supported by hydrogen-bonding, with the phosphonate group.

Author contributions

MK conceived the project. MK, KE conducted the synthesis and analysis. JM performed crystal analysis, IJ massspectrometric analysis, AM theoretical calculations. All authors contributed to the discussion. MK and TK wrote the manuscript with contributions from all authors. TK supervised the project.

Conflicts of interest

There are no conflicts to declare.

Acknowledgements

This research was funded by the Estonian Ministry of Education and Research (grant no. PRG1031 and PRG399) and the Centre of Excellence in Molecular Cell Engineering (2014–2020.4.01.15-0013). We thank Dr Kadri Kriis for her help with the synthesis of catalyst **A**, Dr Aleksander-Mati Müürisepp for the IR spectra and Dr Marina Kudrjašova for the ^{19}F NMR measurements.

Notes and references

‡ However, it should be noted that the *Z*-isomers obtained were not as pure as the *E*-isomers.

§ The products were stable throughout purification by column chromatography on silica gel and subsequent solvent removal under reduced pressure. However, product decomposition was observed if left at temperatures above 50 °C for prolonged periods.

1 C. G. R. Desiraju, P. Shing Ho, L. Kloo, A. C. Legon, R. Marquardt, P. Metrangolo, P. Politzer, G. Resnati and K. Rissanen, *Pure Appl. Chem.*, 2013, **85**, 1711–1713.

2 For selected reviews, see: (*a*) L. C. Gilday, S. W. Robinson, T. A. Barendt, M. J. Langton, B. R. Mullaney and P. D. Beer, *Chem. Rev.*, 2015, **115**, 7118–7195; (*b*) G. Cavallo, P. Metrangolo, R. Milani, T. Pilati, A. Priimagi, G. Resnati and G. Terraneo, *Chem. Rev.*, 2016, **116**, 2478–2601; (*c*) H. Wang, W. Wang and W. J. Jin, *Chem. Rev.*, 2016, **116**, 5072–5104; (*d*) Á. M. Montaña, *ChemistrySelect*, 2017, **2**, 9094–9112; (*e*) *Halogen Bonding in Solution*, ed. S. Huber, Wiley, Weinheim, Germany, 2021.

3 A. Bruckmann, M. A. Pena and C. Bolm, *Synlett*, 2008, 900–902.

4 For recent reviews on the use of XBs in organocatalysis, see: (*a*) J. Bamberger, F. Ostler and O. G. Mancheño, *ChemCatChem*, 2019, **11**, 5198–5211; (*b*) R. L. Sutar and S. M. Huber, *ACS Catal.*, 2019, **9**, 9622–9639; (*c*) M. Breugst and J. J. Koenig, *Eur. J. Org. Chem.*, 2020, **2020**, 5473–5487; (*d*) H. Yang and M. W. Wong, *Molecules*, 2020, **25**, 1045; (*e*) M. Kaasik and T. Kanger, *Front. Chem.*, 2020, **8**, DOI: 10.3389/fchem.2020.599064.

5 (*a*) S. Kuwano, T. Suzuki, Y. Hosaka and T. Arai, *Chem. Commun.*, 2018, **54**, 3847–3850; (*b*) S. Kuwano, Y. Nishida, T. Suzuki and T. Arai, *Adv. Synth. Catal.*, 2020, **362**, 1674–1678.

6 (*a*) Y. Takeda, D. Hisakuni, C. H. Lin and S. Minakata, *Org. Lett.*, 2015, **17**, 318–321; (*b*) R. Haraguchi, S. Hoshino, M. Sakai, S. Tanazawa, Y. Morita, T. Komatsu and S. Fukuzawa, *Chem. Commun.*, 2018, **54**, 10320–10323; (*c*) M. Kaasik, A. Metsala, S. Kaabel, K. Kriis, I. Järving and T. Kanger, *J. Org. Chem.*, 2019, **84**, 4295–4303; (*d*) T. Suzuki, S. Kuwano and T. Arai, *Adv. Synth. Catal.*, 2020, **362**, 3208–3212.

7 (*a*) S. M. Walter, F. Kniep, E. Herdtweck and S. M. Huber, *Angew. Chem., Int. Ed.*, 2011, **50**, 7187–7191; (*b*) F. Kniep, S. H. Jungbauer, Q. Zhang, S. M. Walter, S. Schindler, I. Schnapperelle, E. Herdtweck and S. M. Huber, *Angew. Chem., Int. Ed.*, 2013, **52**, 7028–7032; (*c*) L. Zong, X. Ban, C. W. Kee and C. H. Tan, *Angew. Chem., Int. Ed.*, 2014, **53**, 11849–11853; (*d*) S. H. Jungbauer and S. M. Huber, *J. Am. Chem. Soc.*, 2015, **137**, 12110–12120.

8 (*a*) S. H. Jungbauer, S. M. Walter, S. Schindler, L. Rout, F. Kniep and S. M. Huber, *Chem. Commun.*, 2014, **50**, 6281–6284; (*b*) F. Heinen, E. Engelage, A. Dreger, R. Weiss and S. M. Huber, *Angew. Chem., Int. Ed.*, 2018, **57**, 3830–3833.

9 (*a*) D. Von Der Heiden, E. Detmar, R. Kuchta and M. Breugst, *Synlett*, 2018, **29**, 1307–1313; (*b*) J. P. Gliese, S. H. Jungbauer and S. M. Huber, *Chem. Commun.*, 2017, **53**, 12052–12055; (*c*) R. A. Squitieri, K. P. Fitzpatrick, A. A. Jaworski and K. A. Scheidt, *Chem.–Eur. J.*, 2019, **25**, 10069–10073; (*d*) H. Zhang and P. H. Toy, *Adv. Synth. Catal.*, 2021, **363**, 215–221.

10 (*a*) J. J. Koenig, T. Arndt, N. Gildemeister, J. M. Neudörfl and M. Breugst, *J. Org. Chem.*, 2019, **84**, 7587–7605; (*b*) A. Dreger, P. Wonner, E. Engelage, S. M. Walter, R. Stoll and S. M. Huber, *Chem. Commun.*, 2019, **55**, 8262–8265.

11 M. Saito, N. Tsuji, Y. Kobayashi and Y. Takemoto, *Org. Lett.*, 2015, **17**, 3000–3003.

12 A. Matsuzawa, S. Takeuchi and K. Sugita, *Chem.–Asian J.*, 2016, **11**, 2863–2866.

13 S. Kuwano, T. Suzuki, M. Yamanaka, R. Tsutsumi and T. Arai, *Angew. Chem., Int. Ed.*, 2019, **58**, 10220–10224.

14 (*a*) M. G. Sarwar, B. Dragisic, L. J. Salsberg, C. Gouliaras and M. S. Taylor, *J. Am. Chem. Soc.*, 2010, **132**, 1646–1653; (*b*) C. Laurence, J. Graton, M. Berthelot and M. J. El Ghomari, *Chem.–Eur. J.*, 2011, **17**, 10431–10444; (*c*) L. González, F. Zapata, A. Caballero, P. Molina, C. Ramírez De Arellano, I. Alkorta and J. Elguero, *Chem.–Eur. J.*, 2016, **22**, 7533–7544; (*d*) A. Borissov, J. Y. C. Lim, A. Brown, K. E. Christensen, A. L. Thompson, M. D. Smith and P. D. Beer, *Chem. Commun.*, 2017, **53**, 2483–2486; (*e*) A. S. Ostras, D. M. Ivanov, A. S. Novikov and P. M. Tolstoy, *Molecules*, 2020, **25**, 1406; (*f*) Y. P. Chang, T. Tang, J. R. Jagannathan, N. Hirbawi, S. Sun, J. Brown and A. K. Franz, *Org. Lett.*, 2020, **22**, 6647–6652.

15 For selected reviews, see: (*a*) M. Mikolajczyk and P. Balczewski, in *New Asp. Phosphorus Chem. II*, ed. J.-P. Majoral, Springer, Berlin, Heidelberg, 2003, pp. 161–214; (*b*) *Phosphorus Ligands in Asymmetric Catalysis*, ed. A. Börner, Wiley-VCH, Weinheim, 2008; (*c*) O. I. Kolodiazhnyi, V. P. Kukhar and A. O. Kolodiazhna, *Tetrahedron: Asymmetry*, 2014, **25**, 865–922; (*d*) W. W. Metcalf and W. A. Van Der Donk, *Annu. Rev. Biochem.*, 2009, **78**, 65–94; (*e*) R. Morodo, P. Bianchi and J. C. M. Monbaliu, *Eur. J. Org. Chem.*, 2020, **2020**, 5236–5277.

16 For selected reviews, see: (*a*) J. A. Bisceglia and L. R. Orelli, *Curr. Org. Chem.*, 2015, **19**, 744–775; (*b*) I. Janicki and P. Kiełbasiński, *Adv. Synth. Catal.*, 2020, **362**, 2552–2596.

17 For selected reviews, see: (*a*) R. Engel, *Chem. Rev.*, 1977, **77**, 349–367; (*b*) *Aminophosphonic and Aminophosphinic Acids: Chemistry and Biological Activity*, ed. V. P. Kukhar and H. R. Hudson, John Wiley & Sons, Chichester, 2000; (*c*) F. Orsini,

G. Sello and M. Sisti, *Curr. Med. Chem.*, 2010, **17**, 264–289; (*d*) K. M. Heidel and C. S. Dowd, *Future Med. Chem.*, 2019, **11**, 1625–1643.

18 For selected reviews, see: (*a*) L. Albrecht, A. Albrecht, H. Krawczyk and K. A. Jørgensen, *Chem.–Eur. J.*, 2010, **16**, 28–48; (*b*) D. Zhao and R. Wang, *Chem. Soc. Rev.*, 2012, **41**, 2095–2108; (*c*) M. Dzięgielewski, J. Pięta, E. Kamińska and Ł. Albrecht, *Eur. J. Org. Chem.*, 2015, **2015**, 677–702; (*d*) L. Chen, *Synthesis*, 2018, **50**, 440–469.

19 (*a*) K. Rissanen, *CrystEngComm*, 2008, **10**, 1107–1113; (*b*) P. Metrangolo, H. Neukirch, T. Pilati and G. Resnati, *Acc. Chem. Res.*, 2005, **38**, 386–395.

20 T. Clark, M. Hennemann, J. S. Murray and P. Politzer, *J. Mol. Model.*, 2007, **13**, 291–296.

21 R. L. Sutar, E. Engelage, R. Stoll and S. M. Huber, *Angew. Chem., Int. Ed.*, 2020, **59**, 6806–6810.

22 F. Ostler, D. G. Piekarski, T. Danelzik, M. S. Taylor and O. G. Mancheño, *Chem.–Eur. J.*, 2021, **27**, 2315–2320.

23 T. Yanai, D. P. Tew and N. C. Handy, *Chem. Phys. Lett.*, 2004, **393**, 51–57.

24 F. Weigend and R. Ahlrichs, *Phys. Chem. Chem. Phys.*, 2005, **7**, 3297–3305.

25 M. J. Frisch, G. W. Trucks, H. B. Schlegel, G. E. Scuseria, M. A. Robb, J. R. Cheeseman, G. Scalmani, V. Barone, B. Mennucci, G. A. Petersson, H. Nakatsuji, M. Caricato, X. Li, H. P. Hratchian, A. F. Izmaylov, J. Bloino, G. Zheng, J. L. Sonnenberg, M. Hada, M. Ehara, K. Toyota, R. Fukuda, J. Hasegawa, M. Ishida, T. Nakajima, Y. Honda, O. Kitao, H. Nakai, T. Vreven, J. A. Montgomery Jr, J. E. Peralta, F. Ogliaro, M. Bearpark, J. J. Heyd, E. Brothers, K. N. Kudin, V. N. Staroverov, R. Kobayashi, J. Normand, K. Raghavachari, A. Rendell, J. C. Burant, S. S. Iyengar, J. Tomasi, M. Cossi, N. Rega, J. M. Millam, M. Klene, J. E. Knox, J. B. Cross, V. Bakken, C. Adamo, J. Jaramillo, R. Gomperts, R. E. Stratmann, O. Yazyev, A. J. Austin, R. Cammi, C. Pomelli, J. W. Ochterski, R. L. Martin, K. Morokuma, V. G. Zakrzewski, G. A. Voth, P. Salvador, J. J. Dannenberg, S. Dapprich, A. D. Daniels, Ö. Farkas, J. B. Foresman, J. V. Ortiz, J. Cioslowski and D. J. Fox, *Gaussian 09, Revision D.01*, Gaussian, Inc., Wallingford CT, 2009.

26 J. Tomasi, B. Mennucci and R. Cammi, *Chem. Rev.*, 2005, **105**, 2999–3093.

27 T. Janecki, J. Kêdzia and T. Wąsek, *Synthesis*, 2009, **2009**, 1227–1254.

28 (*a*) "Supramolecular.org – Binding Constant Calculators|Supramolecular" can be found at http://supramolecular.org/, 2021; (*b*) D. B. Hibbert and P. Thordarson, *Chem. Commun.*, 2016, **52**, 12792–12805.

29 D. von der Heiden, A. Vanderkooy and M. Erdélyi, *Coord. Chem. Rev.*, 2020, **407**, 213147.

30 D. A. Decato, A. M. S. Riel, J. H. May, V. S. Bryantsev and O. B. Berryman, *Angew. Chem., Int. Ed.*, 2021, **60**, 3685–3692.

Appendix 4

Publication IV

Ward, J. S.; Martõnova, J.; Wilson, L. M. E.; Kramer, E.; Aav, R.; Rissanen, K. (2022). Carbonyl Hypoiodites from Pivalic and Trimesic Acid and their Silver(I) Intermediates. *Dalton Transactions*, 14646−14653. DOI: 10.1039/d2dt01988d

Dalton Transactions

ROYAL SOCIETY OF CHEMISTRY

PAPER

View Article Online
View Journal | View Issue

Cite this: *Dalton Trans.*, 2022, **51**, 14646

Carbonyl hypoiodites from pivalic and trimesic acid and their silver(I) intermediates†

Jas S. Ward, *[a] Jevgenija Martõnova,[b] Laura M. E. Wilson, [a] Eric Kramer,[a] Riina Aav [b] and Kari Rissanen [a]

Received 22nd June 2022,
Accepted 2nd September 2022
DOI: 10.1039/d2dt01988d
rsc.li/dalton

The first *tris*(O–I–N) carbonyl hypoiodites have been synthesised based on trimesic acid and pyridine or 4-methylpyridine, with their structures definitively confirmed by single crystal X-ray diffraction (SCXRD). The more soluble carbonyl hypoiodites based on pivalic acid have also been studied *via* NMR, SCXRD, and computational analyses, enabling the study of the direct silver(I) precursor and intermediates of the resulting carbonyl hypoiodites generated using a range of substituted pyridines.

Introduction

Halogen bonding, though not as popular as the closely related hydrogen bonding, offers advantages such as being far more directional than hydrogen bonding, in that it enforces linear symmetry due to its electronic origins as a σ-hole interaction.[1] This reliable, high-degree of linear directionality has found much success in endeavours such as toward synthesising supramolecular architectures utilising self-assembling methodologies.[2–4]

The recent revisitation of carbonyl hypoiodites has revitalised interest in these species, both in themselves and their potential use as iodination reagents.[5,6] The use of halogen(I) reagents, such as the ubiquitous Barluenga's reagent, [I(pyridine)$_2$]BF$_4$, to effect iodination and oxidation reactions has been well established for over two decades.[7–10] Halogen(I) (also known as *halonium*) ions are the incarnation of a fully ionised halogen atom to a formally cationic state, X^+ (X = Cl, Br, I). Despite their reactivity, a growing number of these halogen(I) complexes have been characterised in the solid state by X-ray diffraction studies, with the largest subset of those incorporating the comparatively more stable iodine(I) species (as stability follows the trend: $I^+ > Br^+ \gg Cl^+$).[11–13]

Owing to their ease of preparation from suitable pairs of halogen bond (XB) donors (*e.g.*, haloimides, halosulfonimides) and acceptors (*e.g.*, pyridine derivatives, pyridine-N-oxides), neutral N–I···N and N–I···O–N halogen-bonded systems have enjoyed widespread study.[14–19] The closely related anionic dioxoiodane complexes, $[O–I–O]^-$, are also known and have been previously utilised as organic reagents.[20]

Similarly, hypoiodites (R-OI; R = alkyl) also have a well-documented history of being used as iodination reagents.[21,22] However, these reagents are often generated *in situ*,[23] with their exact structures only being speculated, such as with "^{t}BuOI",[24,25] where molecular weight measurements suggest another species may exist in equilibrium with the carbonyl hypoiodite form, and makes discerning the structure–reactivity relationships of these reagents difficult. Similarly, the carbonyl hypoiodite iodine monoacetate, $CH_3C(O)OI$, has only been characterised by ^{1}H NMR spectroscopy and spectrophotometrically,[26,27] despite a proven track record of being used as an iodination reagent.[27] The handful of examples of trapped or *stabilised* carbonyl hypoiodites,[5,6,28] where the carbonyl hypoiodite is stabilised by a Lewis base *via* halogen bonding, for which the solid-state structures are known are therefore a valuable resource to better understand such relationships. Comparisons between the ion-pair iodine(I) complexes and overall neutral stabilised carbonyl hypoiodites have revealed the two subsets of species possess structurally similar I–N bond lengths in the solid-state, characteristic of iodine(I) ions.[5,6]

As iodination reagents, halogen(I) ions are consumed stoichiometrically, making the potential of multi-iodination reagents attractive targets to increase atom economy and efficiency of their use. Halogen(I) complexes of the form $[N–I–N]^+$ like Barluenga's reagent maintain good solubility in organic solvents, despite being an ion-pair complex, owing to their stabilising Lewis bases, mono-cationic charge, and the identity of the anion, which overall greatly contributes to their utility as reagents. Unfortunately, the inclusion of a two or more cationic $[N–I–N]^+$ centres in one complex, for which only a single *bis*($[N–I–N]^+$) example exists,[4] would be expected to be concomitant with a decrease in solubility in organic solvents,

[a]*University of Jyvaskyla, Department of Chemistry, Jyväskylä 40014, Finland. E-mail: james.s.ward@jyu.fi*
[b]*Department of Chemistry and Biotechnology, School of Science, Tallinn University of Technology, Tallinn, Estonia*

†Electronic supplementary information (ESI) available: Synthesis, NMR and X-ray crystallographic. CCDC 2173463–2173470. For ESI and crystallographic data in CIF or other electronic format see DOI: **https://doi.org/10.1039/d2dt01988d**

that would become increasingly prominent as more $[N–I–N]^+$ moieties were incorporated.

However, this is not an issue for carbonyl hypoiodites, which incorporate a neutral O–I–N moiety, with four examples of *bis*(O–I–N) compounds being reported in the solid-state to date (Fig. 1),[6,28] all of which maintained good solubility in dichloromethane (DCM). This is not including a fifth example of a *bis*(O–I–N) compound (a structural isomer of two of the other examples), which was only able to be characterised by NMR studies.[6]

The potential of *bis*(O–I–N) as multi-iodination reagents are currently untested, undoubtedly due to their rarity in the literature. The silver(I) intermediates of the relatively straightforward one-pot process for the synthesis of carbonyl hypoiodites are not fully understood, as in contrast to the analogous formation of $[N–I–N]^+$ halogen(I) complexes, the silver(I) precursors and intermediates are effectively insoluble in the solvents used. Therefore, a better understanding of the silver(I) intermediates involved in the formation of carbonyl hypoiodites would facilitate the study of these species, and enable other scaffolds to be incorporated into their design.

Results and discussion

Derivatives of pivalic acid

The carboxylic acid pivalic acid, ^{t}BuC(O)OH, was selected for these studies, as the organic-solvent solubility imparted to its derivatives by the ^{t}Bu substituent was envisioned to be sufficient to overcome the ensuing insolubility of its respective silver(I) precursor (**1**) and intermediates (**1a–1d**; Scheme 1). Compound **1** was formed in excellent yields through deprotonation with NaOH, followed by subsequent Na^+ to Ag^+ cation exchange upon reaction with $AgNO_3$, and could be easily prepared in bulk. However, **1** was effectively insoluble in DCM and MeCN, with good solubility only being observed in dimethyl sulfoxide (DMSO).

The solid-state structure of **1** revealed 1D polymeric chains comprised of dimeric subunits (Ag–Ag = 2.8613(8) and 2.8649 (8) Å; Ag–O = 2.170(6)–2.255(6) Å) arrayed into bilayers possessing extensive Ag···Ag argentophilic interactions (2.9479(7)–3.0662(8) Å)[29,30] and Ag···O (2.457(5)–2.530(5) Å) interactions (Fig. 2), as has been previously observed in related systems.[31] These 1D polymeric chains explain the poor solubility of **1**, given that a significant network of intra- and intermolecular

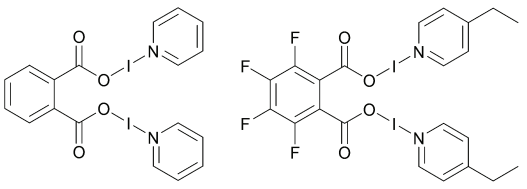

Fig. 1 Two examples of structurally characterised *bis*(O–I–N) compounds.[6,28]

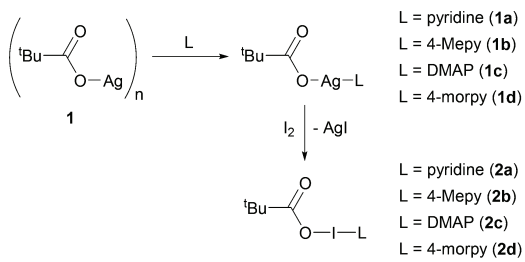

Scheme 1 The procedure to synthesise carbonyl hypoiodite derivatives of pivalic acid.

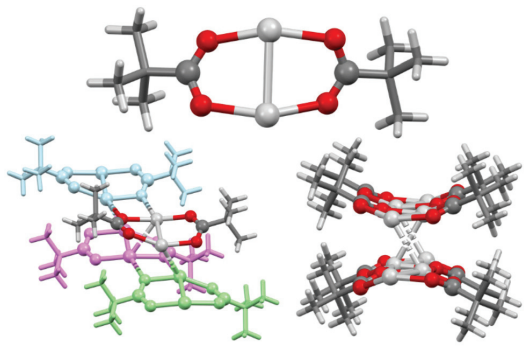

Fig. 2 The X-ray crystal structure of a dimeric unit of **1** (top), the intermolecular bonding between four dimeric units of **1** (with three of the dimeric units block coloured for clarity; bottom left), and the view along the axis of the polymer chains showing the bilayer structure (bottom right; all alkyl groups simplified for clarity). Colour key: light grey = silver, red = oxygen, dark grey = carbon, white = hydrogen.

bonds would need to be broken in order to liberate a single monomeric unit.

The silver(I) intermediates (**1a–1d**) formed upon addition of a stoichiometric amount of Lewis base to **1** (**1a** = pyridine; **1b** = 4-Mepy; **1c** = DMAP; **1d** = 4-morpy; where 4-Mepy = 4-methylpyridine, DMAP = dimethylaminopyridine, 4-morpy = 4-morpholinopyridine), displayed improved DCM and MeCN solubility in comparison to **1**, though none were observed to have stoichiometric ratios of their ^{t}Bu : Lewis base chemical shifts in their respective ^{1}H NMR spectra, again necessitating the use of DMSO as the NMR solvent to ensure complete dissolution of the components. Unfortunately, **1a** and **1b**, the weaker Lewis bases, were observed to decompose in the DMSO media such that only their ^{1}H NMR spectra could be reliably obtained. However, **1c** and **1d** displayed increased stability in DMSO, permitting more extensive NMR studies to be conducted.

The ^{1}H NMR spectra of **1a–1d** displayed effectively negligible downfield changes in their chemical shifts compared to their respective neat Lewis bases and **1**, all within the range of 0.01–0.09 ppm. This is in contrast to the formation of the [N–

Ag–N]$^+$ silver(I) precursors which display more noticeable perturbations in the chemical shifts,[32] though unsurprising given the contrasting solvents (DMSO rather than DCM) and the potential coordinating nature of DMSO to the silver(I) centre being in competition with the Lewis bases in solution. The carboxylate carbon atoms were also probed by ^{13}C NMR studies for **1c** (182.2 ppm) and **1d** (182.1 ppm), though again only negligible changes were observed from **1** (181.8 ppm). However, the directly-involved pyridinic nitrogen atoms were probed by ^{1}H–^{15}N HMBC studies and revealed much more indicative changes for **1c** (−144.6 ppm) and **1d** (−132.3 ppm) when compared to their corresponding Lewis base components of DMAP (−105.3 ppm) and 4-morpy (−94.7 ppm). The resulting coordination-induced shifts of −39.3 (**1c**) and −37.6 (**1d**) ppm are reminiscent of, but slightly smaller than, the large coordination shifts observed for [N–Ag–N]$^+$ complexes, *e.g.*, the ^{15}N NMR coordination shift of the pyridinic nitrogen atoms (in DCM) for pyridine (−67.7 ppm) to [Ag(pyridine)$_2$]PF$_6$ (−122.7 ppm) is −55.0 ppm, and similarly for DMAP (−108.9 ppm) to [Ag(DMAP)$_2$]PF$_6$ (−169.8 ppm) is −60.9 ppm.[32]

The single crystal X-ray structures were determined for both **1b** and **1c**, albeit only at an isotropic level of accuracy for **1b** which prevented detailed interrogation of the crystallographic parameters, but nonetheless was able to confirm the stoichiometry, identity, and linear nature of the O–Ag–N moiety (Fig. 3), fully analogous to the expected linear O–I–N bonding motif induced by the I$^+$ centre. In contrast, **1c** was observed as a discrete dimer (Fig. 4), possessing a similar, but slightly shorter (2.7854(8) Å), argentophilic Ag–Ag bond and pair of bridging pivalate molecules (Ag–O = 2.225(3) and 2.230(4) Å) as was found in **1**, though in this instance with no additional intermolecular interactions of any significance. As a result of the neutral nature of **1** and **1a–1d**, mass spectrometry analysis was also unable to provide any additional insights, with none of the structures being observed as either 2-coordinate silver(I) 'monomers' or 4-coordinate silver(I) dimers. The linear, 2-coordinate [N–Ag–N]$^+$ precursors of [N–I–N]$^+$ complexes are common in the literature,[32–35] as are 4-coordinate AgN$_4$ species,[36,37] though 3-coordinate AgN$_3$ examples have also been reported.[38–40] Similarly, whilst the O–Ag–N motif is present in the literature,[41,42] as are other examples of

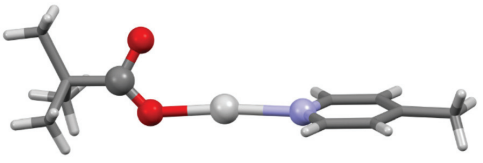

Fig. 3 The X-ray determined connectivity model of **1b** (aryl and alkyl groups simplified for clarity) showing the 2-coordinate silver(I) centre with a linear O–Ag–N geometry, analogous to the linear O–I–N geometry observed for stabilised hypoiodite compounds. Colour key: light grey = silver, red = oxygen, blue = nitrogen, dark grey = carbon, white = hydrogen.

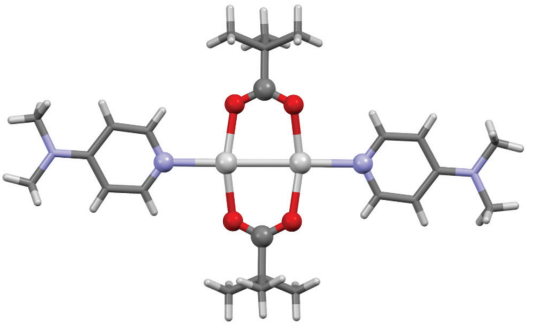

Fig. 4 The X-ray crystal structure of **(1c)$_2$** (aryl and alkyl groups simplified for clarity). Colour key: light grey = silver, red = oxygen, blue = nitrogen, dark grey = carbon, white = hydrogen.

expanded coordination spheres incorporating similar ligands, suggesting that the adaptable nature of the Ag$^+$ centre can accommodate a myriad of potential structures and coordination modes, which are somewhat independent of the identity of the ligands involved.

The silver(I) species are important precursors for the synthesis of carbonyl hypoiodites, as they provide a strong driving force for the reaction (*via* loss of AgI). However, the coordinative geometry of these silver(I) species is relevant to their subsequent use as precursors for the synthesis of carbonyl hypoiodites, as prior studies have found that more coordinatively saturated silver(I) species (≥4) have proven unreactive toward I$_2$ when trying to synthesise more traditional [N–I–N]$^+$ complexes.[37,40]

The subsequent conversions of **1a–1d** to their stabilised carbonyl hypoiodite analogues **2a–2d** upon reaction with one equivalent of elemental iodine were attempted in DMSO, however, mixtures were observed in all cases, necessitating that **2a–2d** be synthesised from **1** in DCM and not DMSO, including their subsequent solution studies. This solvent change, though unfortunate with respect to drawing direct comparisons to the previously discussed **1** and **1a–1d** without the need to consider the influence of the solvents, is useful given that nearly all modern NMR studies performed on carbonyl hypoiodites and halogen(I) complexes have been performed in deuterated DCM (or a closely-related chlorinated solvent).

The ^{1}H–^{15}N HMBC determined ^{15}N NMR chemical shifts revealed large coordination shifts of the pyridinic nitrogen atoms going from the free ligands to the stabilised carbonyl hypoiodites **2b–2d**.‡ The complexation-induced chemical shift change, $\Delta\delta_N$, defined here as $\delta(^{15}N_{O-I-N})$-$\delta(^{15}N_L)$, with O–I–N being the stabilised carbonyl hypoiodite compounds **2b–2d**, and **L** being their corresponding free substituted pyridines (4-Mepy, DMAP, or 4-morpy, respectively), all determined in CD_2Cl_2 for the aforementioned reasons. The $\Delta\delta_N$ values

‡The ^{15}N NMR chemical shift could not be accurately determined for **2a** due to decomposition being observed during the ^{1}H–^{15}N HMBC experiment.

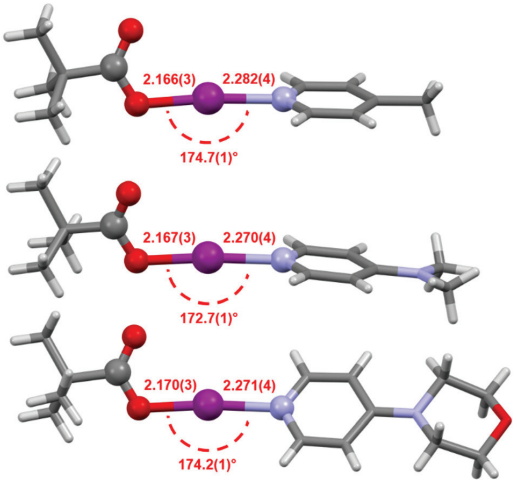

Fig. 5 The X-ray crystal structures of **2b** (top), **2c** (middle), and **2d** (bottom), annotated with their I–O and I–N bond lengths (in Å), and O–I–N angles (aryl and alkyl groups simplified for clarity; additional crystallographically independent molecules of **2c** and **2d** not shown).

ranged from −79.3 ppm for the complexation of 4-Mepy (−75.1 ppm) in **2b** (−154.4 ppm), to −94.2 ppm for the complexation of 4-morpy (−99.1 ppm) in **2d** (−193.3 ppm), reflecting in all cases a dramatic change in the environment of the nitrogen atoms (Fig. S54†). These large coordination shifts correspond with those observed for other O–I–N compounds,[5,6] as well as for [N–I–N]$^+$ complexes which have also been observed to demonstrate analogously large values, *e.g.*, [I(DMAP)$_2$]PF$_6$ had a $\Delta\delta_N$ value of −108.9 ppm,[32] which closely approximates the $\Delta\delta_N$ value observed for **2c** of −92.9 ppm. This indicates that despite the difference of a ligand between [I(DMAP)$_2$]PF$_6$ and **2c**, the influence on the pyridinic nitrogen atom in the DMAP, upon coordination to the I$^+$ centre, is predominantly the same between the two species.

The solid-state structures for the stabilised carbonyl hypoiodites **2b–2d** were determined by single crystal X-ray crystallography (Fig. 5), with only **2a** remaining elusive, agreeing with the solution-state observations. The I–O bond lengths for **2b** (2.166(3) Å), **2c** (2.167(3), 2.169(4), 2.175(3) Å; three crystallographically independent molecules present in the asymmetric unit cell), and **2d** (2.155(3), 2.170(3) Å; two crystallographically independent molecules present in the asymmetric unit cell) were all effectively indistinguishable within the 3σ tolerance. The I–N bond lengths for **2b** (2.282(4) Å), **2c** (2.254(3), 2.268(4), 2.270(4) Å), and **2d** (2.271(4), 2.292(3) Å) showed slightly greater variability, though all still very much within the known range of all reported [N–I–N]$^+$ iodine(I) complexes§ of 2.23(1)–2.316(6) Å.[42,43] The O–I–N bond angles for **2b** (174.7(1)°), **2c** (172.7(1), 173.3(1), 175.8(1)°), and **2d** (174.13(9), 174.2(1)°), all stray beyond the 180° linear ideal and also, with the exception of 175.8(1)°, the most deviated example reported for [N–I–N]$^+$ iodine(I) complexes of 175.2(2)° for [I(4-trifluoromethylpyridine)$_2$]BF$_4$.[34] However, these angles are consistent with those reported for analogous O–I–N compounds bearing the same or similar 4-substituted pyridines and benzoyl moieties.[5]

The computational structures of **2a–2d** were calculated at the M06-2X/def2-TZVP level of theory[44] using the SPARTAN18 program[45] with dichloromethane (dielectric = 8.82) as the solvent using the conductor like polarizable continuum model (C-PCM)[46,47] to confirm the higher reactivity observed experimentally for **2a** (Fig. 6). The computational models of **2b–2d** all showed good agreement with their crystallographic structures (Table S3†), validating the level of theory used. The model of **2a** had an I–N bond length of 2.318 Å, which is at the extreme end of the range of those observed for solid-state [N–I–N]$^+$ complexes,[43] supporting that the pyridine ligand, a weaker Lewis base than those in the other complexes, would only be weakly bound and therefore more likely to be labile in solution as was observed experimentally.

There are limited solid-state examples for a direct comparison to **2b** and **2d**, though differing substituent of the carbonyl group in **2c** can be directly compared with (acetyl-OI)(DMAP) (I–O = 2.20(1) Å; I–N = 2.24(1) Å; O–I–N = 172.9(5)°) and (benzoyl-OI)(DMAP) (I–O = 2.210(3) Å; I–N = 2.241(3) Å; O–I–N = 178.1(1)°).[5] As the comparison of these three compounds shows, **2c** has the shortest I–O bond lengths and the longest I–N bond lengths. This is consistent with the electronic influence of the carbonyl substituent, with the ^{t}Bu group of the pivalyl in **2c** being the most electron donating, which could be equated to **2c** having the least iodopyridinium character of the three compounds. Compound **2c** lies between the two literature examples with respect to O–I–N bond angles, but these angles are undoubtedly heavily influenced by other factors than the electronic contributions of the substituents, such as packing effects, making this a less informative metric to consider in comparison to the bond lengths. Comparisons could also be drawn with the literature complex [N^{n}Bu$_4$][AcO–I–succinimide],[48] despite its anionic charge, given that it contains the same linear O–I–N motif. However, the I–O (2.293(2) and 2.299(2) Å) and I–N (2.166(2) and 2.168(2) Å) bond lengths of that complex clearly reflect that it contains significant covalent

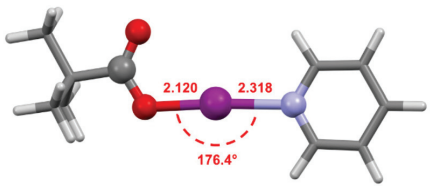

Fig. 6 The computationally generated geometry of **2a** calculated at the M06-2X/def2-TZVP level of theory, annotated with the I–O and I–N bond lengths (in Å), and the O–I–N bond angle.

§ Incorporating sp^2-nitrogen Lewis bases, which form by far the largest subset of reported [N–I–N]$^+$ iodine(I) complexes.

character in its I–N bond,[5] and is therefore best described as an acetate anion coordinating to a neutral molecule of *N*-iodosuccinimide.

Derivatives of trimesic acid

The installation of multiple O–I–N moieties into a single compound, as previously discussed, is a worthwhile endeavour toward potentially more atom-economical iodinating reagents. Toward this goal, trimesic acid was seen as a natural progression from the benzene-dicarboxylic acids that have found prior success in synthesising *bis*(O–I–N) compounds. The silver(I) precursor Ag_3(trimesate) (**3**) was synthesised in an analogous fashion to **1**, adjusting for the 3 : 1 stoichiometry, and was obtained in excellent yields. Unlike for compound **1**, no suitable solvent could be found to even partially dissolve **3**, even at elevated temperatures, precluding solution studies. This apparent insolubility extended to the 3 : 1 stoichiometric pyridine (**3a**) and 4-Mepy (**3b**) derivatives of **3**, though a huge excess of pyridine doped with a modest amount of DMSO was able to generate $[Ag_3(\text{trimesate})(\text{py})_7]_n$ (**3a·(py)$_4$**; Fig. S4†). This polymeric structure demonstrated a 7 : 1 pyridine : trimesate ratio, wherein two of the carboxylate groups of each trimesate formed a 1D chain with bridging Ag^+ centres coordinated to two carboxylates and two molecules of pyridine, whilst the third carboxylate of each trimesate would terminate as a Ag^+ centre coordinated to one oxygen atom and three molecules of pyridine.

The stabilised *tris*(O–I–N) carbonyl hypoiodites of trimesic acid with pyridine (**4a**) or 4-Mepy (**4b**) were successfully prepared in a one-pot reaction in DCM, despite the near insolubility of the silver(I) precursor and intermediates, the first and only examples of *tris*(O–I–N) compounds to date. The ^{1}H NMR studies of **4a** and **4b** confirmed the 3 : 1 pyridine/4-Mepy : trimesyl ratio, but ^{1}H–^{15}N HMBC studies to determine the ^{15}N NMR chemical shifts could not be adequately obtained before decomposition was observed. Rapidly isolated samples of **4a** and **4b**, which were white solids, also clearly showed noticeable discolouration from decomposition within minutes, even under an inert atmosphere, preventing more detailed NMR studies. However, despite their highly reactive nature, the identity of **4a** and **4b** were definitively confirmed by single crystal X-ray diffraction studies (Fig. 7).

Both **4a** and **4b** were found to possess monoclinic symmetry and were solved in the space group $P2_1/n$, and whilst **4b** had no additional accoutrements, surprisingly **4a** was found to also include a single molecule of H_2O (per molecule of **4a**) as a solvate, intermolecularly bridging the C=O groups of two neighbouring molecules of **4a**. The I–O and I–N bond lengths of **4a** (I–O = 2.170(3), 2.174(3), 2.186(3) Å; I–N = 2.255(3), 2.277(3), 2.291(3) Å) and **4b** (I–O = 2.181(4), 2.193(4), 2.214(4) Å; I–N = 2.264(4), 2.277(4), 2.281(4) Å) reveal a slight elongation of the average I–O bond length in **4b** (2.196 Å) *versus* **4a** (2.177 Å), concordant with the stronger Lewis base in **4b** inducing more iodopyridinium (O···I–N) character in the O–I–N bonds. However, this is not clearly reflected in the I–N bond lengths of the two species, the ranges of which effectively overlap, as

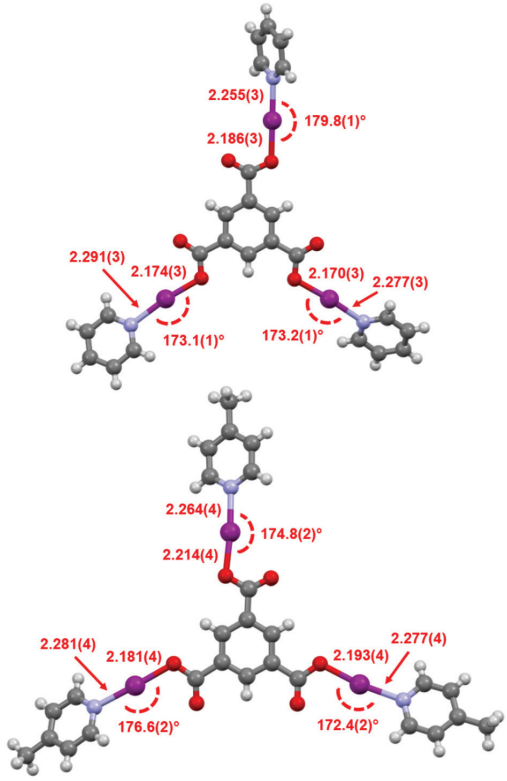

Fig. 7 The X-ray crystal structures of **4a** (top) and **4b** (bottom), annotated with their I–O and I–N bond lengths (in Å) and O–I–N angles.

the two Lewis bases are still relatively quite similar in their basicities. This effect of influencing the electronic character of the O–I–N halogen bond between the two extremes of a pyridine-stabilised carbonyl hypoiodite (O–I···N) or a carboxylate-iodopyridinium ion pair (O···I–N) has been previously explored with other carbonyl hypoiodites,[5] with only minor differences in the I–O and I–N bond lengths being noted when varying the strength of Lewis base used. Similar to the relatively large range of O–I–N angles observed for **2b–2d**, **4a** (173.1(1), 173.2(1), 179.8(1) Å) and **4b** (172.4(2), 174.8(2), 176.6(2) Å) were also observed to demonstrate significant variability in their O–I–N angles, again likely a reflection of the packing, rather than electronic, effects.

The comparison of **4a** and (benzoyl-OI)(pyridine) (I–O = 2.14(1), 2.14(1) Å; I–N = 2.29(1), 2.31(1) Å),¶[28] which can be considered the respective *mono*(O–I–N) analogue of **4a**, does indicate that the presence of the two additional O–I–N moieties has a tangible impact on the I–O and I–N bond lengths in

¶The bond lengths and esds given are those reported in the original 1981 publication, though are in slight contrast to the bond lengths reported in the CSD (refcode: BZPRIA) for which no esds are given.

4a, with an elongation of the I–O and shortening of the I–N bond lengths when compared to the average values in **4a** (I–O (average) = 2.177 Å; I–N(average) = 2.274 Å). This would suggest that the two additional O–I–N moieties in **4a** are causing the trimesyl group to be more electron withdrawing than the benzoyl group, inducing comparatively more iodopyridinium character in **4a**. This is an interesting observation, as the inclusion, placement, and proximity of multiple O–I–N moieties had contributed to making compound **4a** more reactive, and such factors will invariably have an impact on future scaffold design for other *multi*(O–I–N) compounds.

The silver(I) precursors of pyromellitic acid (benzene-1,2,4,5-tetracarboxylic acid), Ag_4(pyromellitate), and mellitic acid (benzenehexacarboxylic acid), Ag_6(mellitate), were also successfully prepared, and attempts were made to prepare the respective *tetrakis*(O–I–N) and *hexakis*(O–I–N) stabilised carbonyl hypoiodites. However, the reactivity of these species was found to be extreme to the point that the reactions displayed clear signs of decomposition even before complete addition of the elemental iodine.

Conclusions

The silver(I) derivatives of pivalic acid were synthesised to try and better understand the species present and ultimately facilitate the synthesis of a greater range of carbonyl hypoiodite compounds in the future. However, despite the high solubility of pivalic acid and its derivatives due to the inclusion of a ^{t}Bu substituent, the ruinously poor solubility of the silver(I) precursor **1** or its pyridine-based derivatives **1a–1d**, still proved a strong obstacle, with potentially even more soluble carboxylic acid starting materials needing to be considered in future studies. However, the use of the strongly polar solvent dimethyl sulfoxide (DMSO) permitted detailed solution-state studies to be conducted on the complexes incorporating the stronger Lewis bases DMAP (**1c**) and 4-morpy (**1d**), which displayed similar coordination shifts as their analogous $[N–I–N]^+$ iodine(I) counterparts. The respective stabilised carbonyl hypoiodites were successfully synthesised (**2a–2d**), and all but the least stable **2a** (which was supported by computational calculations), were characterised in the solid state.

The first examples of *tris*(O–I–N) compounds, **4a** and **4b**, derivatives of trimesic acid, were also successfully prepared and, despite their observed reactivity, were definitely characterised in the solid-state by X-ray crystallography. The two structures revealed metrics comparable to their *mono*(O–I–N) analogues, which belied their observed increased reactivity, possibly indicating that additional factors contribute to the stability of stabilised hypoiodites. This was also supported by the attempts to synthesise *tetrakis*(O–I–N) and *hexakis*(O–I–N) stabilised hypoiodites being met with immediate failure due to greatly increased reactivities. However, the successful first report of *tris*(O–I–N) compounds presents a significant step forward in the field of halogen(I) chemistry, and heralds the emergence of more efficient iodination reagents potentially being developed in the future.

Experimental

General considerations

All reagents and solvents were obtained from commercial suppliers and used without further purification. For structural NMR assignments, ^{1}H NMR and ^{1}H–^{15}N NMR correlation spectra were recorded on a Bruker Avance III 500 MHz spectrometer at 25 °C in CD_2Cl_2, or at 30 °C in $(CD_3)_2SO$ (DMSO melting point = 19 °C). Chemical shifts are reported on the δ scale in ppm using the residual solvent signal as internal standard (CH_2Cl_2 in CD_2Cl_2: δ_H 5.32, δ_C 53.84; $(CH_3)_2SO$ in $(CD_3)_2SO$: δ_H 2.50, δ_C 39.52), or for ^{1}H–^{15}N NMR spectroscopy, to an external CD_3NO_2 standard. For the ^{1}H NMR spectroscopy, each resonance was assigned according to the following conventions: chemical shift (δ) measured in ppm, observed multiplicity, observed coupling constant (J Hz), and number of hydrogens. Multiplicities are denoted as: s (singlet), d (doublet), t (triplet), q (quartet), m (multiplet), and br (broad). For the ^{1}H–^{15}N HMBC spectroscopy, spectral windows of 4 ppm (^{1}H) and 300 ppm (^{15}N) were used, with 1024 points in the direct dimension and 512 increments used in the indirect dimension, with subsequent peak shape analysis being performed to give the reported ^{15}N NMR resonances. The NMR data for neat pyridine and neat DMAP in CD_2Cl_2 have been previously reported.[32]

The single crystal X-ray data for **1**, **1b**, **2c**, **2e**, **4a**, and **4b** were collected at 120 K using an Agilent SuperNova dual wavelength diffractometer with an Atlas detector using mirror-monochromated Cu-Kα (λ = 1.54184 Å) radiation. The single crystal X-ray data for $(\mathbf{1c})_2$, **2b** and **3a·(py)$_4$** were collected at 120 K using an Agilent SuperNova diffractometer with an Eos detector using mirror-monochromated Mo-Kα (λ = 0.71073 Å) radiation. The program CrysAlisPro[49] was used for the data collection and reduction on the SuperNova diffractometers. All structures were solved by intrinsic phasing (SHELXT)[50] and refined by full-matrix least squares on F^2 using Olex2,[51] utilising the ShelXL-2015 module.[52] Anisotropic displacement parameters were assigned to non-H atoms and isotropic displacement parameters for all H atoms were constrained to multiples of the equivalent displacement parameters of their parent atoms with U_{iso}(H) = 1.2U_{eq} (aromatic; cyclic alkyl) or U_{iso}(H) = 1.5U_{eq} (acyclic alkyl) of their respective parent atoms.

Synthetic and characterisation details, including annotated NMR assignments, of all new compounds are included in the accompanying ESI.†

Author contributions

J.S.W. was responsible for the conceptualisation of the research and provided supervision, as well as performing the investigation of the solution and X-ray studies. J.M., L.M.E.W.,

and E.K. were responsible for the preparation of crystallographic samples and solution studies. The visualisation and writing of the manuscript were undertaken by J.S.W., with R.A. and K.R. contributing to the reviewing and editing. J.S.W., R. A., and K.R. were responsible for the acquisition of funding.

Conflicts of interest

There are no conflicts to declare.

Acknowledgements

The authors would like to thank the University of Jyväskylä mass spectrometry service for their time and expertise, and gratefully acknowledge the Magnus Ehrnrooth Foundation (J. S. W.), the ERDF DORA travel grant (J. M.), the Estonian Research Council (R.A. grant no. PRG399), the Academy of Finland (K.R. grant no. 317259), and the University of Jyväskylä, Finland for financial support.

References

1 J. Pancholi and P. D. Beer, *Coord. Chem. Rev.*, 2020, **416**, 213281.
2 L. Turunen, U. Warzok, R. Puttreddy, N. K. Beyeh, C. A. Schalley and K. Rissanen, *Angew. Chem., Int. Ed.*, 2016, **55**, 14033–14036.
3 L. Turunen, U. Warzok, C. A. Schalley and K. Rissanen, *Chem*, 2017, **3**, 861–869.
4 A. Vanderkooy, A. K. Gupta, T. Földes, S. Lindblad, A. Orthaber, I. Pápai and M. Erdélyi, *Angew. Chem., Int. Ed.*, 2019, **58**, 9012–9016.
5 S. Yu, J. S. Ward, K.-N. Truong and K. Rissanen, *Angew. Chem., Int. Ed.*, 2021, **60**, 20739–20743.
6 E. Kramer, S. Yu, J. S. Ward and K. Rissanen, *Dalton Trans.*, 2021, **50**, 14990–14993.
7 G. Cavallo, P. Metrangolo, R. Milani, T. Pilati, A. Priimagi, G. Resnati and G. Terraneo, *Chem. Rev.*, 2016, **116**, 2478–2601.
8 J. Barluenga, J. M. González, M. A. Garcia-Martin, P. J. Campos and G. Asensio, *J. Chem. Soc., Chem. Commun.*, 1992, 1016–1017.
9 J. Ezquerra, C. Pedregal, C. Lamas, J. Barluenga, M. Pérez, M. A. García-Martín and J. M. González, *J. Org. Chem.*, 1996, **61**, 5804–5812.
10 G. Espuña, G. Arsequell, G. Valencia, J. Barluenga, M. Pérez and J. M. González, *Chem. Commun.*, 2000, 1307–1308.
11 E. S. Stoyanov, I. V. Stoyanova, F. S. Tham and C. A. Reed, *J. Am. Chem. Soc.*, 2010, **132**, 4062–4063.
12 A. Karim, M. Reitti, A.-C. C. Carlsson, J. Gräfenstein and M. Erdélyi, *Chem. Sci.*, 2014, **5**, 3226–3233.
13 L. Turunen and M. Erdélyi, *Chem. Soc. Rev.*, 2020, **49**, 2688–2700.
14 O. Makhotkina, J. Lieffrig, O. Jeannin, M. Fourmigué, E. Aubert and E. Espinosa, *Cryst. Growth Des.*, 2015, **15**, 3464–3473.
15 E. Aubert, E. Espinosa, I. Nicolas, O. Jeannin and M. Fourmigué, *Faraday Discuss.*, 2017, **203**, 389–406.
16 K. Raatikainen and K. Rissanen, *CrystEngComm*, 2011, **13**, 6972–6977.
17 K. Raatikainen and K. Rissanen, *Chem. Sci.*, 2012, **3**, 1235–1239.
18 R. Puttreddy, O. Jurček, S. Bhowmik, T. Mäkelä and K. Rissanen, *Chem. Commun.*, 2016, **52**, 2338–2341.
19 R. Puttreddy, J. M. Rautiainen, T. Mäkelä and K. Rissanen, *Angew. Chem., Int. Ed.*, 2019, **58**, 18610–18618.
20 K. Muñiz, B. García, C. Martínez and A. Piccinelli, *Chem. – Eur. J.*, 2017, **23**, 1539–1545.
21 D. D. Tanner and G. C. Gidley, *J. Am. Chem. Soc.*, 1968, **90**, 808–809.
22 J. Barluenga, F. González-Bobes and J. M. González, *Angew. Chem., Int. Ed.*, 2002, **41**, 2556–2558.
23 R. Kawasumi, S. Narita, K. Miyamoto, K. Tominaga, R. Takita and M. Uchiyama, *Sci. Rep.*, 2017, **7**, 17967.
24 R. Montoro and T. Wirth, *Org. Lett.*, 2003, **5**, 4729–4731.
25 D. D. Tanner, G. C. Gidley, N. Das, J. E. Rowe and A. Potter, *J. Am. Chem. Soc.*, 1984, **106**, 5261–5267.
26 J. L. Courtneidge, J. Lusztyk and D. Pagé, *Tetrahedron Lett.*, 1994, **35**, 1003–1006.
27 T. Hokamp, A. T. Storm, M. Yusubov and T. Wirth, *Synlett*, 2018, 415–418.
28 H. Hartl and M. Hedrich, *Z. Naturforsch., B: Anorg. Chem., Org. Chem.*, 1981, **36**, 922–928.
29 S. Sculfort and P. Braunstein, *Chem. Soc. Rev.*, 2011, **40**, 2741–2760.
30 H. Schmidbaur and A. Schier, *Angew. Chem., Int. Ed.*, 2015, **54**, 746–784.
31 Z.-H. Yan, X.-Y. Li, L.-W. Liu, S.-Q. Yu, X.-P. Wang and D. Sun, *Inorg. Chem.*, 2016, **55**, 1096–1101.
32 J. S. Ward, G. Fiorini, A. Frontera and K. Rissanen, *Chem. Commun.*, 2020, **56**, 8428–8431.
33 M. Bedin, A. Karim, M. Reitti, A.-C. C. Carlsson, F. Topić, M. Cetina, F. Pan, V. Havel, F. Al-Ameri, V. Sindelar, K. Rissanen, J. Gräfenstein and M. Erdélyi, *Chem. Sci.*, 2015, **6**, 3746–3756.
34 A.-C. C. Carlsson, K. Mehmeti, M. Uhrbom, A. Karim, M. Bedin, R. Puttreddy, R. Kleinmaier, A. A. Neverov, B. Nekoueishahraki, J. Gräfenstein, K. Rissanen and M. Erdélyi, *J. Am. Chem. Soc.*, 2016, **138**, 9853–9863.
35 S. Yu, E. Kalenius, A. Frontera and K. Rissanen, *Chem. Commun.*, 2021, **57**, 12464–12467.
36 K. V. Goodwin, D. R. McMillin and W. R. Robinson, *Inorg. Chem.*, 1986, **25**, 2033–2036.
37 S. Yu, P. Kumar, J. S. Ward, A. Frontera and K. Rissanen, *Chem*, 2021, **7**, 948–958.
38 C. B. Aakeröy, A. M. Beatty and B. A. Helfrich, *J. Chem. Soc., Dalton Trans.*, 1998, 1943–1946.
39 D. A. Beauchamp and S. J. Loeb, *Supramol. Chem.*, 2005, **17**, 617–622.

40 J. S. Ward, A. Frontera and K. Rissanen, *Inorg. Chem.*, 2021, **60**, 5383–5390.
41 X. Zhang, L. W. Liu, Z. C. Hao and G. H. Cui, *Transit. Met. Chem.*, 2016, **41**, 459–466.
42 C. R. Groom, I. J. Bruno, M. P. Lightfoot and S. C. Ward, *Acta Crystallogr. Sect. B*, 2016, **72**, 171–179.
43 J. S. Ward, K.-N. Truong, M. Erdélyi and K. Rissanen, in Reference Module in Chemistry, Molecular Sciences and Chemical Engineering, Elsevier, 2022, DOI: **10.1016/B978-0-12-823144-9.00043-1**.
44 Y. Zhao and D. G. Truhlar, *Theor. Chem. Acc.*, 2008, **120**, 215–241.
45 *Spartan'18*, Wavefunction Inc., Irvine CA, USA, 2018.
46 X. Zhang and J. M. Herbert, *J. Phys. Chem. B*, 2014, **118**, 7806–7817.
47 A. W. Lange and J. M. Herbert, *Chem. Phys. Lett.*, 2011, **509**, 77–87.
48 A. J. Guzmán Santiago, C. A. Brown, R. D. Sommer and E. A. Ison, *Dalton Trans.*, 2020, **49**, 16166–16174.
49 *CrysAlisPro*, Agilent Technologies Ltd, 2014.
50 G. M. Sheldrick, *Acta Crystallogr., Sect. A: Found. Adv.*, 2015, **71**, 3–8.
51 O. V. Dolomanov, L. J. Bourhis, R. J. Gildea, J. A. K. Howard and H. Puschmann, *J. Appl. Crystallogr.*, 2009, **42**, 339–341.
52 G. M. Sheldrick, *Acta Crystallogr., Sect. C: Struct. Chem.*, 2015, **71**, 3–8.

Appendix 5

Publication V

Nikonovich, T.; Jarg, T.; Martõnova, J.; Kudrjašov, A.; Merzhyievskyi, D.; Kudrjašova, M.; Gallou, F.; Aav, R; Kananovich, D. (2024). Protecting-group-free mechanosynthesis of amides from hydroxycarboxylic acids: application to the synthesis of imatinib. *RSC Mechanochemistry*, 1 (2), 189−195. DOI: 10.1039/D4MR00006D

RSC Mechanochemistry

ROYAL SOCIETY OF CHEMISTRY

PAPER

View Article Online
View Journal | View Issue

Cite this: *RSC Mechanochem.*, 2024, **1**, 189

Protecting-group-free mechanosynthesis of amides from hydroxycarboxylic acids: application to the synthesis of imatinib†

Tatsiana Nikonovich, [a] Tatsiana Jarg, [a] Jevgenija Martõnova, [a] Artjom Kudrjašov,[ab] Danylo Merzhyievskyi, [ac] Marina Kudrjašova, [a] Fabrice Gallou, [d] Riina Aav *[a] and Dzmitry Kananovich *[a]

Received 1st February 2024
Accepted 11th March 2024

DOI: 10.1039/d4mr00006d

rsc.li/RSCMechanochem

Despite considerable advancements in mechanochemical amide couplings, there is a paucity of studies addressing chemoselective issues in these transformations, such as the tolerance of unmasked hydroxyl groups. In view of the high practical significance of amide coupling reactions in the synthesis of active pharmaceutical ingredients (APIs), we aimed to investigate the tolerance of unprotected hydroxyls in carboxylic acids towards various reported mechanochemical amide coupling conditions. 1-Ethyl-3-(3-dimethylaminopropyl)carbodiimide hydrochloride (EDC·HCl) in combination with ethyl acetate as a liquid-assisted grinding (LAG) additive was revealed as the most selective amide coupling system that delivers 76–94% yields of amides from a range of hydroxycarboxylic acids, including *N*-Boc-protected amino acids serine and tyrosine. The EDC-mediated amide coupling protocol was employed in the synthesis of imatinib, an anticancer drug included in the World Health Organization's List of Essential Medicines. The target API was synthesized in an overall 86% yield and 99% HPLC purity through a two-step mechanochemical C–N bond assembling reaction sequence starting from 4-(hydroxymethyl)benzoic acid.

Introduction

Mechanochemistry has shown great potential as a powerful tool for advancing the sustainability goals in the synthesis of active pharmaceutical ingredients (APIs).[1–5] Focusing on the applications of mechanochemical C–N bond forming reactions,[6,7] our objective was to develop a mechanochemical method for the synthesis of imatinib, an anti-cancer drug included in the World Health Organization's List of Essential Medicines.[8] The planned synthetic route involved the amide coupling of 4-(hydroxymethyl) benzoic acid (**1**), followed by a subsequent nucleophilic substitution reaction at the benzylic hydroxyl (Scheme 1). In our previous work,[7] we noticed that amide coupling of **1** with *N*-Boc piperazine mediated by the TCFH reagent (chloro-*N*,*N*,*N*′,*N*′-tetramethylformamidinium hexafluorophosphate) did not affect the hydroxyl group of **1**. However, regarding the synthesis of imatinib, we were uncertain whether using a poorly nucleophilic aromatic amine would be equally successful, considering that competitive esterification reactions can be facilitated by common coupling reagents.[9–15] While numerous mechanochemical amide coupling protocols have been reported,[6,16–25] limited attention has been given to studying the chemoselectivity issues in these transformations. In particular, the amide bond formation in the presence of a free hydroxyl group in starting materials has not

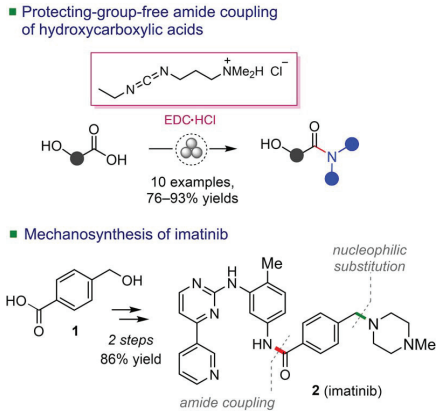

Scheme 1 Outline of the work.

[a]*Department of Chemistry and Biotechnology, Tallinn University of Technology, Akadeemia tee 15, 12618, Tallinn, Estonia. E-mail: riina.aav@taltech.ee; dzmitry.kananovich@taltech.ee*

[b]*Tallinna Tõnismäe Reaalkool, Pärnu mnt 50, Tallinn, Estonia*

[c]*Department of Chemistry of Bioactive Nitrogen-containing Heterocyclic Bases, V. P. Kukhar Institute of Bioorganic Chemistry and Petrochemistry, National Academy of Sciences of Ukraine, Academician Kukhar Str. 1, 02094 Kyiv, Ukraine*

[d]*Novartis Pharma AG, Novartis Campus, 4056 Basel, Switzerland*

† Electronic supplementary information (ESI) available. CCDC 2287665. For ESI and crystallographic data in CIF or other electronic format see DOI: https://doi.org/10.1039/d4mr00006d

been systematically explored, with only sporadic instances of such reactions reported.[7,26–30] As a prerequisite for the synthesis of imatinib, we aimed to perform a systematic screening of previously reported protocols[6,16,17,21] on a model amide coupling reaction of **1**. The goal was to identify a coupling reagent with the best tolerance to the unmasked hydroxyl functionality of **1** and to outline the limits of such tolerance by exploring amines with varying nucleophilicities.

The study identified 1-ethyl-3-(3-dimethylaminopropyl) carbodiimide hydrochloride (EDC·HCl) as the most efficient amide coupler for **1** and other examples of hydroxycarboxylic acids. Subsequently, we demonstrate the application of the established chemoselective amide coupling methodology in the two-step synthesis of imatinib **2**.

Results and discussion

The mechanochemical amidation protocols have been screened for the model coupling reaction of hydroxycarboxylic acid **1** with 4-bromo-3-methylaniline **3** as a poorly nucleophilic aromatic amine[31] (Table 1).

Initially, we expected that free hydroxyl of **1** could act as a competitive nucleophile,[9–15] thereby leading to the formation of ester by-products. However, we observed a variety of side processes, the prevalence of which was influenced by the specific coupling conditions employed. The combination of TCFH with K_2HPO_4 (Table 1, entry 1)[7] afforded amide **4** in low 26% yield due to a competitive reaction between TCFH and amine **3** with the formation of a guanidinium derivative **3a**. 1,1′-Carbonyldiimidazole (CDI, entry 4)[16] demonstrated a low 10% yield of **4** since the process was accompanied by self-condensation of **1** that delivered ester-type by-products. Several other reported methodologies[17,21] failed to provide the amide product at all. The highest yield of **4** (90% by ^{1}H NMR) was attained with the EDC·HCl reagent (entry 7) and ethyl acetate as a green LAG additive.[32] The use of EDC·HCl for the mechanochemical amide coupling in combination with nitromethane as a LAG additive was first reported by Štrukil and co-workers,[21] which was followed by several examples of peptide couplings, where nitromethane was replaced by ethyl acetate.[22,33] In our case, ethyl acetate demonstrated comparable efficacy to nitromethane and sulfolane as LAG additives (Table S1, entries 1–3 in the ESI†). This is particularly important from a safety perspective, as it is essential to avoid the use of hazardous nitromethane[32] under mechanochemical conditions. Pure amide **4** was isolated in 89% yield by following an operationally simple work-up protocol, which involved treatment with water, filtration and drying.

The results demonstrate that the amide coupling is generally more favoured with many of the tested reagent systems compared to the ester capping of the hydroxyl group. To further clarify the respective chemoselectivity concerns, certain amide

Table 1 Screening experiments for amide coupling of **1** and **3**[a]

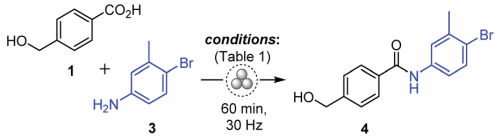

Entry	Coupling reagent/base	LAG additive, η (μL mg^{-1})	Yield of **4**[b], %
1	TCFH/K_2HPO_4	EtOAc (0.19)	26[c]
2	COMU/K_2HPO_4	EtOAc (0.19)	83[d,e]
3	TCFH/NMI	Without	74[c]
4	CDI	Without	10[e]
5	*t*-BuOK	Without	0[f,g]
6	EDC·HCl/DMAP	CH_3NO_2 (0.25)	0[g]
7	EDC·HCl	EtOAc (0.25)	90[h]

Structures of the reagents and identified by-products:

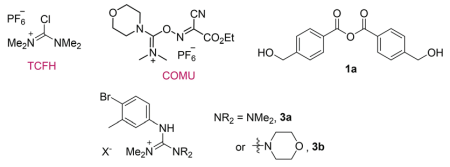

NMI = 1-methylimidazole, CDI = carbonyldiimidazole.

[a] General conditions: acid **1** (0.66 mmol, 100 mg), amine **3** (0.9–1 equiv.), coupling reagent (1–1.1 equiv.), base (0.85–3 equiv.), LAG additive (η = 0.19–0.25 μL mg^{-1}), and ball milling at 30 Hz for 60 min (see the ESI for the details). [b] Yields are determined by ^{1}H NMR with an internal standard (1,3,5-trimethoxybenzene). [c] Guanidinium derivative **3a** was formed by the reaction of TCFH with **3**. [d] Guanidinium derivative **3b** was formed as a by-product. [e] Ester by-products resulting from self-condensation of **1** were observed. [f] The reaction was performed with ethyl ester of **1**. [g] Almost no reaction: starting materials with a trace of unidentified by-products. [h] Anhydride **1a** was formed in a reaction without amine **3**.

Table 2 Esterification of **4** with 4-(hydroxymethyl)benzoic acid **1**[a]

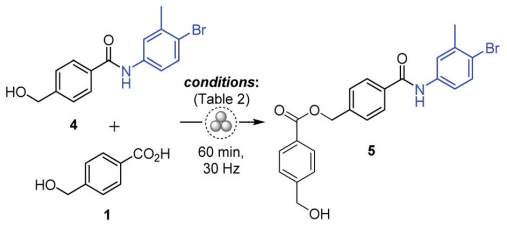

Entry	Coupling reagent/base	LAG additive, η (μL mg^{-1})	Yield of **5**[b], %
1	COMU/K_2HPO_4	EtOAc (0.19)	31
2	TCFH/NMI	Without	40
3	TCFH/K_2HPO_4	EtOAc (0.19)	5[c]
4	EDC·HCl	EtOAc (0.25)	<1[d]

[a] General conditions: amide **4** (0.19 mmol, 60 mg), acid **1** (1 equiv.), coupling reagent (1–1.1 equiv.), base (3 equiv.), LAG additive (η = 0.19–0.25 μL mg^{-1}), and ball milling at 30 Hz for 60 min. [b] Yields are determined by ^{1}H NMR. [c] Anhydride **1a** was formed in 70% yield. [d] Starting materials are left and anhydride **1a** was formed in 30% yield.

coupling conditions were also tested for producing ester **5** through the reaction of **4** with **1** (Table 2). Both COMU/K_2HPO_4 and TCFH/NMI systems afforded **5** at moderate yields of 31% and 40%, respectively (Table 2, entries 1 and 2). However, using TCFH/K_2HPO_4 or EDC·HCl (entries 3 and 4) resulted in only trace amounts of **5**, with the predominant process being the generation of anhydride **1a**.

This suggests that COMU/K_2HPO_4 and TCFH/NMI systems are equally effective for synthesizing both esters and amides, thus requiring to incorporate protecting groups in the starting materials to achieve optimal yields. Conversely, EDC·HCl can be reliably used for amide synthesis in the presence of unprotected hydroxyls.

Then, the scope of the EDC-promoted coupling was briefly investigated (Scheme 2). First, we explored the effect of the nucleophilicity of the amine partner on the amide coupling of **1** (Scheme 2a). As a result, more nucleophilic *N*-Boc piperazine smoothly delivered amide **8** in a high 91% yield, while the least nucleophilic electron-deficient ethyl 4-aminobenzoate and sterically hindered 2,4,6-trimethylaniline formed the corresponding amides **6** and **7** in reduced 76% and 77% yields, respectively. These results confirm that poor nucleophilic amines are less reactive, but still amenable substrates. Besides the hydroxycarboxylic acid **1**, the amino group in (4-(aminomethyl)phenyl)methanol was selectively acylated with benzoic acid, affording amide **9** in 85% yield, with no ester isomer of **9**

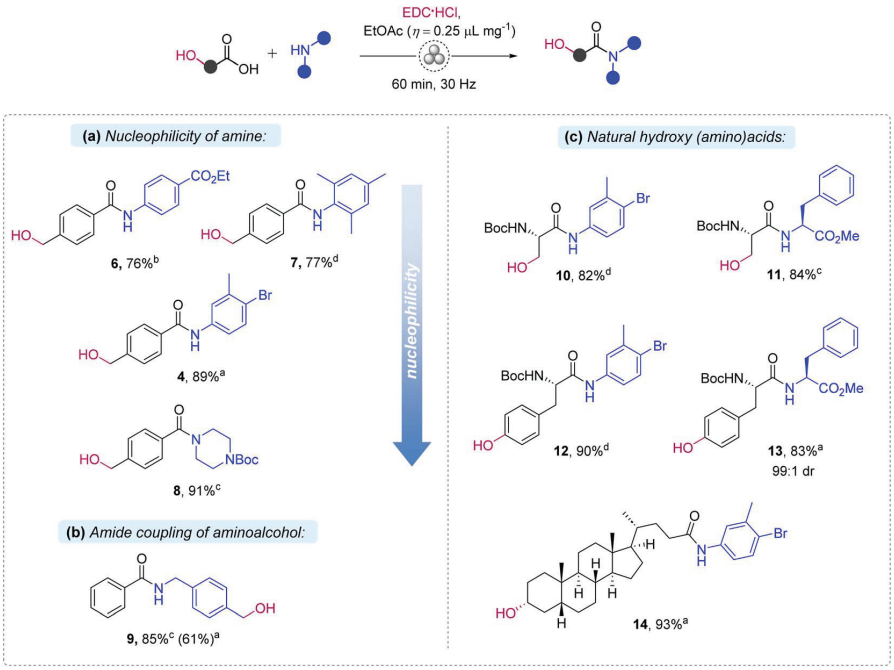

Scheme 2 Scope of EDC-mediated mechanochemical amide coupling: (a) influence of amine's nucleophilicity; (b) amide coupling of aminoalcohol; (c) synthesis of amides and dipeptides from natural hydroxy (amino)acids. [a]Yield of the isolated product after treatment with water, filtration and drying in air. [b]Yield determined by ^{1}H NMR with an internal standard. [c]Yield of the isolated product after extraction work-up. [d]Product isolated by silica gel column chromatography.

being formed (Scheme 2b). The outcome complies with the analogous reactions in solution[34,35] and by mechanochemistry.[26–28] Next, we explored hydroxyl group containing amino acids, namely *N*-Boc-L-serine and *N*-Boc-L-tyrosine, in the reaction with aniline **3** and L-phenylalanine methyl ester (Scheme 2c). Notably, previous examples of mechanochemical peptide coupling reactions relied on the use of hydroxyl-protecting groups in serine and tyrosine.[18,19] Amides **10** and **12** were prepared in good 82% and 90% yields in the reactions with **3**. However, column chromatography purification was needed in these cases to separate unreacted amine **3**. Dipeptides **11** and **13** were flawlessly prepared by coupling with L-phenylalanine methyl ester. Pure products were isolated in 84% and 83% yields after extractive workup. Importantly, dipeptide **13** was obtained with high diastereomeric purity (99 : 1 dr), indicating the absence of notable epimerization. Lithocholic acid in its coupling with **3** produced amide **14** in a high 93% yield, after simple treatment of the reaction mixture with water and drying in air. To compare the mechanochemical protocol with solution synthesis, dipeptide **11** was additionally prepared in CH_2Cl_2 solution. The solution-based reaction followed by extractive workup also afforded pure **11** in 90% yield, demonstrating that the chemoselectivity of the amide coupling is attributable to the coupling reagent rather than the mechanochemical conditions applied.

Subsequently, the EDC-mediated amide coupling protocol was employed in the synthesis of anticancer drug imatinib **2** (the trade name Gleevec®) from the World Health Organization's List of Essential Medicines.[8] The first synthetic route was patented in 1993 by Zimmermann,[36] followed by a number of improved protocols,[37–48] including flow-based approaches,[49–52] and microwave-assisted solid-phase synthesis.[53] However, mechanochemical preparations have not been reported yet.

Importantly, our planned route bypasses the formation of a chlorinated intermediate **17** with known genotoxic properties (Scheme 3), the content of which is strictly regulated (10 ppm)[41] and which is commonly encountered in the mainstream synthetic strategies.[38–40,44–47,49–51,53]

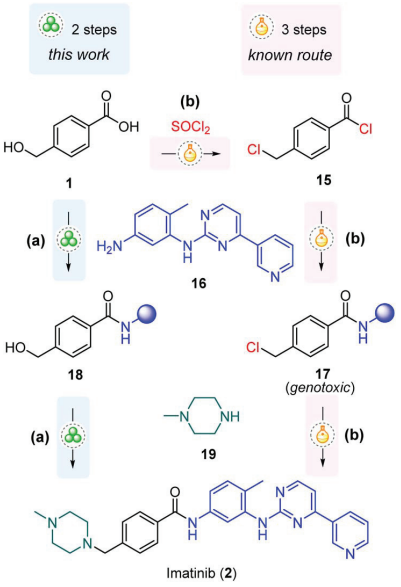

Scheme 3 The developed mechanochemical route (a) and previously reported mainstream solution-based (b) approach for the synthesis of imatinib (**2**).

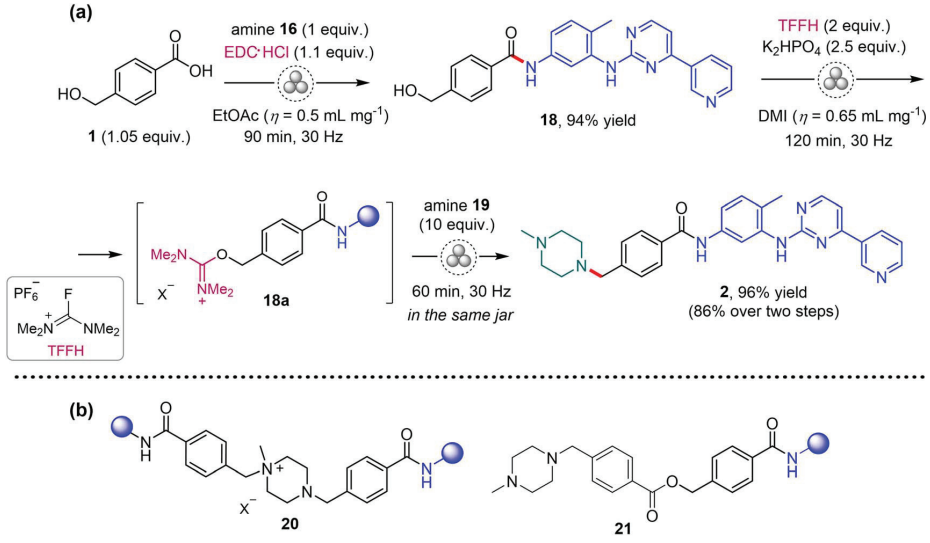

Scheme 4 (a) Mechanochemical synthesis of imatinib (**2**). DMI = dimethyl isosorbide. (b) The main impurities identified in the crude **2**.

After short optimization of the reaction conditions (see Tables S4 and S5 in the ESI†), imatinib **2** was prepared by EDC-mediated amide coupling of **1** with amine **16**, followed by nucleophilic substitution of the hydroxyl group in the formed amide **18** with 1-methylpiperazine **19** *via* generation of reactive isouronium intermediate **18a** (Scheme 4a).[7] The crude API was obtained in 86% overall yield, taking into account its 95% HPLC purity. The main impurities in **2** were identified as unreacted **18** (1.3%), quaternary salt **20** (2%) and **21** (1.4%; Scheme 4b). Purification of the crude **2** was achieved through recrystallization from a methanol-ethyl acetate mixture (1 : 1 ratio), yielding the target API with an HPLC purity of 99%. Crystals of intermediate **18** suitable for single-crystal X-ray diffraction analysis were obtained by crystallization from methanol solution and its solid-state structure was revealed, in a form of methanol solvate (CCDC 2287665, see Section 5 in the ESI†).

The genotoxic potential of intermediate **18** was checked by performing *in silico* assessment. Knowledge-based and statistical systems were used to predict potential mutagenicity following the recommendations of the ICH M7 (R1) (2018) guideline. As a result, **18** displayed no structural concern for mutagenicity. However, genotoxic amine **16** was still present in the product, in a content of *ca.* 560 ppm (see the ESI† for the details). This is similar to the content in the crude imatinib obtained by other methods and could be minimized during the downstream processing (see Section 6.2 in the ESI†).[54]

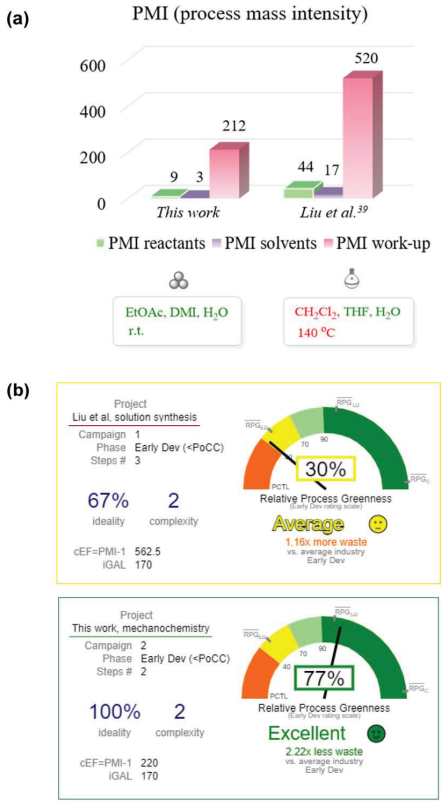

Fig. 1 (a) Comparison of PMI values for the mechanochemical and a benchmarking solution-based method.[39] (b) Graphical illustration of green chemistry innovation using the iGAL scorecard.

Next, we applied the CHEM21 toolkit[55] to reveal the advantages of the developed mechanochemical synthesis in comparison to the similar early-stage development solution protocol described by Liu *et al.*[39] (extended data and calculations for other similar routes are shown in Table S6 in the ESI†).

The main advantages of the mechanochemical protocol compared to the benchmarking solution-based approach included reduced process mass intensity (PMI, 221 *vs.* 564), the use of green and sustainable solvents (ethyl acetate, dimethyl isosorbide, and water) and room temperature operation (Fig. 1a). The exclusion of the genotoxic intermediate **17** (Scheme 3) was another important improve.

In order to expose the green chemistry-related innovations of the developed method even more clearly, we applied the "innovation Green Aspiration Level" (iGAL) methodology[56] by using the respective scorecard web calculator.[57] The mechanochemical method demonstrated an excellent relative process greenness (RPG) of 77%, which is much higher when compared to the RPG (30%) of the solution-based method by Liu *et al.*, used as a benchmark early-stage development process (Fig. 1b). Importantly, the mechanochemical approach exhibits a lower waste output of 2.22 times when compared to the average value at the early development stage. However, the developed methodology still relies on the use of stoichiometric coupling reagents (EDC·HCl and TFFH), which may pose environmental, safety or health hazards[58] and reduce the atom economy of the reaction. Consequently, there is a need for further development of mechanochemical amidation methods with improved atom efficiency through the avoidance of stoichiometric amide coupling reagents.[59]

Conclusions

Here we demonstrated that mechanochemical amide coupling can be performed with unprotected hydroxycarboxylic acids by using EDC·HCl as a coupling reagent in combination with ethyl acetate as a LAG additive. High 76–94% yields of amides can be achieved, while the use of poor nucleophilic amines results in reduced coupling efficacy. The presence of an unmasked hydroxyl group in the obtained amide products allows their straightforward functionalization in a step-economical manner, such as nucleophilic substitution of the hydroxyl group. The application is illustrated by the first mechanochemical synthesis of imatinib, an anticancer drug included in the World Health Organization's List of Essential Medicines. The target API was prepared in 86% total yield and HPLC purity of 99% through a two-fold mechanochemical C–N bond construction sequence.

Conflicts of interest

The authors declare no conflict of interest.

Acknowledgements

The research was supported by the Estonian Research Council grant PRG399 and COST Action CA18112 "Mechanochemistry for Sustainable Industry". This project has received funding from the European Union's Horizon 2021–2027 research and innovation programme under grant agreement No. 101057286 (IMPACTIVE). Danylo Merzhyievskyi is grateful to the Education and Youth Board of Estonia for financial support of his research stay at the Tallinn University of Technology.

References

1 P. Ying, J. Yu and W. Su, *Adv. Synth. Catal.*, 2021, **363**, 1246–1271.
2 O. Bento, F. Luttringer, T. Mohy El Dine, N. Pétry, X. Bantreil and F. Lamaty, *Eur. J. Org Chem.*, 2022, e202101516.
3 X. Yang, C. Wu, W. Su and J. Yu, *Eur. J. Org Chem.*, 2022, e202101440.
4 M. Pérez-Venegas and E. Juaristi, *ACS Sustainable Chem. Eng.*, 2020, **8**, 8881–8893.
5 O. Galant, G. Cerfeda, A. S. McCalmont, S. L. James, A. Porcheddu, F. Delogu, D. E. Crawford, E. Colacino and S. Spatari, *ACS Sustainable Chem. Eng.*, 2022, **10**, 1430–1439.
6 T. Dalidovich, K. A. Mishra, T. Shalima, M. Kudrjašova, D. G. Kananovich and R. Aav, *ACS Sustainable Chem. Eng.*, 2020, **8**, 15703–15715.
7 T. Dalidovich, J. V. Nallaparaju, T. Shalima, R. Aav and D. G. Kananovich, *ChemSusChem*, 2022, **15**, e202102286.
8 World Health Organization, *WHO Model List of Essential Medicines 23rd List*, 2023.
9 M. Tsakos, E. S. Schaffert, L. L. Clement, N. L. Villadsen and T. B. Poulsen, *Nat. Prod. Rep.*, 2015, **32**, 605–632.
10 B. Neises and W. Steglich, *Angew. Chem., Int. Ed.*, 1978, **17**, 522–524.
11 A. Chighine, S. Crosignani, M.-C. Arnal, M. Bradley and B. Linclau, *J. Org. Chem.*, 2009, **74**, 4753–4762.
12 J. K. Twibanire and T. B. Grindley, *Org. Lett.*, 2011, **13**, 2988–2991.
13 M. Pittelkow, F. S. Kamounah, U. Boas, B. Pedersen and J. B. Christensen, *Synthesis*, 2004, 2485–2492.
14 N. R. Luis, K. K. Chung, M. R. Hickey, Z. Lin, G. L. Beutner and D. A. Vosburg, *Org. Lett.*, 2023, DOI: **10.1021/acs.orglett.3c01611**.
15 H. Nishikawa, M. Kuwayama, A. Nihonyanagi, B. Dhara and F. Araoka, *J. Mater. Chem. C*, 2023, **11**, 12525–12542.
16 T.-X. Métro, J. Bonnamour, T. Reidon, J. Sarpoulet, J. Martinez and F. Lamaty, *Chem. Commun.*, 2012, **48**, 11781–11783.
17 W. I. Nicholson, F. Barreteau, J. A. Leitch, R. Payne, I. Priestley, E. Godineau, C. Battilocchio and D. L. Browne, *Angew. Chem., Int. Ed.*, 2021, **60**, 21868–21874.
18 L. Gonnet, T. Tintillier, N. Venturini, L. Konnert, J.-F. Hernandez, F. Lamaty, G. Laconde, J. Martinez and E. Colacino, *ACS Sustainable Chem. Eng.*, 2017, **5**, 2936–2941.
19 J. Bonnamour, T.-X. Métro, J. Martinez and F. Lamaty, *Green Chem.*, 2013, **15**, 1116–1120.
20 C. Bolm and J. G. Hernández, *ChemSusChem*, 2018, **11**, 1410–1420.
21 V. Štrukil, B. Bartolec, T. Portada, I. Đilović, I. Halasz and D. Margetić, *Chem. Commun.*, 2012, **48**, 12100–12102.
22 V. Porte, M. Thioloy, T. Pigoux, T.-X. Métro, J. Martinez and F. Lamaty, *Eur. J. Org Chem.*, 2016, 3505–3508.
23 C. Duangkamol, S. Jaita, S. Wangngae, W. Phakhodee and M. Pattarawarapan, *RSC Adv.*, 2015, **5**, 52624–52628.
24 T. Lainer, F. Czerny and M. Haas, *Org. Biomol. Chem.*, 2022, **20**, 3717–3720.
25 J. G. Hernández, K. J. Ardila-Fierro, D. Crawford, S. L. James and C. Bolm, *Green Chem.*, 2017, **19**, 2620–2625.
26 T. Portada, D. Margetić and V. Štrukil, *Molecules*, 2018, **23**, 3163.
27 Q. Cao, D. E. Crawford, C. Shi and S. L. James, *Angew. Chem., Int. Ed.*, 2020, **59**, 4478–4483.
28 F. Ravalico, S. L. James and J. S. Vyle, *Green Chem.*, 2011, **13**, 1778–1783.
29 M. Anselmi, P. Stavole, E. Boanini, A. Bigi, E. Juaristi and L. Gentilucci, *Future Med. Chem.*, 2020, **12**, 479–491.
30 F. Santino, R. Petruzzelli, J. Zhao, E. Boanini and L. Gentilucci, *Sustainable Chem. Pharm.*, 2021, **24**, 100540.
31 T. Kanzian, T. A. Nigst, A. Maier, S. Pichl and H. Mayr, *Eur. J. Org Chem.*, 2009, 6379–6385.
32 D. Prat, A. Wells, J. Hayler, H. Sneddon, C. R. McElroy, S. Abou-Shehada and P. J. Dunn, *Green Chem.*, 2016, **18**, 288–296.
33 N. Pétry, H. Benakki, E. Clot, P. Retailleau, F. Guenoun, F. Asserar, C. Sekkat, T.-X. Métro, J. Martinez and F. Lamaty, *Beilstein J. Org. Chem.*, 2017, **13**, 2169–2178.
34 D.-K. Kim, J. Y. Lee, J.-S. Kim, J.-H. Ryu, J.-Y. Choi, J. W. Lee, G.-J. Im, T.-K. Kim, J. W. Seo, H.-J. Park, J. Yoo, J.-H. Park, T.-Y. Kim and Y.-J. Bang, *J. Med. Chem.*, 2003, **46**, 5745–5751.
35 M. Parmentier, M. K. Wagner, K. Magra and F. Gallou, *Org. Process Res. Dev.*, 2016, **20**, 1104–1107.
36 J. Zimmermann, *EP Pat.*, 0564409, 1993.
37 B. J. Deadman, M. D. Hopkin, I. R. Baxendale and S. V. Ley, *Org. Biomol. Chem.*, 2013, **11**, 1766–1800.
38 Y. Heo, D. Hyun, M. R. Kumar, H. M. Jung and S. Lee, *Tetrahedron Lett.*, 2012, **53**, 6657–6661.
39 Y.-F. Liu, C.-L. Wang, Y.-J. Bai, N. Han, J.-P. Jiao and X.-L. Qi, *Org. Process Res. Dev.*, 2008, **12**, 490–495.
40 X. Zhang, J. Sun, T. Chen, C. Yang and L. Yu, *Synlett*, 2016, **27**, 2233–2236.
41 A. Kompella, B. R. K. Adibhatla, P. R. Muddasani, S. Rachakonda, V. K. Gampa and P. K. Dubey, *Org. Process Res. Dev.*, 2012, **16**, 1794–1804.
42 K. C. Nicolaou, D. Vourloumis, S. Totokotsopoulos, A. Papakyriakou, H. Karsunky, H. Fernando, J. Gavrilyuk, D. Webb and A. F. Stepan, *ChemMedChem*, 2016, **11**, 31–37.
43 C. Wang, X. Bai, R. Wang, X. Zheng, X. Ma, H. Chen, Y. Ai, Y. Bai and Y. Liu, *Org. Process Res. Dev.*, 2019, **23**, 1918–1925.
44 Z. Szakács, S. Béni, Z. Varga, L. Örfi, G. Kéri and B. Noszál, *J. Med. Chem.*, 2005, **48**, 249–255.
45 W. Szczepek, W. Luniewski, L. Kaczmarek, B. Zagrodzki, D. Samson-Lazinska, W. Szelejewski and M. Skarzynski, *World Pat.*, 2006071130A2, 2006.

46 A. Kompella, A. K. S. Bhujanga Rao, N. Venkaiah Chowdary and R. Srinivas, *World Pat.*, 2004108699A1, 2004.
47 O. Loiseleur, D. Kaufmann, S. Abel, H. M. Buerger, M. Meisenbach, B. Schmitz and G. N. Sedelmeier, *World Pat.*, 2003066613, 2003.
48 M. D. Khunt, N. S. Patil, H. S. Pagire and N. S. Pradhan, *World Pat.*, 2011095835A1, 2011.
49 M. D. Hopkin, I. R. Baxendale and S. V. Ley, *Chem. Commun.*, 2010, **46**, 2450–2452.
50 J. C. Yang, D. Niu, B. P. Karsten, F. Lima and S. L. Buchwald, *Angew. Chem., Int. Ed.*, 2016, **55**, 2531–2535.
51 N. Collins, D. Stout, J.-P. Lim, J. P. Malerich, J. D. White, P. B. Madrid, M. Latendresse, D. Krieger, J. Szeto, V.-A. Vu, K. Rucker, M. Deleo, Y. Gorfu, M. Krummenacker, L. A. Hokama, P. Karp and S. Mallya, *Org. Process Res. Dev.*, 2020, **24**, 2064–2077.
52 W. C. Fu and T. F. Jamison, *Org. Lett.*, 2019, **21**, 6112–6116.
53 F. Leonetti, C. Capaldi and A. Carotti, *Tetrahedron Lett.*, 2007, **48**, 3455–3458.
54 E. Grendele and A. Soldà, *Eur. Pat.*, 2927223B1, 2015.
55 C. R. McElroy, A. Constantinou, L. C. Jones, L. Summerton and J. H. Clark, *Green Chem.*, 2015, **17**, 3111–3121.
56 F. Roschangar, Y. Zhou, D. J. C. Constable, J. Colberg, D. P. Dickson, P. J. Dunn, M. D. Eastgate, F. Gallou, J. D. Hayler, S. G. Koenig, M. E. Kopach, D. K. Leahy, I. Mergelsberg, U. Scholz, A. G. Smith, M. Henry, J. Mulder, J. Brandenburg, J. R. Dehli, D. R. Fandrick, K. R. Fandrick, F. Gnad-Badouin, G. Zerban, K. Groll, P. T. Anastas, R. A. Sheldon and C. H. Senanayake, *Green Chem.*, 2018, **20**, 2206–2211.
57 **https://www.acs.org/green-chemistry-innovation-scorecard**, 2023.
58 J. C. Graham, A. Trejo-Martin, M. L. Chilton, J. Kostal, J. Bercu, G. L. Beutner, U. S. Bruen, D. G. Dolan, S. Gomez, J. Hillegass, J. Nicolette and M. Schmitz, *Chem. Res. Toxicol.*, 2022, **35**, 1011–1022.
59 T. Stolar, J. Alić, G. Talajić, N. Cindro, M. Rubčić, K. Molcanov, K. Užarević and J. G. Hernández, *Chem. Commun.*, 2023, **59**, 13490–13493.

Appendix 6

Publication VI

Tamm, J.; Kaabel, S.; Shubin, K.; Ward, J.S.; Adamson, J.; Aav, R. (2025). Solvent Exchange in Cobalt-Metal Organic Framework. *Supramolecular Chemistry*. DOI: 10.1080/10610278.2025.2587118

Supramolecular Chemistry

ISSN: 1061-0278 (Print) 1029-0478 (Online) Journal homepage: www.tandfonline.com/journals/gsch20

Solvent exchange in cobalt-metal organic framework

Jevgenija Tamm , Sandra Kaabel , Kirill Shubin , Jas S. Ward , Jasper Adamson & Riina Aav

To cite this article: Jevgenija Tamm , Sandra Kaabel , Kirill Shubin , Jas S. Ward , Jasper Adamson & Riina Aav (2026) Solvent exchange in cobalt-metal organic framework, Supramolecular Chemistry, 37:1-2, 22-27, DOI: 10.1080/10610278.2025.2587118

To link to this article: https://doi.org/10.1080/10610278.2025.2587118

SUPRAMOLECULAR CHEMISTRY
2026, VOL. 37, NOS. 1–2, 22–27
https://doi.org/10.1080/10610278.2025.2587118

Solvent exchange in cobalt-metal organic framework

Jevgenija Tamm[a], Sandra Kaabel[a,b], Kirill Shubin[c], Jas S. Ward[d], Jasper Adamson[e,f] and Riina Aav[a]

[a]Department of Chemistry and Biotechnology, Tallinn University of Technology, Tallinn, Estonia; [b]Department of Chemistry and Materials Science, Aalto University, Espoo, Finland; [c]Latvian Institute of Organic Synthesis, Riga, Latvia; [d]Department of Chemistry, University of Jyvaskyla, Jyväskylä, Finland; [e]Laboratory of Chemical Physics, National Institute of Chemical Physics and Biophysics, Tallinn, Estonia; [f]Virumaa College, School of Engineering, Tallinn University of Technology, Kohtla-Järve, Estonia

ABSTRACT

The cobalt-based framework $\{[Co_{1.5}(TTPA)(BTC)(H_2O)]_2 \cdot 13\ H_2O\}_n$ (Cobalt-MOF), assembled from *tris* (4-(1 H-1,2,4-triazol-1-yl)phenyl)amine (TTPA) and trimesic acid (BTC), was investigated for its capacity for guest inclusion and its stability during solvent exchange. Seven solvents were tested to replace residual DMF in as-synthesised crystals. The ^{1}H-NMR spectra were used to assess solvent exchange kinetics and the structural integrity was probed by single-crystal X-ray diffraction. Pyridine caused framework degradation, while chloroform and dioxane achieved significant exchange without major pore collapse. Cyclohexane showed the most promising profile for preserving crystallinity and facilitating guest inclusion. Incorporation of isosorbide as a guest was confirmed by NMR analysis, revealing a bi-exponential decay rate during sorption suggestive of bulk solvent exchange and subsequent conformational rearrangement of the guest inside the MOF pores during adsorption. These findings underline the importance of solvent choice in preserving MOF integrity and enabling guest capture, reinforcing Cobalt-MOF's potential as a crystalline sponge for small organic analytes.

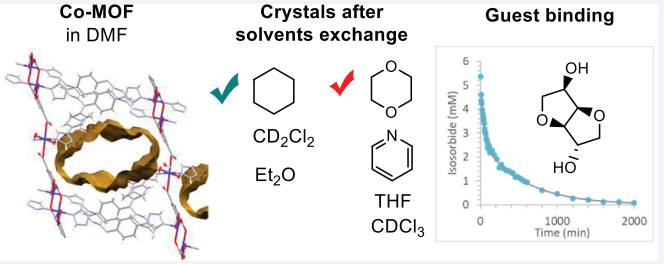

ARTICLE HISTORY
Received 10 September 2025
Accepted 3 November 2025

KEYWORDS
Metal-organic framework; solvent exchange; single crystal analysis; guest binding

Introduction

Metal-organic frameworks (MOFs), the developers of which were awarded with the Nobel Prize in Chemistry this year [1], represent a class of inorganic-organic hybrid materials endowed with a well-defined porous structure [2–6]. This characteristic enables them to absorb various molecules, such as liquids, volatile substances, natural compounds and also some chiral substances within their pores. The crystalline sponge method, pioneered by Fujita and collaborators [7–11], provides a means of characterising analytes in small quantities by complexing them into a metal-organic framework (MOF), which exhibits the capacity to absorb and desorb guest molecules [7–27].

MOFs selected for use in crystalline sponge method must possess the stability necessary to withstand the removal of solvents incorporated during their synthesis [23,28–31]. Additionally, MOFs should exhibit suitable interactions with analytes to ensure their uniform orientation within the framework's pores [32–34]. In certain instances, an initial incorporation of the analyte may be followed by an additional solvent exchange step [32–34]. This precautionary measure is taken to prevent the collapse of the porous network and enhance the likelihood of preserving the structural integrity of the metal-organic framework [32–34].

CONTACT Riina Aav riina.aav@taltech.ee Department of Chemistry and Biotechnology, Tallinn University of Technology, Akadeemia Tee 15, Tallinn 12618, Estonia

Supplemental data for this article can be accessed online at https://doi.org/10.1080/10610278.2025.2587118

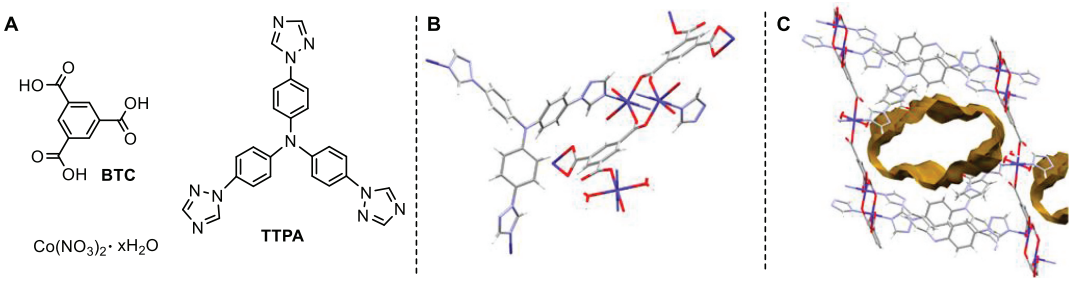

Figure 1. Structures of starting compounds (A), crystal structure of $\{[Co_{1.5}(TTPA)(BTC)(H_2O)]_2 \cdot 13H_2O\}_n$ CCDC 1,414,118 [35] highlighting coordination centres (B) and voids (C), water molecules omitted for clarity.

Cobalt-MOF ($\{[Co_{1.5}(TTPA)(BTC)(H_2O)]_2 \cdot 13\ H_2O\}_n$, Cobalt-MOF, CCDC 1,414,118) is a readily synthesisable metal-organic framework (MOF), made from tripodal *tris* (4-(1 H-1,2,4-triazol-1-yl)phenyl)amine (TTPA) ligand and trimesic acid (BTC) as a bridging ligand, coordinating high-spin cobalt (II) ions (Figure 1).

The structural elements of Cobalt-MOF foster formation of a porous network with varied interaction sites [35]. Due to its straightforward synthesis, high porosity, and the observation of high-quality single crystals, it potentially could accommodate organic analytes in its crystalline and porous framework, therefore acting as a crystalline sponge. Performing the solvent exchange before introducing an analyte proves to be a more time-efficient process compared to immediate insertion into the pores in the presence of the solvent used during synthesis. This approach enhances the likelihood of preserving the porous structure of the metal-organic network [32,36]. The consideration of using less polar solvents in the exchange process was driven by the intention to weaken electrostatic interactions, thereby facilitating subsequent binding interactions with small analytes within the MOF framework. In this study, the stability of the Cobalt-MOF metal-organic framework during solvent exchange and the kinetics of the latter process, as well as affinity of this Cobalt-MOF towards an organic guest, was studied.

Results and discussion

The synthesis of Cobalt-MOF was performed according to the known procedure and crystals with structure agreeing with literature data (CCDC 1414118) were chosen for solvent exchange experiments [35]. In samples synthesised for this work, a new solvate of the desired complex with mostly water and some dimethylformamide (DMF) solvate (DMF@Cobalt-MOF) was observed, so it was taken into consideration during solvent exchange experiments. Cyclohexane, diethyl ether, chloroform, 1,4-dioxane, tetrahydrofuran, pyridine, and dichloromethane (CH_2Cl_2) were selected as representative solvents, which vary in size, shape, surface tension, and polarity.

Ma and colleagues [32] observed exchange of DMF by dichloromethane and subsequently by n-hexane in Zn-based MOF UMCM-9; we hoped to learn if exchange of DMF in Cobalt-MOF crystals is feasible by the chosen solvents (Figure 2). Cobalt-based crystalline sponges might provide a more robust, symmetric, and chemically flexible platform for guest inclusion and X-ray structural

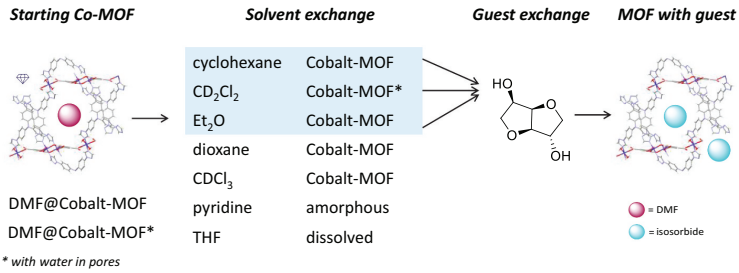

Figure 2. Outline of performed solvent and subsequent isosorbide exchange.

determination – especially in demanding scenarios involving harsh solvents, complex guests, or repeated exchange cycles, thus cobalt-based system was chosen for this study [37–39]. Any DMF that remained in Cobalt-MOF pores from MOF synthesis was exchanged by repeated submerging of the crystals into fresh solutions of the chosen solvents. Starting crystals of Cobalt-MOF contained *ca* 9 molecules of DMF per one unit cell, helping to evaluate solvent exchange kinetics, that was determined by following DMF concentration change via ^{1}H-NMR spectroscopy (Figure 2). Preservation of the $\{[Co_{1.5}(TTPA)(BTC)(H_2O)]_2{\cdot}13\,H_2O\}_n$ framework after the solvent exchange procedure was assessed by single-crystal X-ray diffraction (SCXRD) analysis. Subsequently, the suitability of Cobalt-MOF for binding the guest molecule isosorbide was also evaluated.

Measurements with SCXRD after the solvent exchange of DMF with studied solvents showed mixed results. Repeating the synthesis of Cobalt-MOF gave, besides the already published Cobalt-MOF crystal structure, another new solid-state structure (Cobalt-MOF*), which contained mostly water and some DMF solvates in its pores, as well as a slightly smaller pore size (approx. 2800 vs 2000 Å^3) (see SI Table S1). The breathing phenomenon of MOF structures is common upon a change of the surrounding environment [40–42].

From the seven solvents that were explored, the integrity of the porous MOF structure was preserved after solvent exchange with chloroform, dioxane, diethyl ether, dichloromethane, and cyclohexane, with the first three yielding unit cell parameters similar to Cobalt-MOF, and last two were in agreement with the water-populated Cobalt-MOF* crystal structure (see details in SI). Apart from previous results, addition of pyridine led to a loss of crystallinity, probably due to the competing Lewis base character of the pyridine, which was present in an overwhelming excess, that could lead to an exchange of ligands on the Co(II). In the presence of tetrahydrofuran, the cobalt-MOF dissolved (Figure 1). Crystal structure analysis showed that for most of the structures, a poorly defined hydrogen-bonding network of water molecules was present in some parts of the void, which might suggest that the added solvents are probably only exchanged in the part of the void where water molecules were not retained.

In addition to SCXRD analysis, solvent exchange was also followed by ^{1}H-NMR spectroscopy. The rise of the DMF concentration, due to its release from the MOF pores, during solvent exchange experiments is visualised in the upper graphs of Figure 3, with Table S2 detailing the rate constants of the fitted kinetics curves (additional details in SI).

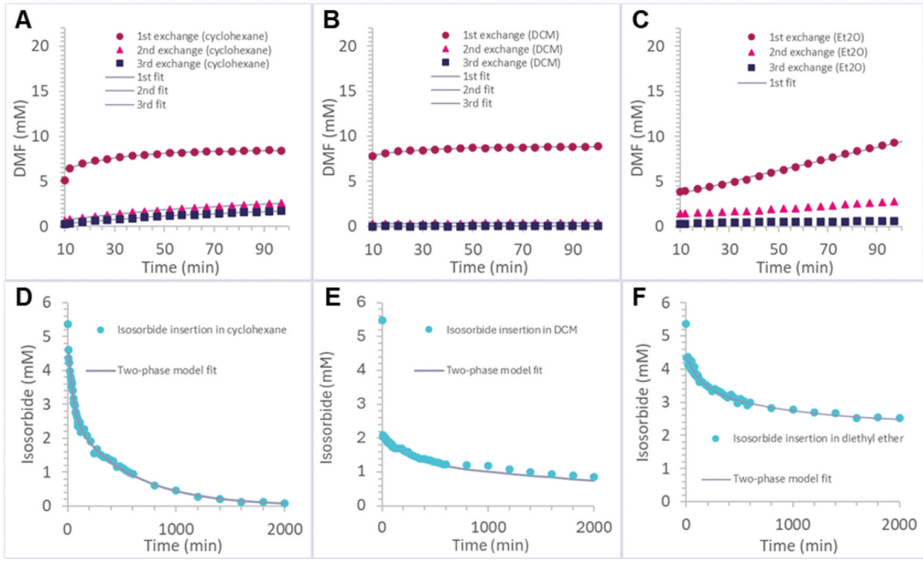

Figure 3. Kinetic data of solvent exchanges with cyclochexane (A), with CH_2Cl_2 (B), with Et_2O (C) and subsequent isosorbide binding to cobalt-MOF in cyclohexane (D), in CH_2Cl_2 (E) and in Et2O (F). See details in SI.

Each solvent was exchanged three times and the exchange kinetics fitted to the same function for all cycles, with the exception of diethyl ether. The release of DMF in cyclohexane, dichloromethane, and pyridine followed an exponential decay function, *e.g.*, in diethyl ether a linear function reflected the kinetic behaviour of the first solvent exchange experiment. Cyclohexane exchange showed well-fitting kinetics in all three solvent exchange steps, indicating the crystalline nature of MOF was maintained throughout. On the other hand, trends exhibited by CH_2Cl_2 in the ^{1}H-NMR spectroscopy kinetics experiments might back up the tendencies observed in the SCXRD measurements. As CH_2Cl_2 was observed to bind to the new MOF variant, Cobalt-MOF*, then the gradual rise of the kinetics curve from the NMR spectroscopy studies might indicate that the sample measured contained more of the Cobalt-MOF than Cobalt-MOF*, with the latter being more prone to solvent exchange, thus its smaller rise in DMF concentration. Although the crystal structure for chloroform was measured, the observed NMR spectra displayed comparatively rapid solvent exchange within the first two hours. However, upon addition of chloroform to the crystalline MOF samples, crystals rose to the surface indicating that the crystals were less dense than the chloroform. In the case of 1,4-dioxane, despite the fact that SCXRD data showed that the solvent is displacing the DMF, NMR spectroscopy experiments exhibited the same demeanour as chloroform. Unfortunately, the fit of the diethyl ether kinetics did not demonstrate an unambiguous result, even though the kinetics curves indicated the release of some DMF into the solution. The surface tension of pyridine is similar to that of DMF, but it is a much stronger Lewis base than DMF, leading to pore collapse and loss of crystallinity upon exposure to pyridine, this was also evident by ^{1}H-NMR spectroscopy during the isosorbide binding experiment (Figure S3).

As the evacuation of the pores of DMF was largely successful, the guest molecule isosorbide was subsequently introduced to the treated MOF crystals by adding an isosorbide solution, in an appropriate solvent, onto the crystalline MOF. The guest insertion into the pores of Cobalt-MOF was measured by ^{1}H-NMR spectroscopy by following the gradual decay of the isosorbide concentration in solution around the Cobalt-MOF crystals (Figure 3, lower graphs). In all three instances, the observed decrease of isosorbide concentration converged to a bi-exponential decay model (details in SI). This reflects the occurrence of several simultaneous processes, which have distinct rates, each with a unique half-life and occurring in parallel. We observed that rate constants vary, depending on the solvent that is replaced from the cavities, therefore we postulate that perhaps faster exchange occurs via replacement of bulk solvent molecules in the MOF channels and slow exchange might be caused by the additional positional rearrangement of relatively rigid isosorbide guest and subsequent formation of specific hydrogen bonding inside the MOF pores. This two-step process would allow tighter packing of the guest. Again, CH_2Cl_2 demonstrated some questionable trends as the initial concentration of the isosorbide drops drastically in the first 10 minutes, and the change of concentration after that slows down, never reaching the same levels as was the case for cyclohexane and pyridine. All of this suggests that in the case of CH_2Cl_2 partial pore collapse may occur, slowing down the encapsulation of the guest. Studies of diethyl ether displayed similar trends to that of cyclohexane initially, but then decelerated quite fast, never reaching the same concentration levels. This indicates that isosorbide is only partially exchanging with diethyl ether. Unfortunately, SCXRD analysis of crystals after guest binding did not yield the guest structure inside the MOF pores, either due to an insufficient number populating the cavity or a large amount of disorder of the guest molecules inside the MOF pores.

Conclusions

The investigation of the Cobalt-MOF metal-organic framework, a cobalt-based MOF constructed from TTPA and BTC ligands, demonstrates that effective solvent exchange is critical for preserving the framework's porous architecture and enabling its function as a crystalline sponge. The results indicate that the choice of solvent substantially influences the stability and crystallinity of the MOF during exchange of the residual DMF from synthesis. The solvents cyclohexane, dichloromethane, chloroform, Et_2O, and 1,4-dioxane maintained the structural integrity of the MOF during solvent exchange, however, only cyclohexane, dichloromethane and Et_2O allowed absorption of a guest. Use of pyridine as a solvent led to significant degradation of the framework, presumably due to its strong Lewis base character interfering with the coordinating triazole groups that the MOF architecture is comprised of. Moreover, differences in exchange kinetics, as monitored via ^{1}H-NMR spectroscopy, revealed a biphasic sorption behaviour when incorporating the guest molecule isosorbide, indicating that during guest absorption after fast replacement of some solvent molecules, subsequent rearrangement of the guest position and interactions allow tighter packing of the guest in the MOF pores. These observations underscore the necessity of selecting solvents that not only remove synthesis remnants effectively but also

minimise deleterious interactions with the MOF structure. Ultimately, this study reinforces the potential of Cobalt-MOF as a robust crystalline sponge, contingent upon optimised solvent conditions that safeguard its porous network while promoting targeted guest absorption.

Author contributions

CRediT: **Jevgenija Tamm:** Data curation, Formal analysis, Investigation, Methodology, Validation, Visualization, Writing – original draft, Writing – review & editing; **Sandra Kaabel:** Data curation, Investigation, Methodology, Supervision; **Kirill Shubin:** Methodology, Resources, Supervision; **Jas S. Ward:** Data curation, Formal analysis, Investigation, Supervision, Writing – review & editing; **Jasper Adamson:** Conceptualization, Data curation, Investigation, Methodology, Supervision; **Riina Aav:** Conceptualization, Data curation, Funding acquisition, Investigation, Methodology, Resources, Supervision, Visualization, Writing – review & editing.

Disclosure statement

No potential conflict of interest was reported by the author(s).

Funding

The research was funded by Estonian Research Council grant [PRG2169], and by the Ministry of Education and Research through Centre of Excellence in Circular Economy for Strategic Mineral and Carbon Resources [01.01.2024–-31.12.2030, TK228]. The project "Increasing the knowledge intensity of Ida-Viru entrepreneurship" co-funded by the European Union [2021–2017.6.01.23–0034].

Data availability statement

All experimental and characterisation data and detailed experimental procedures are available in the published article and ESI.

References

[1] Nobel Prize in Chemistry 2025. NobelPrize.org. [cited 2025 10 14]. Available from: https://www.nobelprize.org/prizes/chemistry/2025/press-release/
[2] Furukawa H, Cordova KE, O'Keeffe M, et al. The chemistry and applications of metal-organic frameworks. Science. **2013**;341(6149):1230444. doi: 10.1126/science.1230444
[3] Yaghi OM, O'Keeffe M, Ockwig NW, et al. Reticular synthesis and the design of new materials. Nature. **2003**;423(6941):705–714. doi: 10.1038/nature01650
[4] Guo J, Chu S, Yuan F, et al. Soft porous crystals: flexible MOFs as a new class of adaptive materials. Ind Chem Mater. **2025**. doi: 10.1039/D5IM00067J
[5] Kitagawa S, Kitaura R, Noro S. Functional porous coordination polymers. Angew Chem Int Ed. **2004**;43(18):2334–2375. doi: 10.1002/anie.200300610
[6] Batten SR, Robson R. Interpenetrating nets: ordered, periodic entanglement. Angew Chem Int Ed. **1998**;37(11):1460–1494. doi: 10.1002/(SICI)1521-3773(19980619)37:11<1460:AID-ANIE1460>3.0.CO;2-Z
[7] Inokuma Y, Yoshioka S, Ariyoshi J, et al. X-ray analysis on the nanogram to microgram scale using porous complexes. Nature. **2013**;495(7442):461–466. doi: 10.1038/nature11990
[8] Yoshioka S, Inokuma Y, Hoshino M, et al. Absolute structure determination of compounds with axial and planar chirality using the crystalline sponge method. Chem Sci. **2015**;6(7):3765–3768. doi: 10.1039/C5SC01681A
[9] Hoshino M, Khutia A, Xing H, et al. The crystalline sponge method updated. IUCrJ. **2016**;3(2):139–151. doi: 10.1107/S2052252515024379
[10] Yan K, Dubey R, Arai T, et al. Chiral crystalline sponges for the absolute structure determination of chiral guests. J Am Chem Soc. **2017**;139(33):11341–11344. doi: 10.1021/jacs.7b06607
[11] He W, Yu Y, Iizuka K, et al. Supramolecular coordination cages as crystalline sponges through a symmetry mismatch strategy. Nat Chem. **2025**;17(5):653–662. doi: 10.1038/s41557-025-01750-x
[12] Bloch WM, Champness NR, Doonan CJ. X-ray crystallography in open-framework materials. Angew Chem Int Ed. **2015**;54(44):12860–12867. doi: 10.1002/anie.201501545
[13] Choi D, Lee H, Lee JJ, et al. Practical porous matrix for molecular structure determination of general liquid chemicals. Cryst Growth Des. **2017**;17(12):6677–6683. doi: 10.1021/acs.cgd.7b01301
[14] Rizzuto FJ, Carpenter JP, Nitschke JR. Multisite binding of drugs and natural products in an entropically favorable, heteroleptic receptor. J Am Chem Soc. **2019**;141(22):9087–9095. doi: 10.1021/jacs.9b03776
[15] Zhang S-Y, Fairen-Jimenez D, Zaworotko MJ. Structural elucidation of the mechanism of molecular recognition in chiral crystalline sponges. Angew Chem Int Ed. **2020**;59(40):17600–17606. doi: 10.1002/anie.202006438
[16] Wada Y, Usov PM, Chan B, et al. Atomic-resolution structure analysis inside an adaptable porous framework. Nat Commun. **2024**;15(1):81. doi: 10.1038/s41467-023-44401-w
[17] Song J-G, Zheng J, Wei R-J, et al. Crystalline mate for structure elucidation of organic molecules. Chem. **2024**;10(3):924–937. doi: 10.1016/j.chempr.2023.12.004
[18] Liu J-C, Huang W-P, Tian Y-X, et al. A new versatile crystalline sponge for organic structural analysis without the need for activation. J Mater Chem A. **2024**;12(21):12609–12618. doi: 10.1039/D3TA07946E
[19] Rissanen K. Crystallography of encapsulated molecules. Chem Soc Rev. **2017**;46(9):2638–2648. doi: 10.1039/C7CS00090A
[20] Ward AR, Snow CD. Porous crystals as scaffolds for structural biology. Curr Opin Struct Biol. **2020**;60:85–92. doi: 10.1016/j.sbi.2019.12.008
[21] Liu W, Stoddart JF. Emergent behavior in nanoconfined molecular containers. Chem. **2021**;7(4):919–947. doi: 10.1016/j.chempr.2021.02.016

[22] Habib F, Tocher DA, Carmalt CJ. Applications of the crystalline sponge method and developments of alternative crystalline sponges. Mater Today Proc. **2022**;56:3766–3773. doi: 10.1016/j.matpr.2022.01.018
[23] Metherall PJ, Carroll CR, Coles JS, et al. Advanced crystallisation methods for small organic molecules. Chem Soc Rev. **2023**;52(6):1995–2010. doi: 10.1039/D2CS00697A
[24] Li H, Li Y, Jiao J, et al. Recent research progress on crystallization strategies for difficult-to-crystallize organic molecules. Results Chem. **2023**;5:100859. doi: 10.1016/j.rechem.2023.100859
[25] Kubota R, Tashiro S, Shiro M, et al. In situ X-ray snapshot analysis of transient molecular adsorption in a crystalline channel. Nat Chem. **2014**;6(10):913–918. doi: 10.1038/nchem.2044
[26] Han Z, Huang W, Cheng P, et al. Functional guest in metal-organic frameworks. Chin J Chem. **2025**;43(8):956–966. doi: 10.1002/cjoc.202401056
[27] Li S, Yu L, Zhou X, et al. Molecular sieving separation of hexane isomers by an aluminum-based metal-organic framework with NIA topology. Chin J Chem. **2025**;43(20):2637–2641. doi: 10.1002/cjoc.70149
[28] Yang X-Y, Yuan S, Qin J-S, et al. A flexible thioether-based MOF as a crystalline sponge for structural characterization of liquid organic molecules. Mater Chem Front. **2017**;1(9):1764–1767. doi: 10.1039/C7QM00152E
[29] Peng S, Ji X, Dong H, et al. Designing MOFs/CuCo-LDHs hybrid-based superhydrophobic sponge for speedy eliminating microplastics, dyes, and oils from high-salinity water. Colloids Surf Physicochem Eng Asp. **2024**;692:133996. doi: 10.1016/j.colsurfa.2024.133996
[30] Tang S, Wang Y, He P, et al. Recent advances in metal–organic framework (MOF)-based composites for organic effluent remediation. Materials. **2024**;17(11):2660. doi: 10.3390/ma17112660
[31] Habib F, Tocher AD, Carmalt JC. Encapsulation of N-containing compounds in a new hydrophilic Cd-based crystalline sponge via coordinative alignment method. Cryst Eng Comm. **2023**;25(35):5001–5011. doi: 10.1039/D3CE00592E
[32] Ma J, Kalenak AP, Wong-Foy AG, et al. Rapid guest exchange and ultra-low surface tension solvents optimize metal–organic framework activation. Angew Chem Int Ed. **2017**;56(46):14618–14621. doi: 10.1002/anie.201709187
[33] Woo H, Devlin AM, Matzger AJ. In situ observation of solvent exchange kinetics in a MOF with coordinatively unsaturated sites. J Am Chem Soc. **2023**;145(33):18634–18641. doi: 10.1021/jacs.3c06396
[34] Wright KR, Nath K, Matzger AJ. Superior metal-organic framework activation with dimethyl ether. Angew Chem Int Ed. **2022**;61(52):e202213190. doi: 10.1002/anie.202213190
[35] Shi Z, Pan Z, Zhang C, et al. Syntheses, structures, and properties of six cobalt(II) complexes based on a tripodal tris(4-(1H-1,2,4-triazol-1-yl)phenyl)amine ligand. Dalton Trans. **2015**;44(38):16854–16864. doi: 10.1039/C5DT02774H
[36] Woo H, Robinson JW, Matzger AJ. Solvent exchange dynamics in M2(DOBDC): an interplay among binding strength, exchange kinetics, and cooperativity. J Am Chem Soc. **2024**;146(26):18136–18142. doi: 10.1021/jacs.4c05355
[37] Do HH, Truong HB. Ni, Co, Zn, and Cu metal-organic framework-based nanomaterials for electrochemical reduction of CO2: a review. Beilstein J Nanotechnol. **2023**;14:904–911. doi: 10.3762/bjnano.14.74
[38] Zhang J, Zhu E, Li R, et al. Research progress of cobalt-based metal organic frameworks and their derivatives in energy storage and conversion. ACS Omega. **2024**;9(47):46643–46663. doi: 10.1021/acsomega.4c06571
[39] Dhakshinamoorthy A, Montero Lanzuela E, Navalon S, et al. Cobalt-based metal organic frameworks as solids catalysts for oxidation reactions. Catalysts. **2021**;11(1):95. doi: 10.3390/catal11010095
[40] Zhao P, Tsang SCE, Fairen-Jimenez D. Structural heterogeneity and dynamics in flexible metal-organic frameworks. Cell Rep Phys Sci. **2021**;2(9):100544. doi: 10.1016/j.xcrp.2021.100544
[41] Formalik F, Neimark AV, Rogacka J, et al. Pore opening and breathing transitions in metal-organic frameworks: coupling adsorption and deformation. J Colloid Interface Sci. **2020**;578:77–88. doi: 10.1016/j.jcis.2020.05.105
[42] Senkovska I, Bon V, Abylgazina L, et al. Understanding MOF flexibility: an analysis focused on pillared layer MOFs as a model system. Angew Chem Int Ed. **2023**;62(33):e202218076. doi: 10.1002/anie.202218076

Appendix 7

Publication VII

Suut-Tuule, E.; Jarg, T.; Tikker, P.; Lootus, K.-M.; Martõnova, J.; Reitalu, R.; Ustrnul, L.; Ward, J. S.; Rjabovs, V.; Shubin, K.; Nallaparaju, J. V.; Vendelin, M.; Preis, S.; Öeren, M.; Rissanen, K.; Kananovich, D.; Aav, R. (2024). Mechanochemically driven covalent self-assembly of a chiral mono-biotinylated hemicucurbit[8]uril. *Cell Reports Physical Science*, 5, 9. DOI: 10.1016/j.xcrp.2024.102161

Cell Reports
Physical Science

CellPress
OPEN ACCESS

Article

Mechanochemically driven covalent self-assembly of a chiral mono-biotinylated hemicucurbit[8]uril

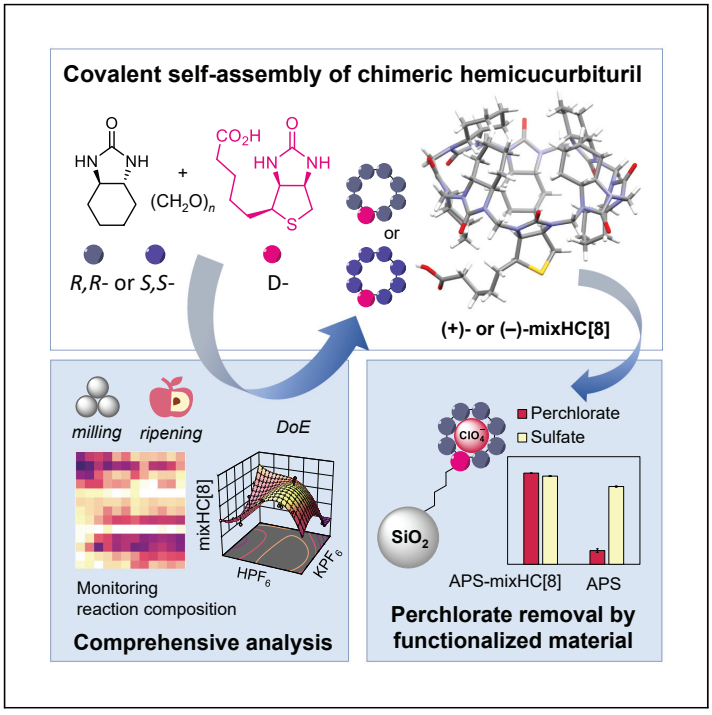

Suut-Tuule and Jarg et al. demonstrate that mechanochemistry enhances reactivity and significantly improves selectivity in the solid-state synthesis of mono-biotinylated hemicucurbit[8]urils. The application of the chimeric macrocycle is showcased by its immobilization on silica and subsequent use as a selective solid-phase extraction material for perchlorate removal.

Elina Suut-Tuule, Tatsiana Jarg, Priit Tikker, ..., Kari Rissanen, Dzmitry Kananovich, Riina Aav

riina.aav@taltech.ee

Highlights

Dynamic covalent chemistry in solid state delivers chimeric hemicucurbit[8]urils

Two major products are amplified from ca. 50,000 possible compounds

Mechanochemistry and anionic templation drive covalent self-assembly

Silica modified by biotinylated macrocycle is suitable for perchlorate capture

Suut-Tuule et al., Cell Reports Physical Science 5, 102161
September 18, 2024
https://doi.org/10.1016/j.xcrp.2024.102161

Cell Reports
Physical Science

CellPress
OPEN ACCESS

Article

Mechanochemically driven covalent self-assembly of a chiral mono-biotinylated hemicucurbit[8]uril

Elina Suut-Tuule,[1,8] Tatsiana Jarg,[1,8] Priit Tikker,[2] Ketren-Marlein Lootus,[1] Jevgenija Martõnova,[1] Rauno Reitalu,[1] Lukas Ustrnul,[1] Jas S. Ward,[3] Vitalijs Rjabovs,[4,5] Kirill Shubin,[6] Jagadeesh V. Nallaparaju,[1] Marko Vendelin,[7] Sergei Preis,[2] Mario Öeren,[1] Kari Rissanen,[3] Dzmitry Kananovich,[1] and Riina Aav[1,9,10,*]

SUMMARY

Solution-based synthesis of complex molecules with high efficiency leverages supramolecular control over covalent bond formation. Herein, we present the mechanosynthesis of chiral mono-biotinylated hemicucurbit[8]urils (mixHC[8]s) via the condensation of D-biotin, (*R,R*)- or (*S,S*)-cyclohexa-1,2-diylurea, and paraformaldehyde. The selectivity of self-assembly is enhanced through mechanochemistry and by fostering non-covalent interactions, achieved by eliminating solvents and conducting the reaction in the solid state. Rigorous analysis of intermediates reveals key processes and chemical parameters influencing dynamic covalent chemistry. The library of ca. 50,000 theoretically predicted intermediates and products leads to covalent self-assembly of chiral hemicucurbiturils. Mechanochemically prepared diastereomeric (−)- and (+)-mixHC[8]s are suitable for anion binding and derivatization. Immobilization of the macrocycles on aminated silica produces a functional material capable of selective capture of anions, as demonstrated by efficient perchlorate removal from a spiked mineral matrix.

INTRODUCTION

The spontaneous organization of molecular species relies on non-covalent interactions, resulting in intricate aggregates. Such supramolecular self-assembly can facilitate the formation of covalent bonds leading to complex molecules and may be exceptionally responsive to minor changes in the reaction conditions, resulting in the amplification of particular products.[1] In the case of increased molecular crowding, the dynamics of an interaction between species is accelerated compared to a dilute environment, which has been demonstrated for strongly hydrogen-bonded base pairs of nucleic acids.[2] Furthermore, in the solid state at extreme concentrations, unobstructed by solvent, the number of non-covalent interactions between counterparts increases, enabling the formation of products that are less favored in solution.[3,4] Mechanochemical activation enhances chemical reactivity and provides a solvent-free sustainable approach in chemical syntheses.[5–7]

Single-bridged cucurbituril-type molecular containers, hemicucurbit[*n*]urils (HC[*n*]s) are renowned for their anion-binding properties and typically assembled from urea monomers in a one-pot reaction with dynamic covalent chemistry (DCC).[8–10] Although the size of the macrocycle can be controlled by anion templation,[8,11–15] HC[*n*]s prevalently consist of six units.[12,16,17] Up to date, 8-membered HC[*n*]s have been synthesized exclusively from chiral C_2-symmetric cyclohexa-1,2-diylurea (CU)

[1]Tallinn University of Technology, Department of Chemistry and Biotechnology, 12618 Tallinn, Estonia

[2]Tallinn University of Technology, Department of Materials and Environmental Technology, 19086 Tallinn, Estonia

[3]University of Jyvaskyla, Department of Chemistry, 40014 Jyväskylä, Finland

[4]National Institute of Chemical Physics and Biophysics, 12618 Tallinn, Estonia

[5]Institute of Chemistry and Chemical Technology, Riga Technical University, 1048 Riga, Latvia

[6]Latvian Institute of Organic Synthesis, 1006 Riga, Latvia

[7]Tallinn University of Technology, Department of Cybernetics, 12618 Tallinn, Estonia

[8]These authors contributed equally

[9]X (formerly Twitter): @RiinaAav

[10]Lead contact

*Correspondence: riina.aav@taltech.ee

https://doi.org/10.1016/j.xcrp.2024.102161

monomers, and the corresponding (*R*,*R*)- and (*S*,*S*)-cyclohexanohemicucurbit[8]urils (cycHC[8]s) can be assembled both in solution[18] and the solid state.[17] Their larger cavity expands the range of applications, and the insertion of another functional monomer, such as D-biotin, into the cycHC[8] scaffold can further enhance receptor versatility. Biotin is a naturally occurring and commercially available compound with a carboxylic group suitable for derivatization. Furthermore, it has previously been used in the synthesis of chiral macrocycles.[13] So far, the reported chimeric HC[*n*]s assembled from non-equivalent urea monomers have been limited to 6-membered hybrid HC[*n*]s prepared in solution via multi-step approaches[19,20] and mono-functionalized bambus[6]urils obtained in a one-pot reaction.[21–23] The difficulties in the single-step formation of non-uniformly composed macrocycles arise from a plethora of possible linear and cyclic intermediates. Consequently, arranging a chaotic mixture into a well-organized molecule presents considerable challenges, and the number of combinations increases with the number of monomeric units.

Mechanochemistry has been utilized in the synthesis of several macrocycles,[17,24–30] inducing covalent assembly of uniformly structured monomers. As mechanosynthesis enables overcoming the solubility barriers and promotes reactions between compounds with drastic polarity differences, its potential can be exploited even further. To the best of our knowledge, there have been no reports describing covalent self-assembly of macrocycles from mixtures of various monomers in the solid state. The formation of chiral chimeric HC[*n*]s via DCC in the solid state could pave the way to novel synthetic approaches, unlocking access to versatile applications.

The present work describes a mechanochemically activated solid-state condensation of (*R*,*R*)- or (*S*,*S*)-CU, D-biotin ((*S*,*S*,*R*)-B), and paraformaldehyde and their selective covalent self-assembly into the enantiopure mono-biotinylated HC[8]s (−)-((*S*,*S*,*R*)(*R*,*R*)$_7$)-mixHC[8] or (+)-((*S*,*S*,*R*)(*S*,*S*)$_7$)-mixHC[8], along with homomeric cycHC[8]s. The challenges of assembling a chimeric mono-functionalized 8-membered macrocycle are related to the number of possible combinations of monomeric units and their chemical reactivity. Fine-tuning of the reaction conditions enabled amplification of the two major products, chimeric mixHC[8] and homomeric cycHC[8], among 498 potential 8-membered HC[*n*]s[31] (Figure 1; theoretical number of linear cyclic oligomers in the supplemental experimental procedures; Data S1).

The covalent assembly process is essentially solvent free and has a very low process mass intensity (PMI; the mass of all used reagents per formed product[32]). The most significant chemical and technical factors affecting macrocyclization were identified with response surface methodology (RSM) and thorough analysis of intermediates by high-performance liquid chromatography-mass spectrometry (HPLC-MS) provided mechanistic insight into this complex process. The affinity of mixHC[8] for selected anions and the subtle differences in the binding properties of the two chimeric diastereomers were determined by isothermal titration calorimetry (ITC) and characterized by single-crystal X-ray crystallography (SC-XRD) and modeling studies. Furthermore, a practical example of the selective anion capture by silica-immobilized mixHC[8] was demonstrated in the efficient removal of perchlorate from a spiked mineral matrix.

RESULTS AND DISCUSSION

Covalent assembly of hemicucurbiturils in the solid state

The first attempts to synthesize mono-functionalized mixHC[8] in solution according to the protocol developed for cycHC[8][18] were promising. The condensation of

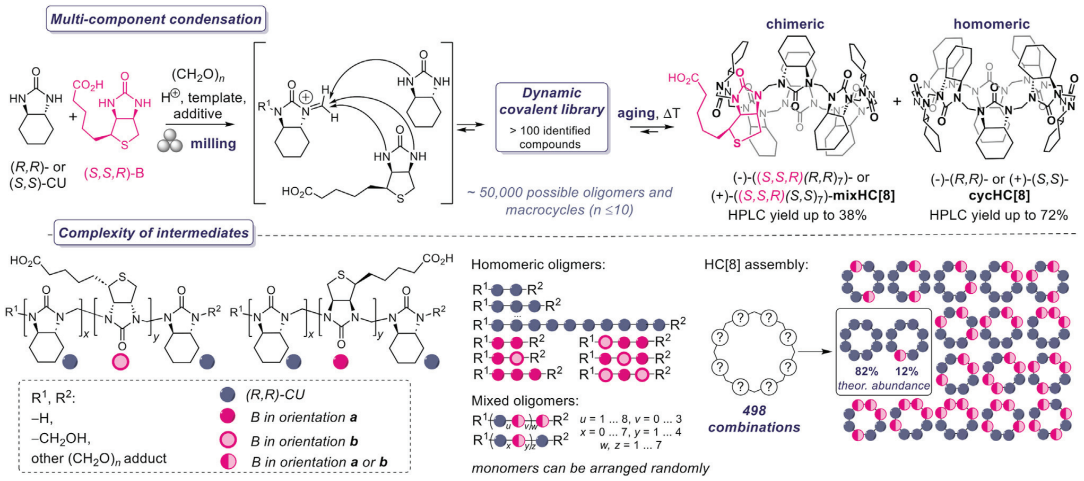

Figure 1. Synthetic scheme and complexity of intermediates during formation of the HC[8]s studied in this work

Multi-component condensation of (*S,S,R*)-biotin (B) and (*R,R*)- or (*S,S*)-cyclohexa-1,2-diylurea (CU) to homomeric cycHC[8]s and chimeric mixHC[8]s. The complexity of the intermediates in the DCL is expressed via possible numbers of oligomers, HC[8]s, and the abundance of major HC[8]s resulting from the 1:7 (B:CU) ratio of starting materials (theoretical number of linear cyclic oligomers in the supplemental experimental procedures; Data S1). The best reaction conditions afford 38% and 34% yields of mixHC[8] and cycHC[8], respectively: 1 equiv B, 7 equiv CU, 8 equiv $(CH_2O)_n$ in the presence of 2 equiv HPF_6 and 1 equiv KPF_6, milled at 30 Hz for 60 min and aged at 60°C for 3 h. (Table S15). The highest yield (72%) of cycHC[8] was observed under the following conditions: 1 equiv B, 15 equiv CU, 16 equiv $(CH_2O)_n$ in the presence of 3 equiv $HClO_4$, milled at 30 Hz for 60 min and aged at 45°C for 24 h (Table S2).

biotin and CU taken in stoichiometric 1:7 molar ratio with paraformaldehyde, mediated by trifluoroacetic acid in acetonitrile, produced mixHC[8] and cycHC[8] in 9% and 38% yields, respectively (see synthesis in solution in the supplemental experimental procedures; Data S1). The ratio of the macrocycles did not reflect the statistical distribution based on the starting monomer ratio, which implied a strong influence of the chemical parameters. In solution-based synthesis, compatibility between the solvent and reagents governs the fast diffusion and mixing of starting materials, intermediates, and products, as well as their reactivity. Poor solubility can obstruct reactions, especially in DCC, due to suppressed exchange between reactants. We envisioned that mixHC[8]s may be assembled with higher efficiency in the solid state, where solubility is not critical, non-covalent interactions are not obstructed by the solvent, and templation is enhanced due to a high concentration of reactants.[3] According to the previous study,[17] covalent self-assembly in the solid state required just a minute amount of a liquid additive[33–35] to facilitate proton transfer and delivery of the anionic template, as well as to promote conformational flexibility. The complexity of the dynamic covalent library (DCL) drastically increases in multi-component reactions; for instance, the incorporation of non-C_2 symmetric (*R,S*)-CU units resulted in higher stereochemical diversity and the formation of several diastereomeric HC[*n*]s (i.e., *cis*-cycHC[6] and inverted-*cis*-cycHC[6]).[36] Similarly, condensation of chiral CU and non-C_2 symmetric biotin into linear and cyclic oligomers can be realized via various combinations, considering the possibility of different orientations of the biotin unit (Figure 1). For instance, all forms with a length of 2 to 10 monomers result in ca. 50,000 cyclic and linear oligomers. However, the number of possible products can be decreased by templation. Variation of position, orientation, and number of B and CU monomers leads to 498 potential 8-membered macrocycles[31] (Figure 1; theoretical number of linear cyclic oligomers in the

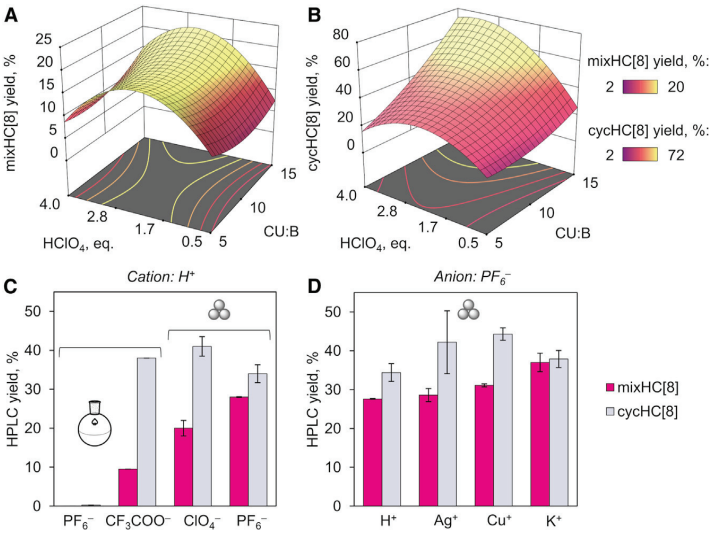

Figure 2. 3D response surfaces and bar charts expressing the formation of HC[8]s

(A and B) 3D response surfaces displaying the influence of the ratio of monomers and loading of aq. $HClO_4$ on the HPLC yields of (A) mixHC[8] and (B) cycHC[8].

(C and D) Bar charts comparing the effect of the acid anions (CF_3COO^-, ClO_4^-, and PF_6^-) in solution and the solid state (C) and hexafluorophosphate salt cations (Ag^+, Cu^+, K^+) in the solid state (D) on the yields of cycHC[8] (gray) and mixHC[8] (magenta). Error bars on HPLC yields express standard deviation between reproduced reactions (n= 2–8). For more details, see Table S7.

supplemental experimental procedures; Data S1). Full conversion of the 1:7 ratio of B and CU into HC[8]s is expected to direct 498 combinations to 12% and 82% of mixHC[8] and cycHC[8], respectively (Figure 1; Table S1).

The fact that solution-phase synthesis did not result in a statistical ratio of more favored HC[8]s encouraged us to study if the selectivity of mono-biotinylated mixHC[8] formation can be increased via tuning the conditions of the mechanosynthesis. To investigate the effect of multiple reaction parameters on the assembly of 8-membered macrocycles, we utilized RSM for experimental design and screening of reaction conditions.[37] The HPLC yields of mixHC[8] and cycHC[8] obtained after the aging step were plotted as 3D response surfaces, highlighting the conditions favorable for the assembly of mixHC[8] compared to cycHC[8] (Figures 2A, 2B, S3, and S4; Tables S2–S6). The ratio of monomers, loading of aqueous mineral acid ($HClO_4$), milling duration, and aging temperature, which affect macrocyclization,[8] were simultaneously explored.

The formation of mixHC[8] and cycHC[8] proved to be sensitive to the monomer ratio and acid loading (Figures 2A and 2B). Variations of the monomer ratios within the range of 1:5 to 1:15 did not significantly affect the yield of chimeric mixHC[8] (Figure 2A; Table S2); however, using an excess of CU clearly resulted in the enhanced generation of cycHC[8] (Figure 2B; Table S2). The quantity of $HClO_4$ appeared to be the vital parameter affecting the formation of mixHC[8]. The highest yields of mixHC[8] were attained within the specific range of $HClO_4$ loadings of 1.2–3.0 equiv (Figure 2A), while cycHC[8] was less dependent on the quantity of acid catalyst. This observation highlights the difference in formation of mixHC[8] and cycHC[8] in

response to varied reaction conditions. The impacts of milling time and aging temperature appeared to be less significant, and the optimal temperature for ripening mixHC[8] was found to range from 40°C to 65°C. RSM helped to reach a 20% yield of mixHC[8] under standard conditions—3 equiv of template, 1 h ball milling followed by 24 h aging at 60°C—selected for further optimization studies.

It was hypothesized that an alternative template could amplify the formation of the target macrocycle. The binding studies for the cycHC[8] receptor revealed the following ranking of anion affinity: SbF_6^- > PF_6^- > ReO_4^- > ClO_4^-.[11] The use of hexafluoroantimonate (SbF_6^-) as a template did not seem practical since $HSbF_6$ mainly exists as the HF/SbF_5 superacid system.[38,39] Hexafluorophosphate (PF_6^-), on the other hand, serves as an efficient template for the synthesis of homomeric cycHC[8] in solution.[18] Due to its advantageous templating potential, HPF_6 was chosen as an alternative reagent to mediate the solid-state synthesis of mixHC[8]. In addition, it is safer to handle than perchlorates, which are known for their undesirable oxidative, flammable, and explosive hazards.[40,41] Interestingly, the use of HPF_6 resulted in decreased formation of homomeric cycHC[8], contrary to an improved yield (28%) of mixHC[8] (Figure 2C; Table S7). Since the mixHC[8] assembly was highly sensitive to the quantity of acid (Figure 2A), we tested three hexafluorophosphate salts ($AgPF_6$, $[Cu(CH_3CN)_4]PF_6$, and KPF_6) as additives to partially substitute the acid while keeping the amount of template anion constant (Figure 2D; Table S7). Additionally, we anticipated that the Ag^+ and Cu^+ cations could serve as potential promoters for the generation of mixHC[8] due to their affinity for biotin.[42–44] As depicted in Figure 2D, the Ag^+ and Cu^+ salts had a negligible effect on the formation of mixHC[8] while improving the yield of homomeric cycHC[8] compared to the reaction with HPF_6. The latter points at the effective decrease in the concentration of antagonistic[45] CU-rich mixed oligomers, which reassembled and provided CU to cyclize into cycHC[8]. The best result was achieved with KPF_6, which afforded the highest yield of mixHC[8] (37%) with the accompanying formation of cycHC[8] (38%) (Figure 2D). Further variation of HPF_6/KPF_6 equivalence by RSM, however, did not improve the formation of mixHC[8] (Tables S8–S12; Figure S8). It was additionally confirmed that the stoichiometric ratio of the starting monomers provided the best mixHC[8] yield (Table S13). Once the key chemical parameters had been identified, the durations of ball milling and aging at moderately elevated temperatures were optimized, leading to the best 38% yield of mixHC[8] in a 4 h total reaction time (Tables S14 and S15; for conditions, see the Figure 1 caption).

The changes in the content of intermediates and products were analyzed by HRMS. Altogether, over 100 reaction species were identified in the crude reaction mixtures during different stages of covalent assembly and mapped based on MS signal intensities (Figures 3A and S9–S13; Tables S16 and S29; MatchMass tool[46]). The results display the dynamic changes in the composition of the reaction mixture during milling and aging. Biotin was found to be incorporated into different linear oligomers $(CU)_x(B)_y$ (x = 1 … 8, y = 1 … 4), as well as into a number of mono-, di-, tri-, and tetra-biotinylated mixHC[n]s (n = 6 … 8). Homomeric CU oligomers dominate at the initial phase of the polycondensation reaction (milling time: 5 min) and are kinetically favored products. Consequently, the milling time must be sufficient (60 min; Tables S14 and S15) to enable the accumulation of the slowly generated mixed biotin-containing chains. The content of the mixed oligomers (n = 6–8), which are essential for mixHC[n] formation, significantly increased after 45–60 min milling. This difference in the contents of the short- and long-milled mixtures emphasizes the dynamic shuffling of the monomers, which resulted in an increased random distribution of biotin upon prolonged milling. The low content of macrocycles in DCL

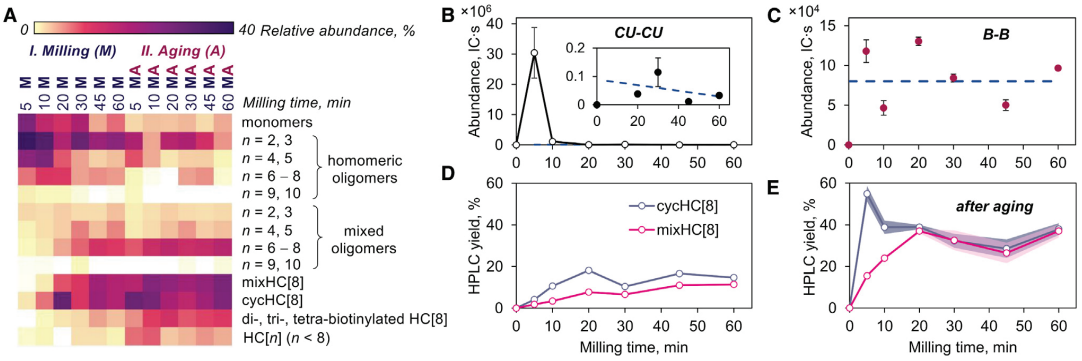

Figure 3. Dynamic covalent library composition and changes in the content of dimers and HC[8]s during mechanosynthesis

DCL composition summarized in a heatmap (A) based on MS abundance of the detected species (Tables S29 and S16; Figure S10); content of homomeric dimers CU-CU (B) and B-B (C) and HPLC yields of macrocycles (D and E) during milling and after aging. The content of the dimers is reported as the MS abundance for triplicate measurements ($n = 3$) ± standard deviation, and the linear fit is expressed as dashed lines. The yields of macrocycles are presented as mean values obtained in a series of replicated experiments ($2 \leq n \leq 4$) with confidence intervals. More details are provided in Figures S11–S15 and Table S19.

directly after milling can be attributed to the unfavorable complexation with the template,[11,17] most likely due to increased entropy during mechanical agitation. The macrocyclic products predominantly ripened at the aging stage, at which point the mixed and homomeric oligomers underwent additional, although less intense, crossover unit exchange. Moreover, crossover between monomers from macrocycles was observed under similar conditions using cycHC[*n*]s and biotin as the starting materials for mixHC[8] synthesis (Table S17), which confirms the dynamic character of the covalent self-assembly.

Further understanding of the dynamic processes and interconversion of intermediates occurring at the milling stage was obtained by tracking the fate of selected short oligomers (Figures 3B and 3C; Table S18). The changes in the content of characteristic dimers and trimers prior to and after the aging stage were determined by HPLC-MS analyses. The collected data confirmed that coupling between the CU monomers is kinetically preferred and occurs at the initial phase of the polycondensation reaction. Thus, the quantity of the CU-CU dimer drastically increased after 5 min of milling and subsequently underwent rapid decay (Figure 3B). Such fast dynamics and decay were absent for the biotin units, reflecting a major difference in the condensation between biotin and CU. In contrast to CU, the condensation of the biotin units to the respective dimer, B-B, reached its maximum at the beginning of the reaction and probably acts as a transient intermediate (Figures 3B and 3C). Similar behavior was observed for the respective trimers (Table S18). The yields of the macrocycles generated at the milling stage did not exceed 20% but greatly increased during aging (Figures 3D and 3E). Notably, the macrocyclic content in the aged mixtures is significantly affected by milling duration, when monomer shuffling occurs. Thus, aging of the short-milled (5 min) reaction mixture, which contained mainly homomeric CU oligomers, resulted in the ripening of cycHC[8] as the dominant product (55% yield), along with a minor quantity of mixHC[8] (16% yield). However, fast reversible C–N bond formation and cleavage during milling caused rapid dynamic changes in the oligomeric profile with a random distribution of the biotin units. Upon prolonged milling (60 min; Tables S14 and S15), the yield of mixHC[8] notably increased from 16% to 37%, with a concurrent decrease in the yield of cycHC[8] to 38%, resulting

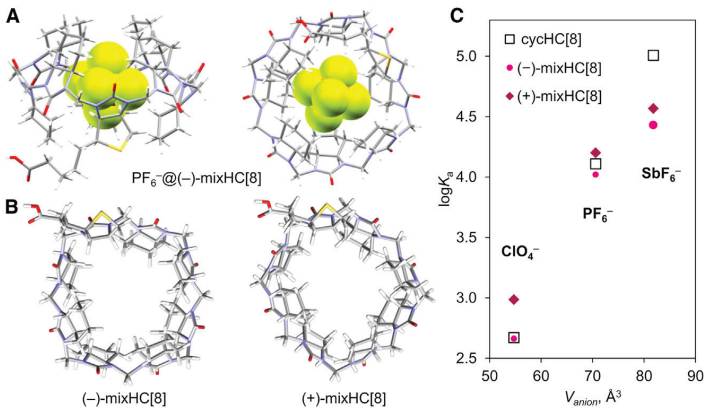

Figure 4. Structures of mixHC[8]s and data on anion binding

PF_6^-@(−)-mixHC[8] inclusion complex from SC-XRD (A) (CCDC: 2251913). DFT low-energy structures of (−)- and (+)-mixHC[8] diastereomers (B) (see the computational study in the supplemental experimental procedures; Data S2). Correlation between anion volumes (V_{anion}) and association constants ($\log K_a$) was determined by ITC for complexes with (TBA)ClO_4, (TBA)PF_6 (TBA = tetrabutylammonium), and $NaSbF_6$ salts in methanol using one-to-one binding model (C) (Table S6.1).

in a 1:1 product ratio. Finally, a close examination of the aging duration (Table S15) revealed that the maximum content of mixHC[8] was achieved in 3 h, when the templated self-assembly process was essentially complete.

The developed mechanochemical procedure significantly surpassed mixHC[8] synthesis in solution, yielding superior selectivity and conversion rates (Table S30). Solution-state processes are affected by diffusion, with diffusion constants varying for monomers, aggregates, and oligomeric intermediates due to size differences. In mechanochemistry, reaction rates do not directly depend on the molecular size of the intermediates but rather on the number of molecular collisions.[47] In addition to the chemical advantages, solvent-free synthesis produces less waste (PMI = 4) compared to the reaction in solution (PMI = 306) and is more sustainable based on the respective green metrics (Table S30).[32]

Diastereoisomeric (−)- and (+)-mixHC[8]s were synthesized via condensation of either (*R*,*R*)-CU or (*S*,*S*)-CU with (*S*,*S*,*R*)-B, isolated in 16% and 11% yields with high purity (88% and 90%, respectively), and characterized by nuclear magnetic resonance (NMR) and infrared spectroscopy (Figures S16–S32).

Anion binding properties

The encapsulation of suitably sized anionic guests by HC[*n*]s is likely governed by electrostatic and orbital interactions.[48] In addition, the anions form weak interactions with C-H groups of HC[*n*]s pointing inside the cavity.[49] Efficient anion recognition has been reported for bambusurils,[22,50–53] heterobambusurils,[54] biotinurils,[55,56] and cycHC[*n*]s.[11] We were fortunate to obtain single crystals of the PF_6^- inclusion complex with (−)-mixHC[8] (Figures 4A and S33–S39; Tables S19 and S20). A DFT modeling study of the mixHC[8] diastereomers (Figure S40; Tables S21–S24; Data S2) revealed clear differences in their conformations (Figure 4B; Data S2). The cavity, which is mainly surrounded by CU units, is mostly

distorted by the biotin position. Therefore, its influence on the anion binding properties was evaluated via comparison of the three HC[8] hosts.

Encapsulation of the selected anions by the mixHC[8]s was studied by ITC (Figures 4C and S51–S54; Table S25); the data for cycHC[8] were available from a previous work.[11] Complexation between the mono-biotinylated macrocycles and chaotropic anions (ClO_4^-, PF_6^-, and SbF_6^-) in methanol and a methanol-water mixture (1:1) occurred as an exothermic enthalpy-driven process. The association constants for PF_6^- were greater than that of ClO_4^- in both media, which explains the better templating properties of PF_6^-. Noticeably, the differences between the affinities of the three HC[8] derivatives are the smallest for the templating PF_6^- anion, while for ClO_4^- and SbF_6^-, either (+)-mixHC[8] or cycHC[8], respectively, exhibit stronger binding. The noted dissimilarities highlight distinctions in the cavities and point to the steric differences of these host compounds, which have potential in a diverse array of applications and unique guest-binding properties.

Selective capture of perchlorate by immobilized mixHC[8]

The mixHC[8] can be utilized to afford functional materials, which was showcased by the selective removal of perchlorates from contaminated soil samples. Perchlorate is a persistent pollutant that adversely affects human health by interfering with thyroid hormone production and occurs in soil, ground water, and food.[40,41] The accumulation of perchlorate in fertilizers, soil, and irrigation water leads to increased plant uptake and subsequent food-chain transfer.[57,58] This pollutant has been found in various environmental matrices and typically originates from human activities.

The carboxylate side chain of mixHC[8] enabled its facile covalent immobilization on the surface of 3-aminopropyl silica gel (APS; Figure 5A).[59] The resulting solid perchlorate-extracting material (mixHC[8]-APS) contained ca. 12% (w/w) of mixHC[8], based on infrared spectroscopic analysis (Figures 5B and S55). Once covalently attached to APS, the macrocycle remains in the solid phase even in the solvents where it is commonly soluble (i.e., dichloromethane, methanol) and can, therefore, be applied in solid-phase extraction. To prove the removal of perchlorate in the presence of other minerals, a regolith simulant[60] was employed as the matrix of the known composition and spiked with $(TBA)ClO_4$, imitating contamination with perchlorate (1% w/w). The obtained model mixture contained cations (Ca^{2+}, Mg^{2+}, Fe^{2+}, Fe^{3+}), oxides, and kosmotropic anions (SO_4^{2-}, CO_3^{2-}) but was essentially free of the organic matter (Table S26). According to ion chromatography analysis (Tables S27 and S28; Figures S56–S59), the methanolic extract of the contaminated matrix contained primarily perchlorate and sulfate, the latter arising from the $MgSO_4$ component (Table S26). Treatment of the methanolic extract with solid mixHC[8]-APS resulted in the complete removal of ClO_4^-, in contrast to non-modified APS, which adsorbed ca. 15% ClO_4^- (Figures 5C and S59; Table S28).

The extraction of sulfate occurred with similar efficiency (ca. 85%–97%) using both APS and mixHC[8]-APS materials, demonstrating that mixHC[8] is not the main contributor responsible for the capture of SO_4^{2-}. The absence of mixHC[8] affinity toward sulfate was additionally confirmed by an ITC experiment (Table S25; Figures S47 and S54).

The captured perchlorate was easily removed by washing mixHC[8]-APS material with water, taking advantage of the weaker binding in the aqueous medium, which demonstrates the potential for the material's reusability.[61]

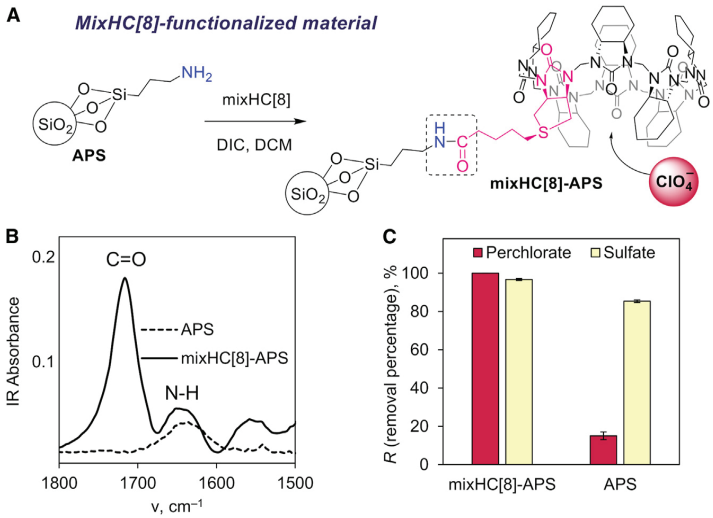

Figure 5. Derivatization of aminated silica by mixHC[8] and perchlorate removal efficiency of the obtained material

Immobilization of mixHC[8] on APS (A), DIC – *N,N′*-diisopropylcarbodiimide, and DCM (dichloromethane); characterization of material by infrared (IR) (B) and perchlorate removal from spiked mineral matrix using mixHC[8]-APS and non-modified APS, determined by ion chromatography (C). The error bars represent the standard deviation between the parallel experiments ($n \geq 2$) (isothermal calorimetric titration and immobilization of mixHC[8] on APS in the supplemental experimental procedures).

In conclusion, an efficient mechanochemical protocol for the synthesis of enantiopure mono-biotinylated HC[8]s was developed. The process involves two stages: (1) the mechanochemically assisted and acid-catalyzed polycondensation of D-biotin, (*R,R*)- or (*S,S*)-CU, and formaldehyde and (2) the aging step, in which the template-driven covalent self-assembly of oligomers into macrocycles takes place. Screening experiments uncovered the key process and chemical parameters affecting the assembly: the ratio of the monomers, the loading of the acid catalyst, and the nature of the templating anion. The present study offers insight into the complex mixture of oligomeric intermediates, including their interconversion and self-organization processes en route to the macrocyclic products. HPLC-MS analysis of short oligomers revealed differences in condensation kinetics of paraformaldehyde with biotin and CU into homomeric dimers and trimers under mechanochemical agitation. The faster condensation of CU led to amplification of the homomeric cycHC[8] during the aging of shortly agitated reaction mixtures. On the contrary, upon prolonged ball milling, which ensures sufficient shuffling of monomers, higher efficiency in the formation of the chimeric mixHC[8] in 38% yield was achieved. The mechanochemically driven solid-state approach allowed for the fine-tuning of the composition of the rich DCL and directing covalent self-assembly processes beyond statistical distribution. Diastereomeric (–)- and (+)-mixHC[8]s were isolated and their structures characterized by DFT, NMR, and SC-XRD methods. Furthermore, the comparison of their affinities toward chaotropic anions pointed at specific binding differences, which makes the chimeric family of HC[8] appealing for host-guest chemistry. The biotin carboxylate group of the mixHC[8] enabled its facile covalent immobilization on aminated silica. The functional material obtained was employed in the selective capture of anions, as

demonstrated by the complete removal of perchlorate from an extract of a mineral model mixture. Further applications of these chiral chimeric hemicucurbiturils are currently being studied.

EXPERIMENTAL PROCEDURES

Resource availability

Lead contact

Further information and requests for resources should be directed to and will be fulfilled by the lead contact, Riina Aav (riina.aav@taltech.ee).

Materials availability

All materials generated in this study are available from the lead contact without restrictions for research purposes.

Data and code availability

All data supporting this study's findings are included in the article and its supplemental information and are also available from the authors upon request. Crystallographic data for the structures reported in this paper have been deposited at the Cambridge Crystallographic Data Center under CCDC: 2251913. Copies of these data can be obtained free of charge via www.ccdc.cam.ac.uk/data_request/cif.

SUPPLEMENTAL INFORMATION

Supplemental information can be found online at https://doi.org/10.1016/j.xcrp.2024.102161.

ACKNOWLEDGMENTS

The authors would like to thank Jasper Adamson and Indrek Reile for input on the NMR analysis. The research by R.A., L.U., D.K., J.S.W., and K.R. was funded by the European Union's H2020- FETOPEN grant 828779 (INITIO). E.S.-T., T.J., K.-M.L., J.V.N., J.M., R.R., and M.O. were financed by Estonian Research Council grants PRG399 and PRG2169. R.A. was funded by the Ministry of Education and Research through Centre of Excellence in Circular Economy for Strategic Mineral and Carbon Resources (01.01.2024–31.12.2030, TK228). The authors also acknowledge COST Action CA18112 "Mechanochemistry for Sustainable Industry" for supporting research in mechanochemistry.

AUTHOR CONTRIBUTIONS

All authors contributed to the manuscript's preparation and have provided their approval for the final version of the manuscript. The authors' specific contributions are as follows: E.S.-T. was the main contributor for the development of the synthesis and mixHC[8] characterization and participated in binding studies; T.J. was the main contributor of the chemical analysis, binding, immobilization, and perchlorate removal studies; P.T. and S.P. contributed to perchlorate removal; K.-M.L., K.S., and J.V.N. contributed to the synthesis; J.M., J.S.W., and K.R. contributed to SC-XRD analysis; R.R. and M.Ö. contributed to computational studies; L.U. contributed to the script for MS data analysis and binding studies; M.V. contributed to the assessment of combinatorics; V.R. contributed to NMR analysis; D.K. contributed to conceptualization of the synthesis, perchlorate removal, and assessment of green metrics; and R.A. contributed to conceptualization of the overall research, data analysis, writing, and supervision.

DECLARATION OF INTERESTS

This research has been filed for patent application EP23181344.5 and PCT/IB2024/056236. Authors: R.A., E.S.-T., T.J., Tatsiana Nikonovich, D.K., and L.U. Title: "Method of preparation of chimeric HC[n]s, derivatives, and uses thereof," priority date: June 26, 2023.

Received: May 22, 2024
Revised: July 15, 2024
Accepted: July 29, 2024
Published: August 20, 2024

REFERENCES

1. Schnitzer, T., Preuss, M.D., van Basten, J., Schoenmakers, S.M.C., Spiering, A.J.H., Vantomme, G., and Meijer, E.W. (2022). How subtle changes can make a difference: Reproducibility in complex supramolecular systems. Angew. Chem. *61*, e202206738. https://doi.org/10.1002/ange.202206738.

2. Yamaoki, Y., Nagata, T., Kondo, K., Sakamoto, T., Takami, S., and Katahira, M. (2022). Shedding light on the base-pair opening dynamics of nucleic acids in living human cells. Nat. Commun. *13*, 7143. https://doi.org/10.1038/s41467-022-34822-4.

3. Kwon, T.W., Song, B., Nam, K.W., and Stoddart, J.F. (2022). Mechanochemical enhancement of the structural stability of pseudorotaxane intermediates in the synthesis of rotaxanes. J. Am. Chem. Soc. *144*, 12595–12601. https://doi.org/10.1021/jacs.2c00515.

4. Dračínský, M., Hurtado, C.S., Masson, E., and Kaleta, J. (2021). Stuffed pumpkins: Mechanochemical synthesis of host–guest complexes with cucurbit[7]uril. Chem. Commun. *57*, 2132–2135. https://doi.org/10.1039/D1CC00240F.

5. Friščić, T., Mottillo, C., and Titi, H.M. (2020). Mechanochemistry for synthesis. Angew. Chem. *132*, 1030–1041. https://doi.org/10.1002/ange.201906755.

6. Cuccu, F., De Luca, L., Delogu, F., Colacino, E., Solin, N., Mocci, R., and Porcheddu, A. (2022). Mechanochemistry: New tools to navigate the uncharted territory of "impossible" reactions. ChemSusChem *15*, e202200362. https://doi.org/10.1002/cssc.202200362.

7. Reynes, J.F., Isoni, V., and García, F. (2023). Tinkering with mechanochemical tools for scale-up. Angew. Chem., Int. Ed. Engl. *62*, e202300819. https://doi.org/10.1002/anie.202300819.

8. Kaabel, S., and Aav, R. (2018). Templating effects in the dynamic chemistry of cucurbiturils and hemicucurbiturils. Isr. J. Chem. *58*, 296–313. https://doi.org/10.1002/ijch.201700106.

9. Lehn, J.-M. (1999). Dynamic combinatorial chemistry and virtual combinatorial libraries. Chem. Eur J. *5*, 2455–2463. https://doi.org/10.1002/(SICI)1521-3765(19990903)5:9<2455::AID-CHEM2455>3.0.CO;2-H.

10. Corbett, P.T., Leclaire, J., Vial, L., West, K.R., Wietor, J.-L., Sanders, J.K.M., and Otto, S. (2006). Dynamic combinatorial chemistry. Chem. Rev. *106*, 3652–3711. https://doi.org/10.1021/cr020452p.

11. Kaabel, S., Adamson, J., Topić, F., Kiesilä, A., Kalenius, E., Öeren, M., Reimund, M., Prigorchenko, E., Lõokene, A., Reich, H.J., et al. (2017). Chiral hemicucurbit[8]uril as an anion receptor: Selectivity to size, shape and charge distribution. Chem. Sci. *8*, 2184–2190. https://doi.org/10.1039/C6SC05058A.

12. Andersen, N.N., Lisbjerg, M., Eriksen, K., and Pittelkow, M. (2018). Hemicucurbit[n]urils and their derivatives – Synthesis and applications. Isr. J. Chem. *58*, 435–448. https://doi.org/10.1002/ijch.201700129.

13. Lisbjerg, M., Jessen, B.M., Rasmussen, B., Nielsen, B.E., Madsen, A.Ø., and Pittelkow, M. (2014). Discovery of a cyclic 6 + 6 hexamer of D-biotin and formaldehyde. Chem. Sci. *5*, 2647–2650. https://doi.org/10.1039/C4SC00990H.

14. Havel, V., Yawer, M.A., and Sindelar, V. (2015). Real-time analysis of multiple anion mixtures in aqueous media using a single receptor. Chem. Commun. *51*, 4666–4669. https://doi.org/10.1039/C4CC10108A.

15. Yawer, M.A., Havel, V., and Sindelar, V. (2015). A bambusuril macrocycle that binds anions in water with high affinity and selectivity. Angew. Chem., Int. Ed. Engl. *54*, 276–279. https://doi.org/10.1002/anie.201409895.

16. Lizal, T., and Sindelar, V. (2018). Bambusuril anion receptors. Isr. J. Chem. *58*, 326–333. https://doi.org/10.1002/ijch.201700111.

17. Kaabel, S., Stein, R.S., Fomitšenko, M., Järving, I., Friščić, T., and Aav, R. (2019). Size-control by anion templating in mechanochemical synthesis of hemicucurbiturils in the solid state. Angew. Chem., Int. Ed. Engl. *58*, 6230–6234. https://doi.org/10.1002/anie.201813431.

18. Prigorchenko, E., Öeren, M., Kaabel, S., Fomitšenko, M., Reile, I., Järving, I., Tamm, T., Topić, F., Rissanen, K., and Aav, R. (2015). Template-controlled synthesis of chiral cyclohexylhemicucurbit[8]uril. Chem. Commun. *51*, 10921–10924. https://doi.org/10.1039/C5CC04101E.

19. Zeng, Q., Long, Q., Lu, J., Wang, L., You, Y., Yuan, X., Zhang, Q., Ge, Q., Cong, H., and Liu, M. (2021). Synthesis of a novel aminobenzene-containing hemicucurbituril and its fluorescence spectral properties with ions. Beilstein J. Org. Chem. *17*, 2840–2847. https://doi.org/10.3762/bjoc.17.195.

20. Wang, L., Han, J., Pan, R., Yuan, X., You, Y., Cen, X., Zhang, Q., Ge, Q., Cong, H., and Liu, M. (2022). Synthesis of hybrid thiohemicucurbiturils. Tetrahedron Lett. *101*, 153918. https://doi.org/10.1016/j.tetlet.2022.153918.

21. Maršálek, K., and Šindelář, V. (2020). Monofunctionalized bambus[6]urils and their conjugates with crown ethers for liquid–liquid extraction of inorganic salts. Org. Lett. *22*, 1633–1637. https://doi.org/10.1021/acs.orglett.0c00216.

22. De Simone, N.A., Chvojka, M., Lapešová, J., Martínez-Crespo, L., Slávik, P., Sokolov, J., Butler, S.J., Valkenier, H., and Šindelář, V. (2022). Monofunctionalized fluorinated bambusurils and their conjugates for anion transport and extraction. J. Org. Chem. *87*, 9829–9838. https://doi.org/10.1021/acs.joc.2c00870.

23. Del Mauro, A., Lapešová, J., Rando, C., and Šindelář, V. (2024). Merging bambus[6]uril and biotin[6]uril into an enantiomerically pure monofunctionalized hybrid macrocycle. Org. Lett. *26*, 106–109. https://doi.org/10.1021/acs.orglett.3c03715.

24. Langerreiter, D., Kostiainen, M.A., Kaabel, S., and Anaya-Plaza, E. (2022). A greener route to blue: Solid-state synthesis of phthalocyanines. Angew. Chem., Int. Ed. Engl. *61*, e202209033. https://doi.org/10.1002/anie.202209033.

25. Pascu, M., Ruggi, A., Scopelliti, R., and Severin, K. (2013). Synthesis of borasiloxane-based macrocycles by multicomponent condensation reactions in solution or in a ball mill. Chem. Commun. *49*, 45–47. https://doi.org/10.1039/C2CC37538A.

26. Sim, Y., Shi, Y.X., Ganguly, R., Li, Y., and García, F. (2017). Mechanochemical synthesis of phosphazane-based frameworks. Chem. Eur J. *23*, 11279–11285. https://doi.org/10.1002/chem.201701619.

27. Xi, H.-T., Zhao, T., Sun, X.-Q., Miao, C.-B., Zong, T., and Meng, Q. (2013). Rapid and efficient solvent-free synthesis of cyclophanes based on bipyridinium under mechanical ball milling. RSC Adv. *3*, 691–694. https://doi.org/10.1039/C2RA22802E.

28. Kunde, T., Pausch, T., Guńka, P.A., Krzyżanowski, M., Kasprzak, A., and Schmidt,

B.M. (2022). Fast, solvent-free synthesis of ferrocene-containing organic cages via dynamic covalent chemistry in the solid state. Chem. Sci. *13*, 2877–2883. https://doi.org/10.1039/D1SC06372C.

29. Shy, H., Mackin, P., Orvieto, A.S., Gharbharan, D., Peterson, G.R., Bampos, N., and Hamilton, T.D. (2014). The two-step mechanochemical synthesis of porphyrins. Faraday Discuss *170*, 59–69. https://doi.org/10.1039/C3FD00140G.

30. Su, Q., and Hamilton, T.D. (2019). Extending mechanochemical porphyrin synthesis to bulkier aromatics: Tetramesitylporphyrin. Beilstein J. Org. Chem. *15*, 1149–1153. https://doi.org/10.3762/bjoc.15.111.

31. MathWorld–A Wolfram Web Resource. Weisstein, E. W. Necklace. https://mathworld.wolfram.com/Necklace.html.

32. McElroy, C.R., Constantinou, A., Jones, L.C., Summerton, L., and Clark, J.H. (2015). Towards a holistic approach to metrics for the 21st century pharmaceutical industry. Green Chem. *17*, 3111–3121. https://doi.org/10.1039/C5GC00340G.

33. Friščić, T., Childs, S.L., Rizvi, S.A.A., and Jones, W. (2009). The role of solvent in mechanochemical and sonochemical cocrystal formation: A solubility-based approach for predicting cocrystallisation outcome. CrystEngComm *11*, 418–426. https://doi.org/10.1039/B815174A.

34. Do, J.-L., and Friščić, T. (2017). Chemistry 2.0: Developing a new, solvent-free system of chemical synthesis based on mechanochemistry. Synlett *28*, 2066–2092. https://doi.org/10.1055/s-0036-1590854.

35. Belenguer, A.M., Lampronti, G.I., De Mitri, N., Driver, M., Hunter, C.A., and Sanders, J.K.M. (2018). Understanding the influence of surface solvation and structure on polymorph stability: A combined mechanochemical and theoretical approach. J. Am. Chem. Soc. *140*, 17051–17059. https://doi.org/10.1021/jacs.8b08549.

36. Prigorchenko, E., Kaabel, S., Narva, T., Baškir, A., Fomitšenko, M., Adamson, J., Järving, I., Rissanen, K., Tamm, T., and Aav, R. (2019). Formation and trapping of the thermodynamically unfavoured inverted-hemicucurbit[6]uril. Chem. Commun. *55*, 9307–9310. https://doi.org/10.1039/C9CC04990H.

37. Myers, R.H., Montgomery, D.C., and Anderson-Cook, C.M. (2016). Response Surface Methodology: Process and Product Optimization Using Designed Experiments (John Wiley & Sons).

38. Czapla, M., and Skurski, P. (2015). Strength of the Lewis–Brønsted superacids containing In, Sn, and Sb and the electron binding energies of their corresponding superhalogen anions. J. Phys. Chem. A *119*, 12868–12875. https://doi.org/10.1021/acs.jpca.5b10205.

39. Bour, C., Guillot, R., and Gandon, V. (2015). First evidence for the existence of hexafluoroantimonic(V) acid. Chem. Eur J. *21*, 6066–6069. https://doi.org/10.1002/chem.201500334.

40. Urbansky, E.T. (2002). Perchlorate as an environmental contaminant. Environ. Sci. Pollut. Res. Int. *9*, 187–192. https://doi.org/10.1007/BF02987487.

41. Kumarathilaka, P., Oze, C., Indraratne, S.P., and Vithanage, M. (2016). Perchlorate as an emerging contaminant in soil, water and food. Chemosphere *150*, 667–677. https://doi.org/10.1016/j.chemosphere.2016.01.109.

42. Sigel, H., and Scheller, K.H. (1982). Metal ion complexes of D-biotin in solution. Stability of the stereoselective thioether coordination. J. Inorg. Biochem. *16*, 297–310. https://doi.org/10.1016/S0162-0134(00)80266-4.

43. Aoki, K., and Saenger, W. (1983). Interactions of biotin with metal ions. X-ray crystal structure of the polymeric biotin-silver(i) nitrate complex: metal bonding to thioether and ureido carbonyl groups. J. Inorg. Biochem. *19*, 269–273. https://doi.org/10.1016/0162-0134(83)85031-4.

44. Altaf, M., and Stoeckli-Evans, H. (2013). Chiral one- and two-dimensional silver(I)–biotin coordination polymers. Acta Crystallogr. C *69*, 127–137. https://doi.org/10.1107/S0108270113000322.

45. Lehn, J.-M. (2013). Perspectives in chemistry—steps towards complex matter. Angew. Chem., Int. Ed. Engl. *52*, 2836–2850. https://doi.org/10.1002/anie.201208397.

46. Ustrnul, L., Jarg, T., Jantson, M., Osadchuk, I., Anton, L., and Aav, R. (2024). MatchMass: A web-based tool for efficient mass spectrometry data analysis. Preprint at ChemRxiv. https://doi.org/10.26434/chemrxiv-2024-9j8n7.

47. Ma, X., Yuan, W., Bell, S.E.J., and James, S.L. (2014). Better understanding of mechanochemical reactions: Raman monitoring reveals surprisingly simple 'pseudo-fluid' model for a ball milling reaction. Chem. Commun. *50*, 1585–1587. https://doi.org/10.1039/C3CC47898J.

48. Ortolan, A.O., Madureira, L., Rodríguez-Kessler, P.L., Maturana, R.G., Olea Ulloa, C., Caramori, G.F., Parreira, R.L., and Muñoz-Castro, A. (2023). The nature of the central halide encapsulation in bambusuril hosts (BU[6]). Structural and interaction energy insights in BU[6]·X− (X = Cl, Br, I) from relativistic DFT calculations. Inorg. Chim. Acta. *555*, 121596. https://doi.org/10.1016/j.ica.2023.121596.

49. Öeren, M., Shmatova, E., Tamm, T., and Aav, R. (2014). Computational and ion mobility MS study of (All-S)-Cyclohexylhemicucurbit[6]uril structure and complexes. Phys. Chem. Chem. Phys. *16*, 19198–19205. https://doi.org/10.1039/C4CP02202E.

50. Jašíková, L., Rodrigues, M., Lapešová, J., Lízal, T., Šindelář, V., and Roithová, J. (2019). Bambusurils as a mechanistic tool for probing anion effects. Faraday Discuss *220*, 58–70. https://doi.org/10.1039/C9FD00038K.

51. Sokolov, J., Štefek, A., and Šindelář, V. (2020). Functionalized chiral bambusurils: Synthesis and host-guest interactions with chiral carboxylates. ChemPlusChem *85*, 1307–1314. https://doi.org/10.1002/cplu.202000261.

52. Itterheimová, P., Bobacka, J., Šindelář, V., and Lubal, P. (2022). Perchlorate solid-contact ion-selective electrode based on dodecabenzylbambus[6]uril. Chemosensors *10*, 115. https://doi.org/10.3390/chemosensors10030115.

53. Rando, C., Vázquez, J., Sokolov, J., Kokan, Z., Nečas, M., and Šindelář, V. (2022). Highly efficient and selective recognition of dicyanoaurate(I) by a bambusuril macrocycle in water. Angew. Chem., Int. Ed. Engl. *61*, e202210184. https://doi.org/10.1002/anie.202210184.

54. Reany, O., Mohite, A., and Keinan, E. (2018). Hetero-bambusurils. Isr. J. Chem. *58*, 449–460. https://doi.org/10.1002/ijch.201700138.

55. Lisbjerg, M., Nielsen, B.E., Milhøj, B.O., Sauer, S.P.A., and Pittelkow, M. (2015). Anion binding by biotin[6]uril in water. Org. Biomol. Chem. *13*, 369–373. https://doi.org/10.1039/C4OB02211D.

56. Andersen, N.N., Eriksen, K., Lisbjerg, M., Ottesen, M.E., Milhøj, B.O., Sauer, S.P.A., and Pittelkow, M. (2019). Entropy/enthalpy compensation in anion binding: Biotin[6]uril and biotin-l-sulfoxide[6]uril reveal strong solvent dependency. J. Org. Chem. *84*, 2577–2584. https://doi.org/10.1021/acs.joc.8b02797.

57. Calderón, R., Palma, P., Arancibia-Miranda, N., Kim, U.-J., Silva-Moreno, E., and Kannan, K. (2022). Occurrence, distribution and dynamics of perchlorate in soil, water, fertilizers, vegetables and fruits and associated human exposure in Chile. Environ. Geochem. Health *44*, 527–535. https://doi.org/10.1007/s10653-020-00680-6.

58. Chen, Y., Zhu, Z., Wu, X., Zhang, D., Tong, J., Lin, Y., Yin, L., Li, X., Zheng, Q., and Lu, S. (2022). A nationwide investigation of perchlorate levels in staple foods from China: Implications for human exposure and risk assessment. J. Hazard Mater. *439*, 129629. https://doi.org/10.1016/j.jhazmat.2022.129629.

59. Tabakci, M. (2008). Immobilization of calix[6]arene bearing carboxylic acid and amide groups on aminopropyl silica gel and its sorption properties for Cr(VI). J. Inclusion Phenom. Macrocycl. Chem. *61*, 53–60. https://doi.org/10.1007/s10847-007-9392-2.

60. Cannon, K.M., Britt, D.T., Smith, T.M., Fritsche, R.F., and Batcheldor, D. (2019). Mars global simulant MGS-1: A rocknest-based open standard for basaltic Martian regolith simulants. Icarus *317*, 470–478. https://doi.org/10.1016/j.icarus.2018.08.019.

61. Shalima, T., Mishra, K.A., Kaabel, S., Ustrnul, L., Bartkova, S., Tõnsuaadu, K., Heinmaa, I., and Aav, R. (2021). Cyclohexanohemicucurbit[8]uril inclusion complexes with heterocycles and selective extraction of sulfur compounds from water. Front. Chem. *9*, 786746. https://doi.org/10.3389/fchem.2021.786746.

Curriculum vitae

Personal data

Name: Jevgenija Tamm (Martõnova)
Date of birth: 03.04.1996
Place of birth: Tartu, Estonia
Citizenship: Estonian

Contact data

E-mail: jevgenijatamm@gmail.com; jevgenija.tamm@ravimiamet.ee

Education

2020–2025 Tallinn University of Technology, Chemistry, PhD
2018–2020 Tallinn University of Technology, Applied Chemistry and Biotechnology, MSc, *cum laude*
2015–2018 Tallinn University of Technology, Applied Chemistry and Biotechnology, BSc
2012–2015 Tallinn Secondary School of Science

Language competence

Estonian native language
Russian native language
English fluent
German beginner

Professional employment

05.05.2025-… State Agency of Medicines, Department of Medical Devices, specialist (1,0)
01.09.2024–... Tallinn University of Technology, School of Science, Department of Chemistry and Biotechnology, Junior Research Fellow (0.50)
01.10.2023–31.08.2024 Tallinn University of Technology, School of Science, Department of Chemistry and Biotechnology, Junior Research Fellow (0.20)
15.09.2020–30.09.2023 Tallinn University of Technology, School of Science, Department of Chemistry and Biotechnology, Junior Research Fellow (0.10)
2019–2023 Tallinn Südalinna School, Chemistry teacher

Honours & awards

2022, Jevgenija Martõnova, Dora Plus T1.1 grant for participating in 1st International Supramolecular Chemistry Summer School
2022, Jevgenija Martõnova, ASTRA "TUT Institutional Development Programme for 2016-2022" Graduate school of Functional Materials and Technologies (2014-2020.4.01.16-0032) support for participating in Balticum Organicum Syntheticum conference
2021, Jevgenija Martõnova, Dora Plus T2.1 grant supporting a study visit to the University of Jyväskylä
2021, Jevgenija Martõnova, ASTRA "TUT Institutional Development Programme for 2016-2022" Graduate school of Functional Materials and Technologies (2014-2020.4.01.16-0032) support for travelling to Lund to Max IV Synchrotron

Elulookirjeldus

Isikuandmed

Nimi: Jevgenija Tamm (Martõnova)
Sünniaeg: 03.04.1996
Sünnikoht: Tartu, Eesti
Kodakondsus: eestlane

Kontaktandmed

E-post: jevgenijatamm@gmail.com; jevgenija.tamm@ravimiamet.ee

Hariduskäik

2020–2025 Tallinna Tehnikaülikool, Keemia, PhD
2018–2020 Tallinna Tehnikaülikool, Rakenduskeemia ja biotehnoloogia, MSC, *cum laude*
2015–2018 Tallinna Tehnikaülikool, Rakenduskeemia ja biotehnoloogia, BSC
2012–2015 Tallinna Reaalkool

Keelteoskus

Eesti keel Emakeel
Vene keel Emakeel
Inglise keel Kõrgtase
Saksa keel Algtase

Teenistuskäik

05.05.2025-… Ravimiamet, Meditsiiniseadmete osakond, spetsialist (1,0)
01.09.2024–... Tallinna Tehnikaülikool, Loodusteaduskond, Keemia ja biotehnoloogia instituut, Doktorant-nooremteadur (0,50)
01.10.2023–31.08.2024 Tallinna Tehnikaülikool, Loodusteaduskond, Keemia ja biotehnoloogia instituut, doktorant-nooremteadur (0,20)
15.09.2020–30.09.2023 Tallinna Tehnikaülikool, Loodusteaduskond, Keemia ja biotehnoloogia instituut, doktorant-nooremteadur (0,10)
2019–2023 Tallinn Südalinna Kool, keemiaõpetaja

Teaduspreemiad ja tunnustused

2022, Jevgenija Martõnova, Dora Plus T1.1 grant for participating in 1st International Supramolecular Chemistry Summer School
2022, Jevgenija Martõnova, ASTRA "TUT Institutional Development Programme for 2016-2022" Graduate school of Functional Materials and Technologies (2014-2020.4.01.16-0032) support for participating in Balticum Organicum Syntheticum conference
2021, Jevgenija Martõnova, Dora Plus T2.1 grant supporting a study visit to the University of Jyväskylä
2021, Jevgenija Martõnova, ASTRA "TUT Institutional Development Programme for 2016-2022" Graduate school of Functional Materials and Technologies (2014-2020.4.01.16-0032) support for travelling to Lund to Max IV Synchrotron

ISSN 2585-6901 (PDF)
ISBN 978-9916-80-556-5 (PDF)